國 立 中 央 大 學

物理研究所

博士論文

Photoproduction of Λ and Σ^0 hyperons off protons with linearly polarized photons at $E_\gamma = 1.5 - 3.0$ GeV

研究生: 許軒豪

指導教授: 林宗泰

共同指導: 章文箴
郡英輝

中 華 民 國 一百零七 年 五 月

國 立 中 央 大 學

物理研究所

博士論文

Photoproduction of Λ and Σ^0 hyperons off protons with linearly polarized photons at $E_\gamma = 1.5 - 3.0$ GeV

研究生: 許軒豪

指導教授: 林宗泰

共同指導: 章文箴
郡英輝

中 華 民 國 一百零七 年 五 月

國立中央大學圖書館
碩博士論文電子檔授權書

(104 年 5 月最新修正版)

本授權書授權本人撰寫之碩/博士學位論文全文電子檔(不包含紙本、詳備註 1 說明)，在「國立中央大學圖書館博碩士論文系統」。(以下請擇一勾選)

(✓)同意 (立即開放)

(　　)同意 (請於西元 _____年_____月_____日開放)

(　　)不同意，原因是：_____

在國家圖書館「臺灣博碩士論文知識加值系統」

(✓)同意 (立即開放)

(　　)同意 (請於西元 _____年_____月_____日開放)

(　　)不同意，原因是：_____

以非專屬、無償授權國立中央大學、台灣聯合大學系統圖書館與國家圖書館，基於推動「資源共享、互惠合作」之理念，於回饋社會與學術研究之目的，得不限地域、時間與次數，以紙本、微縮、光碟及其它各種方法將上列論文收錄、重製、與利用，並得將數位化之上列論文與論文電子檔以上載網路方式，提供讀者基於個人非營利性質之線上檢索、閱覽、下載或列印。

研究生簽名: 許軒豪　　學號：962402010

論文名稱:Photoproduction of Λ and Σ^0 hyperons off protons with linearly polarized photons at E_γ=1.5-3.0 GeV

指導教授姓名：林宗泰

系所 ：物理所 ☑博士班 ☐碩士班

填單日期：2018,03,26

備註：

1. 本授權書之授權範圍僅限**電子檔**，紙本論文部分依著作權法第 15 條第 3 款之規定，採推定原則即預設同意圖書館得公開上架閱覽，如您有申請專利或投稿等考量，不同意紙本上架陳列，須另行加填申請書，詳細說明與紙本申請書下載請至本館數位博碩論文網頁。
2. 本授權書請填寫並**親筆**簽名後，裝訂於各紙本論文封面後之次頁（全文電子檔內之授權書簽名，可用電腦打字代替）。
3. 讀者基於個人非營利性質之線上檢索、閱覽、下載或列印上列論文，應遵守著作權法規定。

國立中央大學博士班研究生

論文指導教授推薦書

物理 學系/研究所 許軒豪 研究生所提之論文 Photoproduction of Λ and Σ^0 hyperons off protons with linearly polarized photons at E_γ=1.5-3.0 GeV 係由本人指導撰述，同意提付審查。

指導教授 林宗泰 (簽章)

107 年 2 月 26 日

104.07.24

國立中央大學博士班研究生

論文口試委員審定書

物理 學系/研究所 許軒豪 研究生所提之論文 Photoproduction of Λ and Σ^0 hyperons off protons with linearly polarized photons at E_γ=1.5-3.0 GeV 經本委員會審議，認定符合博士資格標準。

學位考試委員會召集人 陳鎧勳

委員 袁文成

林宗泰

王名儒

郭家銘

高涉文

中華民國 107 年 03 月 23 日

104.07.24

Photoproduction of Λ and Σ^0 hyperons off protons with linearly polarized photons at $E_\gamma = 1.5 - 3.0$ GeV

中文摘要

本論文詳細記述在SPring-8實驗設施中，測量$\gamma p \to K^+\Lambda$ 以及 $\gamma p \to K^+\Sigma^0$反應及其結果。 除了當K^+介子分布在前方角度時的微分反應截面(differential cross sections) 量測外，我們亦提供了光束不對稱(photon-beam asymmetry) 的量測結果。 在入射光能量大於2.4 GeV時的光束不對稱是新的量測結果。

本實驗之資料取得時間於2007年10月6日起至同月18日止，並於同年11月8日起至12月17日止。 實驗資料之取得，係利用光子束能量介於1.5至3.0 GeV之間之線性偏振標記光子束(linearly-polarized tagged-photon beams)，撞擊液態氫之靶材，並探測分布於前方角度的K^+介子。 實驗用的探測儀器是LEPS探測儀(spectrometer)。

利用K^+介子的未量測質量譜(missing-mass spectra)，可以標定出Λ 和 Σ^0的反應。 藉由量測飛行時間，動量以及飛行距離我們可以重建K^+介子之質量。我們可以藉由選定3倍標準差的區間，來作爲K^+介子的粒子標定。此處之標準差乃由動量相關之質量解析度得出。 在高動量的量測區間中，我們利用預測背景譜線的方式來預測錯誤標定的π^+介子對實驗數據可能造成的影響。 而利用蒙地卡羅法產生之模擬數據與實驗數據之一致性亦經由校準t0來達成。

當入射光子束的能量提升時，$\gamma p \to K^+\Lambda$ 以及 $\gamma p \to K^+\Sigma^0$之微分反應截面都呈現緩慢的下降。 在所有的量測能量範圍裡，Λ的微分反應截面都與量測到的K^+介子角度有正相關，即角度越往前，其微分反應截面越高。此一正相關，爲t-通道反應的典型特徵。 而Σ^0的微分反應截面則沒有與量測到的K^+介子角度分布有顯著相關。此一現象代表了t-通道反應可能在此反應並不顯著，並且揭示s-通道之核子共振態(nucleon resonance) 反應可能在此有相當的重要性。

光束不對稱在兩個反應的所有探測區間中的結果都是正值，如此現象可能可以顯示K^*爲t-通道反應過程中的主要交換粒子。 兩個反應的光束不對稱結果皆與入射光束能量有極度的正相關，即入射光束能量越大，其光束不對稱數值越大，其最大值截止於+0.6。 在$K^+\Sigma^0$的反應中，其光束不對稱的測量結果皆大於$K^+\Lambda$反應的結果。 對比於

基於Regge-trajectory 的t-通道模型以及基於核子共振態的模型之理論預測，顯示出t-通道反應在超子光致產生(hyperon photoproduction)過程中， 於此能量範圍的產生機制提供了主要的貢獻，以及核子共振態在此亦有不可忽略的貢獻。

Photoproduction of Λ and Σ^0 hyperons off protons with linearly polarized photons at $E_\gamma = 1.5 - 3.0$ GeV

Abstract

This thesis presents measurements of the reactions $\gamma p \to K^+\Lambda$ and $\gamma p \to K^+\Sigma^0$ at SPring-8. In addition to differential cross sections, the photon-beam asymmetries were measured at forward K^+ production angles. The photon-beam asymmetry in the range of $E_\gamma > 2.4$ GeV were measured first time.

The data were collected from October 6th to October 18th, 2007 and November 8th to December 17th, 2007. Data were obtained at SPring-8 using a linearly-polarized tagged-photon beams in the range of $E_\gamma = 1.5 - 3.0$ GeV with a liquid hydrogen target. Particles produced at the target were detected with the LEPS spectrometer.

The Λ and Σ^0 production was identified in K^+ missing-mass spectra. The particle identification (PID) of the K^+ is done by a 3σ cut on their reconstructed mass based on the measured time of flight, momentum and path length, where σ is the momentum dependent mass resolution. The degree of π^+ contamination in the selected K^+ increased for particles of larger momenta. A side-band method has been applied to estimate the miss-identified π^+ in K^+ at high-momentum region. The t0 correction has been applied to improve the consistency of the mean value of mass squared between Monte-Carlo and real data.

With increasing photon energy, the cross sections for both the $\gamma p \to K^+\Lambda$ and $\gamma p \to K^+\Sigma^0$ reactions decrease slowly. The forward peaking in the angular distributions of cross sections, a characteristic feature of t-channel exchange, is observed for the production of Λ in the whole observed energy range. That Σ^0 production did not show the forward peaking behaviour reflects a less dominant role of t-channel contribution and the importance of s-channel nucleon resonance contributions in this channel.

The photon-beam asymmetries are found to be positive for both reactions in all observed regions and this suggests the dominance of K^*

exchange in the t-channel . These asymmetries are found to increase gradually with the photon energy and have a maximum value of $+0.6$ for both reactions. The photon-beam asymmetries in $K^+\Sigma^0$ channel is systematically higher than those in $K^+\Lambda$ channel. Comparison with theoretical predictions based on the Regge-trajectory in the t-channel and the contributions of nucleon resonances indicates the major role of t-channel contributions as well as non-negligible effects of nucleon resonances to account for the reaction mechanism of hyperon photoproduction in this energy region.

Photoproduction of Λ and Σ^0 hyperons off protons with linearly polarized photons at $E_\gamma = 1.5 - 3.0$ GeV

Acknowledgements / 誌謝

Without the help and support from a huge amount of people, this analysis and thesis would not be possible. Unfortunately, my memory is too weak, and this acknowledgement is too short to include all the people I want to thank. So first of all, I would like to thank those whom I do not mention.

I would like to express my deepest gratitude to my supervisors, Professor 章文箴 and Professor 林宗泰, for giving me the opportunity of seeking for Ph.D degree. I would especially thank to Professor 章文箴 for giving me very great and detailed guidance throughout this long eleven-year period, not only in terms of physics knowledge and the attitude for problem solving, but also to thank him for leading me to know the Lord Jesus Christ. I was always impressed by his clear understanding on nuclear physics both in theoretical and experimental aspects, as well as his ability to find out the possible problems from the basic point of view and draw interesting conclusions from them. His ability to solve questions in physics and integrity in the faith of God is something I hope to match some day. I am always very thankful to him for the kindness, and understanding he always has with me.

I would truly like to thank Professor Kohri Hideki for his guidance and support through this analysis and during the period I visited RCNP. The continued advice and suggestions he gave me during at all stages of this analysis is something I consider very important to succeed in this project. The discussions we had were always very helpful in giving me more understanding about the research topic not only at the experimental level but also at the theoretical level. I also want to thank him for taking the time to carefully and critically read this thesis. Without his help and great effort the completion of this thesis would be a far more painful experience.

Thanks go to Professor Ron Gilman, Professor 張定華, Dr. Jinyuan,

Wu and Professor 陳彥竹 for their kind help during my visit of Rutgers and Fermilab. Without your kind help and advice the completion of the trigger system of E906 is an impossible mission. Particular thanks are given to Professor Ron Gilman, Professor 張定華 and their families for making my time at New Jersey and Illinois a far more pleasant experience. A special thanks goes to Professor 彭仁傑. The E906 trigger paper wouldn't have been possible to be published without his great help and suggestions. I'd also really like to thank Dr. Sawada Takahiro and Dr. 陳家益 for giving me the greatest help in the calibration of the LEPS NTPC data. Your helps are appreciated. I also want to offer thanks to Professor 鄧炳坤 for the help and advice he gave me. The discussion of photography and Tai Chi with Professor 鄧炳坤 enriched my research life.

I am also thankful for the friendship and guidance of a number of people in Nuclear physics group in Academia Sinica: 蘇大順, 謝燦隆, 林伯儒, 王素音, Kei Nagai, Marcia Quaresma, 姚錫泓, 謝佳諭, 洪郁淳, 連昱翔, 黃峻祿, 詹騏, 張富雄, 鄧宇勝, 蔡佩容. Your helps are invaluable to me.

In the E906/SeaQuest Group, I'd like to thank all the staffs and students who provided great help to make my time in the group a very enjoyable one. In particular Chuck Brown, Don Geesaman, Paul Reimer, David Christian, Donald Isenhower, Lamiaa El Fassi, Josh Rubin, Kaz Nakahara, Markus Diefenthaler, Ken-ichi Nakano, Ming Xiong Liu, Randall Evan McClellan, Shou Miyaska, Kun Liu, Florian Sanftl, Bryan Dannowitz, Bryan Kerns, and Arun Tadepalli, among many others.

I am also grateful to the members in the LEPS group: Takashi Nakano, Masaru Yosoi, Norihito Muramatsu, Masayuki Niiyama, Mizuki Sumihama, Atsushi Tokiyasu, Toshihiko Hiraiwa, Yukiyoshi Kon, Keigo Mizutani, Yuhei Morino, and Yohei Nakatsugawa. Without your kind help and effort, this work wouldn't be what it is today.

I would also like to thank my classmates 劉建良, 鄒守峻, 何彥政, 張純綾, 田雍, 巫明帆, 李宏毅, 唐富一, 江書賢, 蔡淵, 龔大勝, 吳政穎 for all the laughter and beer we had.

Most importantly though, I would like to thank my parents, my

wife, my sons and my sister for incredible support, encouragement and patience, and for all they have done to inspire me to get where I am now. Finally, this thesis is dedicated to my grandfather and grandmother who passed away to early to see this work completed.

目 錄

頁次

圖 目 錄

表 目 錄

Chapter 1

Introduction

From the ancient world, starting with Thales of Miletus who suggested water is the arche (the underlying material of the world), humankind is trying to describe the world, natural objects, and phenomena by theories and hypotheses, rather than mythological explanations. After Thales of Miletus ignited the origin spark of science, his successor Anaximander of Miletus, and Anaximander's pupil Anaximenes of Miletus proposed that the arche were the ambiguous substance "apeiron" and "air". In the same period, ancient Greek philosopher like Heraclitus of Ephesus suggested the "fire" is the arche. Anaxagoras introduced the concept of "Nous (Mind)" as an ordering force, which moved and separated out the original mixture. Leucippus, and Leucippus's pupil Democritus developed the theory that everything is composed entirely of various uncuttable, indivisible elements called "atoms". Pythagoras and his students who concluded that "all things are numbers". Parmenides of Elea asserted "Thought and being that it is are the same."

The Pre-Socratic philosophers rejected traditional mythological explanations of the phenomena they saw around them in favour of more thoughtful explanations. While most of them produced significant texts, none of the texts survived in complete form, but their attitude to answer the questions about "the essence of things" continues influenced the later philosophers like Socrates, and Socrates' most important student Plato, and Plato's most outstanding student Aristotle. Aristotle was perhaps the first truly systematic scientist. His views on physical science deeply moulded medieval scholarship. Their influence extended from Late Antiquity and the Early Middle Ages into the Renaissance,

and was not replaced systematically until the Enlightenment or so called Scientific revolution and theories such as classical mechanics.

Figure 1.1: The School of Athens by Italian Renaissance artist Raphael. Some critics believe that almost every great ancient Greek philosopher can be found in the painting. Could you try to find who is Anaximander, Heraclitus, Pythagoras, Parmenides, Socratic, Plato, and Aristotle?

In the 19th century, John Dalton, concluded that each element of nature was composed of a single, unique type of particle which also called atom (The same idea as Democritus, but reasoning on a completely different basis). The word atom, in the Greek word meaning "indivisible", has since then denoted the smallest particle of a chemical element. Physicists soon realized that the atoms are not, in fact, the "arche" of nature, but are conglomerates of even smaller particles, such as the electron. Throughout the 1950s and 1960s, a surprising variety of particles were found in collisions of particles with increasingly high-energy beams. Therefore the large number of particles was explained as combinations of a small number of more fundamental particles. The currently dominant theory explaining these fundamental particles and fields, along with their dynamics, is called the Standard Model [1, 2].

1.1 The standard model

The standard model [1, 2] is a milestone to our understanding of the development of the microscopic world. It is a widely accepted and remarkably accurate framework for understanding almost everything in the known universe, other than gravity. The standard model is a theoretical framework classifying all elementary particles and their interactions. Fig 1.2 shows the fundamental particles and force carriers of standard model. This model includes members of several classes of elementary particles like fermions, gauge bosons, and the Higgs boson. For fermions, standard model classifies all fermions into two groups of elementary particles, leptons and quarks. Six different flavours of quarks grouped in three different generation are described in standard model, up, down, strange, charm, bottom and top in the order of mass. Leptons are similarly grouped in three different generation: the electron, muon, and tau, with corresponding neutrinos. All these fermions have corresponding anti-particles which have opposite sign of electric charge and magnetic moment.

Base on our knowledge of the nature, all kinds of processes in the world come from the interaction of the four fundamental forces gravity, electromagnetic, weak, and strong interactions. The standard model which does not address gravity, provides a uniform framework for describing how the electromagnetic, weak, and strong interactions and explains why some fundamental particles have mass. The three standard-model forces are well understood now. For each force a field theory framework is associated with descriptions of how the force carrier bosons couple to the fundamental fermions. The Standard Model is a quantum field theory, and is based on the gauge symmetry of $SU(3)_C \times SU(2)_L \times U(1)_Y$. The symmetry of strong force based on $SU(3)_C$ colour exchange, and this gives eight force-carrying boson, which is called the gluon. Gluons are massless and electrically neutral. Unlike the photon which is charge-neutral, the gluons carry color charges. The electromagnetic and weak forces are unified successfully to form an electroweak interaction governed by the symmetry of $SU(2)_L \times U(1)_Y$. The force carriers of electroweak interaction are the $W^{\pm}$,Z^0 and photon. The $SU(2)_L$ here

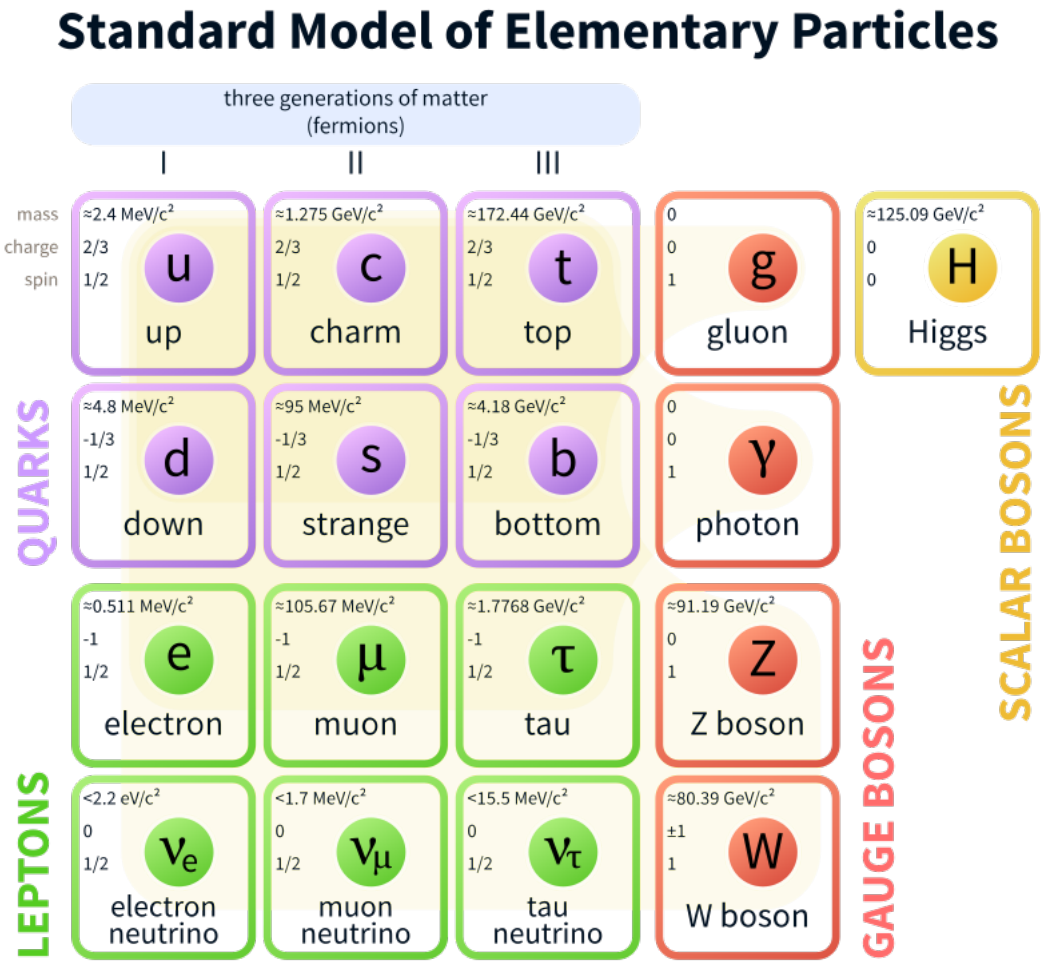

Figure 1.2: List of the fundamental particles according to the standard model: six quarks (up, down, charm, strange, top, bottom); six leptons (electron, muon and tau, with the corresponding neutrinos); and three types of force-carrying gauge bosons (gluon, photon, and the Z/W bosons, responsible for the strong, electromagnetic and weak interactions, respectively). The fifth column shows the scalar bosons Higgs boson.

represents the weak force, which relates to the symmetric states of W and Z boson. The $U(1)_Y$ here represents the gauge boson B_μ. After the symmetry breaking, the gauge bosons will become massive, leaving the gluons and the photon massless. For the strong interaction, the current theory is quantum chromodynamics(QCD). However, currently, there are no economical first principles solution to QCD in the non-perturbative low energy region around few GeV.

1.2 Quantum Chromodynamics

"A straw shows which way the wind blows", in the region of classical mechanics, this might be a statement close to true. But in the

microscopic scale, knowledge of the fundamental processes might not guarantee the accurate description of the whole system, the strong interaction, described by the theory of QCD is the most striking example.

Quantum chromodynamics (QCD) is the theory of the strong interaction between quarks and gluons, the fundamental particles that make up composite hadrons such as the proton, neutron and pion. The hadron is a composite particle composed of quarks. Under the hadron family, there are two groups baryon and meson. As a member of hadron family, both baryon and meson are composed of quarks, the meson composed of a quark-antiquark pair, and the baryon composed of three quarks. The hyperon is a member of baryon family which contains strange quarks, but no charm, bottom or top quark.

QCD describes the quark interactions which involve the extra degrees of freedom of colour exchange. The QCD Lagrangian is composed of individual quark fields and the strong potential in which they move. The general structure of any quantum field theory is from the consideration of internal gauge symmetries [3]. The most general gauge invariant Lagrangian density is

$$\mathcal{L} = -\overline{\psi}\left(\gamma^{\mu}\mathcal{D}_{\mu} + w\right)\psi - \frac{1}{4}F^{\alpha}_{\mu\nu}F^{\mu\nu}_{\alpha} \tag{1.1}$$

where $\mathcal{D}$ stands for the gauge-covariant derivative

$$\mathcal{D}_{\mu} = \partial_{\mu} - igA^{\alpha}_{\mu}t_{\alpha} \tag{1.2}$$

The gauge fields A^{α}_{μ} are massless and spin=1 particles which carries the gauge charge indexed by α. For the gauge group SU(N), the α can be $1\sim(N^2-1)$. In the case of QCD, N=3; $\alpha = 8$. The t_{α} are generators of the gauge transformation for a given representation of the matter fields, in QCD, it is the generators of the SU(3) color group. The g is a generalized charge representing the strength of the interaction which is the coupling constant.

The covariant field tensor, here the color field tensor is defined as the commutator of the covariant derivative

$$F^{\alpha}_{\mu\nu} = [D_{\mu}, D_{\nu}]^{\alpha} = \partial_{\mu}A^{\alpha}_{\nu} - \partial_{\nu}A^{\alpha}_{\mu} - gf^{\alpha\beta\gamma}A^{\beta}_{\mu}A^{\gamma}_{\nu} \tag{1.3}$$

where the $f^{\alpha\beta\gamma}$ indicates the structure constants of the Lie algebra in the commutators $[t^\beta, t^\gamma] = if^{\alpha\beta\gamma}t^\alpha$. In the case of QED, For the U(1) symmetry group the $f^{\alpha\beta\gamma}$'s are all zero. In the case of QCD, the SU(3) is a non-abelian group where the structure constants are non-zero and this non-zero structure constants induced a totally different properties of QCD compared to QED.

It is noted that the flavour $SU(3)_f$ symmetry for the light quarks to be discussed later is different from the color $SU(3)_c$ here. In contrast to flavour $SU(3)_f$, color $SU(3)_c$ is a symmetry expected to be exact since the color charge is a conserved quantity.

Both the QED and QCD have similar structures. In QED the charge is denoted as positive and negative. In QCD there are three different types of charge: color red (r), green (g) and blue (b) associated with the 'anti-'color anti-red ($\overline{r}$), anti-green ($\overline{g}$) and anti-blue ($\overline{b}$). In the case of QED, the electromagnetic interaction is mediated via the exchange of photon which is a massless neutral particle. But in QCD, the gauge bosons called gluons carry color charge. So the gluons not only act as generators of the SU(3) color group, transforming one color state into another, but also act like the role of particles which can couple with quarks and gluons.

In the quantum vacuum, the quark-antiquark pairs and gluons that appear from nothing and immediately disappear. The quark-antiquark pairs tend to screen the color charge. The net effect of polarization of the quark-antiquark pairs in the vacuum is not to screen the field, but to enhance it. This is called anti-screening. Getting closer to a quark will reduce the anti-screening effect of the surrounding quark-antiquark pairs, so the contribution of this effect would become weaker with a decreasing distance.

The anti-screen of the color charge is reflected in the behaviour of the strong coupling constant α_s. At high energies, two quarks interact through color fields of reduced strength (small α_s). When quarks become close enough, they behave as if they were non-interacting (with respect to the strong interaction). This "asymptotic freedom" leads to simplifications in the underlying maths of the theory, the perturbation

and effective potentials approaches can accurately predict the behaviour of the nucleon.

By contrast, at lower energies, the strength of the color field increases (large α_s) with an increasing distance. This makes the analytically perturbative treatment of the physical quantities hard. QCD presents enormous challenges when applied to more common hadrons and energy typical of nuclear physics (medium energy; around few GeV). In this energy region meson and baryon degrees of freedom dominate the physics here, and the usual QCD perturbative approaches can not work well here.

This property of QCD called the running of the coupling constant is also known as asymptotic freedom and was found theoretically by Politzer, Gross, and Wilczek [16, 17]. Experimentally, the value of α_s has been determined from the analysis of various processes. Fig. 1.3 shows the results obtained for α_s from various analyses. From the plot, when the energy becomes larger the α_s becomes smaller.

There are many particles which can carry electric charge, but until now, no observed particles have ever been found to carry color charge. The quarks seem to be confined within mesons and baryons which are colorless. The mechanism called color confinement is believed to keep quark and antiquark stay inside the hadrons.

The electric field between electrically charged particles decreases rapidly as the distance between them becomes large. The gluon field between a pair of color charges forms a narrow flux tube between them. When the distance between this two color charges increases, the gluon field still keeps constant, and the potential energy of the system has to increase proportional to its separation length. Because of this behavior of the gluon field, the strong force between the particles is constant to prevent their separation. When the potential energy in the tube is large enough, it becomes favorable for a new quark–antiquark pair to appear, rather than extending the tube further. Since to separate two quarks needs an infinite amount of energy, it prevents the possibility of breaking the hadron to produce free color charged particles. The property of color confinement can be linked to the symmetric property of

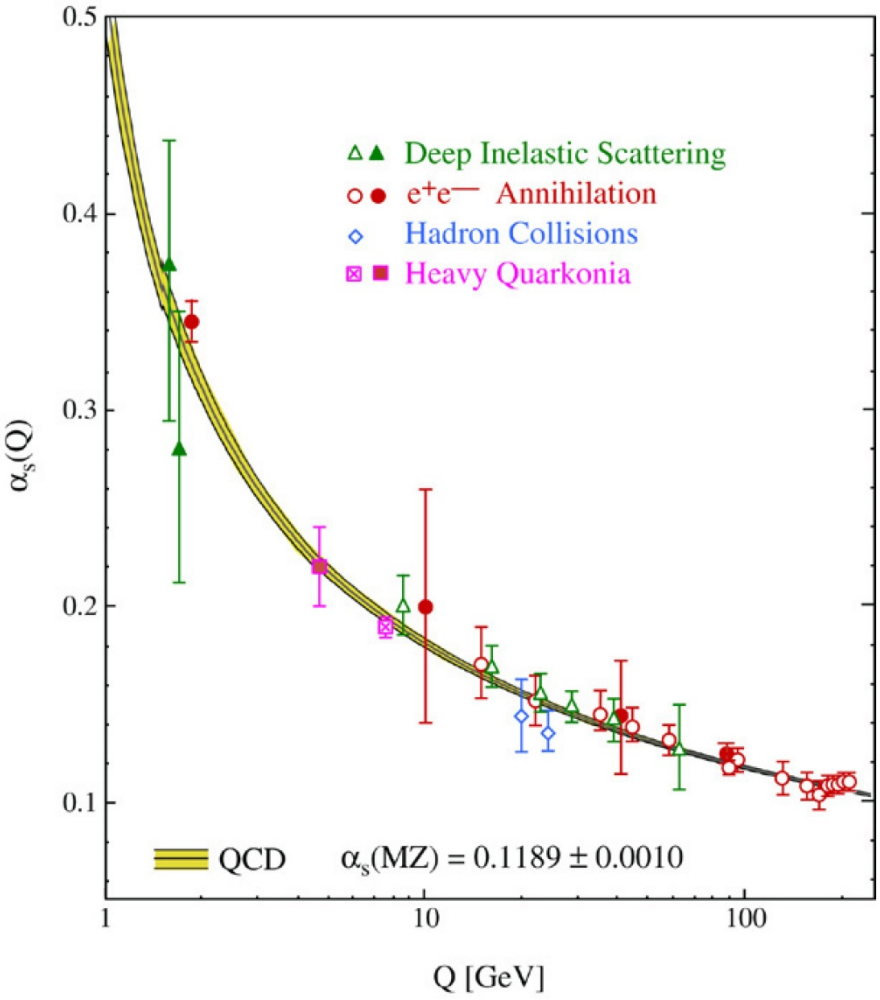

Figure 1.3: Summary of measurements of $\alpha_s(Q)$ as a function of the respective energy scale Q. This plot was taken from [13]

color-neutrality which implies that every observed hadron must be color-neutral, as required by the experimental fact that no isolated quarks have ever been observed.

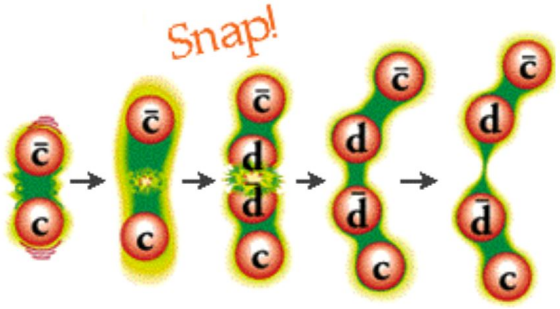

Figure 1.4: Schematic plot of the confinement between a quark (c) and an antiquark ($\bar{c}$). This plot was taken from [15]

The helicity of a particle is right-handed which means the direction

of its spin is the same as the direction of moving. If the directions of spin and moving are opposite, it is left-handed. Chiral symmetry is related to the concept of helicity. For chiral symmetry to be observed, the helicity must be conserved. In the high energy region where the quark masses are insignificant, this chiral symmetry can be approximated.

Under the conditions of broken chiral symmetry, the so called "naked" valence quarks are believed to be "cloaked" or 'dressed' by their interactions with the quark and gluon, and the so called constituent or effective quark mass results from the energy of this dynamic system. Fig. 1.5 is the schematic plot of this idea. This plot shows the total energy in the proton is mostly contributed by the gluon exchange, proceeding via interactions in the vacuum.

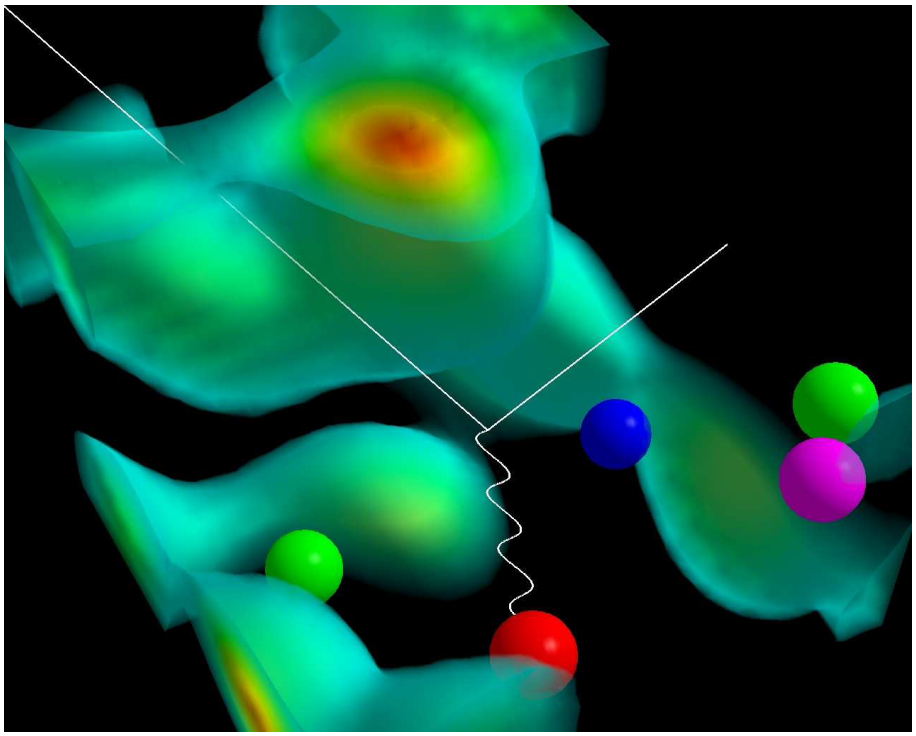

Figure 1.5: An schematic plot based on lattice QCD calculations of gluon exchange in the vacuum [14]. Here, for the proton mass, 97% comes from the gluon field, with just 3% residing in the valence quarks. The three different color red, blue and green stands for the valence quarks, with a virtual pion forming to the right of the picture (shown as a green and magenta pair). A electron interacts with a quark here by way of exchanging a virtual photon (shown as a wavy line). This plot was taken from [14].

Some attempts to calculate the non-perturbative dynamics from the exact QCD Lagrangian have been successful, and these have been based on a computational method called Lattice QCD. Lattice QCD (LQCD)

is the best known tool for addressing the QCD issues like the confinement, chiral symmetry breaking, hadron mass, decay constants, form factors and etc., from first principles approach. This approach considers a discrete space-time framework to allow finite calculations of the quantum field strength inside the nucleon. The Fig. 1.5 is plotted base on the calculation from Lattice QCD Lagrangian vacuum state. Although the lattice QCD can explore QCD in the non-perturbative energy region by first principles numerical calculations and provide some accurate direct solutions of QCD, these calculations remain computationally intensive with the bottleneck of the bandwidth of memory access instead of flops. There is currently no economical first principles solution to QCD at non-perturbative energy.

1.3 Constituent Quark Model and the Missing Resonances Problem

Although QCD perturbative approaches can not describe the meson and baryon dominant region, the QCD is still able to describe the rich variety of hadronic states for example 'isospin', introduced during the development of the standard model. Isospin was introduced by Heisenberg in 1932 shortly after the neutron was discovered. The isospin is a quantum number to describe various related symmetries for the proton and neutron. This isospin symmetry was applied to describe the extremely close masses of the proton and neutron, and as an invariance of the strength of the nuclear force under exchange of nucleons. In the late 1950s, the Λ, Σ's, and the Ξ's were discovered which are of the same spin and similar mass. To describe the increasing number of baryon family, Gell-Mann tried to introduce the "strangeness" quantum number in 1961. By introducing the new quantum number allows for hadrons that have similar properties to be grouped according to the so-called "Eightfold Way". The Fig. 1.6 shows the baryon octet which was arranged based on the Eightfold Way with the Λ and Σ^0 baryon. This arrangement can be interpreted as a consequence of flavour symmetry between the quarks.

The isospin is a very good symmetry, because the mass difference between the isospin member neutron and proton is about 3%, but the

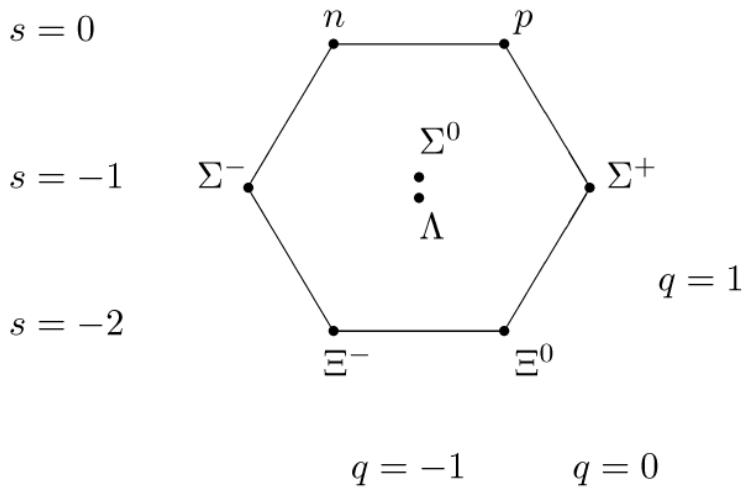

Figure 1.6: The baryon octet which was arranged based on the Eightfold Way. Particles along the same horizontal line share the same strangeness, s, while those on the same diagonals share the same charge, q. This picture was taken from Wikipedia.

mass splitting within the baryon octet is about 40%. The symmetry becomes worse when the "charm" was discovered and tried to be added into the flavour symmetry. The Tab. 1.1 shows the quark bare and effective masses. Apart from the differences in quark masses, the strong interactions treat all flavours equally. The isospin is a good symmetry because the u and d have a very close effective mass. The Eightfold Way is a acceptable symmetry because the effective mass of the s quark is not too far from the mass of u and d quark. To include the heavier c, b and t quark to the flavour symmetry will make the situation become much worse. Although the flavour symmetry is not the basic of QCD, the idea of effective mass still provides us some useful tools to describe the non-perturbative QCD region.

Table 1.1: Quark Masses (MeV/c^2)

	Quark flavor	Bare (current) mass (MeV/c^2)	Effective (constituent) mass (MeV/c^2)	
			in mesons	in baryons
Light quarks	u	4.2	310	363
	d	7.5		
	s	150	483	538
Heavy quarks	c	1100	1500	
	b	4200	4700	
	t	>23000		

There exist serious difficulties to derive hadronic interactions from the first-principle Quantum chromodynamics because of its intrinsic non-perturbative property in the low-energy region. To establish a model which can provide the prediction power among the non-perturbative region, a phenomenological concept called the Constituent Quark Model (CQM) [8] was introduced around 1980s. Fig. 1.7 shows the CQM (left plot) and QCD (right plot) picture of the nucleon.

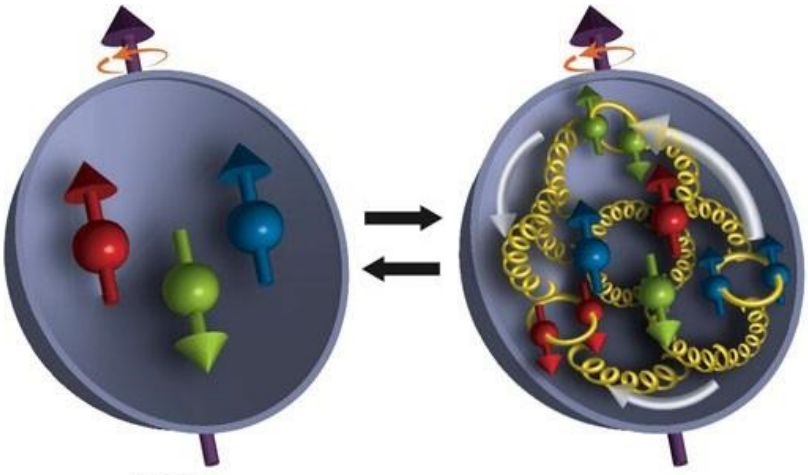

Figure 1.7: The schematic view of CQM (left plot) and QCD (right plot) picture of the nucleon. The QCD considers the three valence quarks with the sea quarks. The CQM considers three constituent quarks only.

The nucleon contains three valence quarks and a huge amounts of gluons and quark–antiquak pairs (sea quarks). This complex system picture is shown in the right part of Fig. 1.7. Comparing with QCD, the CQM (in the left part of Fig. 1.7) is based on assuming the valence quarks to be effective degrees of freedom and the reduction of gluons within the hadrons, which have much larger effective mass than the bare mass of perturbative QCD quarks. The comparison of bare mass and effective mass can be seen in Tab. 1.1. The constituent quark can be seen as an object like a valence quark dressed by clouds of gluons and quark-antiquark pairs. The sea quarks are merged into the constituent quarks to have a larger size, and larger masses. The quantum numbers of these valence quarks are applied to identify the hadrons by the quark flavour and the Poincaré symmetry, J^{PC}, where J is the angular momentum, P is the intrinsic parity, and C is the charge conjugation parity, the isospin could also be applied to identify the hadrons.

The first successful step of CQM comes when the spin-flavour SU(6) symmetry was introduced [4]. Due to the simply assumptions, it is obvious that this approach has restricted possibilities even for the lightest hadrons. But, this simple picture given by the naive non-relativistic quark model still provides us with a qualitative description of hadrons.

The predictions from this model arise from symmetry rather than from detailed dynamics, which makes it useful to determine only properties like masses of ground states or magnetic moments. Table 1.2 shows the CQM predicted magnetic moments and mass with the measurement results. The general agreement of its predictions with experimental data is quite good.

Table 1.2: CQM predicted magnetic moments and mass with the experiment measurements [4].

magnetic moments of baryons in nuclear magnetons.		
Particle	CQM prediction	Experiment
p	3	2.79
n	-2	-1.91
Λ	-0.5	-0.61
Σ^+	2.84	2.46
Σ^-	-1.16	-1.16±0.03
Ξ^0	-1.33	-1.25±0.01
Ξ^-	-0.33	-0.65±0.04
Baryon masses (MeV)		
Baryon	CQM prediction	Experiment
N	930	937
Δ	1230	1232
Σ	1178	1193
Λ	1110	1116
Σ^*	1377	1384
Ξ	1329	1318
Ξ^*	1529	1533
Ω	1675	1672

In 1975, Rújula, Georgi, and Glashow [5] suggested a model of dynamical constituent quark models. Many studies of excited baryon states and electromagnetic transition amplitudes connecting the nucleon and its excited states were developed based on the suggestions of the model suggested by Rújula, Georgi, and Glashow.

In the late 1970s the model of Isgur and Karl [6, 7] has been published. The model treated the interaction V_{ij} between quarks not only by a short-range term but also by a long-range term and neglected all contributions from the spin-orbit force term. This interaction is expressed

as

$$V_{ij} = -\alpha_s \frac{\lambda_i^c \cdot \lambda_j^c}{16 m_i m_j} \left(\frac{8\pi}{3} \delta(r_{ij}) \sigma_i \cdot \sigma_j + \frac{1}{r_{ij}^3} S_{ij} \right) \tag{1.4}$$

The α_s is the well known strong coupling constant, r_i, m_i, σ_i and λ_i^c are the coordinate, mass, spin, and color of the i-th quark, respectively. The $r_{ij} = r_i - r_j$, and S_{ij} is the tensor operator defined by $S_{ij} = 3\sigma_i \cdot \hat{r}_{ij} \sigma_j \cdot \hat{r}_{ij} - \sigma_i \cdot \sigma_j$ with $\hat{r} = \frac{r}{|r|}$. The Isgur-Karl model shows a great success in the description of the higher baryon resonances.

Later, a further introduction of the spin-flavor (SU(6)) and orbital angular momentum (O(3)) leads to a SU(6)×O(3) symmetry of the CQM. Based on the SU(6)×O(3) symmetry, Koniuk and Isgur calculated and predicted a set of baryon resonances and their decay couplings into various channels [8]. Later, Capstick and Roberts further extended the Isgur calculations by adding relativistic corrections with non-strange [41] and strange baryon [42] states.

By comparing the predicted baryon resonances with experimental data, a problem so-called "missing resonances" appears. The number of excited baryon states predicted by CQM is much more than that of the states observed by experiments. The missing resonance problem can be seen in Fig. 1.8 where the states predicted by the quark model from Capstick and Roberts [42] and the experimental data are plotted. A significant number of the predicted states in this plot have no corresponding experimental evidence.

Two explanations are considered for the missing resonance problem. The first is the so called diquark-model. Instead of describing the nucleon as a system of three symmetric constituent quarks, diquark is a hypothetical state of two quarks grouped inside a baryon. The corresponding models of baryons are referred to as quark–diquark models [10]. The quark-diquark model may occur when the colours and spins of the two quarks are anti-symmetric. The force between the two quarks will become attractive due to the anti-symmetry. When the two quarks are in this situation, a low-energy state which restricts the number of internal degrees of freedom of the nucleon occurs. This lowers the level density of baryon resonances and also removes a large number of the

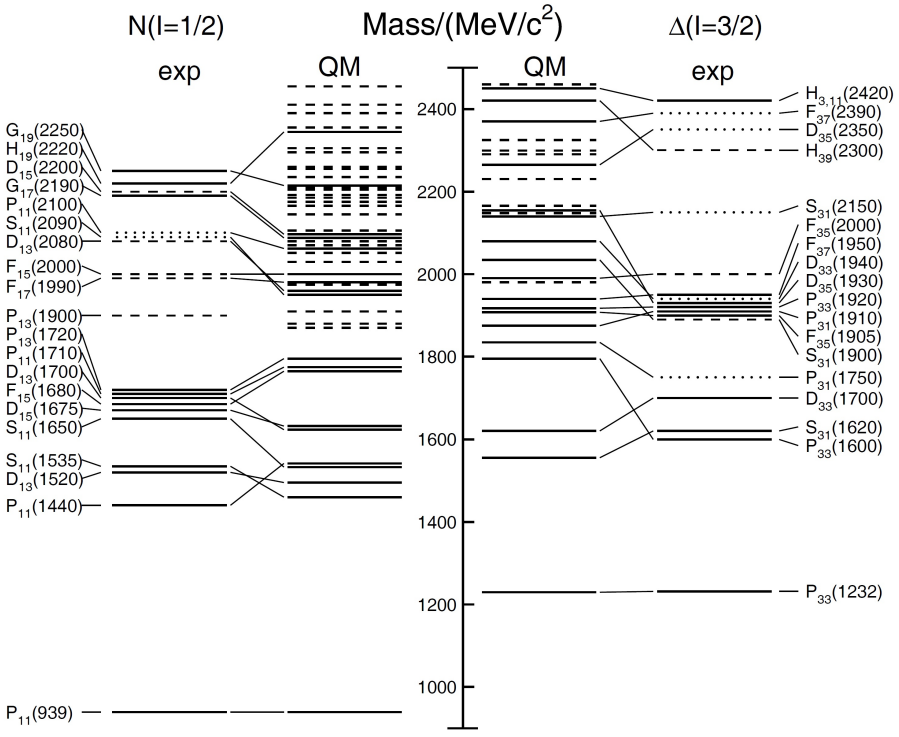

Figure 1.8: Excitation spectrum of the nucleon. Left hand side: isospin $I = 1/2$ N-states, right hand side: isospin $I = 3/2$ Δ-states. Experimental: (columns labeled 'exp'), three and four-star assign by PDG states are indicated by full lines (two-star dashed lines, one-star dotted lines). At the very left and right of the figure, the spectroscopic notation of these states is given. Quark model: (columns labeled 'QM'), full lines: at least tentative assignment to observed states, dashed lines: so far no observed counterparts. This plot was taken from [9]

missing resonance states from the predictions.

Another explanation comes from the experimental measurements. The pion production with πN final states have been the focus of experimental data until recently. Capstick and Roberts have indicated that some missing resonances should couple strongly to strange baryon final state channels in photoproduction reactions such as $K^+\Lambda$ and $K^+\Sigma^0$ in their quark model calculations [42]. Fig. 1.9 shows the Capstick and Roberts predictions for the coupling of nucleon resonances up to 2200 MeV to $K^+\Lambda$, $K^+\Sigma^0$, $N\pi$ and $N\gamma$. The figures show the states with masses above 1850 MeV have not been observed experimentally and might coupled to the $K^+\Lambda$ and $K^+\Sigma^0$ channels.

1.4 Kinematic variables

In the non-perturbative QCD region, the nucleon can be explored through its interaction with low-energy beams, and the nucleon is left

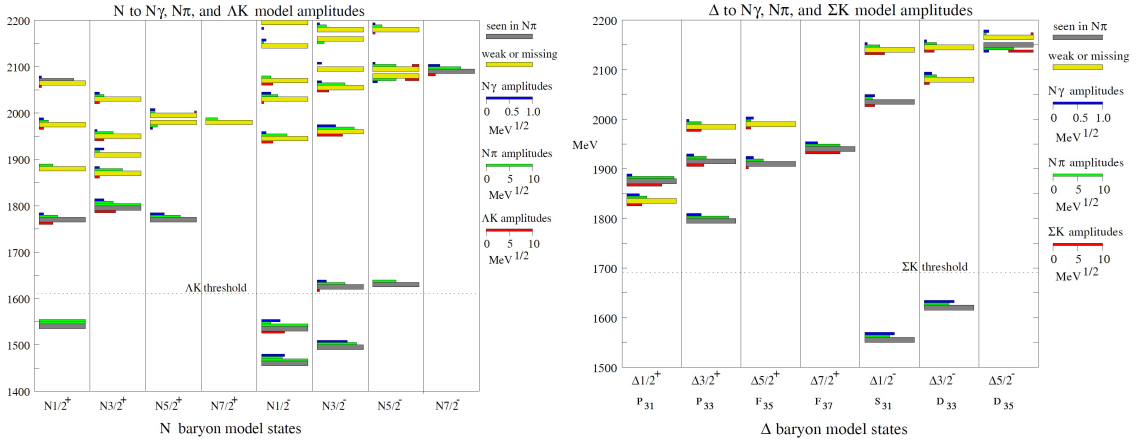

Figure 1.9: Capstick–Roberts predicted amplitudes for N (left) and Δ (right). Several states with masses above 1850 (2000) MeV have not been observed experimentally. This plot was taken from [42]

in an excited state (resonance). The excitation state could reflect the dynamics of the three constituent quarks.

In the past, nearly all resonance information came from πN final state, the excited state is conventionally written as $L(\sqrt{s})_{2I,2J}$ or $L_{2I,2J}(\sqrt{s})$ the L here stands for the orbital angular momentum which was labeled as S, P, D, F, G according to its value L=0, 1, 2, 3, 4. $\sqrt{s}$ is the center-of-mass energy, and I, J are the isospin and total angular momentum. Now, most information has come from the γN initial state experiments. Therefore, the naming scheme for the resonances have been replaced with the spin-parity J^P of the state. This naming scheme should give intrinsic properties of the resonance that are independent of the specific particles and reactions used to study them. Nucleon resonances with $I = \frac{1}{2}$ are called N*; the resonances with $I = \frac{3}{2}$ are called Δ^*.

The Mandelstam variables s, t and u are commonly used set of invariant relations derived from the four-momentum vectors that comprise the initial and final states of an interaction. Fig. 1.10 shows the definitions of variables for a two-body final state where the two particles of momentum p_1 and p_2 and mass m_1 and m_2 scatter to particles of momentum p_3 and p_4 and mass m_3 and m_4.

For here, the s, t, u are defined by

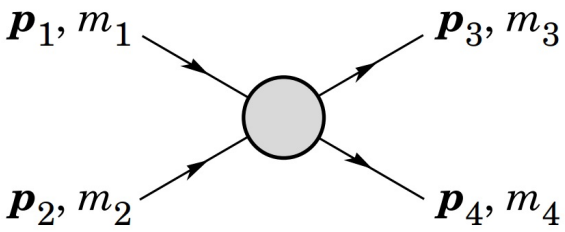

Figure 1.10: The 2 body reactions.

$$s = (p_1 + p_2)^2 = (p_3 + p_4)^2 = m_1^2 + 2E_1E_2 - 2p_1 \cdot p_2 + m_2^2 \quad (1.5)$$

$$t = (p_1 - p_3)^2 = (p_2 - p_4)^2 = m_1^2 - 2E_1E_3 + 2p_1 \cdot p_3 + m_3^2 \quad (1.6)$$

$$u = (p_1 - p_4)^2 = (p_2 - p_3)^2 = m_1^2 - 2E_1E_4 + 2p_1 \cdot p_4 + m_4^2 \quad (1.7)$$

The definitions of t and u appear to be interchangeable (by renaming 3 to 4); it is conventional to define t as the squared difference of the initial and final momentum of the particles with similar properties. For any process, s is the square of the total initial 4-momentum also the center of mass energy.

In the study of photoproduction of $K^+\Lambda$ and $K^+\Sigma^0$, the four most commonly used Feynman diagrams are shown in Fig. 1.11. The digram, from left to right, are s-, u-, t- channels and contact diagram. From the Fig. 1.11, the s-channel corresponds to the photon and nucleon forming an intermediate particle/resonance then split into K and Y. Since the out going particles are split from an intermediate particle/resonance, we can expect the angular distribution of out going particles should be more uniform. The u-channel is the t-channel with role interchange of the K and Y. From the diagram we can see the N split into K and Y or Y^* then the Y or Y^* interact with γ. The outgoing K in the center of mass frame tends to stay in the backward direction. The t-channel represents the reaction in which the photon emits the intermediate particle (K, K^*) and becomes the K, while the nucleon interacts with the K or K^* then becomes the Y. Since the γ forms the K directly, we can expect the out going K will carry on most of the momentum which the γ originally has, so the K tends to stay in the forward direction. The contact diagram is required for maintaining the gauge invariance.

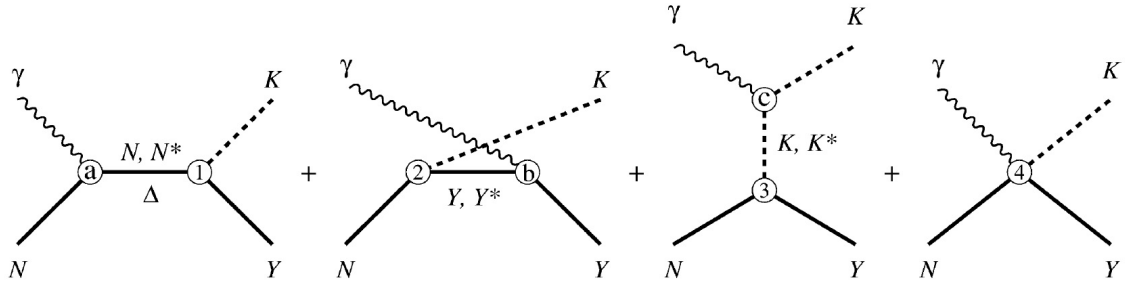

Figure 1.11: Feynman diagram for kaon photoproduction on the nucleon. Contributions from the Δ are only possible in Σ production. Electromagnetic vertices are denoted by (a), (b) and (c), hadronic vertices by (1), (2) and (3). The contact diagram (4) is required in order to restore gauge invariance after introducing hadronic form factors. This graph was taken from [49]

By considering the incident beam linearly or circularly, target, recoil polarization and the combination of each of two, a huge list of asymmetry observables could be obtained. Tab. 1.3 summarises the observables [12, 11]. The physics observables correlated with incident photon beam are useful to clarify the kaon photoproduction mechanisms. The axes for the polarization asymmetries are defined here: $\vec{z} \sim \vec{k}$, $\vec{y} \sim (\vec{k} \times \vec{p}_k)$, $\vec{x} = \vec{y} \times \vec{z}$, $\vec{z}' \sim \vec{p}_k$, $\vec{y}' = \vec{y}$, $\vec{x}' = \vec{y}' \times \vec{z}'$.

In this thesis, the experiment was carried out at the Laser Electron Photon beam line at SPring-8 (LEPS). In LEPS experiment, the linearly polarized beam was used, so we will focus on the measurement of differential cross sections and photon-beam asymmetry (Σ_γ) for $K^+\Lambda$ and $K^+\Sigma^0$ channel.

1.5 Motivation

The main goal of this thesis is to study the spectrum of excited states of the proton via kaon photoproduction in $K^+\Lambda$ and $K^+\Sigma^0$ channel by exciting the proton with a high energy linearly polarized photon. The Tab. 1.4 lists the properties of the particles participated in this analysis.

In this thesis, since the LEPS spectrometer covers the forward region, we decide to study in single K^+ detection mode, then calculate the missing mass for the further selection of the Λ and Σ^0. It is also possible to detect the $p\pi^-$ and selecting the missing mass close to K^+ to detect the $K^+\Lambda$ channel [25].

One of the major motivations for this analysis is to provide the data

Table 1.3: List of the polarized photoproduction observables.

Observable	required polarization		
	Beam	Target	Recoil
$\frac{d\sigma}{d\Omega}$	-	-	-
Single polarization			
Σ_γ	linear	-	-
T	-	along y	-
P	-	-	along y'
Beam-target polarization			
E	circular	along z	-
F	circular	along x	-
G	linear	along z	-
H	linear	along x	-
Beam-recoil polarization			
$C_{x'}$	circular	-	along x'
$C_{z'}$	circular	-	along z'
$O_{x'}$	linear	-	along x'
$O_{z'}$	linear	-	along z'
Target-recoil polarization			
$T_{x'}$	-	along x	along x'
$T_{z'}$	-	along x	along z'
$L_{x'}$	-	along z	along x'
$L_{z'}$	-	along z	along z'

Table 1.4: The properties of K^+, Λ and Σ^0.

	K^+	Λ	Σ^0
mass (MeV)	493.677	1115.683	1192.642
quark content	$u\bar{s}$	uds	uds
spin	0	$\frac{1}{2}$	$\frac{1}{2}$
isospin	$\frac{1}{2}$	0	1
parity	-	+	+
mean life time (s)	1.238×10^{-8}	2.632×10^{-10}	7.4×10^{-20}
main decay channels	$\mu^+\nu_\mu$ (63.4%) $\pi^+\pi^0$ (20.66%)	$p\pi^-$ (63.9%) $n\pi^0$ (35.8%)	$\Lambda\gamma$ (∼100%)

set which could be used for the search of the missing resonance. The linearly polarized photon beam can extract the photon beam asymmetry Σ_γ to help understanding the hadron photoproduction mechanism. The beam asymmetry measurements have also been predicted to be very sensitive to the possible missing resonance. With the constraints of these new data of hyperon Λ and Σ^0 photoproduction at very forward angles for few-GeV photons, we look forward to the progress in theoretical modeling shortly.

To extract the resonance parameters from the experimental data is not the major goal of studying baryon resonance through the photo-

production process. It is the interpretation of such extracted resonances through predictions from phenomenological QCD models that allows one to learn, to think and to understand the underlying physics. Predictions from the constituent quark models, are connected with the understanding of correlations between quarks inside the nucleon. This is indeed, personally, I believe, the main motivation for this long-term studying.

Chapter 2

Past Measurements and Theoretical Models

From 1960s, physicists start to study on the photoproduction of hyperons Λ and Σ^0 channels. The past measurements of cross sections in $\gamma p \to K^+\Lambda$ and $\gamma p \to K^+\Sigma^0$ channels will be introduced in this chapter. The beam asymmetry in $K^+\Lambda$ and $K^+\Sigma^0$ photoproduction will also be introduced. The selection of modern experiments like SAPHIR, CLAS, GRAAL, Crystal Ball and previous LEPS measurements will be shown later. After the introduction of the previous measurements, some of the phenomenological models that are applied in the energy region of non-perturbative QCD will be discussed. We will focus on tree-level isobar model, coupled-channel model and Regge model.

2.1 Past measurements

For the photoproduction of $K^+\Lambda$ and $K^+\Sigma^0$ channels, the differential cross sections and various polarization observables of $\gamma p \to K^+\Lambda$ and $K^+\Sigma^0$ from threshold up to $E_\gamma = 3$ GeV have been measured by following groups, SAPHIR [20, 21, 22], LEPS [23, 24, 25, 26], CLAS [28, 30, 31, 32], and GRAAL [33, 34] and Crystal Ball [36].

In $K^+\Lambda$ channel, a bump like resonance structure of cross sections near the center of mass energy $\sqrt{s} = 1.9 - 1.96$ GeV was observed by SAPHIR [21, 22], CLAS [28, 30], Crystal Ball [36] and LEPS [24]. In the forward angle region of $K^+\Sigma^0$ channel, a small enhancement on cross sections was also observed at $\sqrt{s} = 2.05$ GeV by SAPHIR [21, 22], CLAS [28, 31] and LEPS [24]. The photon-beam asymmetries for both two channels were seen to be positive, and that of $K^+\Sigma^0$ production was

in general larger. A summary of measurements on the two channels is given in Tab. 2.1

Table 2.1: Summary of measurements.

Experiment	Ref.	Final state	Beam energy range (GeV)	Observable							
				$\frac{d\sigma}{d\Omega}$	Σ_γ	T	P	$C_{x'}$	$C_{z'}$	$O_{x'}$	$O_{z'}$
Current analysis		$K\Lambda$	1.5-3.0	*	*						
		$K\Sigma^0$	1.5-3.0	*	*						
LEPS (2006)	[24]	$K\Lambda$	1.5-2.4	*	*						
	[24]	$K\Sigma^0$	1.5-2.4	*	*						
SAPHIR (1998)	[21]	$K\Lambda$	thre.-2.0	*			*				
	[21]	$K\Sigma^0$	thre.-2.0	*			*				
SAPHIR (2004)	[22]	$K\Lambda$	thre.-2.6	*			*				
	[22]	$K\Sigma^0$	thre.-2.6	*			*				
CLAS(2006)	[28],[29]	$K\Lambda$	0.94-3	*				*	*		
	[28],[29]	$K\Sigma^0$	1.1-3	*				*	*		
CLAS(2010)	[30]	$K\Lambda$	0.94-3.8	*			*				
	[31]	$K\Sigma^0$	1.1-3.8	*			*				
CLAS(2016)	[32]	$K\Lambda$	1.1-2.1		*	*	*			*	*
	[32]	$K\Sigma^0$	1.2-2.1		*	*	*			*	*
GRAAL	[33],[34]	$K\Lambda$	thre.-1.5	*	*	*	*			*	*
	[33]	$K\Sigma^0$	thre.-1.5	*	*		*				
Crystal Ball	[36]	$K\Lambda$	thre.-1.5	*							
	[36]	$K\Sigma^0$	thre.-1.5	*							

2.1.1 SAPHIR

The SAPHIR collaboration conducted the experiment in Electron Stretcher Accelerator (ELSA) facility. The ELSA accelerator is a tunable 3.5 GeV electron stretcher accelerator ring which was operated by the university of Bonn. The stretcher ring is basically a storage ring, where the beam of the injector can be stored until the next pulse is ready. In that time it is continuously extracted to the experiments, so that the experiments receive a continuous beam. The electron beam was applied to produce photons by bremsstrahlung in a copper target. The SAPHIR detector is shown in Fig. 2.1.

Although from 1960s some of the data for photoproduction of Λ and Σ^0 channels have already existed, much of the interests were revived by the large coverage and small statistical error results from the SAPHIR collaboration in the 1990s. Three sets of results were published by SAPHIR, the first data were published in 1994 [20], the next results were published in 1998 [21] and the latest results were published in 2004 [22]. The SAPHIR results published in 1998 come from the

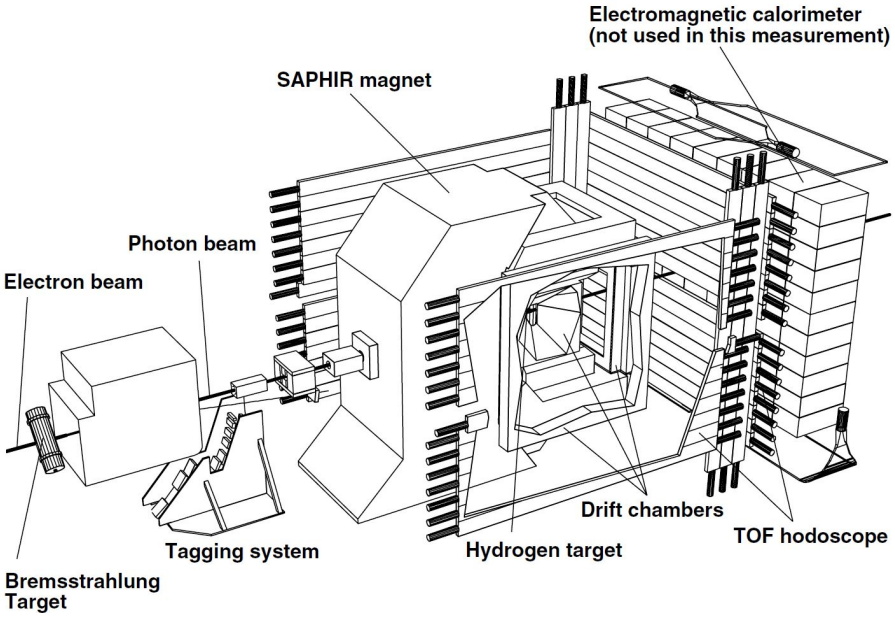

Figure 2.1: Schematic view of SAPHIR detector [22].

re-analysed data from 1994 and a wide angular acceptance, and contain the total, differential cross sections and hyperon polarizations for both the $K^+\Lambda$ and $K^+\Sigma^0$ channels. By analysing the events whose final state contains the K^+, p, π^- for both production channels, the 1998 results show a huge improvement over the previous data. The results were unprecedented in the large coverage and small statistical error.

The results of total cross sections for the $K^+\Lambda$ and $K^+\Sigma^0$ channels are shown in Fig. 2.2.

In the upper part of Fig. 2.2, the results of total cross sections of $K^+\Lambda$ channel are shown. A clear peak structure can be observed from the threshold up to 1.1 GeV. The photon energy of 1.1 GeV corresponds to the center of mass energy $\sqrt{s} = 1.7$ GeV where three N^* resonances $S_{11}(1650)$, $P_{11}(1710)$ and $P_{13}(1720)$ are known to couple to the $K^+\Lambda$ channel [38].

Another peak structure at 1.5 GeV is also observed in the upper part of Fig. 2.2. Kaon-MAID group tried to make the interpretation by Isobar models (to be discussed in sec 2.2.1) that it required an additional 'missing resonance' the $D_{13}(1895)$ to recreate the structure [44](in [44] the $D_{13}(1895)$ has been called $D_{13}(1960)$). The $D_{13}(1895)$ had been predicted by Capstick [42], and it was a missing baryon. This was the first hint that the missing resonance may strongly couple to the $K^+\Lambda$

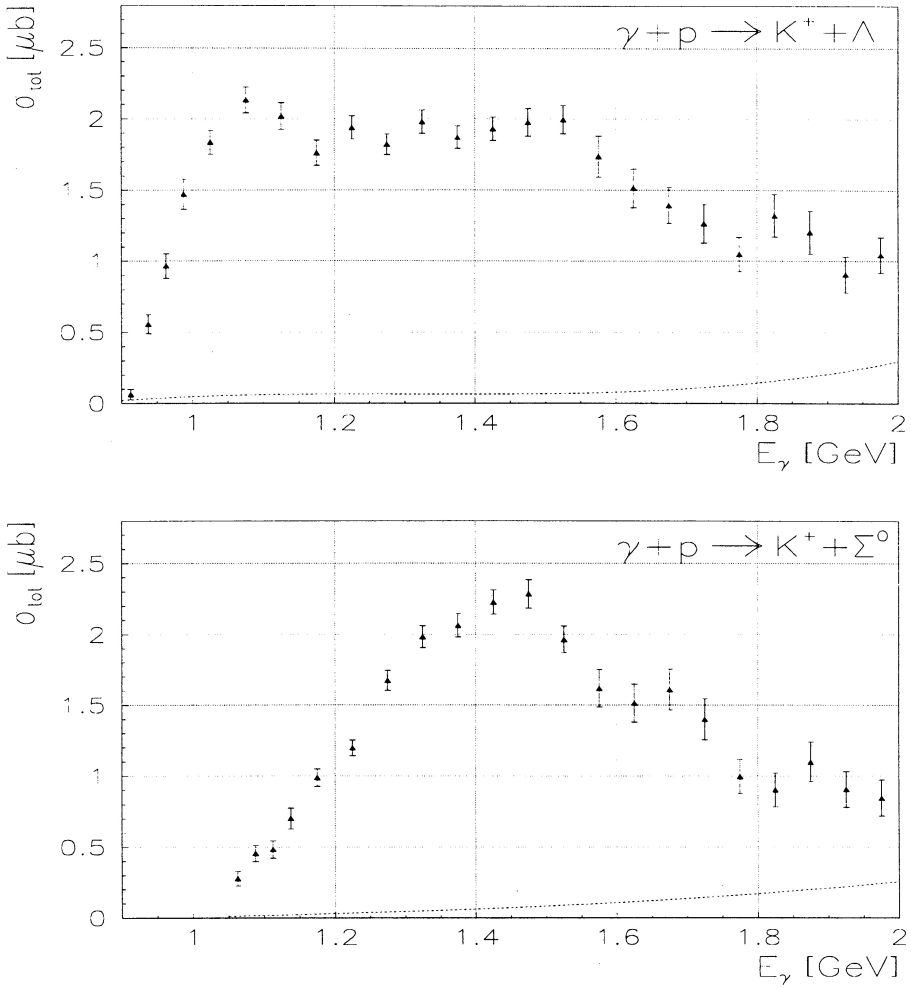

Figure 2.2: Total cross sections for $\gamma p \to K^+\Lambda$ (top) and $\gamma p \to K^+\Sigma^0$ (bottom). The systematic errors are indicated by the dashed lines [21].

production channel.

In the lower part of Fig. 2.2, the results of total cross sections of $K^+\Sigma^0$ channel are shown. The total cross section shows a smooth rise up to a peak around 1.45 GeV. This was interpreted to be attributed to $S_{31}(1900)$ and $P_{31}(1910)$ states that are predicted to couple strongly to $K^+\Sigma^0$ photoproduction [43].

The Fig. 2.3 shows the newest total cross sections data by SAPHIR group published in 2004 [22]. The newest data had a factor of 7-10 times larger statistics than the data taken in 1998. From the upper part of Fig. 2.3, a peak around 1.45 GeV in the total cross sections can still be observed, although it is not as significant as the previous results. With the new results, the SAPHIR collaboration claimed a rise of cross sections at backward kaon angles at this photon energy as shown in

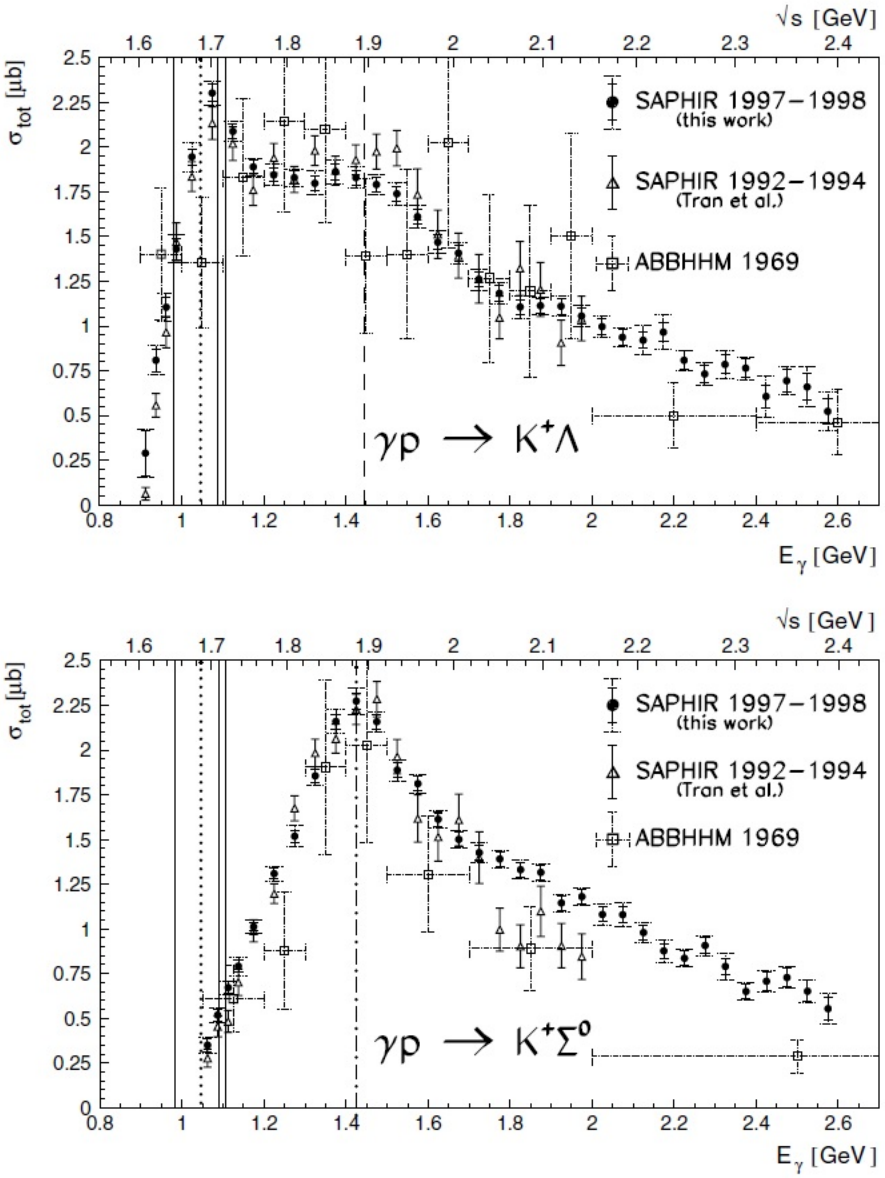

Figure 2.3: Total cross sections for $\gamma p \to K^+\Lambda$ (top) and $\gamma p \to K^+\Sigma^0$ (bottom) results from SAPHIR 2004 [22].

Fig. 2.4. The Fig. 2.4 shows the rise structure. SAPHIR collaboration claimed that this rise was due to the $D_{13}(1895)$.

2.1.2 CLAS

CEBAF, a large acceptance spectrometer (CLAS) experiment, can provide high coverage and high precision data in the Thomas Jefferson National Accelerator Facility (JLab). Fig 2.5 shows the CLAS large acceptance detector. The beam and detector system will be slightly discussed as an example in sec 3.1. Four sets of results were published by CLAS for the measurement of cross sections and beam asymmetries.

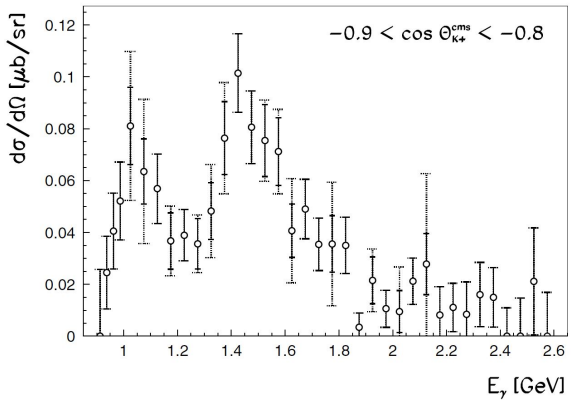

Figure 2.4: The differential cross sections of $\gamma p \rightarrow K^+\Lambda$ at backward angle -0.9<$\cos\theta^{K^+}_{c.m.}$<-0.8 shows an enhancement around 1.45GeV corresponding to a cms energy of 1900 MeV [22].

The first data were published in 2006 [28] with cross sections and target polarization measurement for both channels. The next two results were both published in 2010 for $K^+\Lambda$ [30] and $K^+\Sigma^0$ [31] with cross sections and target polarization measurement, and the newest results were published in 2016 [32] with beam asymmetry, target asymmetry, beam-recoil double polarization.

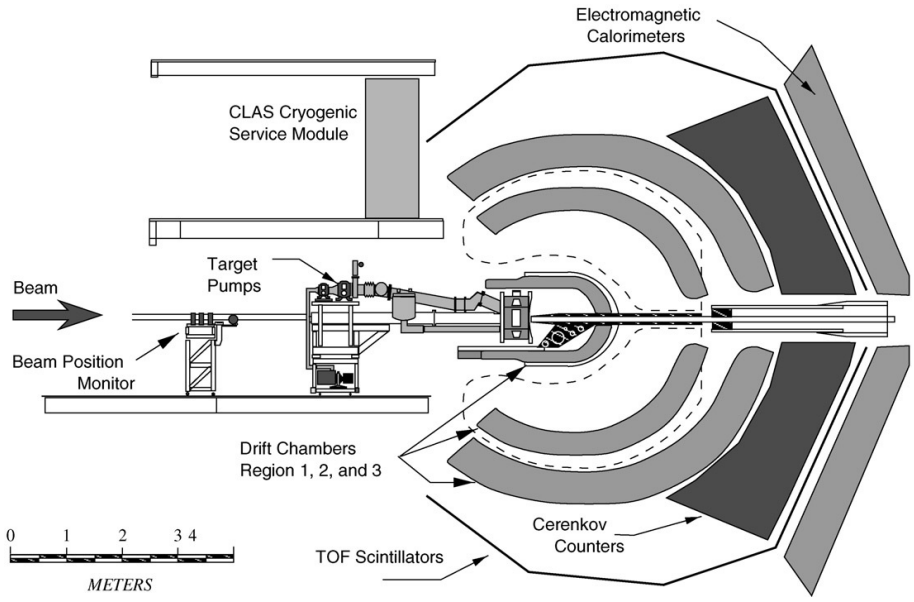

Figure 2.5: The CLAS large acceptance spectrometer [52].

After the SAPHIR 2004 measurements, the CLAS performed a high statistics, high precision measurements of cross sections for both the $K^+\Lambda$ and $K^+\Sigma^0$ channels at 2006 [28]. These measurements were made

for center of mass energy between $\sqrt{s} = 1.6$ and $\sqrt{s} = 2.53$ GeV, covering the $\cos\theta^{K^+}_{c.m.}$ from -0.8 to 0.9 with a circularly polarized photon beam incident on an unpolarized liquid-hydrogen target. By the higher statistics, the results were generally more precise than the SAPHIR measurements, with about two times more energy bins, and one fourth statistical uncertainties.

In Fig. 2.6, the differential cross sections for $K^+\Lambda$ channel are found to be flat as a function of $\cos\theta^{K^+}_{c.m.}$ near the production threshold. With an increasing in energy, the cross sections show a mild rising trend in both the forward and backward angles, before becoming predominantly forward peaked at energies above 2.3 GeV. By applying the fitting which intended to capture the main features of the decay amplitudes contributing to the angular distributions, CLAS collaboration claimed that the flat distribution near threshold can be explained by S-wave behaviour. When the energy increases, the P-wave amplitude becomes significant between threshold and 1.9 GeV. The D-wave amplitude turns on quite strongly near 1.9 GeV, and the F-wave amplitude has a broad dip centered at 2.05 GeV.

As the energy rises to about 1.8 GeV the cross sections show a significant forward raising trend which might come from the contribution either with t-channel contributions or with s-channel interference effects. When the energy becomes higher than $\sim$2.3 GeV, the forward peaking behaviour of the cross sections becomes dominant, which is interpreted as the t-channel exchange dominance.

Fig. 2.7 shows the differential cross sections for $K^+\Sigma^0$ channel. That forward peaking behaviour of the cross sections was not found below 2 GeV, consistent with that s-channel resonance is dominate with small t-channel influence.

The total cross sections for both channels are calculated from the integrated angular distributions. The Fig. 2.8 shows the results of total cross sections results. From this figure, the CLAS cross sections are larger than the SAPHIR cross sections significantly for the $K^+\Lambda$ channel, but in $K^+\Sigma^0$ channel, the measurements show a good agreement. The CLAS collaboration offers no reason for why there is a discrepancy in

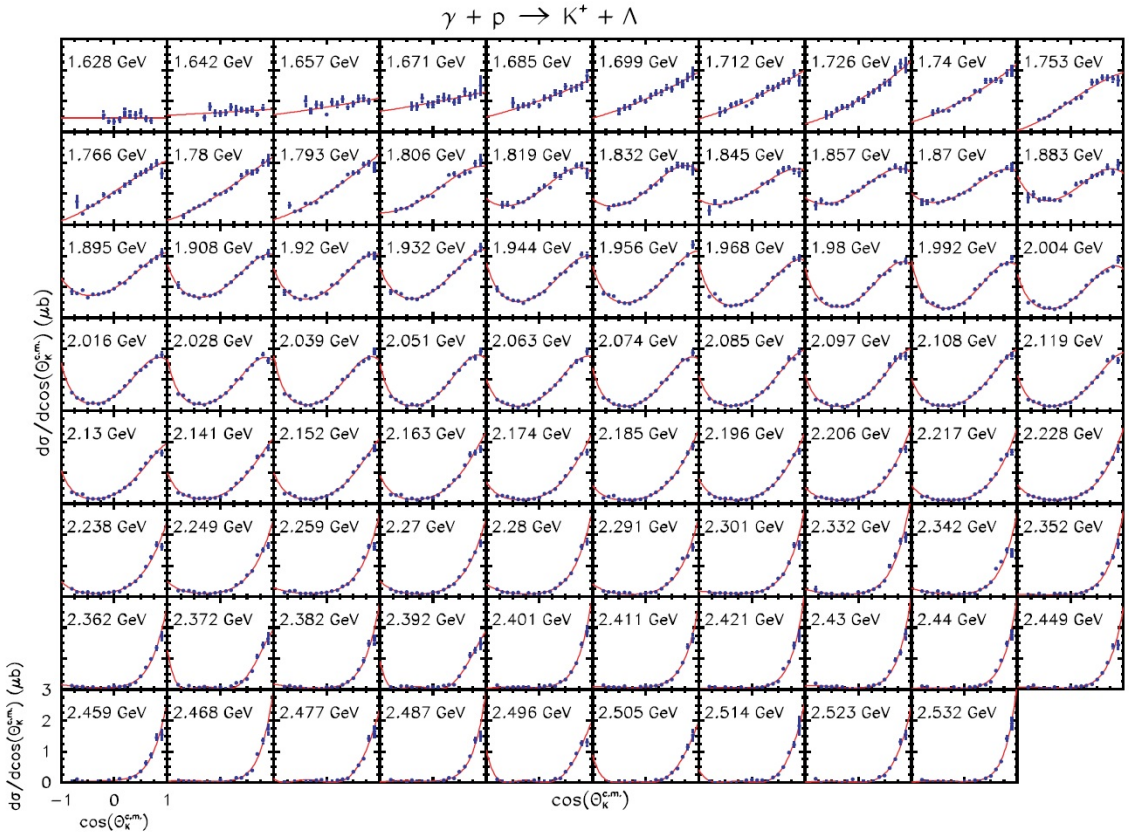

Figure 2.6: Differential cross sections for $\gamma p \to K^+\Lambda$. The number in each panel designates center of mass energy between $\sqrt{s}$. The solid lines are results of the amplitude fits. [28].

one channel but a good agreement in the other channel.

From the Fig. 2.8, in $K^+\Lambda$ channel, although the total cross sections deviate from SAPHIR results, the two structures found in the SAPHIR cross sections at $\sqrt{s} = 1.7$ and $\sqrt{s} = 1.9$ GeV still can be observed in CLAS data. The CLAS collaboration believes that the 1.7 GeV structure is consistent with the contributions from $P_{11}(1710)$ and $P_{13}(1720)$ states. For the structure near 1.9 GeV, which SAPHIR collaboration claimed that this rise was due to the $D_{13}(1895)$, CLAS collaboration expects that the structure is produced by the contributions from several resonances. For the $K^+\Sigma^0$ channel, the strong structure at 1.88 GeV has been observed, and the small bump around 2.05 GeV has also been observed. The peak at 1.88 GeV is believed to be composed of several Δ resonances which couple to the isospin 3/2 final state.

Since the forward peaking behaviour of the $K^+\Lambda$ cross sections has been observed clearly, it suggests that the reaction mechanism by t-channel exchange is dominant, even in the nucleon-resonance region.

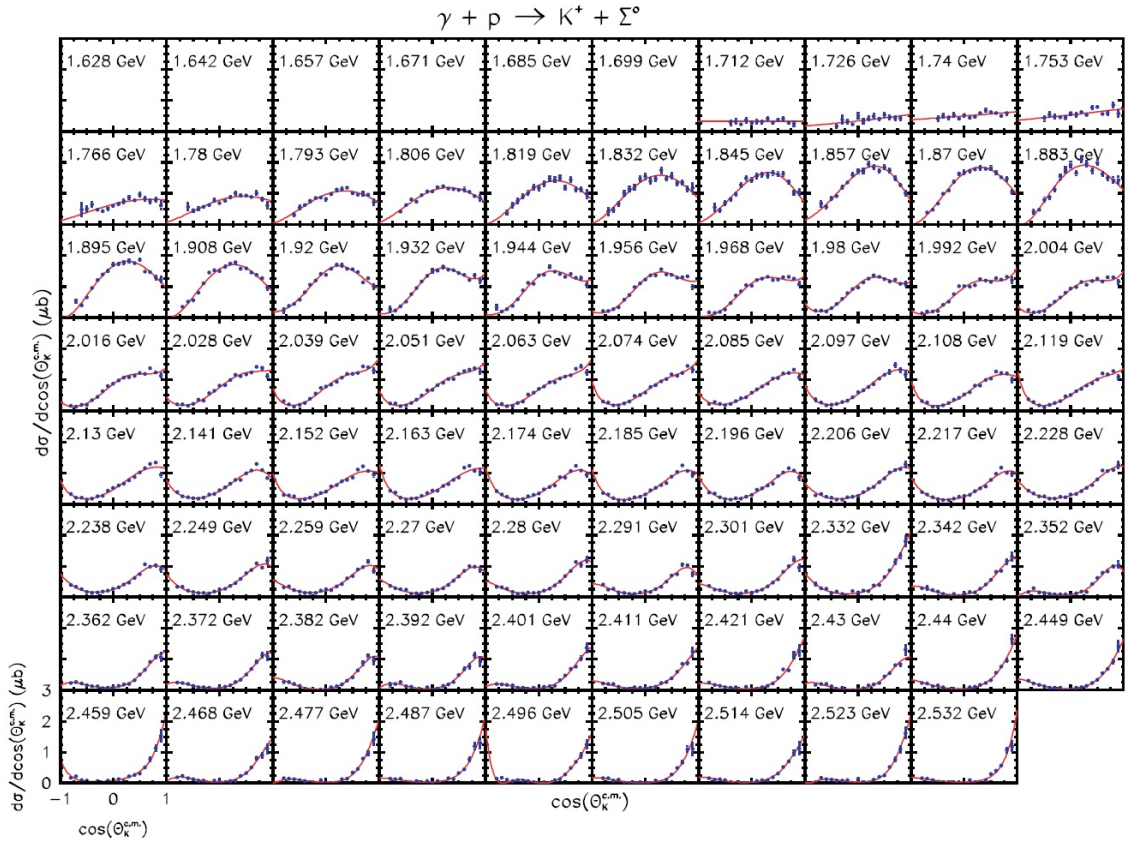

Figure 2.7: Differential cross sections for $\gamma p \to K^+\Sigma^0$. The number in each panel designates center of mass energy between $\sqrt{s}$. The solid lines are results of the amplitude fits. [28].

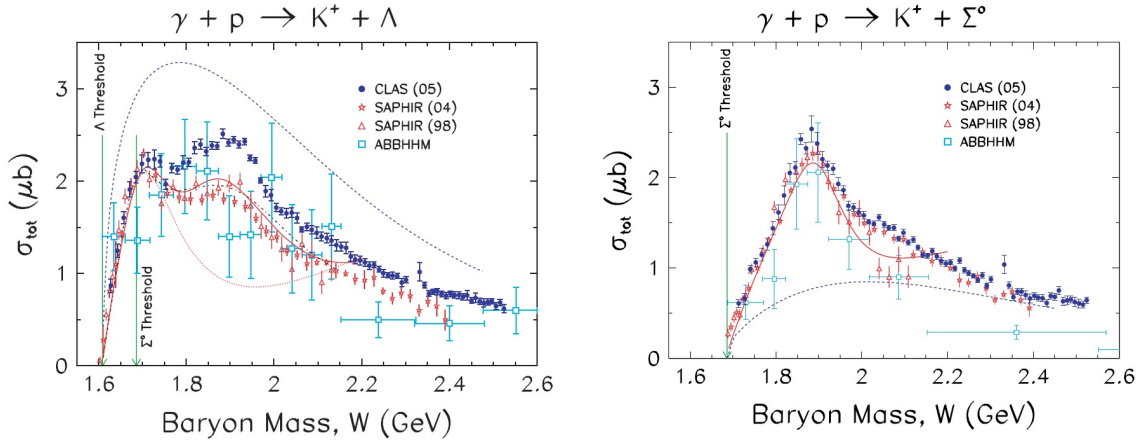

Figure 2.8: Total cross sections for $\gamma p \to K^+\Lambda$ and $\gamma p \to K^+\Sigma^0$ with two sets of SAPHIR results and the results from ABBHHM collaboration. [28]

CLAS collaboration investigated this scenario by obtaining $d\sigma/dt$ as shown in Fig. 2.9.

In the simplest Regge picture involving the exchange of a single trajectory, the cross section can be written as

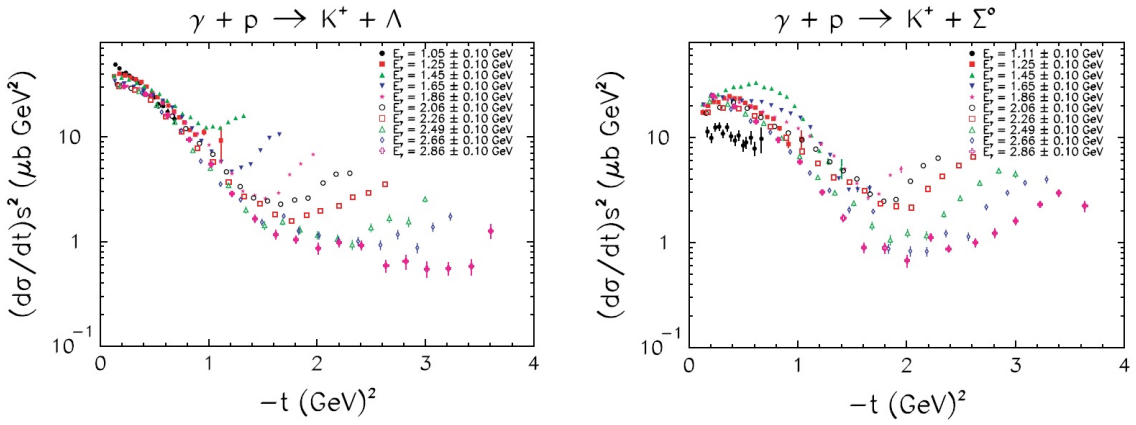

Figure 2.9: The 's^2' scaled cross sections for $K^+\Lambda$ and $K^+\Sigma^0$ channels. [28]

$$\frac{d\sigma}{dt} = D(t)(\frac{s}{s_0})^{2\alpha(t)-1} \tag{2.1}$$

where the D(t) is a function of t only, s_0 is a scale factor which is set to be 1 GeV^2, and α(t) is the slope of Regge trajectory.

The cross sections dσ/dt for $K^+\Lambda$ production are plotted in the left part of Fig. 2.9. By applying the s^2 scaling to the cross sections dσ/dt, we can see the data with different energy now fall on a fairly tight locus of points over a range of -t. CLAS collaboration interprets the departures from this locus as the onset of the s- and u-channel contributions to the reaction mechanism. A 'plateau' structure could be observed near the $|-t| \sim 0$, which also was seen in the data from SLAC [18] in the E_γ= 5,8,11, and 16 GeV region. In the model of Guidal, Laget, and Vanderhaeghen [83], the plateau near t=t_{min} in the differential cross sections was interpreted due to the contributions from a Reggeized s-channel diagram to maintain the gauge invariance and only for the K-exchange. For SLAC data, in the E_γ= 5, 8, 11, and 16 GeV region, it is obvious that the K and K^* exchange contribution are dominant. But the plateau structure in CLAS data is observed for the first time in the resonance region, which suggests the importance of K and K^* exchange throughout this kinematic region.

The cross sections dσ/dt for the $K^+\Sigma^0$ production are shown in the right part of Fig. 2.9. In this production channel, the data do not fall into a tight locus, which indicates a more nucleon resonance dominated picture. There is no consistent trend toward a flattening of the slope,

as was seen in $K^+\Lambda$ production.

In 2010, more CLAS cross sections results were published for $K^+\Lambda$ [30] and $K^+\Sigma^0$ channels [31]. The results of CLAS 2010 $K^+\Lambda$ and $K^+\Sigma^0$ cross sections are shown in Fig. 2.10, Fig. 2.11, and 2.12.

Fig. 2.10 shows, in $K^+\Lambda$ channel, the two peak structures at $\sqrt{s} =$ 1.7 and $\sqrt{s} = 1.9$ GeV still can be observed in 2010 data. The CLAS 2010 cross sections are still systematically larger than the SAPHIR results, and at the forward K^+ angles and higher E_γ region, the results of CLAS 2006 data are significantly higher than 2010 data.

For $K^+\Sigma^0$ channel, the Fig. 2.11 and Fig. 2.11 still show the peak structure at $\sqrt{s} = 1.9$ GeV. Like the $K^+\Lambda$ channel, at the forward $\cos\theta^{K^+}_{c.m.}$ and higher E_γ region, the results of CLAS 2006 data also show a significant higher tendency than 2010 data. Until now, there are still no reasonable explanation about the discrepancy between SAPHIR and CLAS 2006, 2010 data.

By introducing the coherent bremsstrahlung technique the beams of linearly polarized photons were produced by scattering electrons from a diamond radiator. The polarized photons open a new window to measure more physics observables for $\gamma p \to K^+\Lambda$ and $\gamma p \to K^+\Sigma^0$ photoproduction. The beam asymmetry, target asymmetry and beam-recoil double polarization have been published in 2016 [32]. The results of beam asymmetry are shown in Fig. 2.13 and Fig. 2.14 The beam asymmetries in both channels are all positive. The positive beam asymmetry was also seen in the data from SLAC [19] in the E_γ= 16 GeV region. The positive beam asymmetry indicates the reaction was dominated by a natural parity exchange mechanism. This clearly confirms the dominance of the K^* in these two reactions consistent with the Regge model calculation by Guidal, Laget, and Vanderhaeghen [83].

2.1.3 LEPS

The Laser Electron photon beam line at SPring-8 (LEPS) collaboration conducts the experiment in Super Photon ring-8 GeV (SPring-8) facility. The SPring-8 is a third-generation large-scale synchrotron radiation facility which serves the 8 GeV electrons inside the SPring-8 storage ring. By injection of the linear polarized UV laser photon beam into the

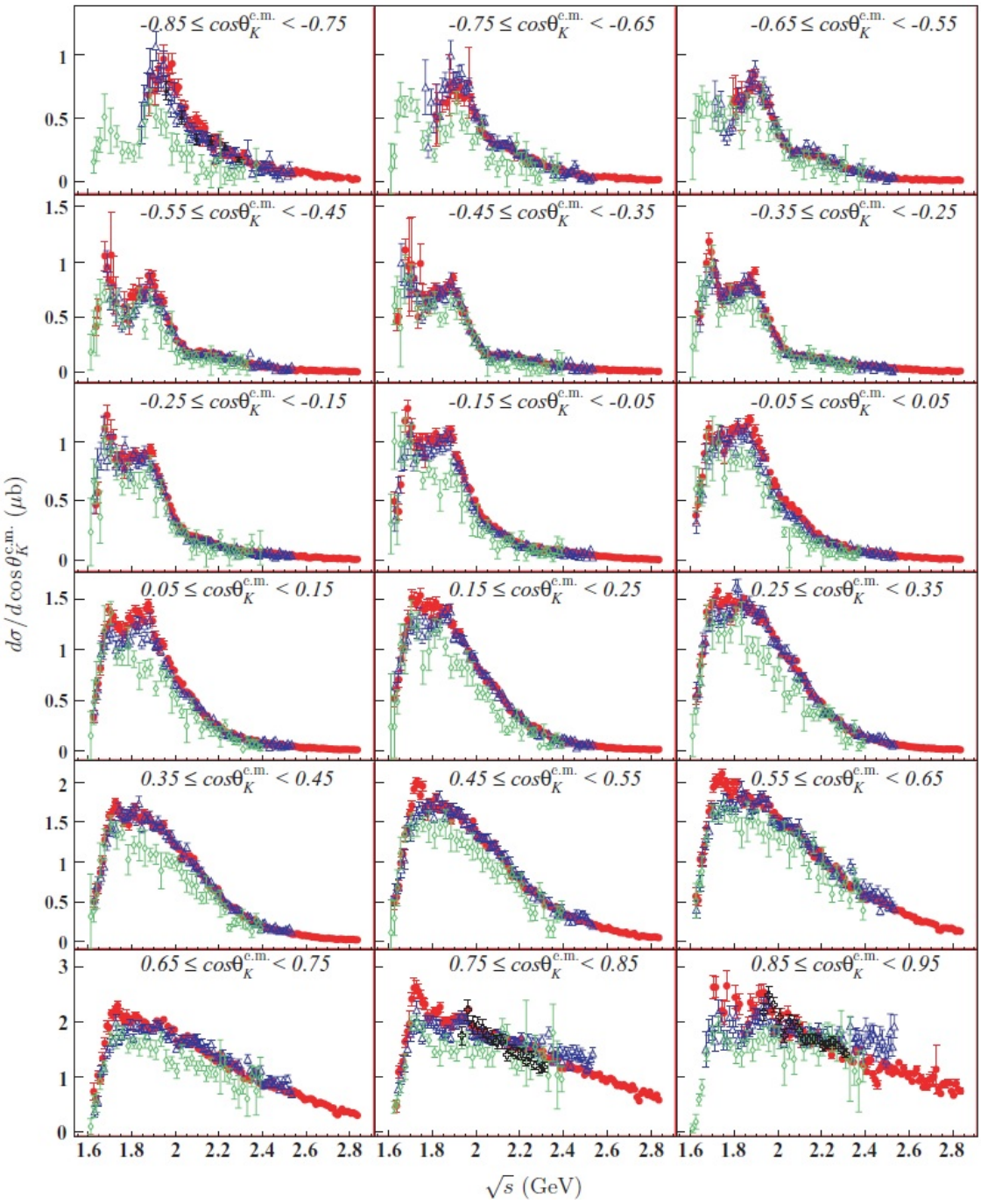

Figure 2.10: The cross sections results for $K^+\Lambda$ channel [30]. The results of the measurement of CLAS in 2010 are shown by closed red circles. The 2006 CLAS results [28] are shown by open blue triangles, 2004 SAPHIR [22] results are shown by open green diamonds, and the LEPS results are shown by open black crosses [24] and by close black stars [25].

SPring-8 electron storage ring, a high degree of linear polarization GeV photon beams could be obtained via the backward compton scattering (BCS) process between the electron and UV laser photon. Unlike the detector of SAPHIR and CLAS experiments can cover almost whole

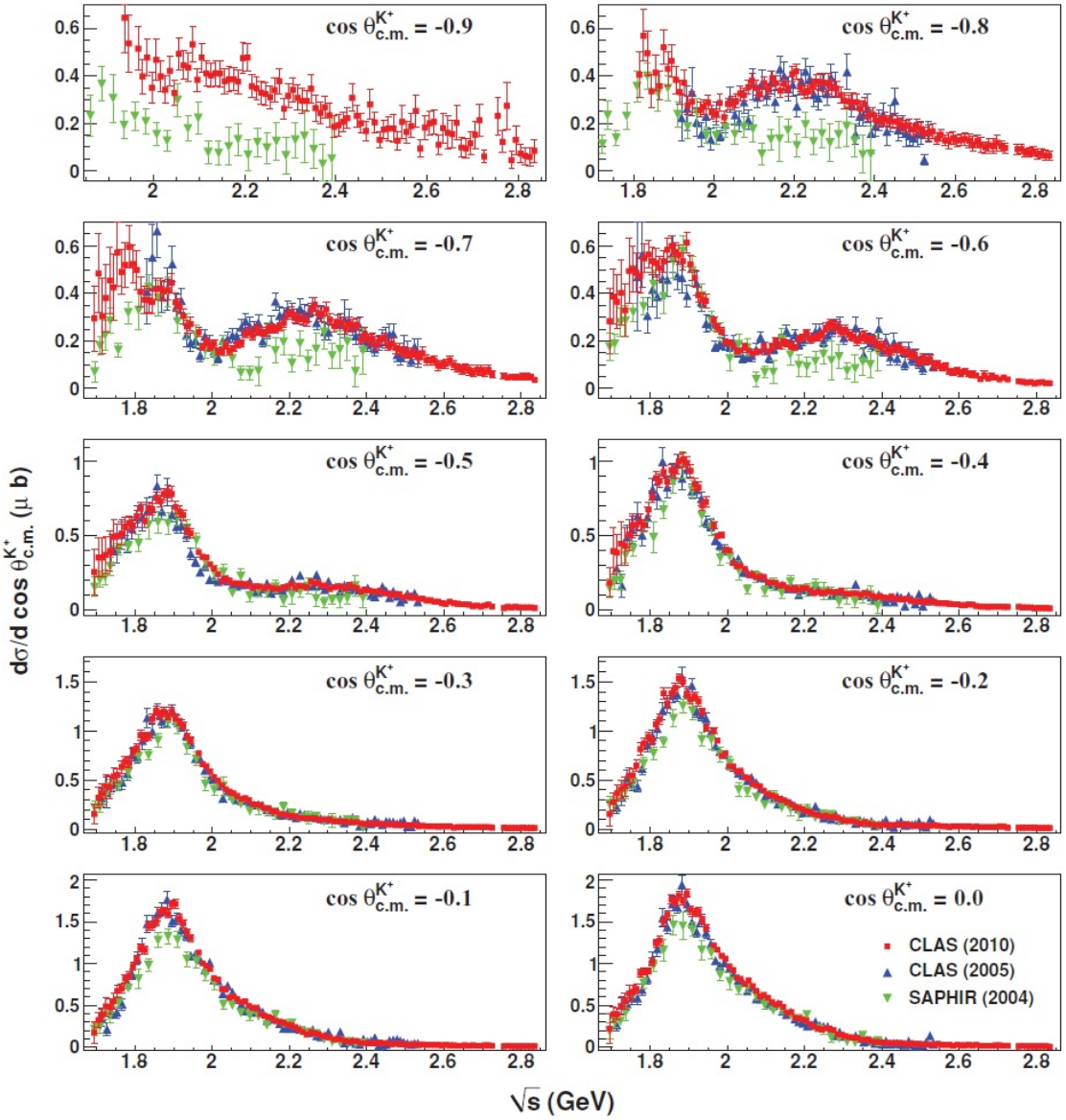

Figure 2.11: The cross sections results for $K^+\Sigma^0$ channel [31] for -0.9<$\cos\theta^{K^+}_{c.m.}$<0.

$\cos\theta^{K^+}_{c.m.}$ region, LEPS spectrometer provides the information in the forward angles that large acceptance detectors like CLAS can not provide as well. The detail of the spectrometer and the experiment setup will be discussed in detail in chapter 3.

There are four publications by LEPS for the measurement of cross sections and beam asymmetry in $\gamma p \to K^+\Lambda$ and $\gamma p \to K^+\Sigma^0$ photoproduction. The photon-beam asymmetry data were published in 2003 [23] for both channels for the fist time in E_γ=1.5-2.4 GeV and $\cos\theta^{K^+}_{c.m.}$=0.6-1.0. The next publication in 2006 [24] is with the cross sections measurement and the beam asymmetry measurement in E_γ=1.5-

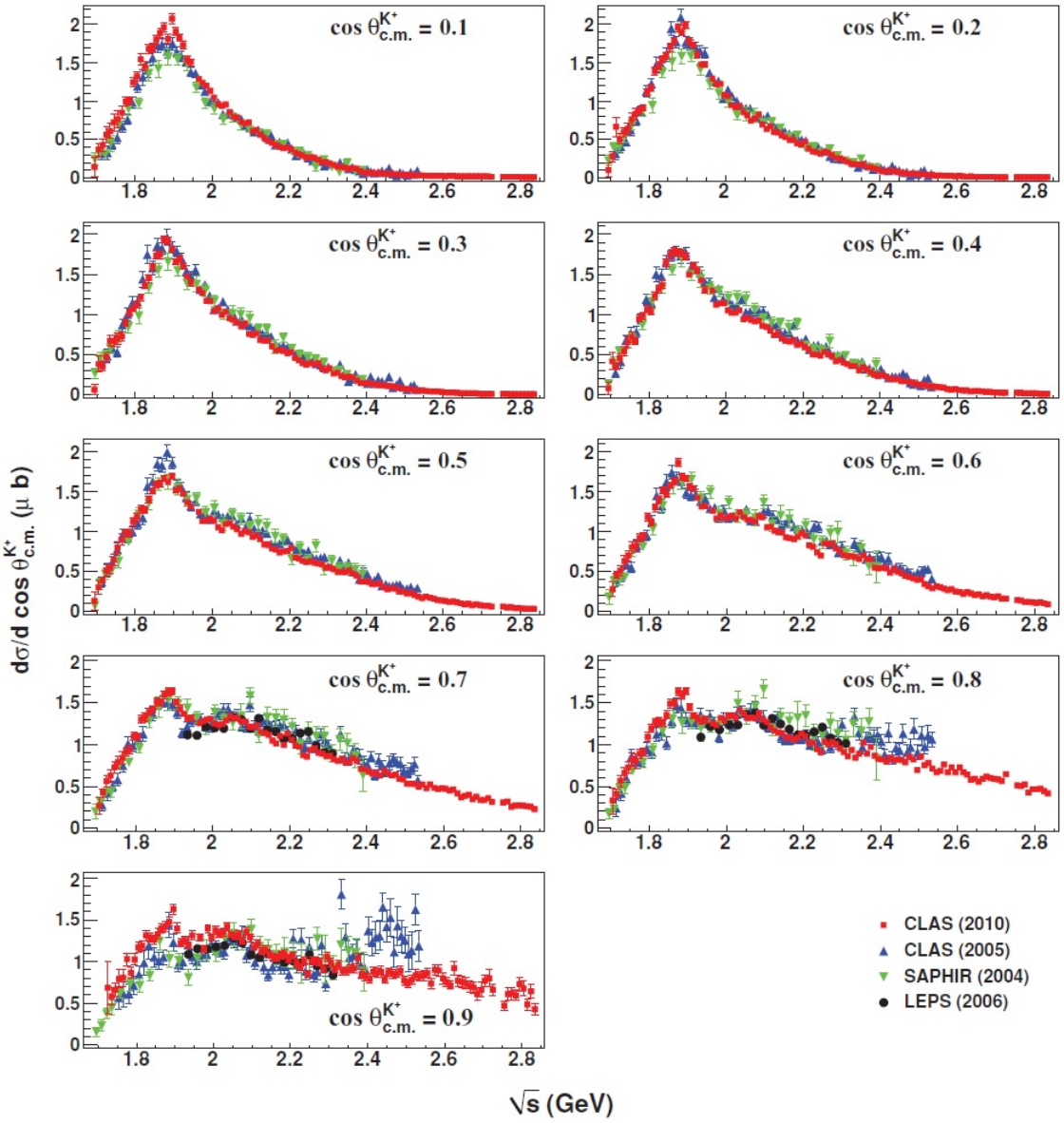

Figure 2.12: The cross sections results for $K^+\Sigma^0$ channel [31] for 0.1<$\cos\theta^{K^+}_{c.m.}$<0.9

2.4 GeV and $\cos\theta^{K^+}_{c.m.}$=0.6-1.0. The above two measurements are all studied in K^+ detection modes to calculate the missing mass at very forward region. In the same year, the publication [26] of the $\gamma n \to K^+\Sigma^-$ and $\gamma p \to K^+\Sigma^0$ photoproduction with liquid deuterium and hydrogen targets in E_γ=1.5-2.4 GeV and $\cos\theta^{K^+}_{c.m.}$=0.6-1.0 with cross sections and beam asymmetry has been published. The results published in 2007 [25] were cross sections and beam asymmetry at very backward region via the $p\pi^-$ detection mode to calculate the invariant mass.

Fig. 2.15 shows the differential cross sections for $K^+\Lambda$ and $K^+\Sigma^0$ channels. The LEPS data are in good agreement with the CLAS data

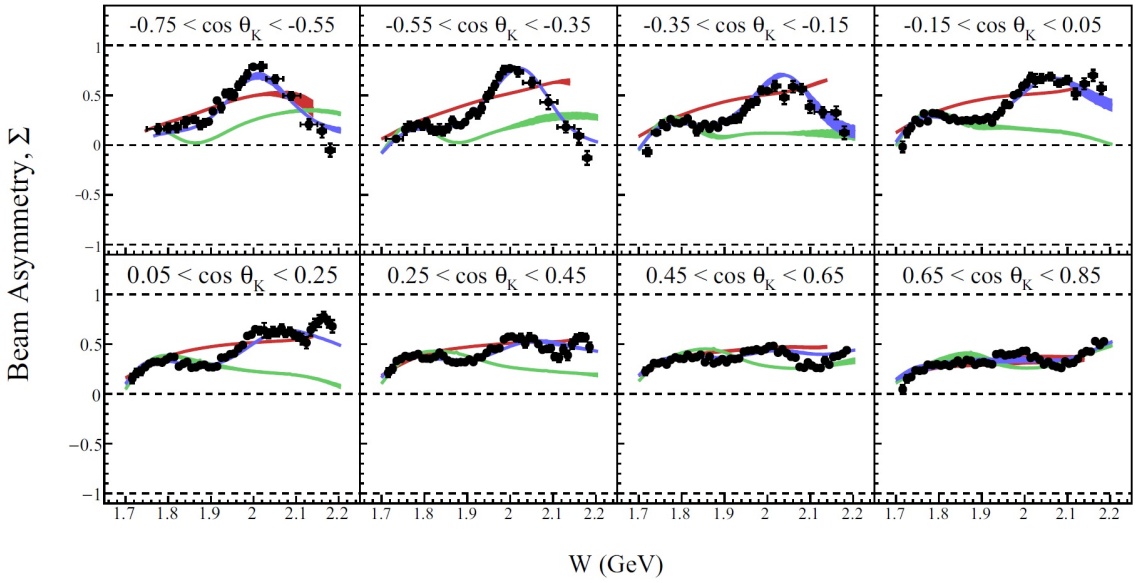

Figure 2.13: The energy dependence of the beam asymmetry (Σ_γ), for $K^+\Lambda$ channel. Red curves: ANL-Osaka predictions from coupled-channels calculations; green curves: predictions from the 2014 solution of the Bonn-Gatchina partial wave analysis; blue curves: Bonn-Gatchina calculations after a refit including the present data, which include additional $N^*(\frac{3}{2}^+)$ and $N^*(\frac{5}{2}^+)$ resonances [32].

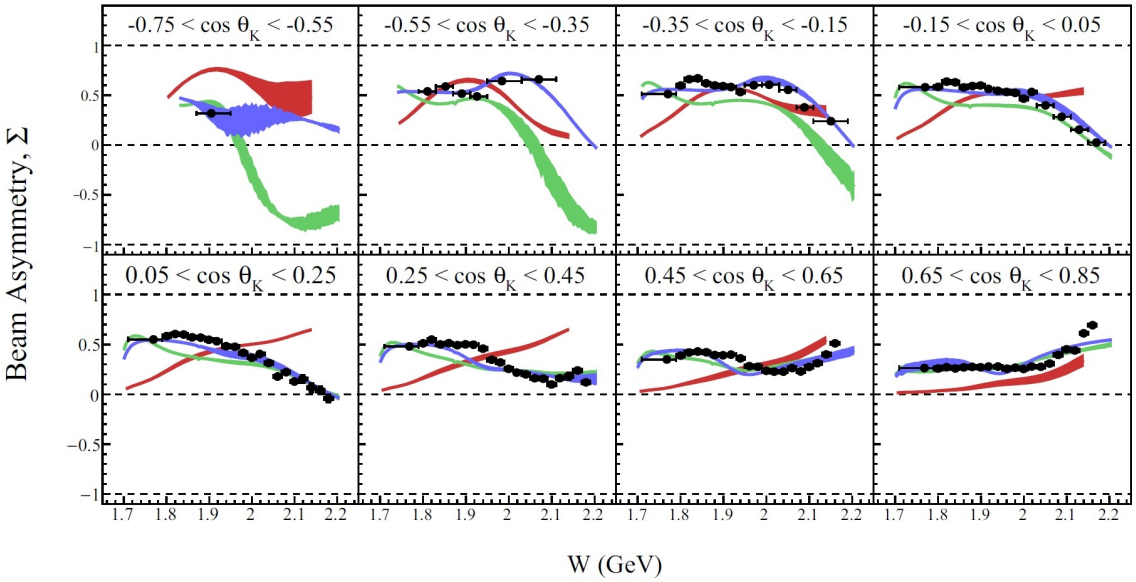

Figure 2.14: The energy dependence of the beam asymmetry (Σ_γ), for $K^+\Sigma^0$ channel. Red curves: ANL-Osaka predictions from coupled-channels calculations; green curves: predictions from the 2014 solution of the Bonn-Gatchina partial wave analysis; blue curves: Bonn-Gatchina calculations after a refit including the present data, which include additional $N^*(\frac{3}{2}^+)$ and $N^*(\frac{5}{2}^+)$ resonances [32].

within the total uncertainty and are systematically higher than the SAPHIR data at all angles. The solid curve representing the mixing models of the Feyman diagram and the Regge model shows a good agreement with the LEPS and the CLAS data in all regions.

The Reggeized K and K* exchanges model calculation overestimates

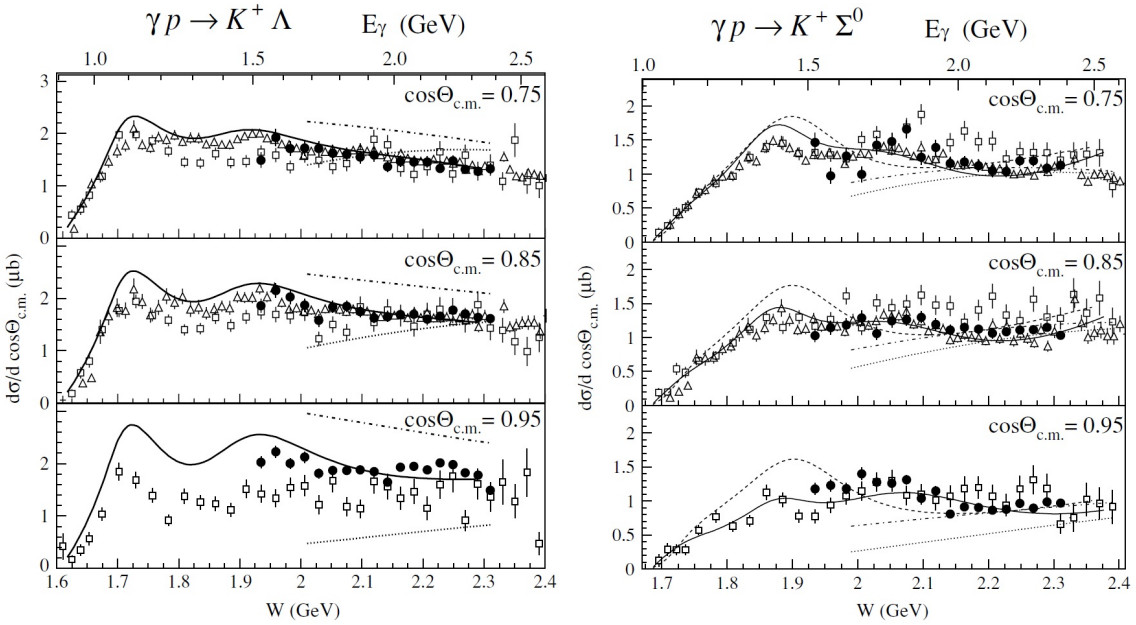

Figure 2.15: The results of cross sections for $K^+\Lambda$ and $K^+\Sigma^0$ channel. The closed circles, open squares, and open triangles are from the LEPS [24], SAPHIR [22], and CLAS [28], respectively. The dot-dashed and dotted curves are the results of the Regge model with the K and K* exchanges and the K* exchange, respectively, obtained by Guidal et al. [84]. The solid curves indicate the result of the mixing models of the Feynman diagram and the Regge model [40].

the data, whereas the K* exchange only calculation underestimates data at forward angles in the $K^+\Lambda$ channel. By comparing the K and K* exchanges model calculation with the K* exchange only calculation, the difference becomes larger at forward angles, this is because the K exchange becomes dominant at forward angles.

The K and K* exchange model underestimates the data at W $<$ 2.15 GeV but shows an agreement with the data at W $>$ 2.15 GeV where the t-channel contribution is expected to be dominant in $K^+\Sigma^0$ reaction. In the Regge model, the contribution of the K exchange for the $K^+\Sigma^0$ reaction is smaller than that for the $K^+\Lambda$ reaction because the coupling constant $|g_{K\Sigma N}|$ is smaller than $|g_{K\Lambda N}|$ [83]. This relation might lead to the result that the difference between the Regge model using K and K* exchange and the model having only K* exchange for the $K^+\Sigma^0$ is smaller than that for the $K^+\Lambda$ reaction.

The beam asymmetry is expected to be sensitive to the resonance. Therefore, the measurements of the photon-beam asymmetry is a powerful tool to check the validity of model calculations. The beam asymmetry results for both the $K^+\Lambda$ and $K^+\Sigma^0$ channels are displayed in

Fig. 2.16. These results show that the beam asymmetry data are positive at all forward angles and increase gradually as the photon beam energy increases.

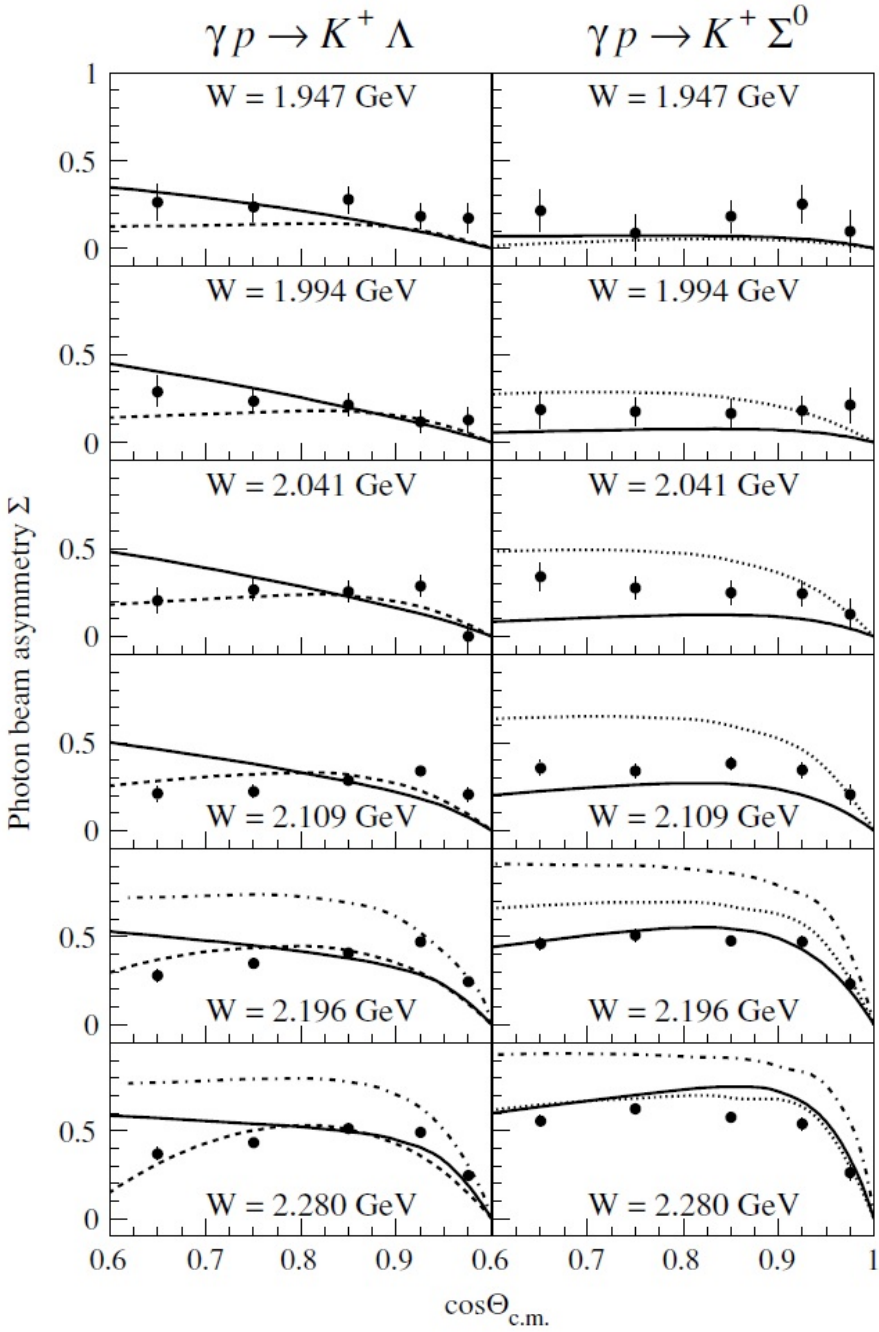

Figure 2.16: The photon-beam asymmetry results for the $\gamma p \to K^+\Lambda$ (left) and $\gamma p \to K^+\Sigma^0$ (right) photoproductions as a function of $\cos\theta^{K^+}_{c.m.}$ [24].

The backward region results for $K^+\Lambda$ are shown in Fig. 2.17. The results cover the very backward region of $\cos\theta^{K^+}_{c.m.}$=0.8-1.0. In the overlapping region with CLAS and SAPHIR, the LEPS 2007 results show

a good agreement with CLAS 2006 [28] and CLAS 2010 [30], and are systematically higher than SAPHIR measurements [22].

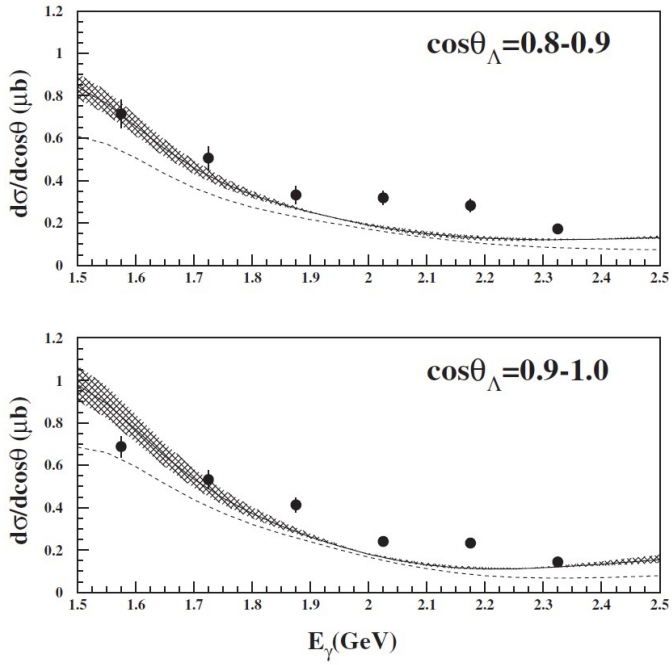

Figure 2.17: The cross sections as a function of photon beam energy for the $\gamma p \to K^+\Lambda$ at backward region [25].

2.1.4 GRAAL

Gr.A.A.L. is the acronym 'GRenoble Anneau Accelerateur Laser'. The GRAAL experiment has been conducted with the GRAAL facility, installed at the European Synchrotron Radiation Facility (ESRF) in Grenoble, France. Like LEPS experiment, the polarized photon beam is produced by Backward Compton Scattering (BCS) process between the 6.03 GeV electrons circulating in the storage ring and 333, 351 and 364 nm UV Laser giving 1.40, 1.47 and 1.53 GeV maximum energies, respectively. The 4π LAγRANGE detector shown in Fig. 2.18 was utilized to detect both neutral and charged particles. A set of MultiWire Proportional Chambers (MWPCs) was applied to provide tracking information for the charged particles. The particle identification (PID) is done by a double plastic scintillator hodoscope which gives time of flight measurements. The detail of this experiment is described in ref. [35].

In 2007, GRAAL collaboration published the results of measurements for the beam asymmetry and hyperon recoil polarization for both $K^+\Lambda$ and $K^+\Sigma^0$ photoproduction reactions, with the photon energies

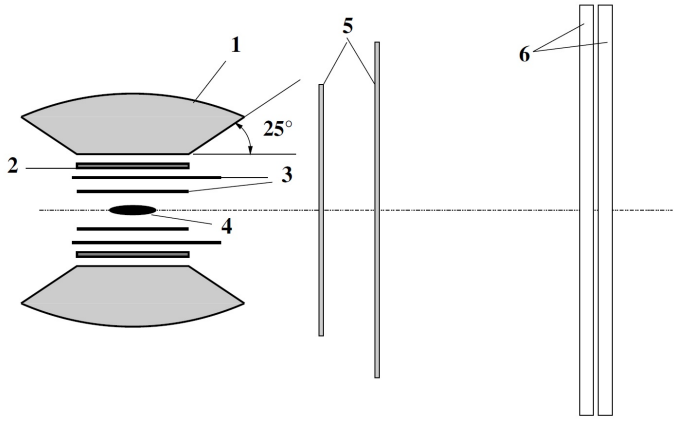

Figure 2.18: Schematic view of the LAγRANGE detector: BGO calorimeter (1), plastic scintillator (2), cylindrical MWPCs (3), target (4), plane MWPCs (5), double plastic scintillator hodoscope (6)(the drawing is not to scale)(L.A.GR.A.N.G.E. is the acronym for Large Acceptance GRaal-beam Apparatus (for) Nuclear Gamma Experiments.). [33].

from threshold up to 1.5 GeV as shown in Fig. 2.19. The photon-beam asymmetry results for the $K^+\Lambda$ channel were displayed in the left panel of figure 2.19. The results for the photon asymmetry cover the energy range from threshold up to 1.5 GeV for the first time. GRAAL collaboration claimed the good agreement with the previously published LEPS beam asymmetry results [24] in the overlapping energy region.

The GRAAL measurements show that the positive photon-beam asymmetry remain for almost the full range of kinematics, and the sign changing occurs only at the energies close to threshold. Due to the different angular axis selection, it is hard to compare the CLAS 2016 [32] beam asymmetry results with GRAAL 2007 data. But the CLAS 2016 beam asymmetry data in $K^+\Lambda$ channel show a mild decreasing trend toward the lower beam energy region. Judging from this observation, the sign changing near the production threshold is possible. For $K^+\Sigma^0$ results, in the right part of Fig. 2.19 the photon-beam asymmetry is all positive for the full range of kinematics.

For the recoil polarization a good agreement between the GRAAL results and previous measurements from both SAPHIR [22] and CLAS [27] is found.

After the GRAAL 2007 publication, the GRAAL collaboration pub-

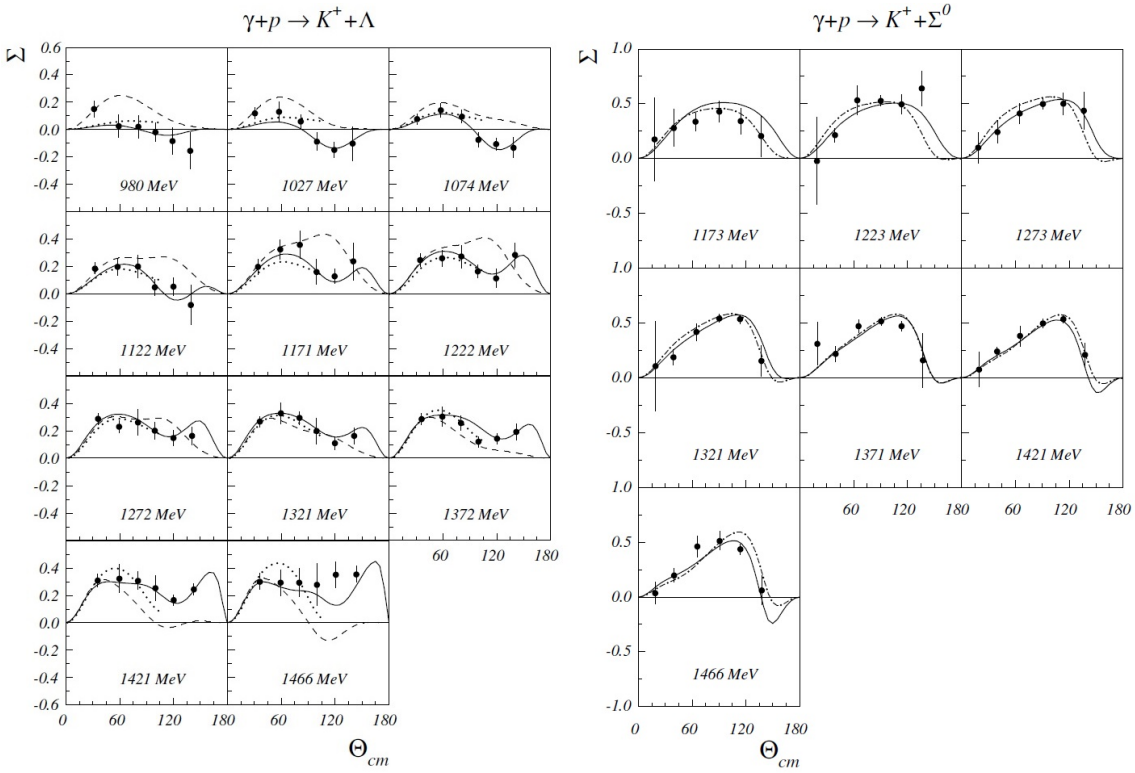

Figure 2.19: Angular distributions of the beam asymmetries in the $\gamma p \to K^+\Lambda$ (left) and $\gamma p \to K^+\Sigma^0$ (right) photoproductions and beam energies ranging from threshold up to 1500MeV. [33].

lished the results of GRAAL 2009 [34] on the measurements of the beam-recoil observables O_x, and O_z and the target asymmetry T for $\gamma p \to K^+\Lambda$ photoproduction. By analysing the GRAAL 2009 data, the Regge Plus Resonance (RPR) groups [72] concluded that the large sensitivity to resonance contributions was observed for target polarization T and the beam-recoil observables O_x, and O_z.

2.1.5 Crystal Ball

The results for the $K^+\Lambda$ and $K^+\Sigma^0$ channels by using the Crystal Ball calorimeter at Mainz Microtron accelerator facility (MAMI-C), were published in 2014 by Jude et al. [36]. The bremsstrahlung photon beam of Crystal Ball experiment was provided by impinging the MAMI-C 1557.4 MeV electron beam on a copper radiator. Fig. 2.20 shows the Crystall Ball detector. By carefully measuring the energy and timing of the two K^+ dominant decay modes $K^+ \to \mu^+\nu_\mu$ and $K^+ \to \pi^+\pi^0$, the Crystal Ball experiment can provide about a factor of 4 to 10 times more improvement of statistics for $\gamma p \to K^+\Lambda$ and $\gamma p \to K^+\Sigma^0$ photoproduction than previous results (For Clarity, in the publication of

Crystal Ball, the data have been rebinned by a factor of two). Fig. 2.21 shows the cross sections of both the channels at -0.7<$\cos\theta^{K^+}_{c.m.}$<0.1 with the CLAS and SAPHIR cross sections for the comparison.

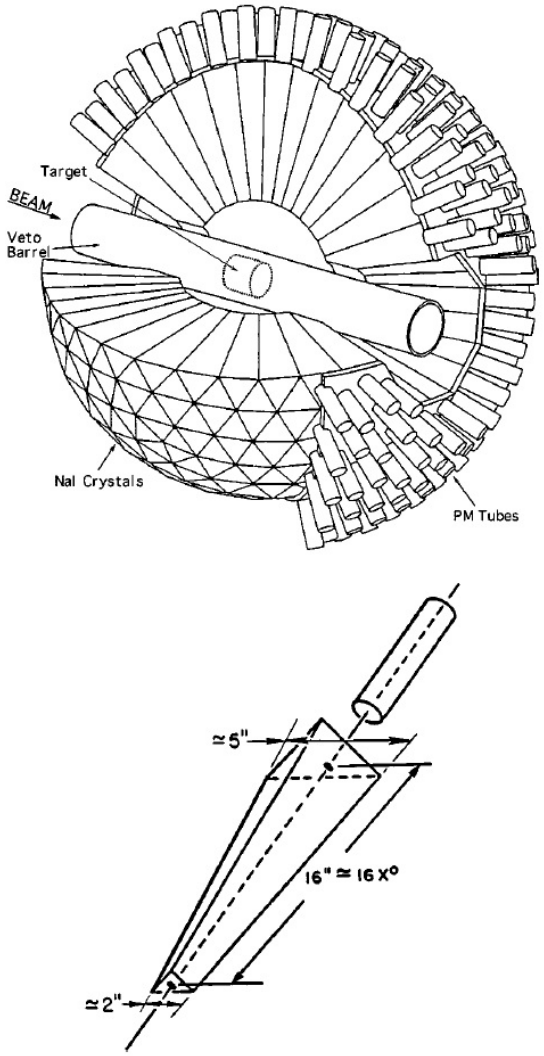

Figure 2.20: The Crystal Ball detector (top) and the dimensions of the Crystal Ball crystals [37]

Figure 2.21 shows the results of Crystal Ball are in good agreement with the previously published data of the $\gamma p \to K^+\Lambda$ channel at the backward K^+ angle region. The conspicuous peak structure near the center of mass energy $\sqrt{s} = 1.7$ has been confirmed in the backward kaon production angle. The well defined structure around 1670 MeV provides a strong constraint on the existence and width of the $P_{11}(1710)$.

For the $\gamma p \to K^+\Sigma^0$ channel, the Crystal Ball results are generally consistent with the previous measurements in most of regions. The

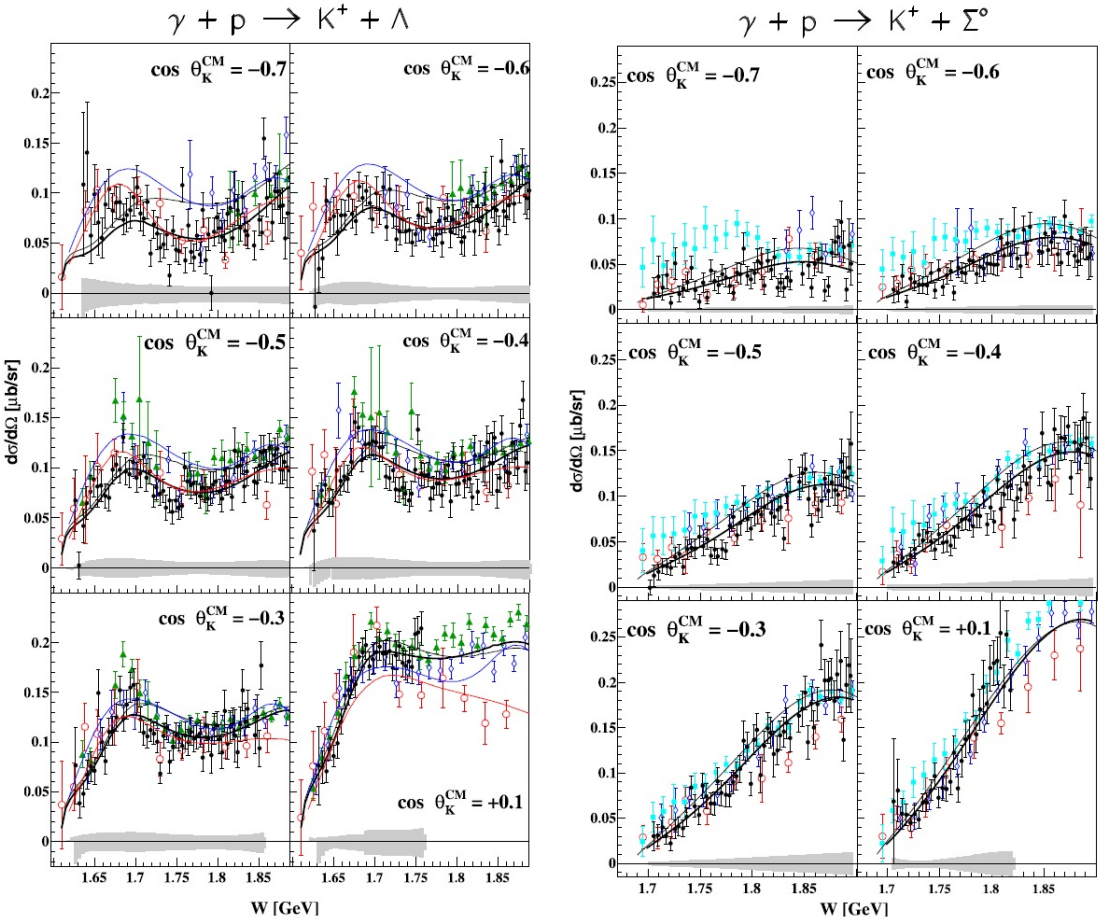

Figure 2.21: Differential cross-sections versus W. for $\gamma p \to K^+\Lambda$ and $\gamma p \to K^+\Sigma^0$ Black filled circles are the Crystal Ball data with systematic uncertainties plotted gray on the abscissa. Red open circles are SAPHIR data [22], blue open diamonds are CLAS 2006 data [28] and green filled triangles (cyan solid squares) are CLAS 2010 data [30, 31].

measurements of CLAS and SAPHIR show a disagreement at backward angles for $\sqrt{s}$ below 1.85 GeV. The results from Crystal Ball experiment have a better agreement with the SAPHIR data. The Crystal Ball collaboration claims that the improved statistical accuracy and energy resolution of the new data allows constraints on the existence of structures in the cross sections arising from narrow resonance states, interferences between resonances or coupled channel effects.

2.2 Theoretical Models

Based on the non-perturbative nature of strong interaction, applying the accessible first-principles QCD based calculation to hadronic processes is almost impossible. The interpretation of our measurements will be complicated and heavily relies on available model calculations. Since the hadronic process can not be fully calculated by

QCD, the model calculations consider the constituent quark degrees of freedom instead of the fundamental quark and gluon degrees of freedom. The theoretical models test the existence of resonances by the comparison of the model predication with the data. In this thesis, the models listed below will be discussed, the isobar calculation based KAON-MAID model [44, 46, 47, 48], the coupled channel analysis based Bonn-Gatchina model [75, 76, 77, 78, 79, 80], and the Regge based RPR model [70, 71, 72].

2.2.1 Isobar Models

The basis of isobar calculations is an effective Lagrangian constructed by a selection of Feynman diagrams. The isobar model is often called the tree-level approximation because only the Feynaman diagrams with the smallest possible number of interaction vertices are considered. The goal of this calculation is to describe the hadronic reactions via the consideration of various tree-level Feynman diagrams for both the resonance and non-resonance exchange of mesons and baryons. Every reaction particle is characterized by its properties such as mass, charge, form factors decay widths and coupling constants as an effective field.

In a typical isobar models, the Feynman diagrams contributing to the $\gamma p \to K^+ Y$ reaction are shown in Fig. 2.22. The s-channel terms involving an excited state (right upper red diagram) can produce resonance structures. The t-, u-, and s-channel Born terms are background contributions. Due to the different isospin (I) properties of Λ ($I = 0$) and Σ^0 ($I = 1$), only $I = 1/2$ N^* intermediate states could couple to $K^+\Lambda$ final state while both $I = 1/2$ N^* and $I = 3/2$ Δ^* intermediate states are allowed for $K^+\Sigma^0$ production. At higher energy region (typically above E_γ=1.5 GeV), the contribution of such Born terms increases dramatically compared to the experimental measurement. To reduce this dramatical increasing the introduction of form factors was applied to the background contribution. Gauge invariance is then respected through the inclusion of contact diagrams which is not shown.

Due to the simple consideration with the smallest possible number of interaction vertices, the tree-level approximation may not account for coupled channel effects and final state interactions. It still provides the

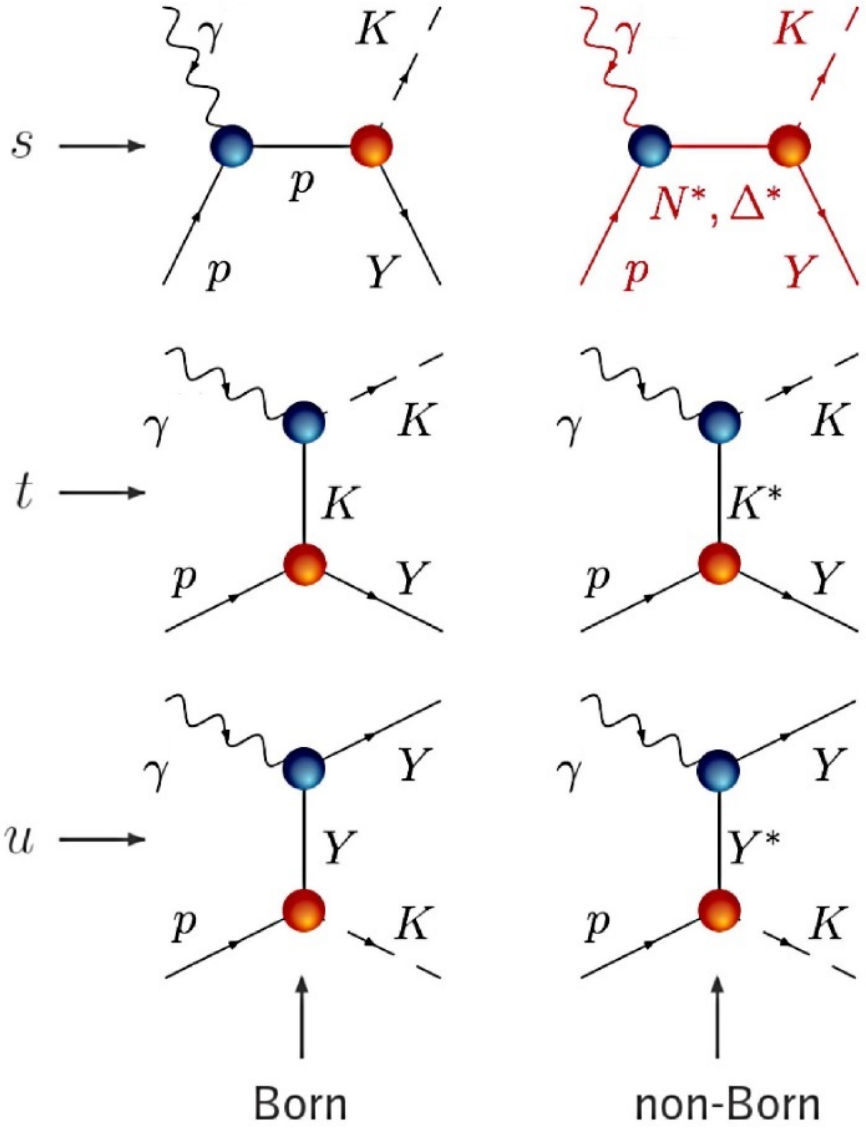

Figure 2.22: The tree-level contributions to the $\gamma p \to K^+ Y$. For this analysis, the Y denotes Λ and Σ^0. It is noted that the Δ^* states can only be exchanged in the $K^+\Sigma^0$ final state for the reasons of isospin conservation.

reduction of the complexity of the interaction and gives a fairly reliable qualitative understanding of the resonance parameters.

T. Mart and C. Bennhold published the isobar model base calculation called KAON-MAID in 1999 [44], which is the first time to search for the missing resonance in strangeness photoproduction by considering the SAPHIR data.

The KAON-MAID selected the resonances of s-channel $S_{11}(1650)$, $P_{11}(1710)$, $P_{13}(1720)$, $D_{13}(1895)$ (missing resonance), and t-channel $K^*(893)$ and $K_1(1270)$. The $D_{13}(1895)$ was first predicted by Capstick and Roberts [42]

as a missing resonance which couples strongly with kaon photoproduction. To reduce the inclusion of free parameters, KAON-MAID utilized SU(3) symmetry for the coupling constant of the background Born term, and kept the coupling constant as free parameters for resonance terms in the fitting to the data. To reduce the strength of the background at higher energy region, the KAON-MAID employs the dipole parametrization form factor

$$F(\Lambda, q^2) = \frac{\Lambda^4}{\Lambda^4 + (q^2 - m^2)^2} \tag{2.2}$$

where m stands for the mass of the exchange particle, the q is the invariant momentum transfer which is obtained by square root of the Mandelstam variable, $\sqrt{s}$, $\sqrt{-u}$ or $\sqrt{-t}$. The Λ here is the form-factor cutoff mass.The KAON-MAID calculator is available on the web page [68]

Fig. 2.23 shows the total cross section data by SAPHIR 1998 publication [21]. The data were fitted by KAON-MAID with and without the $D_{13}(1960)$ ($D_{13}(1895)$). The results of total cross sections were well described by the inclusion of $D_{13}(1960)$ ($D_{13}(1895)$).

Fig. 2.24 shows the photon-beam asymmetry calculation results. The dashed line indicates the calculations without the $D_{13}(1960)$ ($D_{13}(1895)$) resonance, and the solid line has the contribution from $D_{13}(1960)$ ($D_{13}(1895)$). Juding from this calculation, Mart and Bennhold claimed that the photon-beam asymmetry should be very sensitive to the inclusion of the missing resonance.

In the publication by T. Mart and C. Bennhold in 1999 [44], only the data of cross sections were applied for the fitting study to conclude the existence of the missing resonance $D_{13}(1895)$. Twelve years later, in 2012, T. Mart published another paper [45] where the observation of $D_{13}(1895)$ was withdrawn instead the peak structure comes from the $P_{13}(1900)$. The KAON-MAID is valid only for the center of mass energy below 2.2 GeV now. So, in this analysis we will not include the comparison with this model.

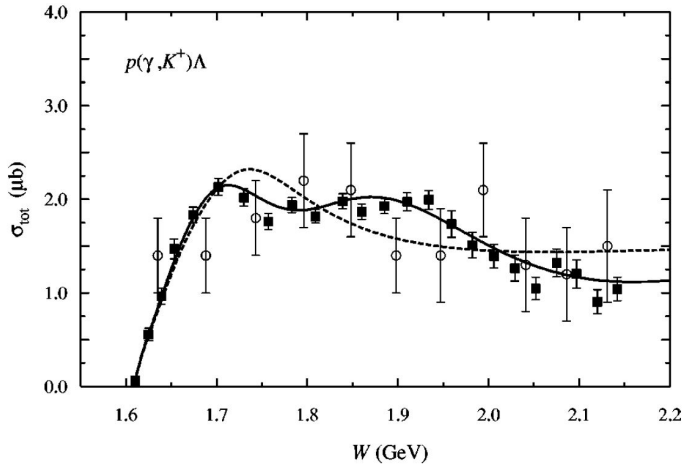

Figure 2.23: Total cross section for $K^+\Lambda$ photoproduction. The dashed line shows the model without the $D_{13}(1960)$ ($D_{13}(1895)$) resonance, while the solid line is obtained by including the $D_{13}(1960)$ ($D_{13}(1895)$) state. The SAPHIR 1998 data [21] are denoted by the solid squares, SAPHIR 1994 data [50], are shown by the open circles [44].

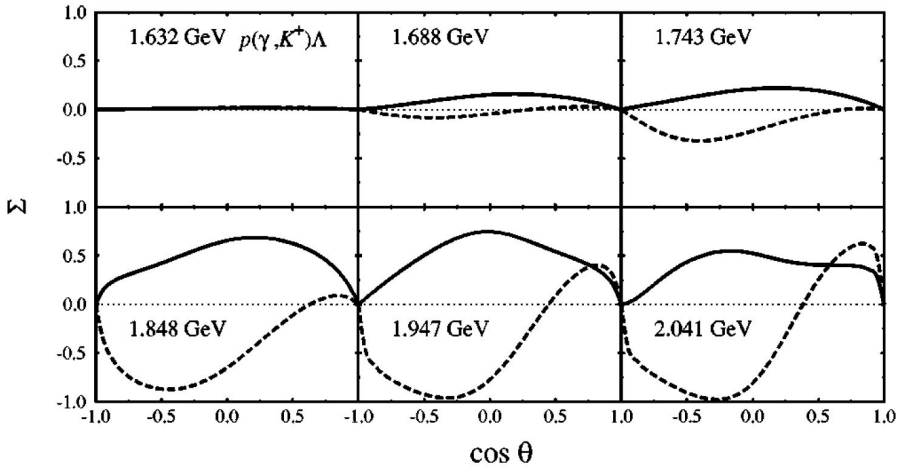

Figure 2.24: Mart and Bennhold calculations for the photon-beam asymmetry [44].

2.2.2 Coupled Channel analysis

The tree-level isobar models are insufficient to account for multi-step, coupled channel effects from the intermediate states. By recent research, it is believed that the multi-step sequence like $\gamma p \to \pi N \to K^+Y$ should play an important role in kaon photoproduction process. It is because the $\gamma p \to \pi N$ process has a significant large amplitude than $\gamma p \to K^+Y$. To overcome this problem, coupled channel analysis aims at simultaneously describing a number of reaction channels, for example, πN, $\pi\pi$N and KY at the same time. The coupling constants between

different channels and the multi-step effects within each separate channel are all taken into account.

In recent several years, Bonn-Gatchina (BG) group has been actively developing their model [75, 76, 77, 78, 80]. The BG group was maintained by both the Helmholtz-Institut für Strahlen- und Kernphysik, Universität Bonn, Germany and Petersburg Nuclear Physics Institute, Gatchina, Russia.

BG group applies the partial wave analysis method in their coupled-channel analysis model. The resonances in this model are introduced as Breit-Wigner functions. BG group also develops a method called 'operator expansion method' to describe baryon resonances in meson- and photon-induced reactions. The operator expansion method makes the calculation of contributions from triangle and box diagrams become very convenient. The operator expansion method also makes the projection of t- and u-channel exchange amplitudes into partial waves become available.

The BG group employs the form factor to regularize the amplitude which is called Blatt-Weisskopf form factors. If a resonance with radius r decays into two particles with momentum square k^2

$$k^2 = \frac{(s-(m_1+m_2)^2)(s-(m_1-m_2))^2}{4s} \tag{2.3}$$

here, the s is square of the total energy, the m_1 and m_2 denote the masses of the final state particles. The first few expressions of form factors $F(L, k^2, r)$ are

$$F(0, k^2, r) = 1 \tag{2.4}$$

$$F(1, k^2, r) = \frac{\sqrt{(x+1)}}{r} \tag{2.5}$$

$$F(2, k^2, r) = \frac{\sqrt{(x^2+3x+9)}}{r^2} \tag{2.6}$$

$$F(3, k^2, r) = \frac{\sqrt{(x^3+6x^2+45x+225)}}{r^3} \tag{2.7}$$

$$F(4,k^2,r)=\frac{\sqrt{(x^4+10x^3+135x^2+1575x+11025)}}{r^4} \tag{2.8}$$

It should be noted that the model was constrained to fit the $\gamma p \to K^+Y$ differential cross section, recoil polarization, and beam asymmetry data and other observables simultaneously. The Tab. 2.2 shows the kaon photoproduction data which were applied to construct the BG parameters (BG-2011). The detail of this table can be found in [79].

Table 2.2: Kaon photoproduction observables fitted in the coupled channel analysis for the solution BG 2011-02

$\gamma p \to K^+\Lambda$	Observable	$\#_{data}$	w_i	$\frac{\chi^2}{\#_{data}}$
CLAS	$\frac{d\sigma}{d\Omega}$	1320	16	0.69
LEPS	Σ_γ	45	10	2.11
GRAAL	Σ_γ	66	8	2.95
CLAS	P	1270	8	1.82
GRAAL	P	66	10	0.59
GRAAL	T	66	15	1.62
CLAS	C_x	160	15	1.52
CLAS	C_z	160	15	1.58
GRAAL	$O_{x'}$	66	12	1.95
GRAAL	$O_{z'}$	66	15	1.66
$\gamma p \to K^+\Sigma^0$	Observable	$\#_{data}$	w_i	$\frac{\chi^2}{\#_{data}}$
CLAS	$\frac{d\sigma}{d\Omega}$	1590	3	1.44
LEPS	Σ_γ	45	10	1.23
GRAAL	Σ_γ	42	10	1.99
CLAS	P	344	12	2.69
CLAS	C_x	94	15	1.95
CLAS	C_z	94	15	1.66
$\gamma p \to K^0\Sigma^+$	Observable	$\#_{data}$	w_i	$\frac{\chi^2}{\#_{data}}$
CLAS	$\frac{d\sigma}{d\Omega}$	48	3	3.84
SAPHIR	$\frac{d\sigma}{d\Omega}$	160	5	1.91
CBT	$\frac{d\sigma}{d\Omega}$	72	10	0.76
CBT	$\frac{d\sigma}{d\Omega}$	72	40	0.62
CBT	P	72	15	0.90
CBT	P	24	30	0.94
CBT	Σ_γ	15	50	1.73

The BG calculator is available on the web page [67]. The up-to-date version of the BG model suggests the baryon resonances significantly coupling to $K^+\Lambda$ was listed below $P_{11}(1710)$, $P_{11}(1880)$, $S_{11}(1650)$, $S_{11}(1895)$, $P_{13}(1720)$, $P_{13}(1900)$, $D_{13}(1875)$, $D_{13}(2150)$, $F_{15}(2000)$, $G_{17}(2190)$. For $K^+\Sigma^0$ the resonances are $P_{11}(1710)$, $S_{11}(1650)$, $P_{13}(1720)$, $P_{13}(1900)$, $D_{13}(1875)$, $D_{15}(2060)$, $P_{31}(1910)$, $S_{31}(1900)$, $P_{33}(1920)$, $F_{35}(1905)$, $F_{37}(1950)$. From the lists above, we can see the BG models also include higher-spin

resonances.

2.2.3 Regge Models

One of the problems which can not be ignored for Isobar models is that the Isobar model does not satisfy a condition which called 'Froissart bound'. The Froissart bound describes the upper limit on the high-energy behaviour of the cross sections [51]. A realistic total scattering cross section in the forward (non-forward) region is allowed to increase with energy no faster than $log^2(s/s_0)$ ($s^{3/4}log^{3/2}(s/s_0)$) as s goes to infinity. In an isobar framework, however, the background contribution comes from the t-, and u-channel diagrams and the s-channel Born term rises as a positive power of s. In the resonance region it is possible to reduce the background contribution by carefully selecting destructive interferences with resonance diagrams. But when the center of mass energy becomes higher than the resonance region, then we can do nothing to reduce the huge background contribution.

This becomes clear in Fig. 2.25, where the total cross sections are computed by an Isobar model without introducing hadronic form factor for Born terms in the reaction process. The computed total cross sections show a miserable increasing.

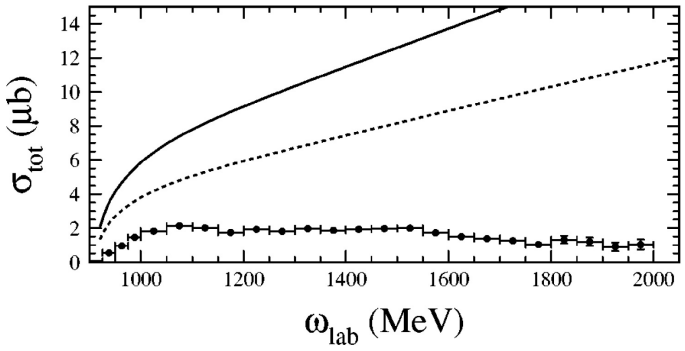

Figure 2.25: Total cross sections for $K^+\Lambda$ photoproduction as a function of photon lab energy. Here, no hadronic form factors were introduced. The solid line is calculated via the SU(3) predictions for $g_{K\Lambda p}$ and $g_{K\Sigma^0 p}$ for the dashed line, the under limit values for the coupling constants are taken for the calculation [69].

One possible solution to describe the high energy scattering was suggested by T. Regge in 1959 [73]. Regge theory started from the consideration of the partial wave amplitudes as a function of a complex

angular momentum. The theory was originally developed as an alternative approach to quantum-mechanical potential scattering. People suddenly realized that the poles of the amplitude are corresponding to resonance states, which could be classified into a number of families or so called Regge trajectory. Fig. 2.26 shows the K and K^* Regge trajectory which was expected to dominate the exchange in t-channel kaon photoproduction.

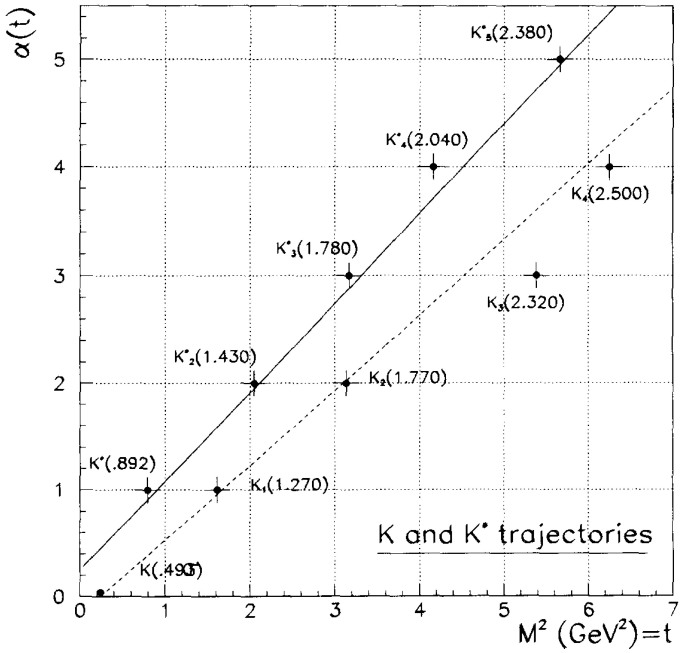

Figure 2.26: K and K^* meson trajectories (Chew-Frautschi plots). This plot was taken from [83].

In each Regge trajectory, the family members have the same internal quantum numbers, like strangeness or isospin, but different total spins. It is proposed that at sufficiently high energies, where individual resonances can no longer clearly be identified, the production process could be described by exchanging entire Regge trajectories as intermediate states instead of individual hadrons.

For a two-body exclusive reactions, the cross section in Regge model by exchange a single trajectory is given by

$$\frac{d\sigma}{dt} = D(t)(\frac{s}{s_0})^{2\alpha(t)-2}. \tag{2.9}$$

Here, s_0 is a scale factor taken to be 1 GeV. s_0 is not actually constant, but a function of t. However, the t-dependence of s_0 is con-

ventionally neglected [83]. $\alpha(t)$ is the slope of Regge trajectory which describes how the angular momentum of the exchange varies with t.

The Regge models are expected to be applicable at high energy and at forward angle regions where s is much greater than $|t|$ or $|u|$, but recent studies have suggested that the Regge models can describe t-channel meson production fairly well in the resonance region [83].

Regge theroy is well known and popular during 1960s and early 1970s. In the late 1990s, Guidal, Laget and Vanderhaeghen published the work of pion and kaon photoproduction which is based on Regge phenomenology [83]. The Regge models, again, received gradually attention.

The Regge model by Guidal, Laget and Vanderhaeghen [83, 84] describes kaon photoproduction reactions $\gamma p \to K^+\Lambda$ and $\gamma p \to K^+\Sigma^0$ via exchanging of the only two t-channel trajectories K and K*. The coupling constants have been derived independently and not from the fitting results of the measurements. Although this model did not consider the s-channel resonance, the prediction power is still fairly good.

One thing to be noted is, that to maintain the gauge invariance, a Reggeized s-channel diagram is used and this diagram is required only for K-exchange.

In Fig. 2.27 and Fig. 2.28, the results of calculations of the Regge model by Guidal, Laget and Vanderhaeghen are compared with the cross sections and beam asymmetry measurements by various experiments. The results of calculations are shown: one considered only K-exchange, the other considered both K- and K^*- exchange. In Fig. 2.27, the prediction shows a reasonable agreement with the measurements of cross sections for the $K^+\Lambda$ channel. The absence of the consideration of s-channel resonance might be the reason of the failing to account for the peak structure around center of mass energy near 1.95 GeV in $K^+\Sigma^0$ channel.

In the comparison of beam asymmetry with LEPS results, in Fig. 2.28, the prediction successfully describes the positive trend of beam asymmetry which is expected by the dominance of natural parity K^* exchange. In the more forward region, a better agreement has been shown.

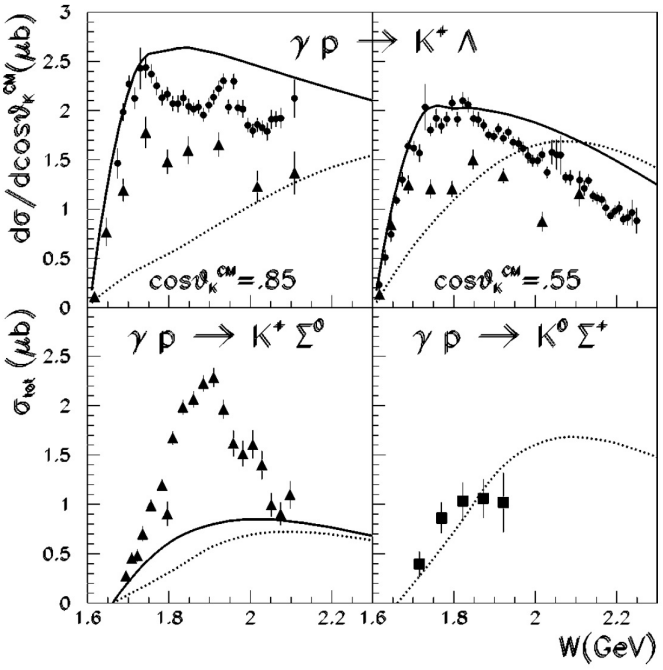

Figure 2.27: W dependence of the $\gamma p \to K^+\Lambda$ differential cross sections at $\cos\theta^{K^+}_{c.m.}$=0.55 and 0.85 and of the $\gamma p \to K^+\Sigma^0$ and $\gamma p \to K^0\Sigma^+$ total cross sections. The solid curve stands for the $K + K^*$ exchanges. The dotted line indicates the exchange of K meson only.

During 2006, an effective-Lagrangian description called Regge Plus Resonance (RPR) for forward-angle $K^+\Lambda$ photoproduction from the proton, valid for photon lab energies from threshold up to 16 GeV, was published by T. Corthals, J. Ryckebusch, and T. Van Cauteren [70].

In comparing this effective-Lagrangian framework with the isobar models, the most significant difference is the background description. The RPR introduced the Regge trajectory exchange in the t-channel by replacing the usual pole-like Feynman propagator to a Regge propagator to describe the kaon photoproduction background. By fitting to the relatively higher energy data and extrapolate into the resonance-domination region, the parameters which were required to describe the background were fixed. This fixed background provides a benefit which allow only the resonance couplings to be left as free parameters in the resonance region. In RPR module for $K^+\Lambda$ process, only three parameters need to be determined.

After the background has been fixed, the RPR evolves into resonance region by adding the core tree-level s-channel resonances to

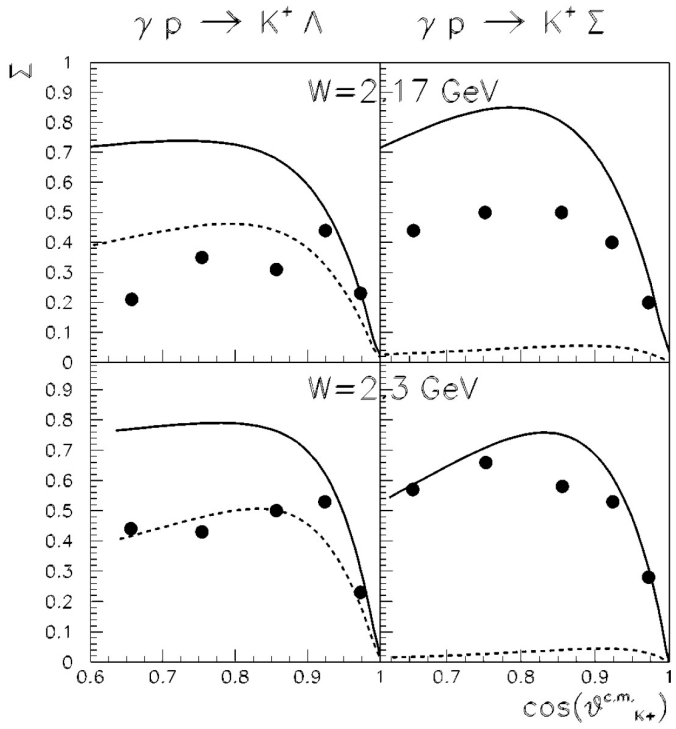

Figure 2.28: $\cos\theta^{K^+}_{c.m.}$ dependence of the photon-beam asymmetry for the $\gamma p \to K^+\Lambda$ and $\gamma p \to K^+\Sigma^0$ process. The solid curve stands for the $K + K^*$ exchanges. The dotted line indicates the exchange of K meson only.

describe the existing data. For example the RPR 2011 for $K^+\Lambda$ includes $S_{11}(1535)$, $S_{11}(1650)$, $F_{15}(1680)$, $P_{13}(1720)$, $P_{11}(1900)$, $F_{15}(2000)$, $D_{13}(1900)$, and $P_{13}(1900)$. The RPR 2007 for $K^+\Sigma^0$includes $S_{11}(1650)$, $P_{11}(1710)$, $P_{13}(1720)$, $P_{13}(1900)$, $S_{31}(1900)$, $P_{31}(1910)$, $P_{33}(1920)$ and $D_{33}(1700)$.

The Isobar model employs the form factor to limit the contribution of amplitude for each resonance, and RPR also applies this phenomenological form factors. Instead of the standard dipole parametrization used in most isobar models (Eq. 2.2), the Gaussian shape form factor has been considered

$$F_{Gauss}(s) = exp\{-\frac{(s - m^2_{N^*})^2}{\Lambda^4_{res}}\} \tag{2.10}$$

with Λ_{res} the cutoff value, which can quench the resonance contribution faster than dipole form.

A schematic diagram of the RPR amplitude is shown in Fig. 2.29. It involves t-channel exchanges of K and K^* trajectories as well as s-channel Feynman diagrams corresponding to individual baryon reso-

nances. In the higher energy region, all resonance contributions should vanish, so that only the Regge part of the amplitude remains. The RPR calculator is available on the web page [66]

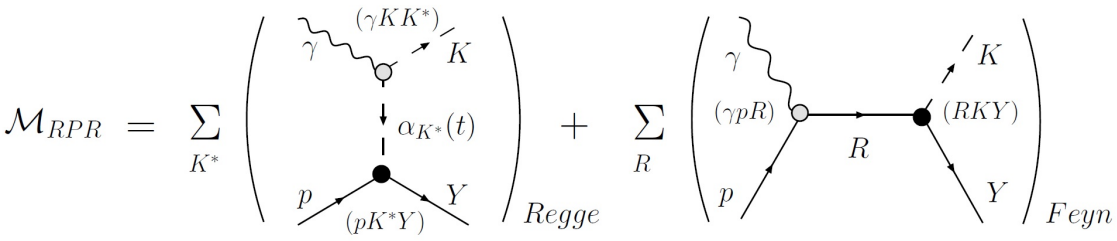

Figure 2.29: The schematic diagram of the RPR amplitude for the $\gamma p \to K^+ Y$ process.

2.3 Current Work

This thesis presents a measurement by LEPS spectrometer of the cross sections and photon-beam asymmetry for the photon energy range of 1.5 GeV to 3.0 GeV. The $\cos\theta^{K^+}_{c.m.}$ coverage of this measurement is $0.6 < \cos\theta^{K^+}_{c.m.} < 1.0$. The results of cross sections of current work will be compared with the measurements of SAPHIR, CLAS and previous LEPS results in the overlapping region. The beam asymmetry results will also be presented in Chapter 5. All the measurements will also be compared with the BG and RPR theoretical calculations to get a deep understanding. Both cross sections and beam asymmetry results provide a strong constraint in modeling Regge trajectories in the t-channel at lower energies, and help to pin down the contributions of heavier nucleon resonances in the transition region. The results of photon-beam asymmetry analysis presented in Chapter 5 of this thesis extend the maximum energy of 2.4 GeV to 3.0 GeV for the measurements and allow a better comparison between the model predictions.

Chapter 3

Experimental Setup

The experiment for the reactions of $\gamma p \to K^+\Lambda$ and $\gamma p \to K^+\Sigma^0$ was carried out at the Laser Electron Photon beam line at SPring-8 (LEPS). The linearly polarized high intensity photon beam with large degree of polarization was provided by the SPring-8 facility. The aerial view of the SPring-8 facility is shown in Fig. 3.1. By the Backward Compton Scattering (BCS) process of the deep UV laser(257nm) photons with 8-GeV electrons circulating in the storage ring of SPring-8, the linearly polarized photon beam with the maximum energy of 3.0 GeV were produced at BL33LEP beamline (LEPS beamline). The energy of polarized photon beam was measured by a tagging system located inside the storage ring. The LEPS spectrometer system was operated to detect and record the information of charged particles produced by photo-reactions.

Figure 3.1: Aerial view of the SPring-8 .

In this Chapter, the Backward-Compton-scattering (BCS) process, LEPS beam line and LEPS spectrometer with the experimental apparatus will be described.

3.1 Backward Compton scattering (BCS) [53]

In 1963 Milburn [54] and Arutyunian and Tumanian [55] are the pioneers who suggested that the γ-ray beams could be generated by the Compton scattering of laser light against high energy electrons. Fig. 3.2 shows the kinematic variables of the BCS process.

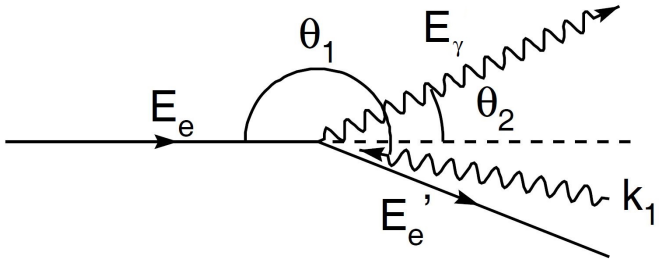

Figure 3.2: Kinematic variables of the backward-Compton-scattering process in the laboratory frame.

It is considered that an energetic electron with an energy E_e(7.975$\pm$ 0.003 [56] in SPring-8) is hit by a laser photon which carries the energy k_1. The θ_1 and θ_2 indicate the directions of the incident and outgoing photons. If the $E_e \gg k_1$, the scattered photon can gain energy to the backward direction from the electron in the recoil process. The energy of the scattered BCS photon E_γ is described as

$$E_\gamma = k_1 \frac{1 - \beta cos\theta_1}{1 - \beta cos\theta_2 + \frac{k_1(1-cos\theta)}{E_e}}. \tag{3.1}$$

Here the β denotes the incident electron velocity in unit of the speed of light, and the $\theta = \theta_2 - \theta_1$. By considering the incident electron energy much larger than the mass of electron where $\gamma = \frac{E_e}{m_e} \gg 1$, the $\beta \approx 1$, $\theta_1 \approx 180^\circ$ and $\theta_2 \ll 1$, the energy of the scattered BCS photon E_γ could be rewritten as

$$E_\gamma = \frac{4E_e^2 k_1}{m_e^2 + 4E_e k_1 + \theta_2^2 \gamma^2 m_e^2} \tag{3.2}$$

The maximum energy of the BCS photon (E_γ^{max}) could be obtained at $\theta_2 = 0^\circ$

$$E_{\gamma}^{max} = \frac{4E_e^2 k_1}{m_e^2 + 4E_e k_1} \tag{3.3}$$

The maximum possible energy of a 257 nm deep UV laser is 2.97 GeV.

By providing the linear polarized laser photons, the polarization is transferred to the BCS photons. The degree of polarization (P_{γ}) of the scattered BCS photon is determined by

$$P_{\gamma} = P_{Laser} \frac{(1 - cos\alpha)^2}{2(\chi + 1 + cos^2\alpha)} \tag{3.4}$$

where

$$cos\alpha = \frac{1 - \rho(1 + a)}{1 - \rho(1 - a)} \tag{3.5}$$

$$\chi = \frac{\rho^2(1 - a)^2}{1 - \rho(1 - a)} \tag{3.6}$$

$$a = \frac{m_e^2}{m_e^2 + 4E_e k_1} \tag{3.7}$$

and the ρ is the photon energy ratio to a maximum photon energy.

$$\rho = \frac{E_{\gamma}}{E_{\gamma}^{max}} \tag{3.8}$$

The P_{Laser} denotes the degree of polarization of the incident laser photon which is approximately to 100%.

In Fig. 3.3 the possible maximum BCS photon energy (E_{γ}) with various laser photon wave lengths as a function of incident electron energy (E_e) has been shown. Fig. 3.4 shows the linear polarization of the BCS photon as a function of E_{γ} by using the 8 GeV incident electron beam with fully polarized laser photon. Some examples of the linear polarization for the wavelengths of 257, 351, 488 nm, the 351 and 488 nm are plotted.

To produce the polarized photon beam, the bremsstrahlung method is also a well known method. Here we take CLAS experiment [57] as an

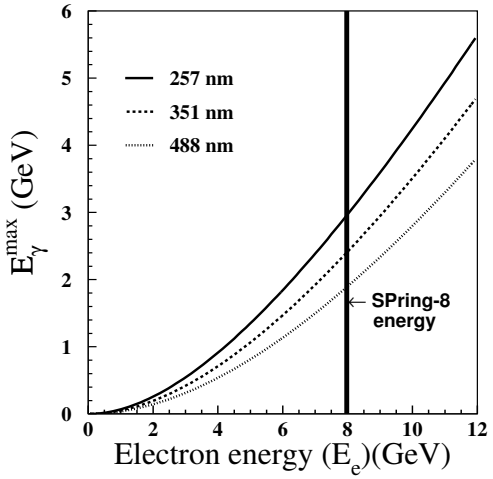

Figure 3.3: The possible maximum BCS photon energy (E_γ) with various laser photon wave lengths as a function of incident electron energy (E_e).

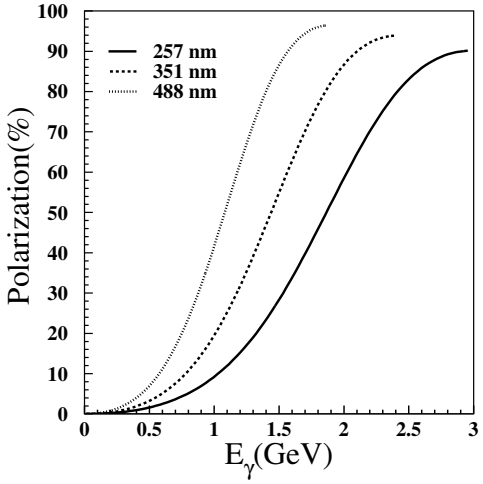

Figure 3.4: The linear polarization of the BCS photon as a function of E_γ by using the 8 GeV incident electron beam with the full polarized laser photon.

example. In CLAS experiment, the Continuous Electron Beam Accelerator Facility (CEBAF) was used to produce a beam of electrons with the beam energy up to 6.1 GeV. This beam was delivered to JLAB's experimental Hall B, where the CLAS experiment was conducted. Within Hall B a diamond radiator was installed to scatter the electrons from CEBAF, by the bremsstrahlung process to produce a linearly polarized photon beam. The photon tagging system was designed by combining the dipole magent and a hodoscope system which contains two planar arrays of plastic scintillators to detect the energy lossed electrons from a thin bremsstrahlung radiator. The typical tagging rate of CLAS system is about 5×10^6 photons/s.

In the bremsstrahlung process, the electrons which are incident on the suitable radiator are by the electromagnetic field of the nuclei in radiator and emit energetic photons. If a radiator with a regular lattice structure is selected, the photons can be produced at discrete energies corresponding to specific momentum transfer of the electrons to the crystal nuclei. This gives an energy spectrum with a characteristic "coherent peak" structure. If one carefully chooses the orientation of the radiator with respect to the incident angle of the electron beam, the photons produced through this process will have a high degree of linear

polarization, particularly for those photons within the coherent peak. The typical linear polarization is up to 84%.

In comparison with LEPS experiment, the tagging rate of CLAS experiment is approximately 10 times higher (tagging rate of LEPS experiment is about 5×10^5 photons/s). In term of polarization degree, the LEPS experiment can provide a highly polarized photon beam with up to 90%(98%) with 257(351) nm laser.

The Fig. 3.5 shows examples of the energy spectra of BCS photon beam and bremsstrahlung beam created by the residual gas in the storage ring. The BCS photon beam was produced by an incident laser photon with 351 nm wave length, and the maximum photon energy is 2.4 GeV. The maximum energy of bremsstrahlung beam is 8 GeV corresponding to the electron beam energy. The BCS photon beam can provide higher intensity than the bremsstrahlung beam.

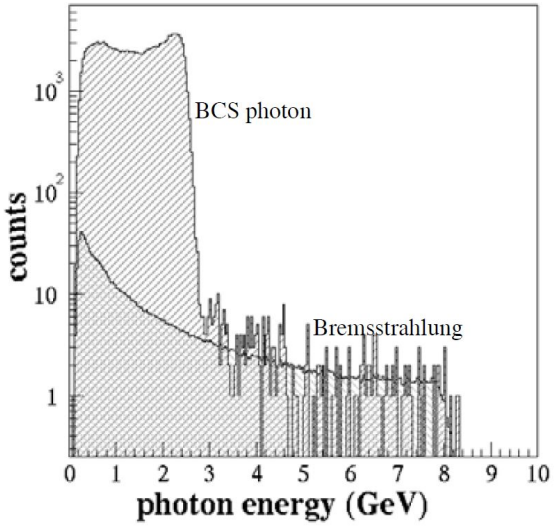

Figure 3.5: Energy spectra of the BCS photons and bremsstrahlung photons measured by a PWO($PbWO_4$) crystal calorimeter [59]. The wave length of the laser photon is 351 nm.

3.2 Laser-electron photon beam

In this sections, the SPring-8 and LEPS facility will be introduced in the beginning. The Laser system, tagging system for measuring the photon energy and the target will also be introduced.

3.2.1 SPring-8

The Super-Photon Ring-8 GeV (SPring-8) is a third generation large synchrotron orbital radiation (SOR) facility. It started to serve the high quality synchrotron radiation in 1997 until now. The SPring-8 facility is located in Harima Science Garden City, Hyogo Prefecture, Japan.

The SPring-8 facility is composed of an injector linear accelerator, a booster synchrotron, and a huge storage ring. Fig. 3.6 shows the schematic view of the main components of SPring-8.

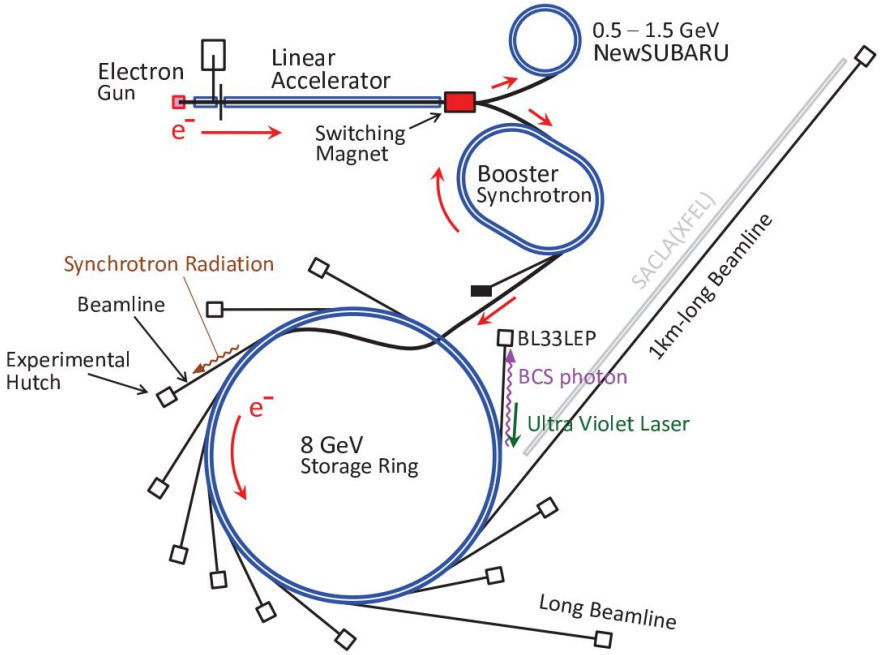

Figure 3.6: The schematic view of SPring-8. The linear accelerator, booster synchrotron, and storage ring can been seen.

The linear accelerator (linac) is designed as an injector to generate the electron beam by a 180 kV electron gun up to 1 GeV. Then the beam is injected to the booster synchrotron or to the NewSUBARU storage ring. In the booster synchrotron, the electron beam from the linac is accelerated up to 8 GeV. The circumference of the booster synchrotron is 396.124 m. The accelerated 8 GeV beam is extracted and transported to the storage ring.

The circumference of the storage ring is 1435.95 m. The storage ring is a synchrotron accelerator for light sources. Electrons are filled in some of the total 2436 bunches with various filling patterns, where the

time interval (RF frquency) of the successive bunches is 1.966 nsec. The maximum current of the 8 GeV electron beam is 100 mA. Synchrotron radiation is the electromagnetic radiation emitted when charged particles are bent by the magnetic field. The synchrotron radiation is emitted at bending magnets and at inserted undulators or a wiggler. The emitted radiation is transported through each beamline to hutches in the experimental hall for experiments.

There are 61 beamlines available for research in Spring-8, the Laser-electron photon (LEPS) facility was built at the beamline BL33LEP which is dedicated for the experiments of quark nuclear physics research.

3.2.2 LEPS facility

The LEPS facility was established by the cooperation of RCNP (Research Center for Nuclear Physics) in Osaka University, JASRI (Japan Synchrotron Radiation Institute) and JAERI (Japan Atomic Energy Research Institute) at SPring-8. At the LEPS facility, a multi-GeV photon beam is produced by the backward-Compton-scattering (BCS) process of laser photons from the circulating 8-GeV electrons which was discussed in sec 3.1. The beam line consists of an interaction region of laser photons with circulating electrons with an tagging system, an laser hutch for laser injection, and an experimental hutch for the experiment. The schematic view of the LEPS facility has been shown in Fig. 3.7

In Fig. 3.7, the laser photons generated in the laser hutch (b) are injected to the storage ring area (a). In the storage ring area a 7.8 m long straight section between two bending magnets can be seen in Fig. 3.7. In this straight section, the laser photon collides with the 8-GeV storage ring electron. The high energy photons produced by the BCS process with the photon- electron collision were transferred to the experimental hutch and interacted with target. The recoiled electrons in storage ring were detected by a tagging system placed at the exit of the bending magnet to measure the photon beam energy. The charged particles produced at the target were detected at forward angle with the LEPS spectrometer. The LEPS spectrometer is located at experimental hutch (c), which consists of a dipole magnet, three multi-wire drift chambers (DC1, DC2 and DC3), a plastic scintillator hodoscope

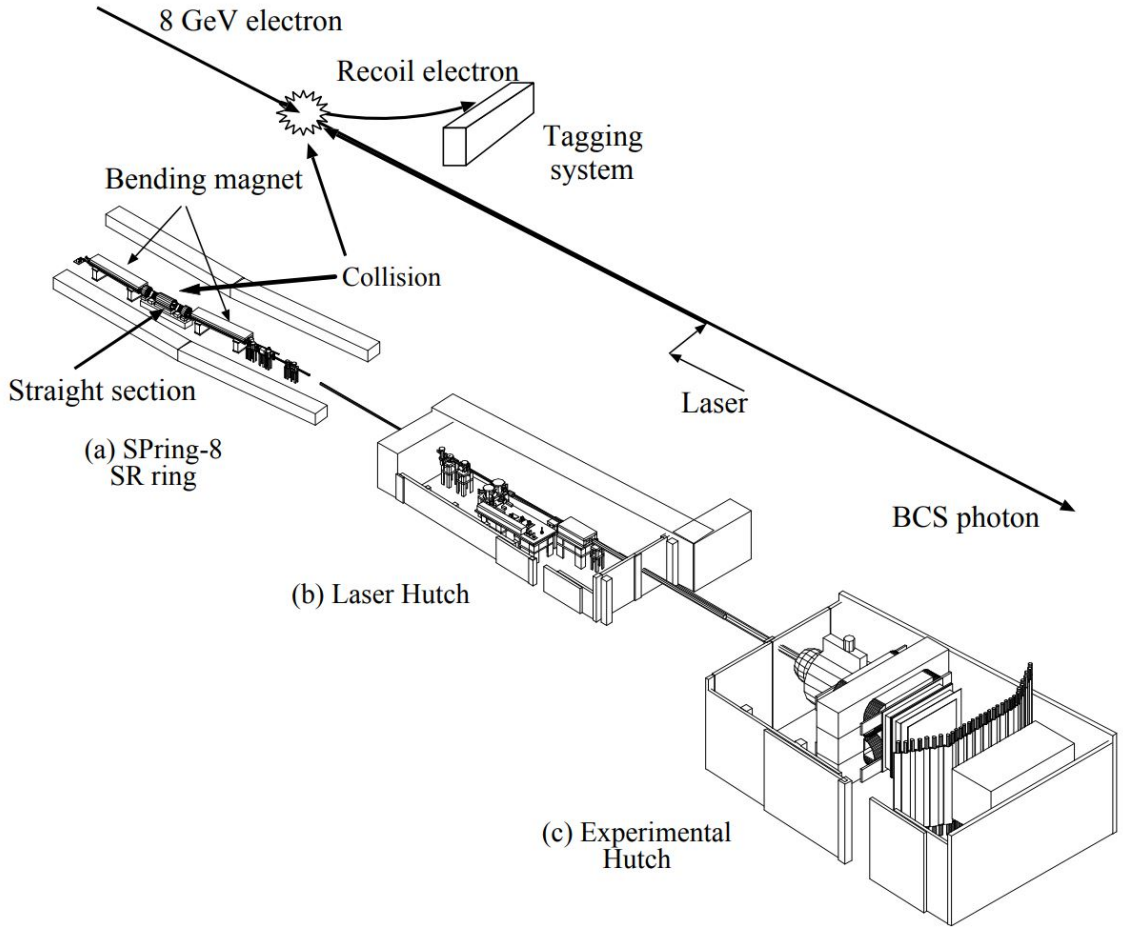

Figure 3.7: Schematic view of the LEPS facility at SPring-8 [85]. LEPS facility consists of three main parts. The (a) Laser-electron collision part and a tagging system in the storage ring, (b) Laser hutch for the injection of laser beam, and (c) the experimental hutch.

(TOF wall), a plastic scintillator (trigger counter) and a silica Aerogel Cherenkov counter (not installed in this analysis) in common experiment setup. The detail of LEPS spectrometer system will be discussed in sec 3.3

3.2.3 Laser system

Figure 3.8 shows the schematic view of laser operation system. The laser operation system consists of an Ar laser (1), a half-wave-length plate ($\lambda/2$ plate) (2), a beam expander (3), four mirrors (4-7) and a polarization monitoring system (8). The deep UV Ar laser with 257 nm wave length was installed in this experiment to produce the high energy BCS photon beam. The UV laser was produced by COHERENT [58] with the model name "Innova Sabre MotoFreD" which can output the 257 nm deep UV laser with a power of 1 W. Since the Ar laser is vertically

polarized in the beginning, no direction change is needed to produce a vertically polarized photon. To produce a horizontally polarized photon beam, the optic axis of the $\lambda/2$ plate is placed at 45° to rotate the laser polarization from vertical to horizontal.

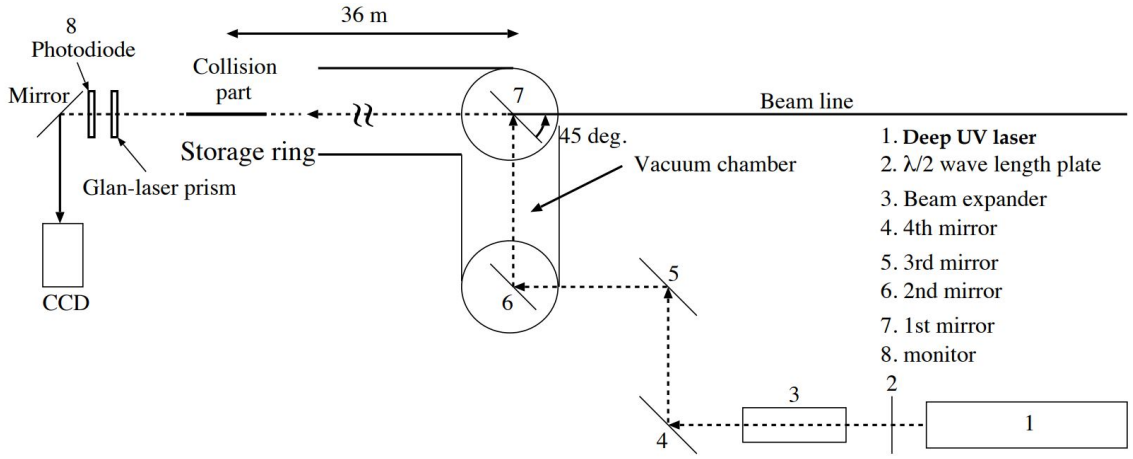

Figure 3.8: Schematic view of laser operation system.

The laser photon beam travels a long distance before the collision with the electron in storage ring. To achieve the maximum luminosity for the collision, the laser beam must be focused at the straight section of the storage ring. The beam expander which consists of a couple of optical lenses enlarges the beam once and focuses it at the straight section.

There are four mirrors in the laser operation system. The direction and position of the laser beam were controlled by the third (5) and the forth mirror (4). These mirrors can be rotated with a motor with 17 μrad/1 pulse and 10 μrad/1 pulse in the horizontal and vertical directions, respectively. The third and forth mirrors are made of quarts. The laser beam is transported from the laser operation system to the beam line by the second mirror (6), and is injected into the storage ring by the first mirror (7). Both mirrors are made of aluminium evaporated silicon.

The polarization of the laser photons is measured at the laser beam end located downstream of the interaction region by using laser photons which pass through the collision part. The polarization monitoring system consists of a Glan-laser prism and photodiode. The measurement of the polarization angle and degree was done by rotating the Glan-laser

prism, the intensity of the laser was measured behind the prism with the photodiode as a function of rotation angle.

3.2.4 Tagging system

By considering the energy conservation of the Backward-Compton scattering, the energy of photons could be determined by measuring the energy of the recoiled electron via the relation,

$$E_\gamma = E_e - E_{e'}, \tag{3.9}$$

where the $E_{e'}$ denotes the recoiled electron energy, E_e is the energy of circulated electron in the storage ring, E_γ is the produced BCS photon beam energy. Since the energy of the recoiled electron is lower than the energy of the circulated electrons, the recoiled electron is bent inward from the normal circulating electron orbit in the storage ring. By detecting the recoiled electrons with the tagging counter which was installed at the downstream of the bending magnet in the storage ring, the $E_{e'}$ could be obtained.

Fig. 3.9 shows the schematic diagram of the tagging counter. The tagging counter was placed at the exit of the bending magnet and outside of the vacuum chamber of the storage ring. The tagging system consists of two layers of scintillating fibers (TAG-SF) and 5 segments with 2 layers plastic scintillator hodoscopes (TAG-PL).

The fiber detectors (TAG-SF) were installed in the upstream of the plastic scintillator hodoscope (TAG-PL), and were composed of the front fiber (xsf fiber) and rear fiber (xsb fiber) layers. The position information was provided by front fiber and rear fiber for the recoiled electron trajectory. The timing signal of the recoiled electron signal was provided by the PMT read out. The true signal of the tagging system is cleaned up by taking a coincidence of the TAG-SF and the TAG-PL. The measurable energy region corresponds to the range of 1.5 - 3.5 GeV for the BCS photons.

3.2.5 Target

In this experiment, we used a 150 mm liquid hydrogen target. Figure 3.10 shows the schematic plot of the target system. The target cell was made of copper with a thickness of 8 mm. The entrance and exit

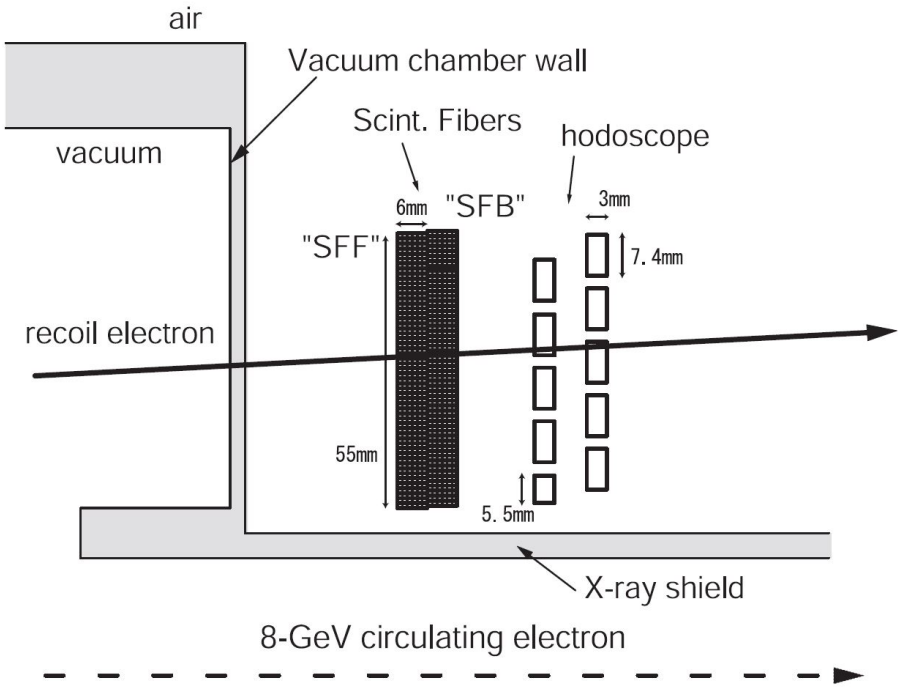

Figure 3.9: Schematic diagram of the tagging system.

windows of the target cell were made of Kapton films with a thickness of 0.125 mm. The trapezoid shape of the target cell was designed to prevent the acceptance loss of the charged particle detection even if the reaction occurs at the most upstream position of the target cell. The temperature and pressure of the target were maintained at ∼20.5 K and ∼1.05 atm, respectively. The target was located at the 953 mm upstream of the center of the dipole magnet which will be discussed in Sec. 3.3.4.

3.3 LEPS spectrometer

The schematic front and rear top view of the LEPS spectrometer is shown in Fig. 3.11. The LEPS spectrometer consists of upstream veto counter (not plotted in Fig. 3.11), a plastic scintillator trigger counter, a silicon strip detector vertex detector, a dipole magnet, e^+e^- blocker, three multi-wire drift chambers (DC1, DC2 and DC3), a newly set up plastic scintillator e^+e^- veto counter in this experiment, a plastic scintillator hodoscope TOF wall, and a Aerogel Cherenkov counter (included in common setup but not installed in this experiment). Table 3.1 lists the locations of spectrometer apparatuses from target to TOF wall where the center of the dipoole magnet is set at 0 mm. The detail of each

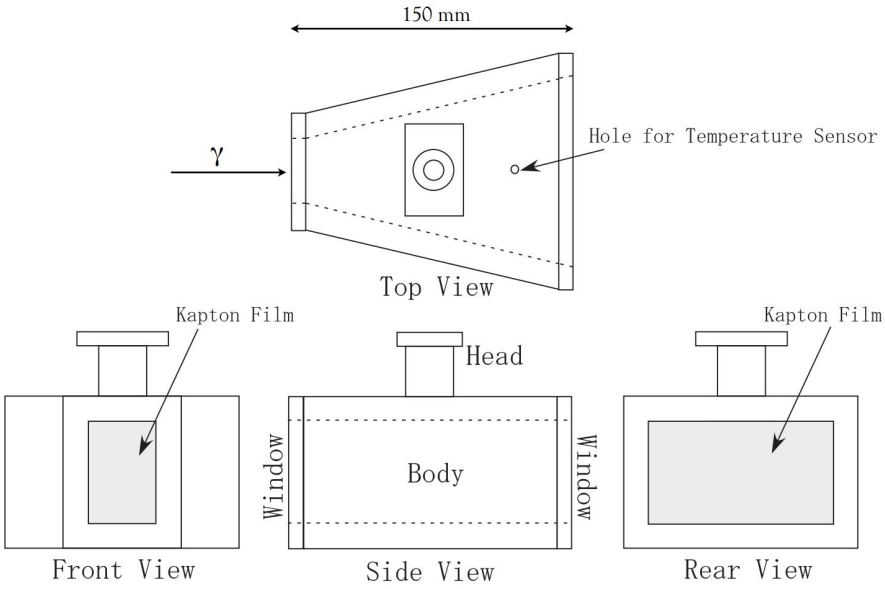

Figure 3.10: Schematic plot of the target system.

apparatus will be discussed in the following sections, and in the end the trigger will also be discussed.

Table 3.1: The locations of spectrometer apparatus from target to TOF wall.

Apparatus	Location (mm)
target	-953
trigger counter	-801.6
vertex detector	-681.1
DC1	-466
dipole magnet	0
e^+e^- blocker	200
DC2	860.5
DC3	1260.5
e^+e^- veto counter	1410.5
TOF wall	3151.5

3.3.1 Upstream veto counter

Parts of the photon beam interact with the residual gas or Al windows of the beam pipe, and lead to e^+e^- pair production. The upstream veto counter was installed to veto the charged particles described above in the trigger level. Fig. 3.12 shows the front view of upstream-veto counter. The upstream veto counter was made of plastic scintillator which was located at 4 m upstream from the target. The height, width and thickness of the counter is 200 mm, 190 mm, and 5 mm, respectively. A 2 inch long PMT was connected to the scintillator via a light guide.

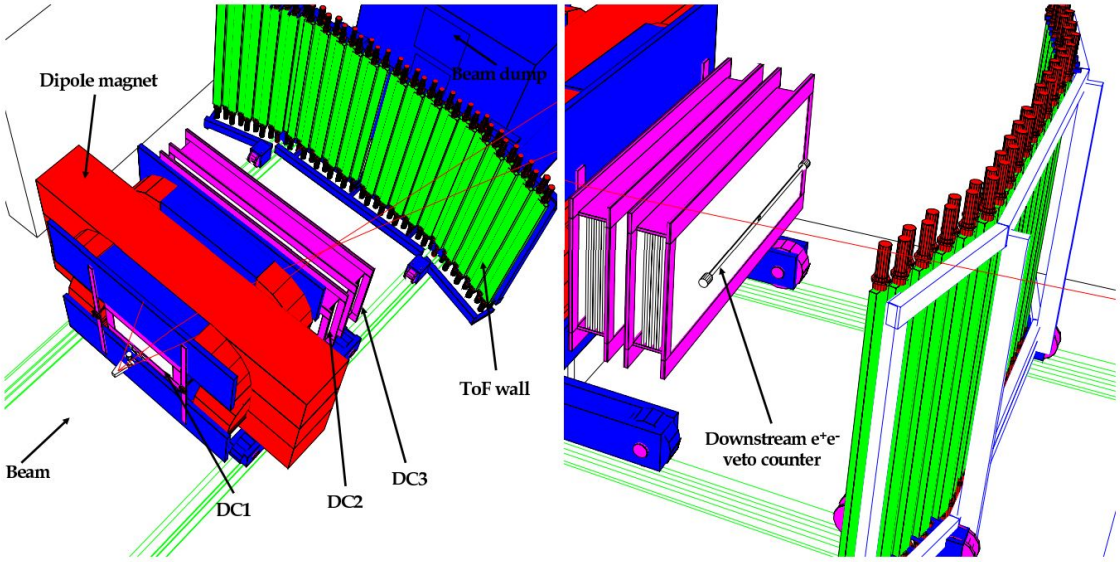

(a) Front-top view (b) Rear-top view

Figure 3.11: Schematic view of the LEPS spectrometer [86].

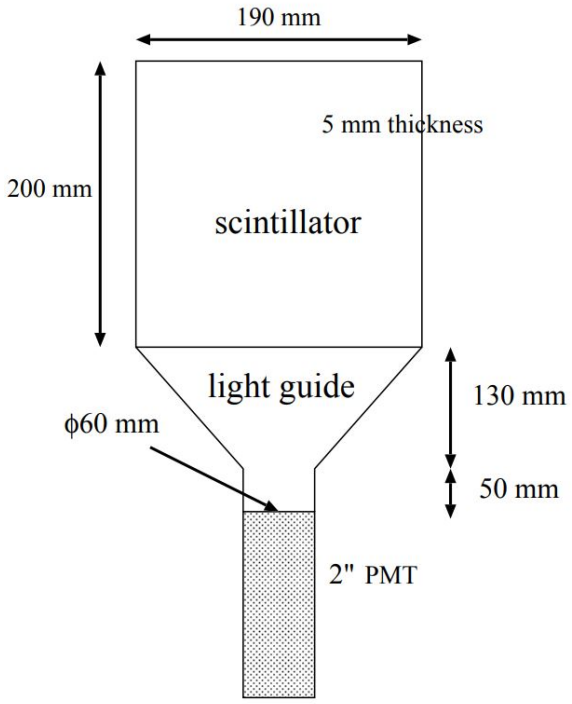

Figure 3.12: Front view of the upstream veto counter [85].

3.3.2 Trigger counter

In order to identify the event signals from charged particles produced via the interaction of photon beam and target, the trigger counter made of the plastic scintillator was set at the position of 151.4 mm

downstream of the center of the target cell. The schematic plot of trigger counter is shown in Fig. 3.13. The trigger counter is a 5 mm thick plastic scintillator with 95 mm high and 150 mm wide. Two PMTs are coupled to the top and bottom of the plastic scintillator through 15 mm thick light guides. The trigger counter is used as a reference counter to measure the time of flight with respect to the RF signals.

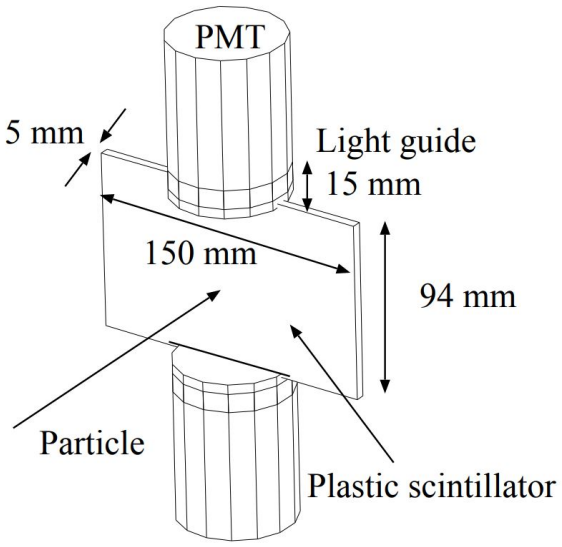

Figure 3.13: Schematic plot of the trigger counter.

3.3.3 Vertex detector

The vertex silicon strip detector (SVTX) in Fig. 3.14, was installed to provide the high precision spatial information near the interaction region. As a charged particle crosses the silicon, the deposited ionization energy produces a uniform electron-hole density along its path. The electrons and holes were attracted by the bias field inside the silicon strip detector. The detector collects the charge at the electrode, giving a signal proportional to the deposited ionization energy. The SVTX consists of two layers of silicon strip detectors. One layer takes the responsibility to measure the x-position information and the other measures the y-position information. The SVTX has a 300 μm thickness and 120 μm pitch. The SVTX was located 271.9 mm downstream of the center of the target cell. The size of a rhombic-shaped hole for the beam path in the middle of SVTX is 10 mm $\times$ 10 mm .

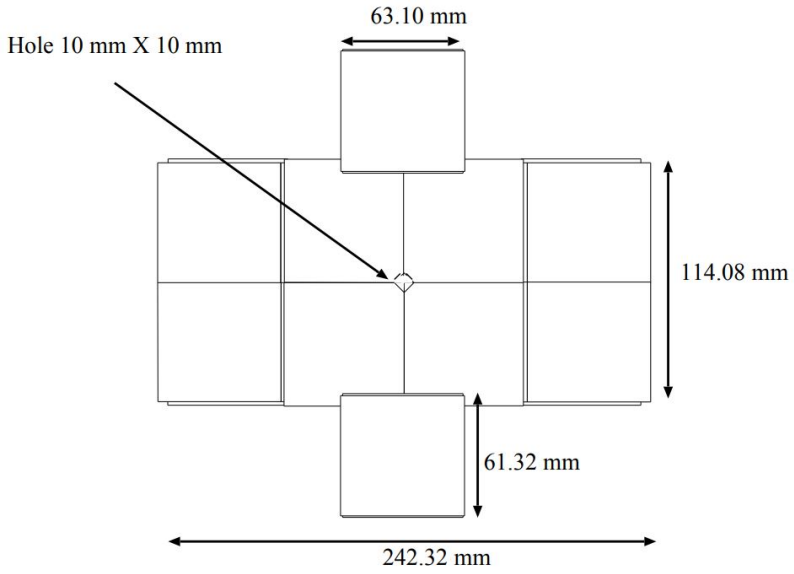

Figure 3.14: Front view of the vertex detector.

3.3.4 Dipole magnet

The dipole magnet with a height of 550 mm, and a width f 1350 mm was installed to maintain the magnetic field for momentum analysis. The length of the pole along the photon beam is 600 mm. At the center of the dipole magnet, when the current was set at 800 A, the field strength is 0.7 T. Fig. 3.15 shows the y-direction magnetic field strength as a function of z-position at x = 0 mm and y = 0 mm.

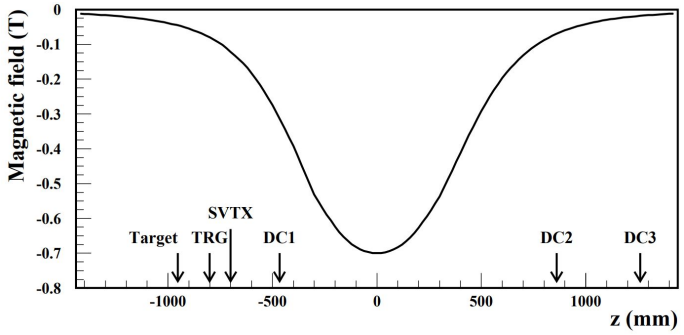

Figure 3.15: The distribution of the y direction magnetic field strength. The distribution is a function of z-position at x = 0 mm and y = 0 mm. [86].

3.3.5 e^+e^- blocker

To block the e^+e^- pair produced at the target, the e^+e^- blocker was installed. The e^+e^- blocker was made of two lead bars which were placed inside the dipole magnet, at the 200mm downstream of the center

of the dipole magnet. The size of each Pb bar is 40 mm high, 440 mm wide, and 100 mm thick. A gap between two Pb bars is 155 mm. It is possible to change the gap width by adding or removing the small pieces of the Pb blocks. The electron and positron with a momentum above 1 GeV/c can still travel through the gap. The produced e^+e^- pair emerges mostly asymmetrically in energy. In most cases, one of the pair is blocked by the blocker, while the other survives and escapes through the 155 mm gap and is stopped by the beam dump. The Pb bars are supported by two thin channels with a 2 mm thickness. A V-shaped thin bar with a thickness of 5 mm connects a thin channel with one another in the center. The V-shape structure opens at 150° and has 15 mm in depth to let the photon beam pass through. Fig. 3.16 shows the top and front view of the e^+e^- blocker, the v-shaped thin bar is also plotted. The blocker is put down by the weight itself and the center in the y-direction is -7 mm.

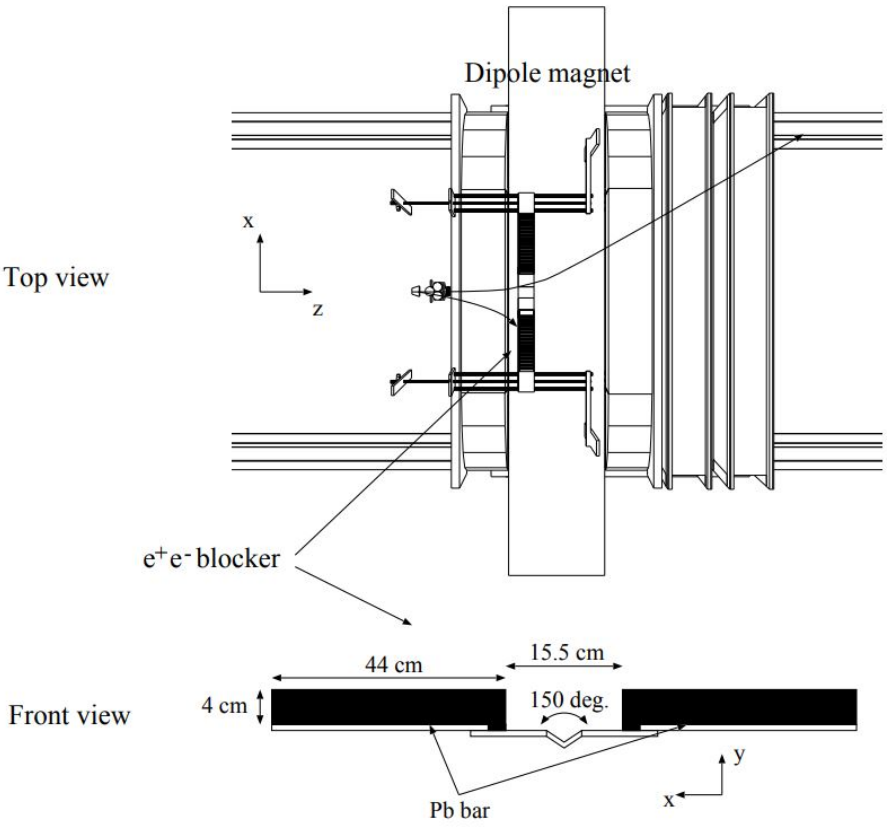

Figure 3.16: Top and front view of the e^+e^- blocker.

3.3.6 Drift chambers

When the charged particles travel through the working area of drift chamber, by tracking the trails of gaseous ionization, the position information can be obtained. The charged particle which passes through the working area of drift chamber ionizes surrounding gaseous atoms. The resulting ions and electrons are accelerated by the electric field across the chamber, causing a localized cascade of ionization. According to the drift time of the cascade electrons, it is possible to determine the accurate hit position by computing the timing and height of the pulses informations measured by TDC and ADC module from all the anode wires, therefore the particle trajectory could be found.

In this experiment, the information from three multi wire drift chambers (MWPC) is analysed with the information from vertex detector for the track reconstruction. The 6 planes x, x', u, u', v and x" multi-wire drift chamber called DC1 was located upstream of the dipole magnet. The active area of DC1 is about 600 $\times$ 300 mm^2. The x" plane was made additionally because a charged particle begins to be spread out caused by the magnetic field near DC1.

Fig. 3.17 shows the drawing of field, shield and sense wires in drift chamber. We can see the sense wires of x-x' and u-u' are positioned with a 6 mm spacing and wires of x" and v are positioned with a 12 mm spacing. The field wires are arranged in a hexagonal shape. The shield wires are located along the windows to shape the electric field. The inclination angle of the u and v wires is 45° with respect to the horizontal plane.

The active area of DC2 and DC3 is 2000 $\times$ 800 mm^2. Both of these two sets have only 5 planes x, x', u, u', and v. DC2 and DC3 are installed downstream of the dipole magnet. The design of DC2 and DC3 is the same as DC1 but except for the x" plane. Sense wires of x-x' and u-u' are positioned with a 10 mm spacing, and the wires of v are positioned with a 20 mm spacing. The u and v directions are inclined by 30° with respect to the vertical plane. The material of the sense wires is the gold plated tungsten (Au-W) and the wire diameter is 25 μm for DC1 and 30 μm for DC2 and DC3. The field and shield wires are made of the

Au-BeCu with a diameter of 100 μm. The windows are made of mylar with a thickness of 125 μm. The parameters of each drift chamber are shown in Tab. 3.2. The gas mixture used to operate the drift chambers are 70% argon and 30% isobutane. The position resolution of the drift chamber is $\sim$ 200 μm. The efficiency is higher than 98% and is typically 99%.

Table 3.2: The parameters of each drift chamber

	Plane	Orientation	#of sense wires	Wire spacing (mm)	Active area (mm^2)	Location (mm)
DC1	x-x'	0°	48 × 2	6	600 × 300	-466.0
	u-u'	+45°	48 × 2	6		
	v	-45°	48	12		
	x"	0°	48	12		
DC2	x-x'	0°	104 × 2	10	2000 × 800	860.5
	u-u'	+30°	78 × 2	10		
	v	-30°	79	20		
DC3	x-x'	0°	104 × 2	10	2000 × 800	1260.5
	u-u'	+30°	78 × 2	10		
	v	-30°	79	20		

3.3.7 e^+e^- veto counter

Since the data set was originally collected for detecting K^{*0} decaying to high-momentum K^+ and π^- [60], the regular spectrometer setup was slightly modified. The signal from a plastic scintillation e^+e^- veto counter (EEveto) placed downstream of the DC3 was used to reject the e^+e^- events in trigger level. In the standard LEPS experiment the Aerogel Cherenkov counter, which had been placed immediately after the target to reject high-momentum electrons, positrons, and pions at the trigger level, was removed to shrink the space between target and spectrometer for increasing the pion acceptance. Figure 3.18 shows the front and top schematic view of the downstream e^+e^- veto counter. The detector was made of a 40 mm high, 185 mm wide and 20 mm thick plastic scintillator. In the center of the EEveto, a 20 mm high and 50 mm wide hole was made for allowing the photon beam to pass through.

3.3.8 TOF wall

The TOF wall was set to measure the time-of-flight of charged particles passing through the whole spectrometer. The TOF wall was composed of 40 2m-long plastic scintillator bars with a thickness of 40

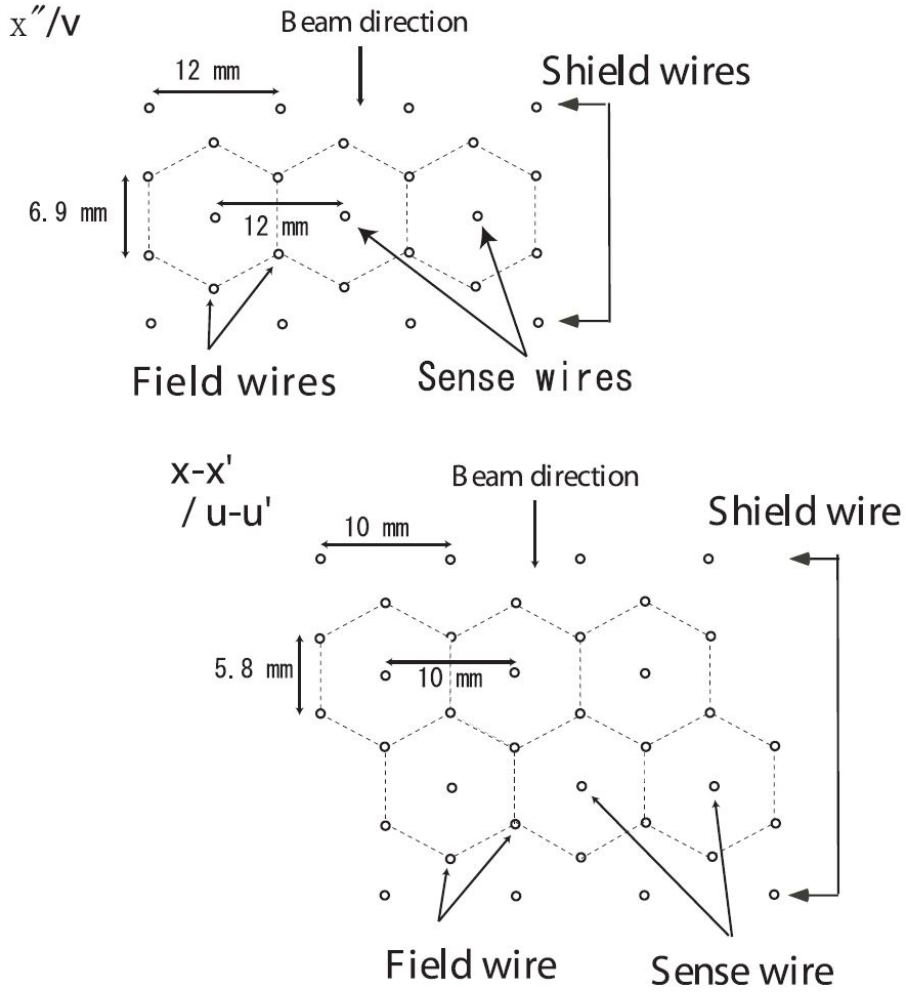

Figure 3.17: Schematic drawing of the wire configuration in the drift chambers.

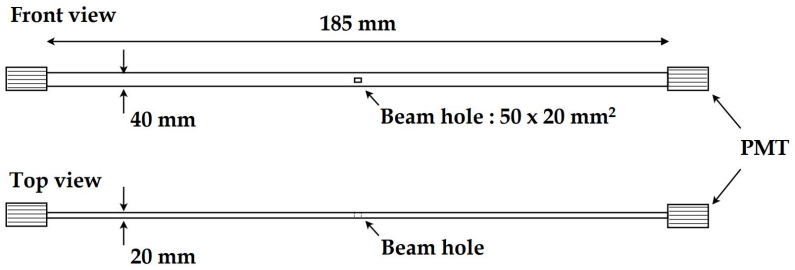

Figure 3.18: Schematic front and top view of the e^+e^- veto counter.

mm and a width of 120 mm and was placed downstream of the DC3. Two 2-inch PMT are attached to both end of the plastic scintillator via a 30 mm thick light guide. Each plastic scintillator bar is overlapped with adjacent bars by 10 mm. The top and front schematic view of TOF wall is plotted in Fig. 3.19. In the top view of the TOF wall, the side bars are aligned in the planes tilted by $\pm$ 15 degrees. Ten bars are arranged in a group and are placed in both the left and right sides. A

40 mm gap between the two center TOF counters allowing the photon beam to pass through has been kept. The z-position of the TOF wall was 3151.5 mm downstream from the center of the dipole magnet.

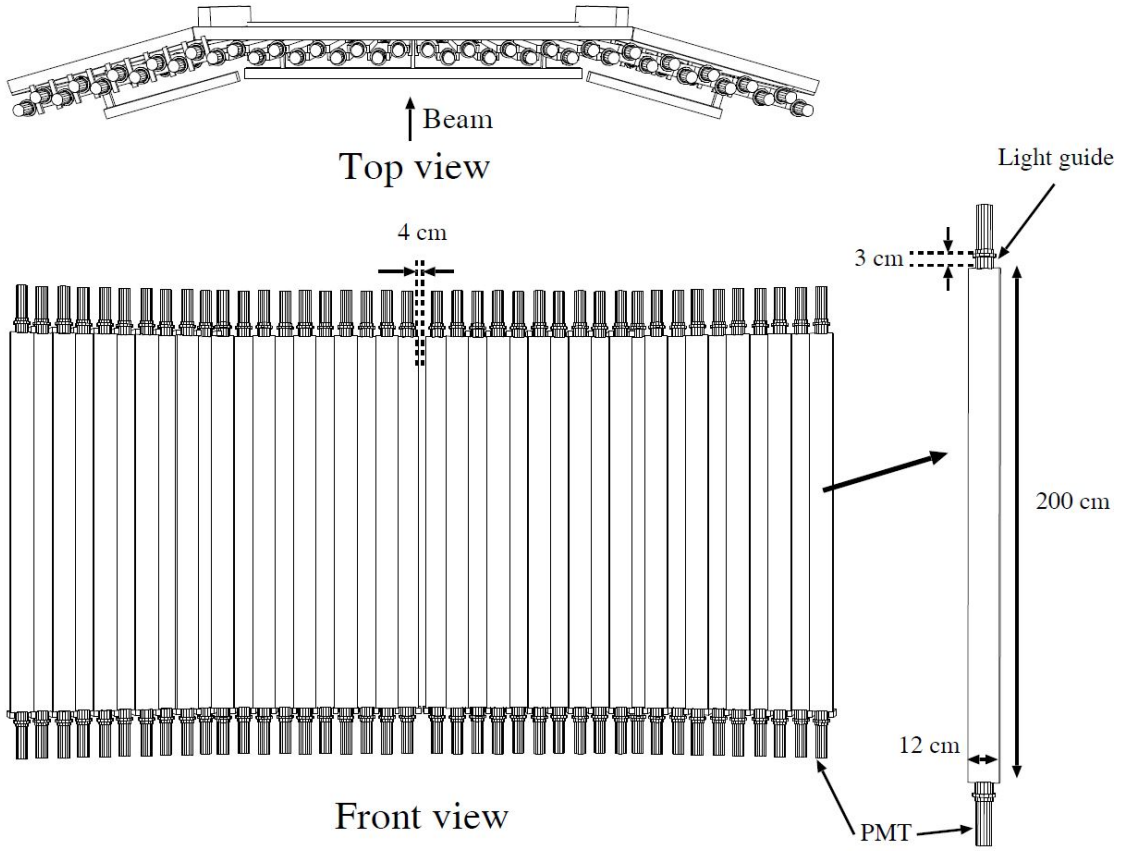

Figure 3.19: Schematic top and front view of TOF wall.

3.3.9 Trigger

The trigger condition for the data taking consists of several different signals. The signals are the signal from tagging system (TAG), the veto signal from upstream veto counter (UPveto), the signal from trigger counter (TRG), the veto signal from downstream e^+e^- veto counter (EEveto) and the signal from time-of-flight wall (TOF).

The readout logic diagram for trigger is displayed in Fig. 3.20. The trigger definition is :

$$(TAG \otimes \overline{UPveto}) \otimes (TRG \otimes \overline{EEveto}) \otimes TOF \qquad (3.10)$$

The typical trigger rate for this experiment was around 100 cps.

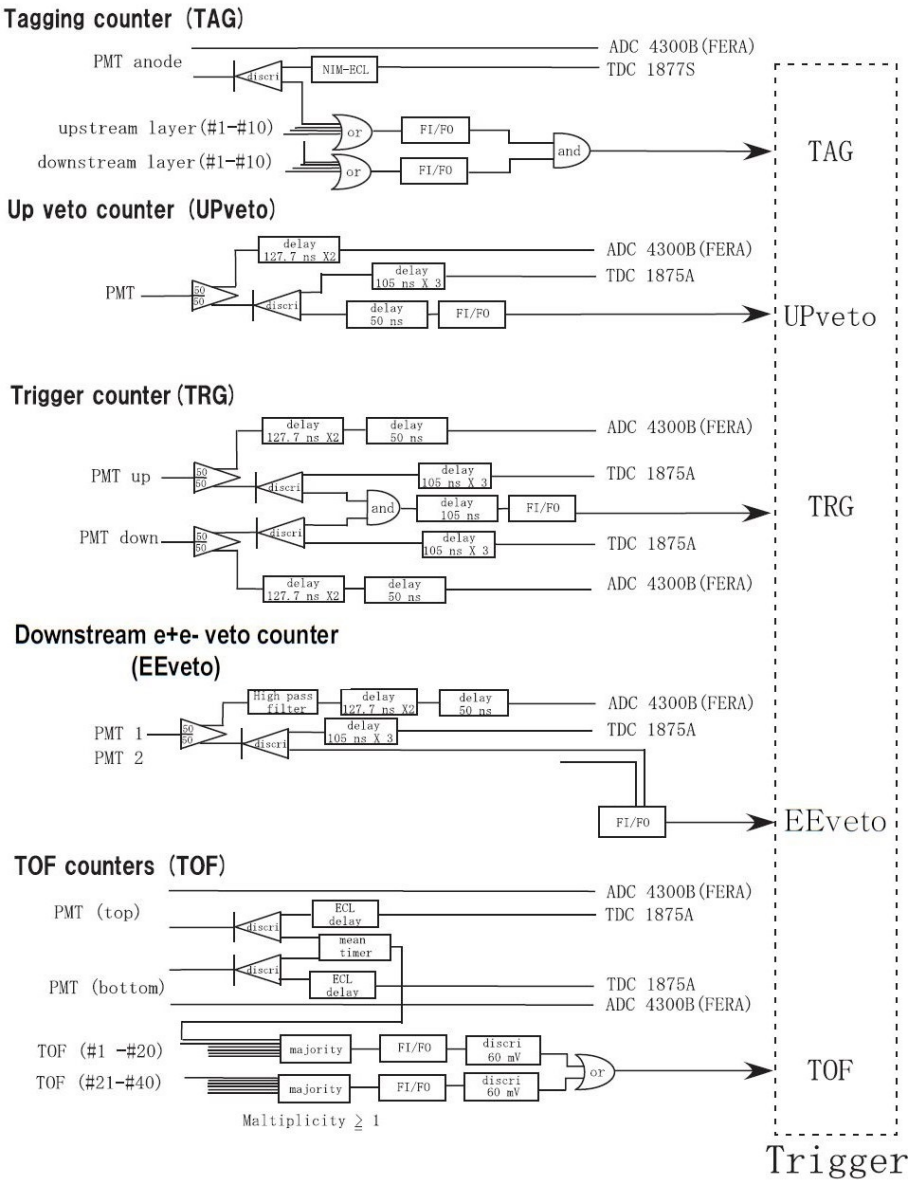

Figure 3.20: The readout logic diagram for trigger [86].

3.4 Analysis overview

The data used in this thesis are summarized here. The filling pattern and trigger condition of the data set are listed in table 3.3. The physics run for the data taking was from October 6th to October 18th, 2007 and November 8th to December 17th, 2007. The total number of tagged photons was 4.048×10^{11}. The run configuration is summarized in table 3.4. The number of horizontally polarized photons was 2.04×10^{11} and that vertically polarized photons was 2.01×10^{11} [61].

Fig. 3.21 shows the momentum vs. mass square for all positive

Table 3.3: Filling Pattern and Trigger Condition

Run number	Filling Pattern	Trigger
37768-37808	4/58 filling + 53 bunches	(TAG $\otimes$ $\overline{\text{UPveto}}$) $\otimes$ (TAG $\otimes$ $\overline{\text{EEveto}}$) $\otimes$ TOF
37809-37912	160 bunch train $\times$ 12	(TAG $\otimes$ $\overline{\text{UPveto}}$) $\otimes$ (TAG $\otimes$ $\overline{\text{EEveto}}$) $\otimes$ TOF
37922-38022	1/14 filling + 12 bunches	(TAG $\otimes$ $\overline{\text{UPveto}}$) $\otimes$ (TAG $\otimes$ $\overline{\text{EEveto}}$) $\otimes$ TOF
38023-38068	160 bunch train $\times$ 12	(TAG $\otimes$ $\overline{\text{UPveto}}$) $\otimes$ (TAG $\otimes$ $\overline{\text{EEveto}}$) $\otimes$ TOF
38069-38314	203 bunches	(TAG $\otimes$ $\overline{\text{UPveto}}$) $\otimes$ (TAG $\otimes$ $\overline{\text{EEveto}}$) $\otimes$ TOF

Table 3.4: Run configurations

Data taken	Oct. 6 - Oct. 18, 2007 Nov. 8 - Dec. 17, 2007
UV laser wavelength	257 nm
Target	LH_2
Run number	r37768 - r38314
Total number of photons	4.048×10^{11}
Total number of horizontally polarized photons	2.038×10^{11}
Total number of vertically polarizated photons	2.010×10^{11}
The LH_2 target was placed at -953 mm. The start counter was placed at -801.6 mm. The aerogel cherenkov detector was replaced by the e^+e^- veto counter downstream of the DC3.	

charged tracks satisfying all selection conditions except the PID cut as an example to show the contaminated PID. In Fig. 3.21 the solid black kaon PID band is contaminated by pion in the region of higher momentum (>1.5 GeV/c) which is highlighted by red dash circle. The impure K^+ PID introduces significant background to the K^+ missing mass for identifying the photoproduction of $K^+\Lambda$ and $K^+\Sigma^0$.

This data set has been analysed by Sumihama [61] and Hwang [62]. In this study, we start from the ntuple level which was provided by Hwang, instead of raw data level. All the calibrations remain the same except for the t0 calibration and the related additional cuts which will be discussed in detail in the following chapter.

The ntuples are available on IPAS data storage at

`/sp8data3/kstar07/nt/*.nt`

The run numbers and the horizontal/vertical ntuples for each run can be found at

`/usrX/shshiu/kstar/ana/ch_all_h.kumac`

and

`/usrX/shshiu/kstar/ana/ch_all_v.kumac`

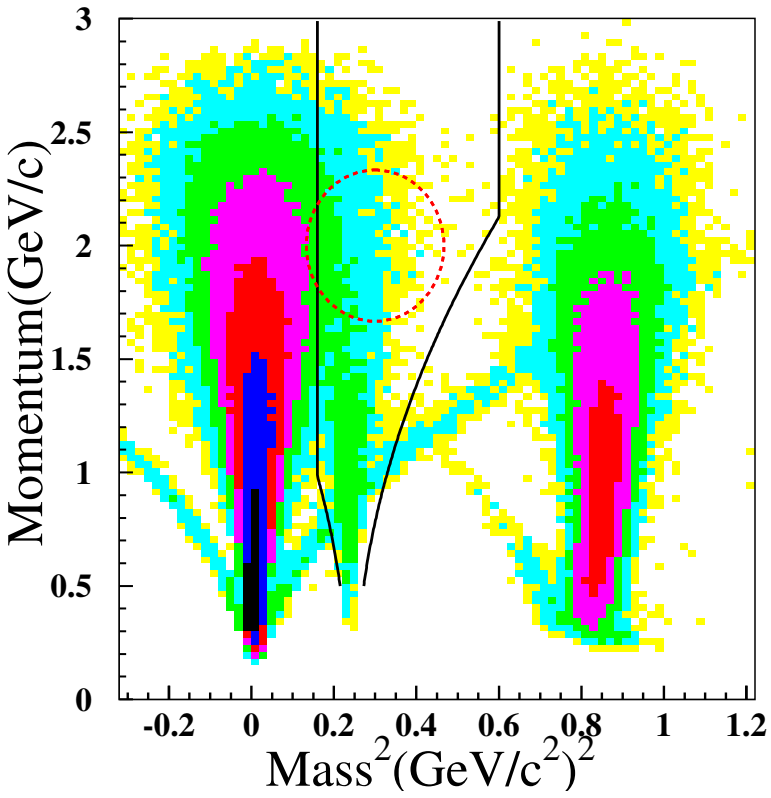

Figure 3.21: The momentum vs. mass square plot for all positive charged tracks satisfying all selection conditions except the PID cut. The solid black line stands for kaon PID boundary. The red dashed circle indicates the region contaminated by pion.

Kaon skimmed ntuples are also available under
`/sp8data3/shshiu/skim_nt1k+_shshiu_largek2`

Chapter 4

Data Analysis

In this analysis, the photoproduction of $\gamma p \to K^+\Lambda$ and $K^+\Sigma^0$ was studied in K^+ detection mode. The schematic diagram of K^+ detection mode can be seen in Fig 4.1 The red line indicates the K^+ emitted from the target, bent by the magnet and passing through the detectors.

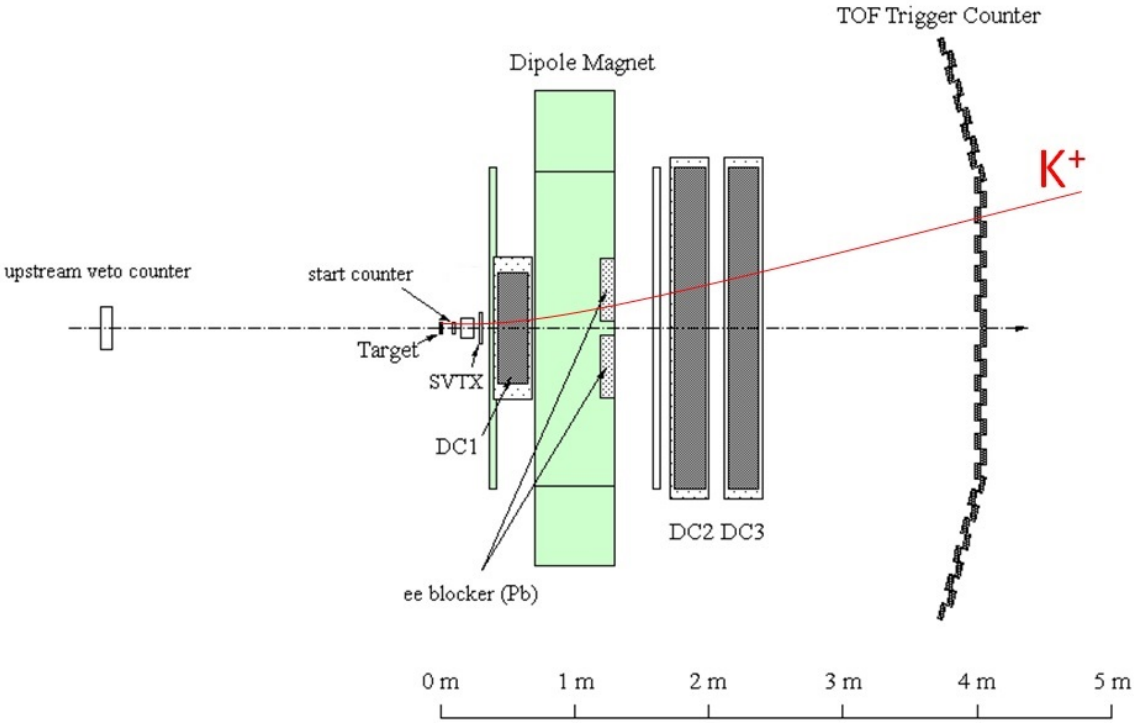

Figure 4.1: The schematic top view of K^+ detection mode.

The detected information was obtained by the detectors and recorded by the data acquisition system for further study. The missing mass calculated by beam energy and particle momentum for the K^+ ($\mathrm{MM}_X(\gamma p, K^+)$) was for the extraction of desired $K^+\Lambda$ and $K^+\Sigma^0$ events. By the fit to the missing mass spectrum with two Gaussian distributions and the

combined estimated background template, the yields of the $K^+\Lambda$ and $K^+\Sigma^0$ productions were extracted.

Since this data set was originally collected for detecting K^{*0} decaying to high-momentum K^+ and π^- [60], the Aerogel Cherenkov counter, which was conventionally placed after the target to reject the high-momentum electrons, positrons, and pions in the trigger level was removed to enhance the π^- acceptance. In this experiment, the Aerogel Cherenkov counter was replaced by a downstream e^+e^- veto counter behind DC3 as discussed in sec. 3.3.7. Due to the absence of Aerogel Cherenkov counter, the high-momentum positrons and pions become the main background to influence the K^+ particle identification (PID) region. In order to estimate the background and extract correct observables for the $K^+\Lambda$ and $K^+\Sigma^0$ productions, the background suppression is one of important developments of this analysis.

The particle identification (PID) of the charged particles is done by a 3σ cut on their reconstructed mass based on the measured TOF, momentum and path length, where σ is the momentum dependent mass resolution. To ensure that the PID efficiency is the same between the real data and Monte-Carlo simulation, the TOF calibration and the consistency check of Monte-Carlo was performed.

In this chapter, the event selections considering the track and tagger cut, decay in flight cut, e^+e^- cut, vertex cut, and particle identification (PID) cut will be shown at first. In the second part, the t0 calibration, and then the background suppression method will be demonstrated in detail. In the last part of this chapter, the Monte-Carlo simulation will be discussed.

4.1 Event selections

In this section, various cut conditions applied for the selection of K^+ events are discussed. The table 4.1 lists the event selection conditions grouped in track and tagger, decay-in-flight, e^+e^- , vertex, PID, and additional cut.

4.1.1 Event selection conditions

- Tagger hit (fntag= 1)

Table 4.1: Event selection conditions

Cut conditions	
ntrk> 1 fntag= 1	Track and tagger cut
prbchi2> 0.02 noutl< 7 ithtofhit> 0 |itof-tofid| < 2 |ytof-tofdiff| < 80mm	Decay-in-flight cut
ybar< −30mm and ybar> 30mm yebar< −50mm and yebar> 50mm	e^+e^- cut
−1042 <vtz< −860mm	vertex cut
3σ K^+ PID	Particle identification (PID) cut
At least having 1 hit in each detector of DC 1, 2, and 3. Remove TOF wall #1,2,39,40	Additional cut

The tagger hit (fntag) cut aims at selecting good tracks of recoil electrons in the tagging system. The energy of photon beam is measured by the tagging system located inside the SPring-8 storage ring. The electron which is scattered by the injected Laser via Backward-Compton scattering process leaves a track in the tagging system. Base on the position information for the recoiled electron track, the beam energy can be decided.

There are background events due to X-ray or electric showers which also trigger the tagging system. Therefore, the requirement of the tagging hit equal to 1 can remove the background events and reduce the complexity to decide the BCS photon beam energy. Fig. 4.2 shows the fntag distribution, and the hatched region shows the selected events.

- χ^2 probability (prbchi2> 0.02)

By considering the fitting to hit positions of the detectors, the track of charged particle could be reconstructed. The Kalman filter [64] method was applied for the tracking in the LEPS analysis. The χ^2 of Kalman filter is a tool for user to test the goodness of the fitting obtained by the filtering. The χ^2 probability (prbchi2) distributes between 0 and 1. Most background and decay-in-flight events have large χ^2 values corresponding to small prbchi2 values. The track with χ^2 probability greater than 0.02 is applied for further analysis. The χ^2 probability distribution is shown in Fig. 4.3, and the hatched region reveals the valid χ^2 events.

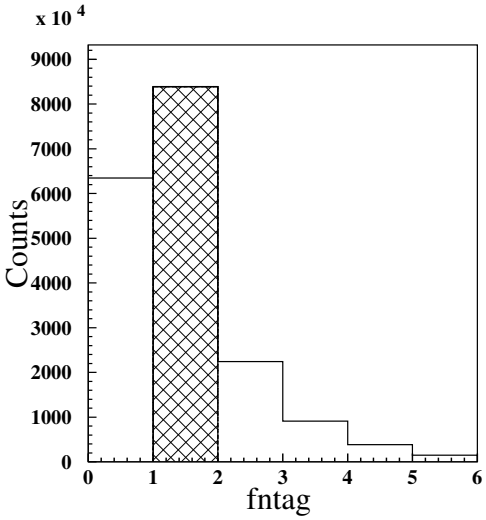

Figure 4.2: The number of tracks at Tagger. The hatched area indicates the events with fntag= 1.

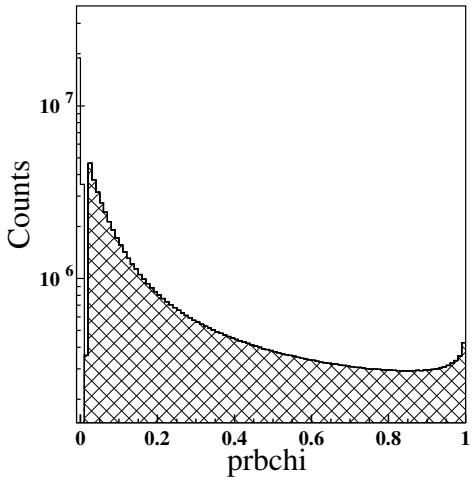

Figure 4.3: χ^2 probability distribution. The hatched area shows the events with χ^2 probability (prbchi2)$>$ 0.02.

- Number of outlier (noutl$<$ 7)

During the tacking process, if the hit position information from tracking chamber deviates from the expected position more than resolution, the hit will be considered as a background hit which is called outlier. The outlier will be removed from the tracking. Most of decay-in-flight events provide the hit information associated with a large number of outliers (noutl), due to the decay in the middle of tracking volume. The selection condition noutl$<$ 7 was applied for eliminating this kind of events. Fig. 4.4 shows the number of outlier hits distribution, and the hatched region illustrates the selected number of outlier events.

- Consistency of TOF hit (ithtofhit$>$ 0, |itof-tofid| $<$ 2, |ytof-tofdiff| $<$ 80mm)

To ensure good PID by removing decay-in-flight events, an extrapolation of the hit position by Runge Kutta method from the DC3 drift chamber to the TOF wall was applied. It is required that at least a hit was detected by the TOF counter (ithtofhit$>$ 0), to maintain the validity of extrapolation of the track information. It is required that the extrapolated vertical hit position (ytof) to be within 80 mm of the estimated one based on the time difference of TOF readout from both

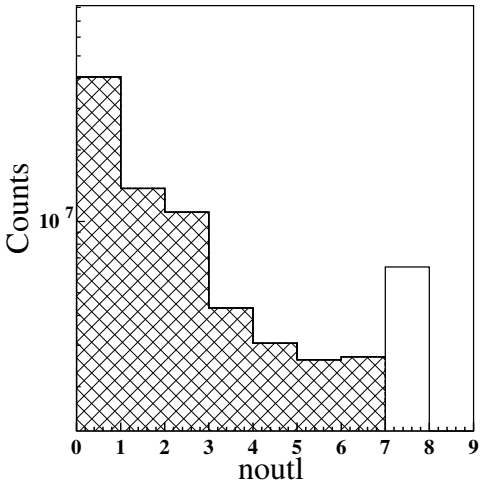

Figure 4.4: The number of outlier hits. The hatched area shows the events with number of outlier (noutl)< 7.

ends of the fired scintillator bar(tofdiff) (|ytof-tofdiff| $<$ 80mm). For the horizontal hit position information, the difference of extrapolated counter number (tofid) and the TOF slat number (itof) was required to be less than 2 (|itof-tofid| $<$ 2). Fig. 4.5, 4.6, 4.7 show the number of fired TOF bars, the difference of the TOF slat numbers, and the difference of TOF vertical hit position distribution, the hatched region represents the selected events.

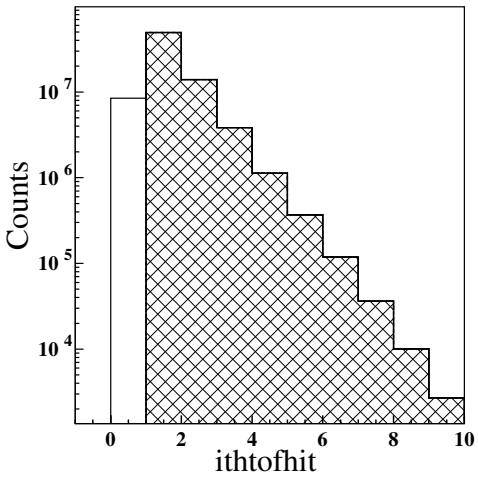

Figure 4.5: Number of hits at TOF counters. The hatched area shows the selection region where at least one hit is required.

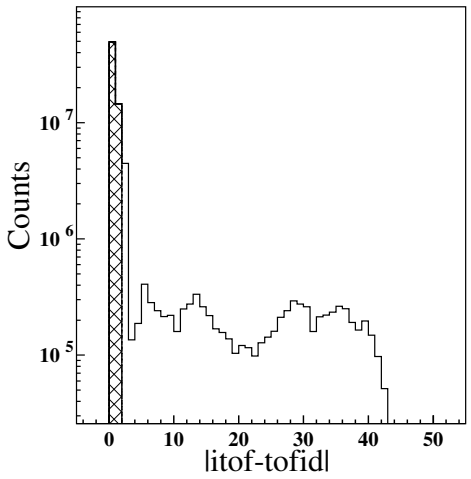

Figure 4.6: TOF slat number difference. The requirement of the TOF slat number difference less than 2 is indicated by the hatched region.

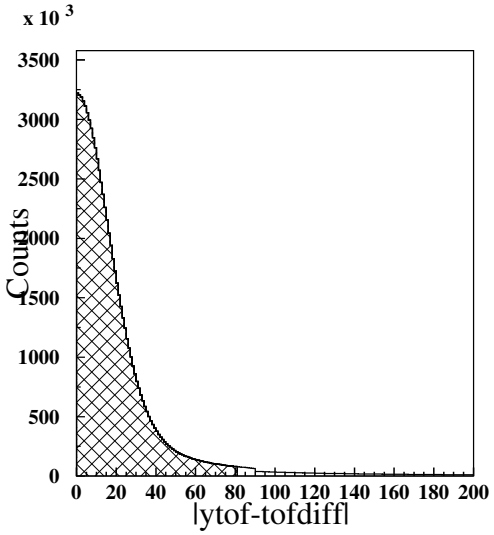

Figure 4.7: Vertical TOF hit position difference. The hatched region indicates the requirement of the difference of TOF vertical hit position less than 80 mm.

- e^+e^- cut (ybar<-30 mm or ybar>30 mm, yebar<-50 mm or yebar>50 mm)

In this analysis cuts on the reconstructed virtual plane of y position for lead blocker (ybar) and e^+e^- veto bar (yebar) were applied. The detailed discussion of the lead blocker and e^+e^- veto bar is written in sec. 3.3.5 and 3.3.7, respectively. The lead blocker in the dipole magnet was installed to block the e^+e^- particles whose momentum was below 1 GeV/c. For the higher momentum e^+e^- events, the e^+e^- veto bar is responsible for rejecting the events in the trigger level. There is a possibility that the e^+e^- events are accepted by the online trigger accidentally, so the y position of a track at both lead blocker and e^+e^- veto bar are applied to remove such events. Fig. 4.8, 4.9 show the reconstructed y position of ybar, and yebar distribution, and the hatched region shows the selected events.

- Vertex cut ($-1042<$vtz<-860 mm)

Depending on the experimental setup, the position of liquid hydrogen target in the z coordinate(vtz) is between -860 mm and -1042 mm.

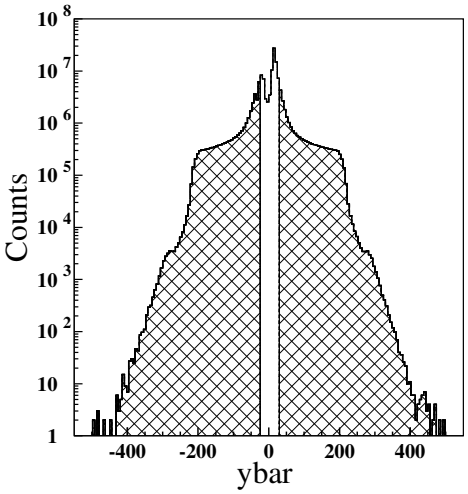

Figure 4.8: ybar virtual plane reconstructed y distribution. The hatched area indicates the ybar< −30mm or ybar> 30mm events.

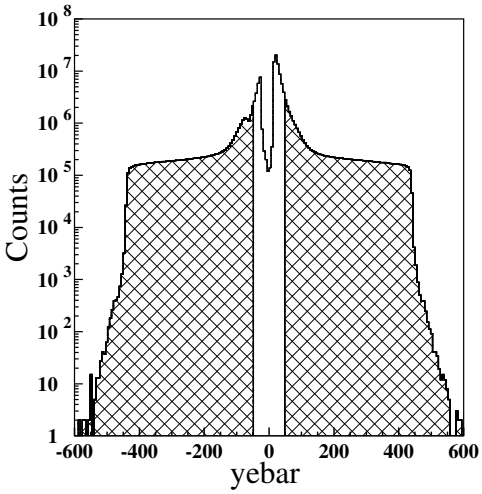

Figure 4.9: yebar virtual plane reconstructed y distribution. The hatched area shows the events with cut conditions yebar< −50mm or yebar> 50mm.

Fig. 4.10 shows the vtz distribution for K^+ events and the hatched region shows the selected 'vtz' region. The structures of the TRG counter and target can been seen.

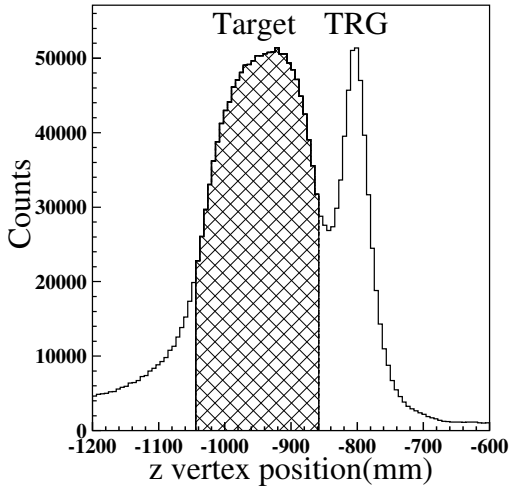

Figure 4.10: Z−Vertex position distribution for K^+ events. The hatched area indicates the selected vtz events.

- Particle identification (PID) cut (3σ K^+ PID)

In this analysis the missing mass for the K^+ was calculated for the

extraction of $K^+\Lambda$ and $K^+\Sigma^0$ events. The graphic cut on momentum vs. mass square was applied for the K^+ particle identification.

The mass of charged particle can be calculated via the formula below.

$$M^2 = p^2 \cdot (\frac{1}{\beta^2} - 1) \tag{4.1}$$

$$\beta = \frac{L}{TOF \cdot c} \tag{4.2}$$

Here the p is momentum, L is path length from the target to the TOF wall, TOF is the time of flight where the RF signal is used to determine a start timing, and c is the speed of light.

The resolution of the mass squared is

$$\sigma_{M^2}^2 = 4M^4 \left(\frac{\sigma_p}{p}\right)^2 + 4c^2p^2 \left(p^2 + M^2\right) \left(\frac{\sigma_{TOF}}{L_{typ}}\right)^2, \tag{4.3}$$

where the average TOF resolution σ_{TOF} is set to 175 ps, and the L_{typ} is set to the typical path length (4100 mm). The σ_p is the resolution of momentum and the $\frac{\sigma_p}{p}$ can be described as

$$\left(\frac{\sigma_p}{p}\right) = \left(\frac{a_1}{\beta}\right)^2 + p^2 {a_2}^2, \tag{4.4}$$

where the a_1 and a_2 are estimated by Monte-Carlo calculation as 0.00458 and 0.00323, respectively. The a_1 term corresponds to the contribution from the multiple scattering, and the a_2 is the contribution from the resolution of the spectrometer. The solid black line indicates the particle identification region for pion, kaon, and proton in Fig. 4.11. The PID boundary for kaon is defined as $3\sigma_{M^2}$ in Eq. 4.3, and the mass boundary cuts for K^+ are set on the squared mass from 0.16 to 0.6. Due to the worse mass resolution and the fewer background events, the boundary of low momentum($<$0.9 GeV/c) proton was set to $0.7 < M^2 < 1.1$.

- At least having 1 hit in each detector of DC 1, 2, and 3.

The momentum reconstruction was base on the information obtain by the SVTX,DC1 ,DC2, and DC3. Due to the insufficient width of

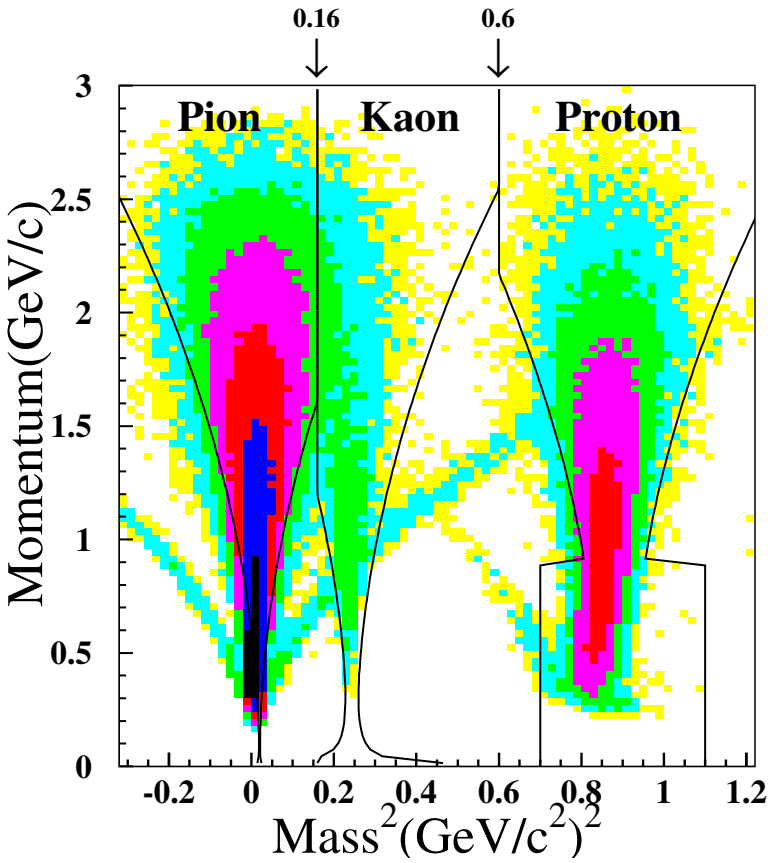

Figure 4.11: PID selection conditions for pion, kaon, and Proton in the scatter plot of momentum vs. mass squared.

DC3, some tracks can pass through the DC2, but can not pass the sensing area of DC3. This selection condition was added to prevent the incorrect path length calculation.

- Remove TOF bar #1, 2, 39, 40

The inconsistency of DC efficiency between Monte-Carlo and real data for slat #1, 2, 39, 40 was found during the calibration. This inconsistency affects the acceptance calculation. In order to maintain the consistency between Monte-Carlo and real data, the data from slat #1,2,39,40 were not used. Fig. 4.12 shows the TOF hits distribution, and the hatched region shows the selected events.

4.1.2 Event selection summary

The number of events surviving after the various cuts are listed in Table 4.2 for each selection condition individually. The surviving events with different photon polarization(vertical and horizontal) are

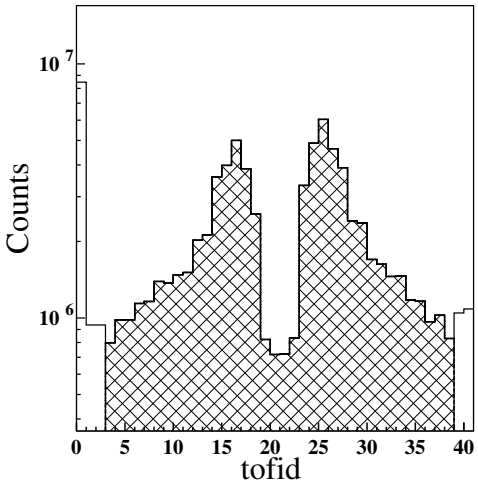

Figure 4.12: The firing distribution of TOF number. The hatched area denotes the selected TOF number.

also listed.

Table 4.2: Event selection conditions and the number of surviving events for K^+ selection.

Cut conditions	All counts	Vert. counts	Hori. counts
All events	2.053×10^8	9.577×10^7	1.095×10^8
ntrk>1	1.191×10^8	5.478×10^7	6.433×10^7
fntag$=1$	8.848×10^7	4.077×10^7	4.770×10^7
prbchi2>0.02	6.569×10^7	3.006×10^7	3.563×10^7
noutl<7	6.329×10^7	2.894×10^7	3.435×10^7
ithtofhit>0	6.307×10^7	2.883×10^7	3.423×10^7
$\lvert$itof-tofid$\rvert<2$	6.306×10^7	2.883×10^7	3.423×10^7
$\lvert$ytof-tofdiff$\rvert<80$mm	6.294×10^7	2.877×10^7	3.416×10^7
e^+e^-blocker cut	2.130×10^7	1.049×10^7	1.081×10^7
eebar cut	1.973×10^7	9.736×10^6	1.000×10^7
Z-vertex cut	1.042×10^7	5.206×10^6	5.217×10^6
3σ K^+ PID cut	2.425×10^5	1.239×10^5	1.186×10^5
At least having 1 hit in each detector of DC 1, 2, and 3.	2.409×10^5	1.230×10^5	1.179×10^5
Remove Tof wall #1,2,39,40	2.398×10^5	1.224×10^5	1.173×10^5

Fig. 4.13 shows the cuts condition distributions before and after the selection cuts. The hatched area in each sub-figures indicates the events after all the selection cuts.

4.2 t0 Calibration

4.2.1 Why we need t0 calibration?

To calculate the Time-of-Flight (TOF) of a charged particle, the information from trigger counter, TOF wall and RF signal from the storage ring are needed. The TOF is calculated by $TOF = T_{stop} -$

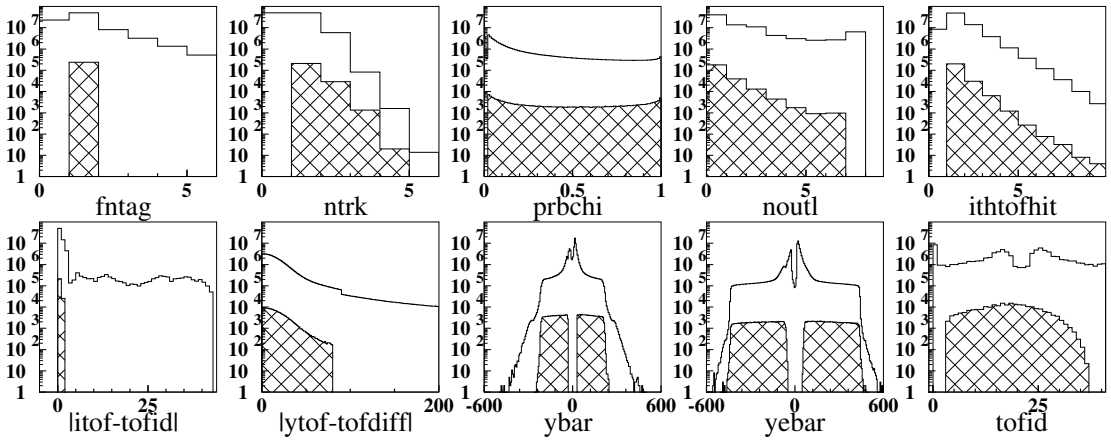

Figure 4.13: The various cut conditions for selecting the good K^+ events.

T_{start}. In the LEPS experiment, the T_{stop} was determined by the TDC information from TOF wall, and the T_{start} time can be determined by the trigger counter or RF signal from the storage ring. Since the RF signal provides a better time resolution [85], in this analysis we select the RF signal as the T_{start}.

The circulating electrons are bunched according to the RF signal at each 1.966 ns in the storage ring, so the BCS photons are synchronized with the RF signal. Since the common start signals of the TDC modules are provided by the trigger counter, the timing information of the RF signal depends on pulse height of the trigger counter photo multiplier tubes. To correct the timing dependence of the pulse height, the pulse-height time-walk correction is needed. The calibration was given by

$$T_{RF}^{corr} = T_{RF} - \frac{1}{2}(T_t^{TRG} + T_b^{TRG} - \frac{A1}{\sqrt{A_t^{TRG}}} - \frac{A2}{\sqrt{A_b^{TRG}}} + \frac{A3}{A_t^{TRG}} + \frac{A4}{A_b^{TRG}}) - A5 \tag{4.5}$$

where the T_{RF} is the raw TDC RF signal, and the $T_t^{TRG} and T_b^{TRG}$ are the top and bottom TDC values, and the $A_t^{TRG} and A_b^{TRG}$ are the ADC values from the trigger counter. The A1-A5 are the coefficients for the time-walk correction.

Since the TOF wall is composed of scintillators, the time-walk correction was also applied to the TOF wall to get the TOF value via

$$TOF = \frac{1}{2}(T_t^{TOF}+T_b^{TOF})-(B1+\frac{B2}{\sqrt{A_t^{TOF}}}+\frac{B3}{\sqrt{A_b^{TOF}}})+B4\times 0.025+T_{Glob}+T_0 \tag{4.6}$$

for the equation above the T_t^{TOF} and T_b^{TOF} stand for the top and bottom TOF TDC raw values after subtracting the T_{RF}^{corr}. The B1-B4 are the coefficients for the TOF time-walk correction. Here, 0.025 ns is the time in one TDC channel. The T_{Glob} and T_0 are global offset of the TOF bar and offset for each TOF channel for getting same mass distributions.

The pulse-height time-walk correction of RF and the TOF counter had been done by Hwang [62, 86]. But during the analysis, an inconsistency of mass square distribution between the Monte-Carlo and real data was observed.

Fig. 4.14 shows the comparison of Gaussian mean value of mass squared between for real π^+ data sample and for the Monte-Carlo π^+ sample. The Gaussian mean value of mass squared was obtained by fitting the mass squared distribution in each momentum slice by Gaussian function. All the track and tagger, decay-in-flight, e^+e^-, vertex cut, and the additional cut conditions were applied. To select the clean π^+ sample, the pion PID, and the missing mass between 0.865-1.015 GeV which is associated with $\gamma p \to \pi^+ n$ channel was selected. The Fig. 4.15 shows the selected missing mass distribution region for the $\gamma p \to \pi^+ n$ channel.

As shown in Fig. 4.14, the inconsistency of mass square distribution as a function of momentum between the real data and Monte-Carlo data becomes significant in the large-momentum regions. To find the cause of the inconsistency, the comparison of the TOF and re-calculated TOF(TOF_{cal}), and the comparison of the TOF and re-calculated TOF (TOF_{cal}) vs. momentum were checked in Fig. 4.16 and Fig. 4.17.

The TOF_{cal} is calculated by the formula below

$$TOF_{cal} = \sqrt{\left(\frac{M_\pi^2}{p^2}+1\right)} \times \frac{L}{c} \tag{4.7}$$

Here the M_π is the pion mass, p is momentum, L is path length,

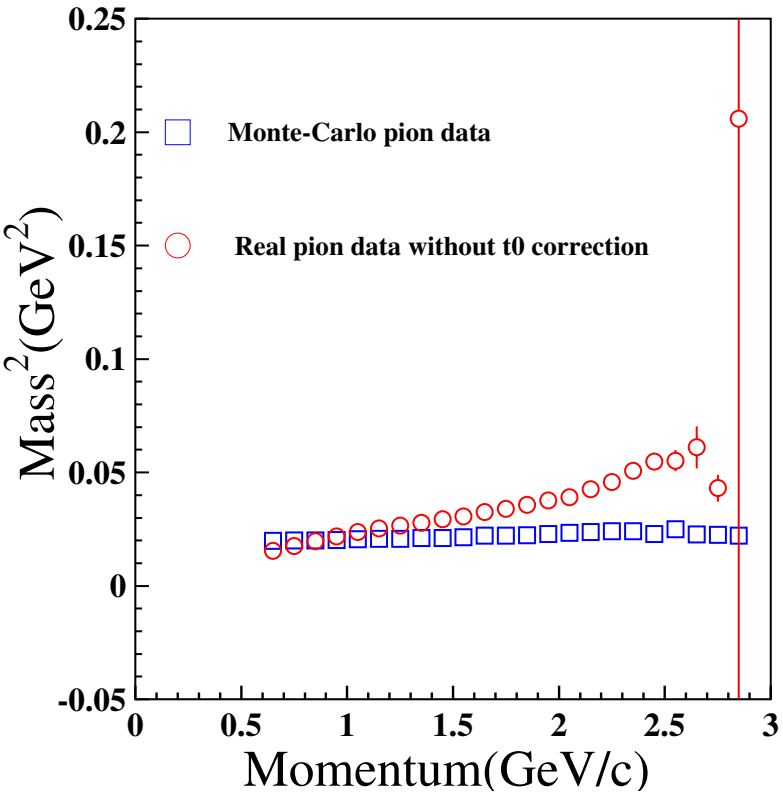

Figure 4.14: The comparison of Gaussian mean value of mass squared for real data π^+ sample and the Monte-Carlo π^+ sample.

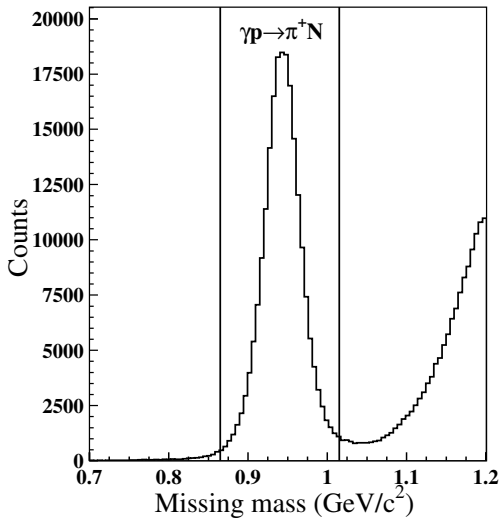

Figure 4.15: The missing mass distribution of $\gamma p \to \pi^+ n$ channel. The bold line indicates the pion selection region between 0.865-1.015 GeV.

and c is the speed of light.

In Fig. 4.16, the mean value of Gaussian fitting which should be around 0, is around 0.045 ns now, and the Gaussian fitting sigma which corresponds to the TOF resolution (σ_{TOF}) in Eq. 4.3 is 0.140 ns. The peak shift indicates the measured TOF is incorrect.

Fig. 4.17 shows the Gaussian mean and sigma of $TOF - TOF_{cal}$ as a function of momentum. Fig. 4.17 shows the $TOF - TOF_{cal}$ has no momentum dependence. In Eq. 4.1 and 4.2 the mass square is a function of momentum and time of flight. Judging from Fig. 4.17, the t0 calibration is needed.

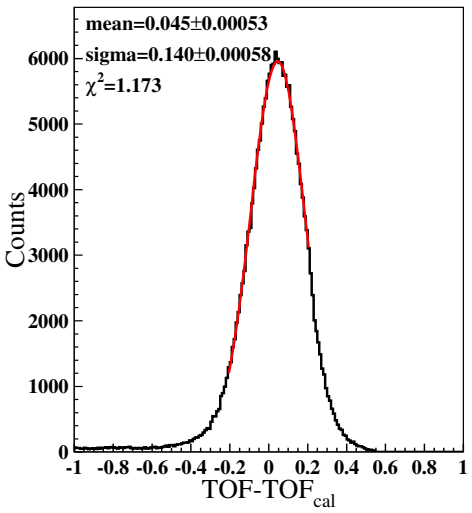

Figure 4.16: The comparison of TOF and calculated TOF.

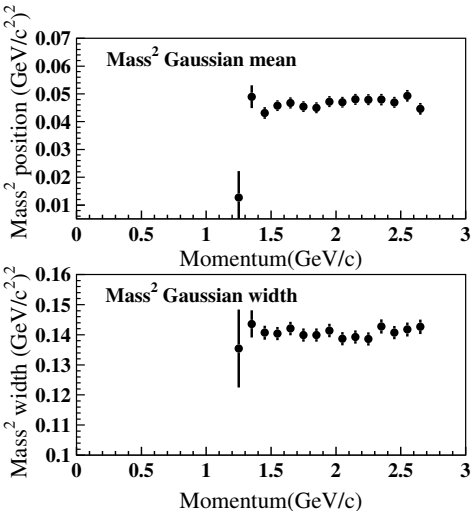

Figure 4.17: The $TOF - TOF_{cal}$ Gaussian mean and sigma value as a function of momentum. The upper part shows the Gaussian mean, the lower part shows the Gaussian sigma. From the plots we can see the $TOF - TOF_{cal}$ have no momentum dependence.

4.2.2 t0 calibration procedure

To get a reliable TOF, the procedure of the t0 calibration is listed below. First, the Gaussian mean values of mass square (M^2) for Monte-Carlo and real pion data with various t0 shifts were calculated. The χ^2 of the consistency between the mean values of M^2 for Monte-Carlo data and real pion was obtained. Fig. 4.18 shows the example of the Gaussian mean values of M^2 as a function of momentum for TOF Slat # 27. Fig. 4.19 demonstrates the χ^2 for various t0 shifts. The t0 shift

value corresponding to the smallest χ^2 is used for the calibration. The time shifts giving χ^2 which is larger than the smallest χ^2 by 1.0 were used to estimate the error boundary.

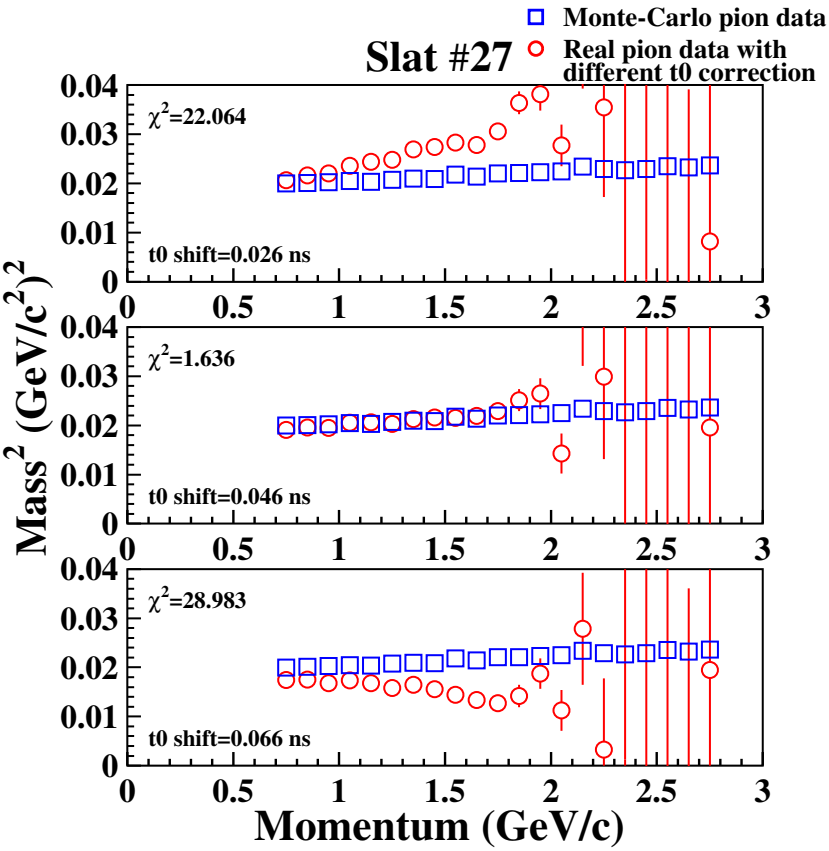

Figure 4.18: The M^2 mean value as a function of momentum for various t0 shifts (red empty circle). The mean value for Monte-Carlo M^2 (blue empty square) has been calculated.

Due to the removal of the Aerogel counter, the positron (electron) becomes a noticeable background to contaminate the π^+ (π^-) sample. The background positron (electron) changes the Gaussian mean of pion mass squared and this changing leads to the failure of t0 calibration. Fig. 4.20 shows the pion momentum distribution with different ybar cuts. Most of positrons(electrons) have relatively small θ angles. Tightening the ybar cuts can reduce the influence from positron and electron. Fig. 4.20 is composed by three plots, with different ybar cuts from 30 to 150 mm. In the upper plot in Fig. 4.20, a significant peak structure around 0.8 GeV (red circled) due to e^+ is seen. When tightening the ybar cut, in the middle and lower plots, the e^+ contamination is reduced.

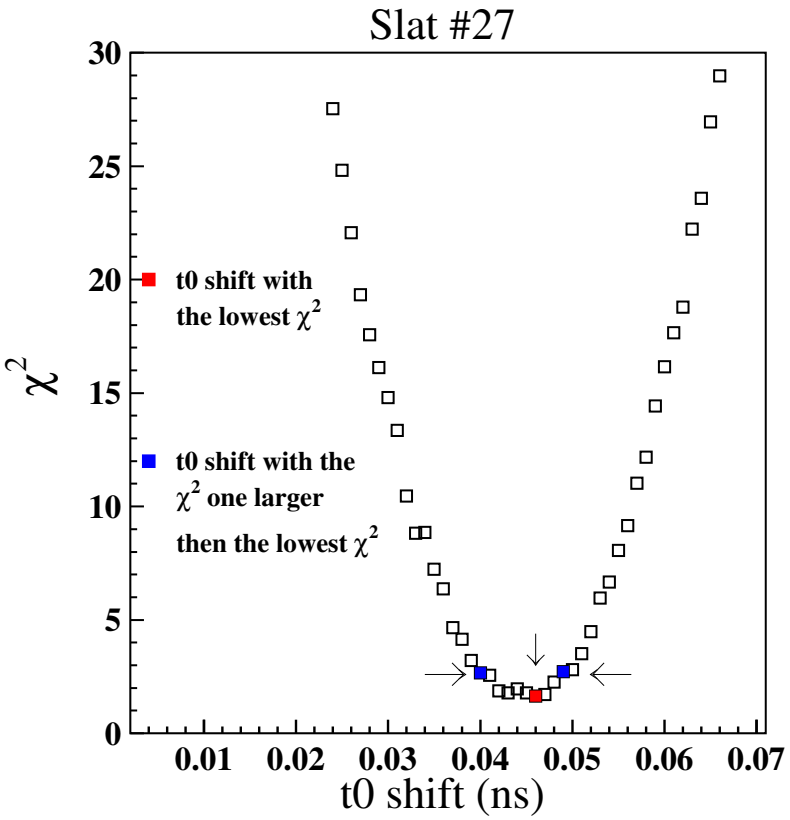

Figure 4.19: The χ^2 between Monte-Carlo data and real π^+ data as a function of t0 shift. The red solid square indicates the t0 value for the smallest χ^2, the blue solid square indicates the t0 value with χ^2 larger than the smallest χ^2 by 1.0.

As an example, the t0 shift with smallest χ^2 in slat # 27 with various ybar cuts is shown in Fig. 4.21. The positron and electron contamination to pion sample is considered to shift the Gaussian mean of mass square distribution to a smaller value. The smaller Gaussian mean leads the t0 shift value become less than it should be. By tightening the ybar cut, the t0 shift value should become stable. In Fig. 4.21 the trend of t0 shift for various ybar cuts agrees with this assumption. To get the stable t0 shift value, the t0 shift for each slat was decided by a fit of the t0 shift with smallest χ^2 with 150, 160,180, and 200 mm ybar cut by a polynomial function. The smallest χ^2 distribution for other slats are shown in Appendix A.

The t0 shifts for every slat used in this analysis are shown in Fig. 4.22 and listed in table 4.3. Fig.4.23 shows M^2 mean for the cali-

brated π^+ data with ybar cut = 160. The t0 shift calibration improves the consistency of the mean value of mass squared between Monte-Carlo and real data. This calibration improves the inconsistency between the Monte-Carlo and real data, which makes the acceptance calculation more reliable.

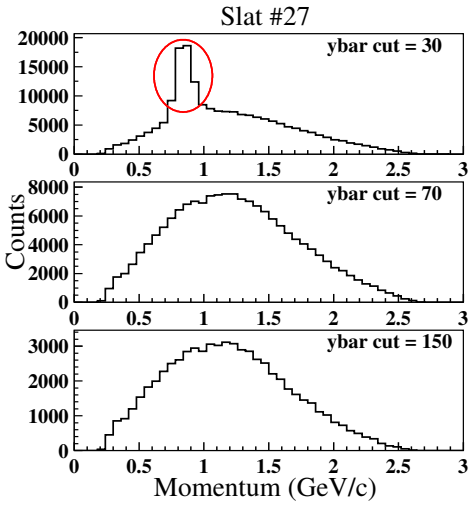

Figure 4.20: The pion momentum distribution for various ybar cuts. By tightening the ybar cut, the contaminations from electron and positron are reduced.

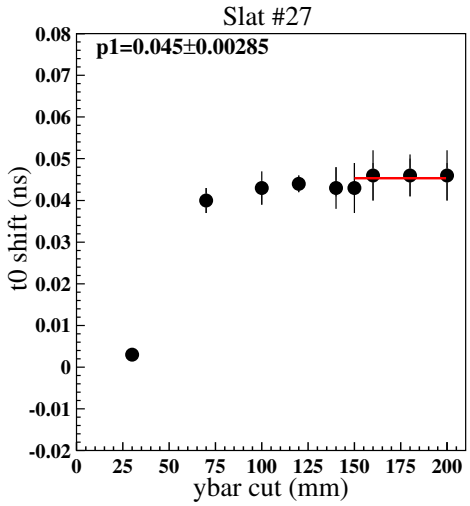

Figure 4.21: The t0 shift with smallest χ^2 in slat # 27 for various ybar cuts. The t0 shift becomes flat when the ybar cut up to 150.

Table 4.3: t0 shift for each TOF slat

Slat #	t0 shift (ns)	Slat #	t0 shift (ns)	Slat #	t0 shift (ns)	Slat #	t0 shfit (ns)
1	-	11	0.057	21	0.040	31	0.090
2	-	12	0.058	22	0.050	32	0.090
3	0.060	13	0.052	23	0.033	33	0.027
4	0.067	14	0.039	24	0.041	34	-0.009
5	0.039	15	0.022	25	0.028	35	-0.001
6	0.080	16	0.024	26	0.025	36	-0.004
7	0.071	17	0.048	27	0.045	37	-0.007
8	0.047	18	0.025	28	0.032	38	-0.002
9	0.084	19	0.042	29	0.024	39	-
10	0.066	20	0.029	30	0.054	40	-

4.3 Background Estimation

When E_γ becomes higher, the M^2 resolution becomes worse and π^+ contamination becomes serious in the K^+ sample. The background estimation method called side-band method for eliminating background events caused by the misidentified π^+ was applied.

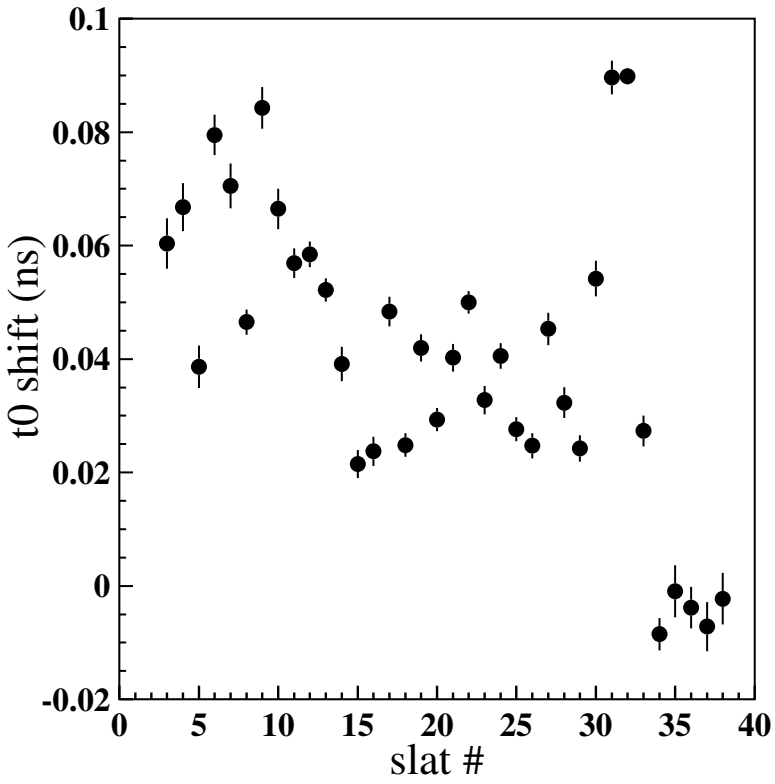

Figure 4.22: The t0 shift for all TOF slats.

Although the side-band method was used as the final background estimation method, it is still worth introducing different methods for the extraction of the data as a teaching material for the future explorers. Here, three methods to suppress the background by estimating the background shape will be discussed, and the first is the contamination fraction method. The second is called the mirror method. The final one is the side-band method.

In Fig. 4.24, the missing mass spectra of K^+ ($\mathrm{MM}_X(\gamma p, K^+)$) in various E_γ regions are shown as examples. The desired production channels in this analysis are $K^+\Lambda(1115)$ and $K^+\Sigma^0(1192)$, and we can find these two peaks in the figures labelled by $\gamma p \to K^+\Lambda$ and $K^+\Sigma^0$. From the plots, we can find the signal/noise ratio in the missing mass region around 1.0-1.3 GeV becomes worse when the beam energy increases. Judging from the height of the $\gamma p \to \pi^+ n$ peak in the missing mass spectra of K^+ ($\mathrm{MM}_X(\gamma p, K^+)$), the background from π^+ misidentifi-

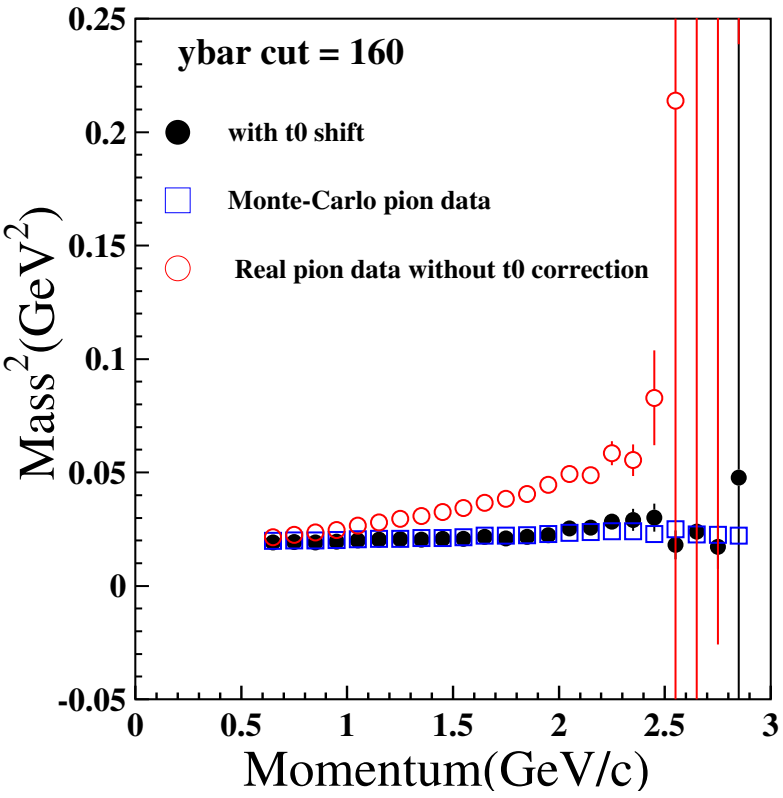

Figure 4.23: The comparison of Gaussian mean value of mass squared with/without t0 shift calibration for real pion data and the Monte-Carlo pion data. After the calibration, the Gaussian mean value of mass squared for real pion data has a good agreement with Monte-Carlo data.

cation becomes more significant with an increase of beam energy. The enormous background blocks the extraction of the desired $K^+\Lambda$ and $K^+\Sigma^0$ events.

The most naive way to estimate the enormous background is assuming the background distribution as a straight line as shown by the purple dot line in Fig. 4.24. For the smaller E_γ region, due to the fewer contamination backgrounds, this assumption might be acceptable. But when the E_γ goes up, this assumption might be not valid.

Fig. 4.25 shows the lethal evidence to deny the naive straight line background assumption. In Fig. 4.25 the π^+ missing mass distribution was calculated by assuming the kaon mass. The dashed line in each subfigure indicates the mass position of $\Lambda(1115)$ and $\Sigma^0(1192)$. From the π^+ missing mass distribution, two obvious structures can be observed,

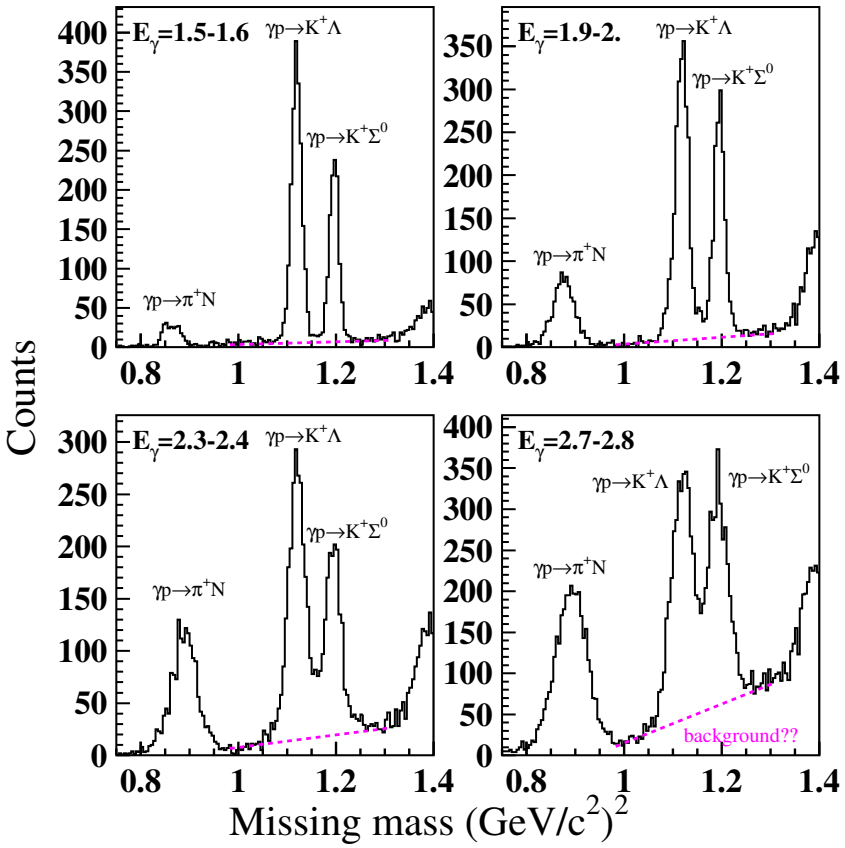

Figure 4.24: The missing mass spectra of K^+ in various E_γ regions. The $\gamma p \to \pi^+ n, K^+\Lambda$, and $K^+\Sigma^0$ peaks can be clearly seen.

the $\gamma p \to \pi^+ n$ and $\gamma p \to \pi^+ \Delta^0$. In our interested mass region, the possible background is not linear. In addition, the $\pi^+\Delta^0$ peak shifts as $E_\gamma$changes. Judging from Fig. 4.25, assuming the background as a straight line is not accurate enough to extract the yields of desired production channels. Better estimation of the background shape is needed for measuring the $K^+\Lambda$ and $K^+\Sigma^0$ yields correctly.

4.3.1 Contamination fraction method

The "contamination fraction" here means the pion contamination rate in kaon sample. From Fig. 3.21, 4.11 and Eq. 4.3 the resolution of mass squared is a function of momentum. By considering the distribution of pion mass squared and the overlapping to kaon PID region($M^2 > 0.16$ GeV). The contamination fraction was calculated by dividing the estimated counts of overlapping area in kaon region by the number of all pion events. The detail is listed below. The pion

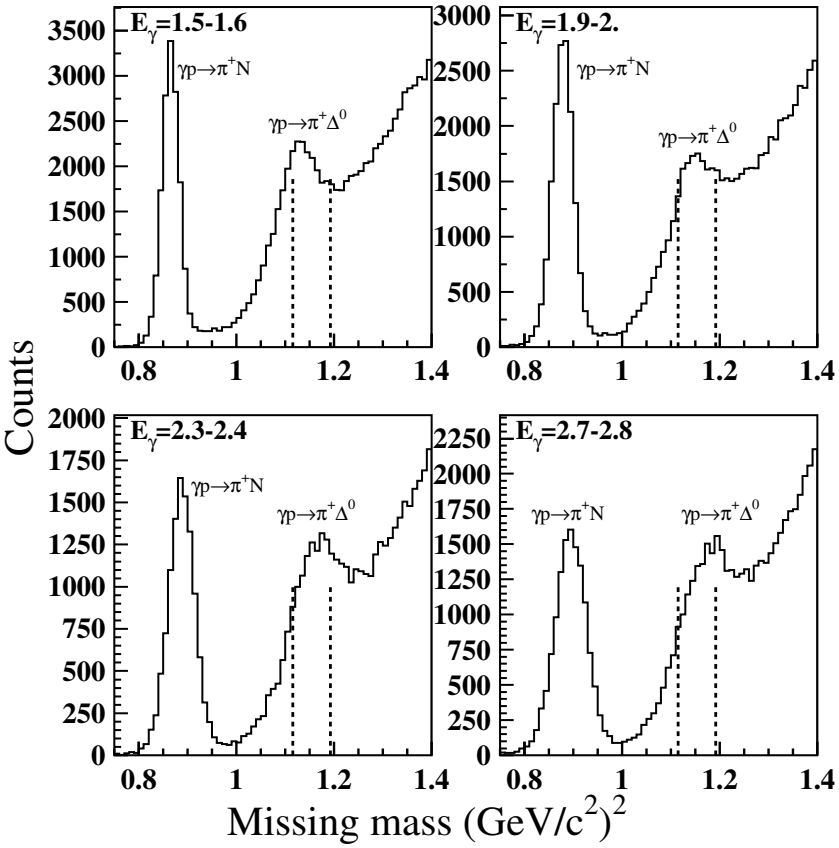

Figure 4.25: The missing mass spectra of π^+ by assuming the kaon mass for the calculation in various E_γ regions. The dashed lines indicate the mass positions of $\Lambda(1115)$ and $\Sigma^0(1192)$. Two structures $\gamma p \to \pi^+ n$ and $\pi^+\Delta^0$ can be observed.

contamination fraction was determined as a function of momentum and angular distribution (p, cosθ). The contamination fraction was applied as the weight in summing up the background distribution from each p and cosθ bin. At each momentum slice, the fitting of the pion distribution by a Gaussian function and the extrapolation of the function to kaon PID region (M^2>0.16) were applied. By dividing the area of the extrapolated function to kaon region by the number of all pion events, the contamination fraction was calculated. Fig. 4.26 shows the fitting of pion and kaon mass squared distribution in various momentum bins. The red line and blue line are the Gaussian fitting functions for pion and kaon, respectively. The black dotted line indicates the PID boundary (M^2=0.16 GeV) between pion and kaon. By considering all the momentum bins, the contamination fraction can be seen in Fig. 4.27.

In Fig. 4.27 the black solid line is the contamination fraction fitted by a 5th-order polynomial function. As an example, Fig. 4.28 shows the background distribution with and without the application of contamination fraction weighting. The missing mass distribution is modified by applying the weighting.

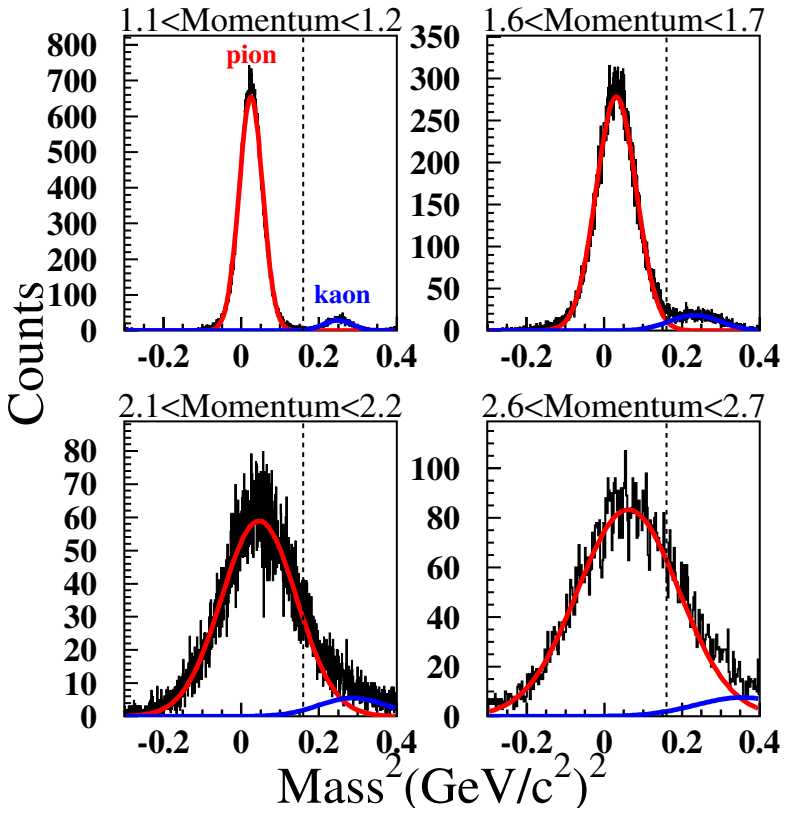

Figure 4.26: The Gaussian fitting of pion and kaon mass squared distribution in various momentum bins. The red and blue solid lines are the Gaussian fitting of pion and kaon, respectively

This method can easily provide the contamination fraction to modify the pion background shape, but the fitting of the pion peak and kaon peak is very sensitive to the fitting region which makes the estimation of background contamination fraction very unstable. As shown by the lower two plots of Fig. 4.26, the huge overlapping area from pion to kaon makes the choice of fitting region hard and unstable. To avoid such unstable fitting, another method called mirror method to estimate the background was developed.

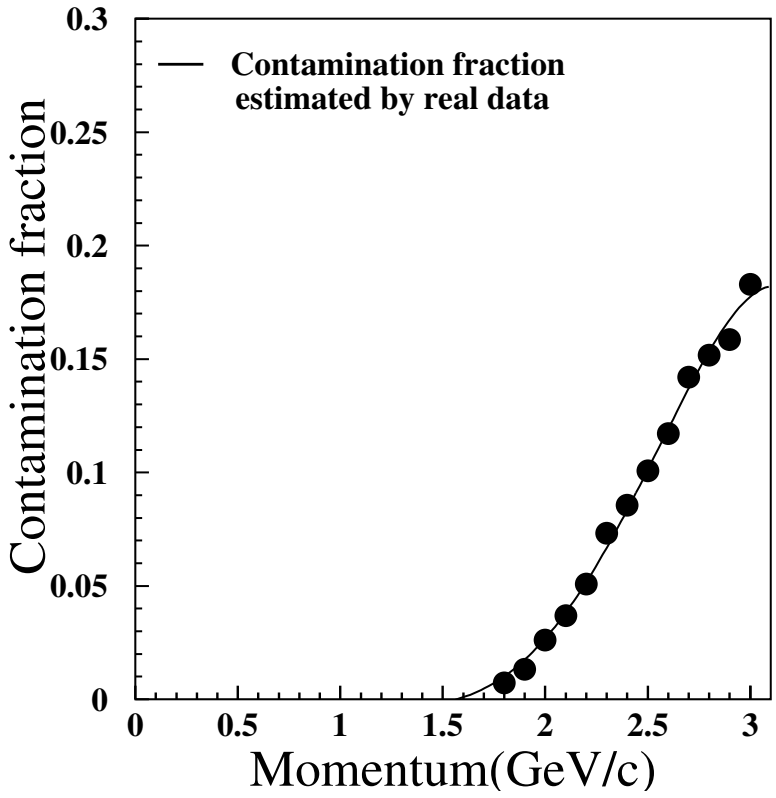

Figure 4.27: The contamination fraction as a function of momentum.

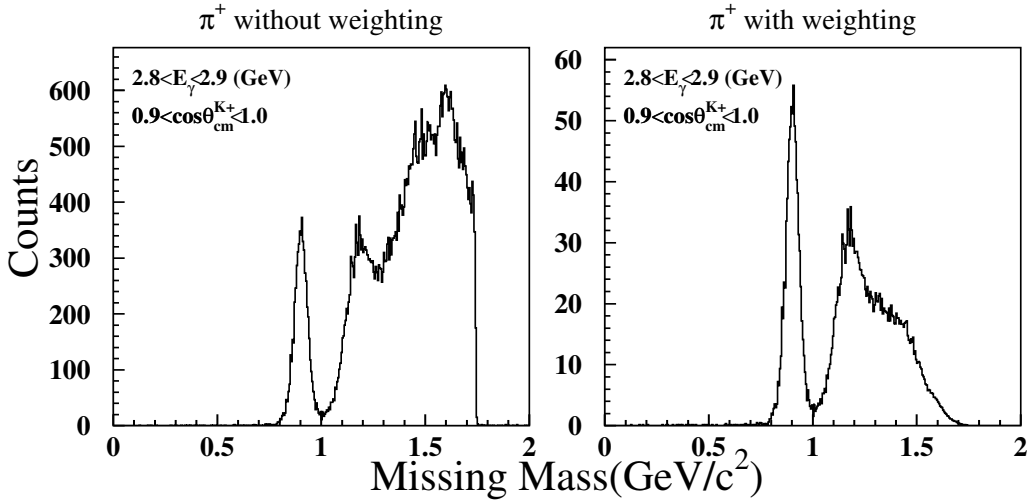

Figure 4.28: π^+ missing mass without and with contamination fraction weighting for E_γ=2.8-2.9 GeV, $\cos\theta^{K^+}_{c.m.}$=0.9-1.0.

4.3.2 Mirror method

The mirror method base on two simple assumptions. Since the LEPS spectrometer has the same acceptance for the negative and posi-

tive charged particles, the first assumption can be obtained easily that the contamination fraction of π^- in K^- sample is the same as π^+ in K^+ sample. Since the mass squared resolution of pions is a function of momentum, the misidentified pion fraction in the kaon sample must be the same between the π^- and π^+ mesons at a certain momentum. Second, in our interested missing mass region, all the observed K^- events are due to miss-identified π^-. Fig. 4.29 shows the schematic diagram of the mirror method. The assumptions above could be generalized into the function below.

$$\frac{\#\left(\pi^-\right) in\ K^- sample}{\#\left(\pi^-\right) in\ \pi^- sample} = \frac{\#\left(\pi^+\right) in\ K^+ sample}{\#\left(\pi^+\right) in\ \pi^+ sample} \tag{4.8}$$

therefore, the number of π^+ contamination events in K^+ sample is calculated as

$$\#\left(\pi^+\right) in\ K^+ sample = \frac{\#\left(\pi^-\right) in\ K^- sample}{\#\left(\pi^-\right) in\ \pi^- sample} \times \#\left(\pi^+\right) in\ \pi^+ sample. \tag{4.9}$$

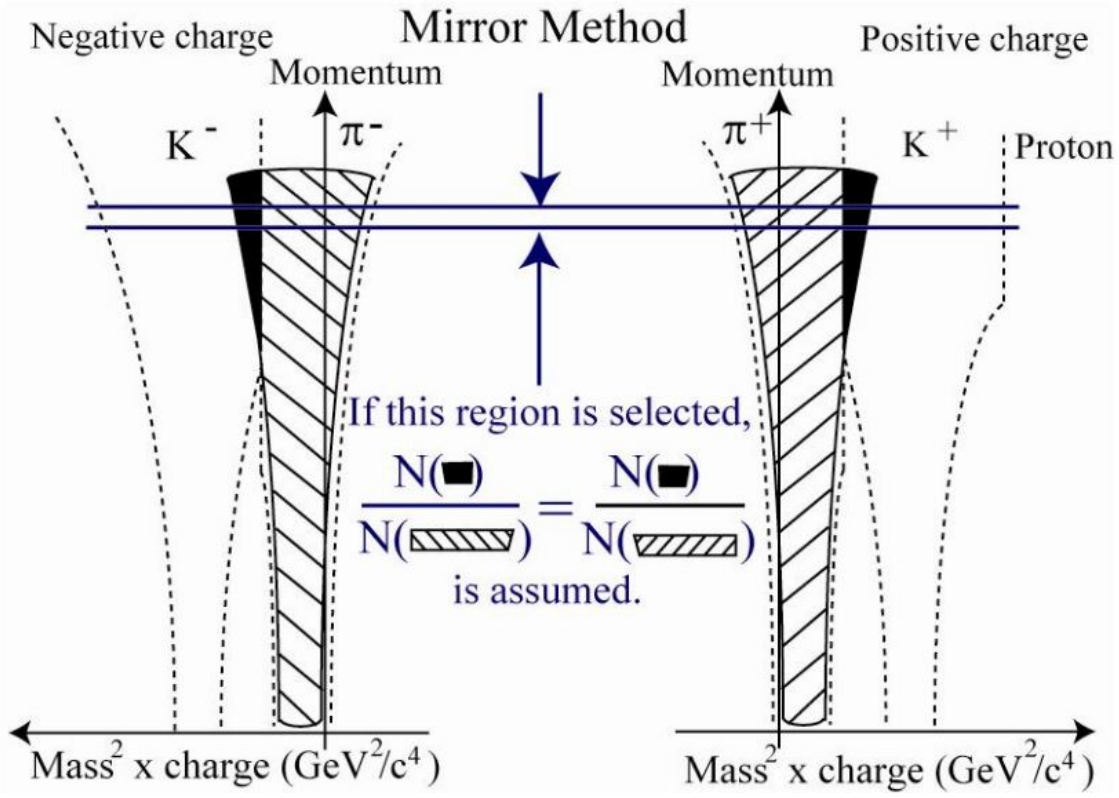

Figure 4.29: Schematic diagram of the mirror method. This plot was taken from [82].

Although mirror can get the contamination fraction more easily, during the checking, an inconsistency of the mirror method was found in positive and negative charged data. Fig. 4.30-4.32 show the comparison of positive and negative contamination fraction in various momentum with different *ybar* cut. The upper part in each sub-figure is the comparison of contamination fraction results of positive charged data with negative charged data. The lower part of each sub-figure shows the ratio of (the fraction for positive charged particles)/(the fraction for negative charged particles). The ybar cut here was selected to reject the *ybar* >=-30,-90,-150 and *ybar* <=30,90,150 events in Fig. 4.30, 4.31 and 4.32. Fig. 4.30 shows that the contamination fractions for positive and negative charged particles are consistent(close to 1) with each other in $0.6<\cos\theta^{K^+}_{c.m.}<0.9$. The discrepancy in $0.9<\cos\theta^{K^+}_{c.m.}<1.0$ (blue dash circled region) should come from the contamination of beam pipe electrons which increase the amount of the negative charged π^- data, and then reduce the height of the contamination fraction. To check the discrepancy in $0.9<\cos\theta^{K^+}_{c.m.}<1.0$, we tried to raise the ybar cut in Fig. 4.31. Even if the ybar cut was tightened to 90, the contamination from beam pipe electron was still very strong (blue dash circled region). After the ybar cut was further tightened to 150, the discrepancy in $0.9<\cos\theta^{K^+}_{c.m.}<1.0$ (blue dash circled region) become improved. Because of the absence of Aerogel information in 2007 data, it is almost impossible to well describe the pion and electron(position) contamination fraction by mirror method. To set the ybar cut to 150 sacrifices too much statistics, so the third method, side-band method was selected.

4.3.3 Side-band method

The side-band method is based on a simple assumption: the background due to contamination in K^+ PID can be reproduced by the missing mass spectrum of tracks inside the π^+ PID region within the same photon energy (E_γ), momentum ($|\vec{P}|$), and production angle $\cos\theta^{K^+}_{c.m.}$ binning. The side-band sample in missing mass calculation was chosen by the π^+ events lying outsides the K^+ PID region in the same bin of track momentum ($|\vec{P}|$), photon energy (E_γ), and production angle by assuming kaon mass ($\cos\theta^{K^+}_{c.m.}$). Using the momentum information of π^+

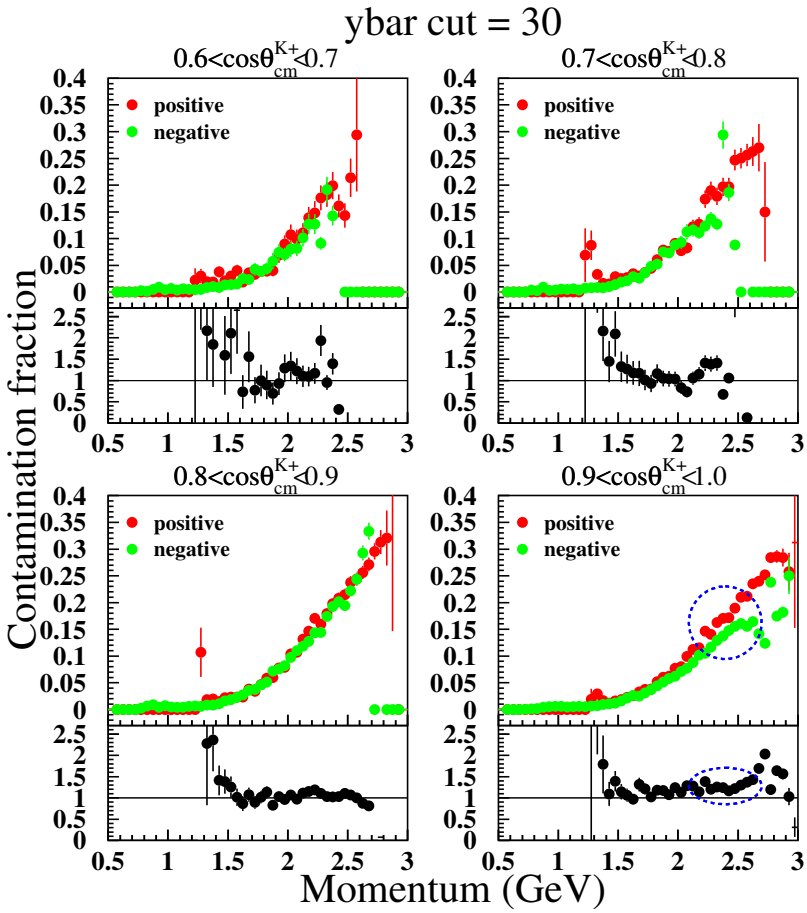

Figure 4.30: The upper parts in each sub-figure is the comparison of contamination fraction results of positive charged data with negative charged data with ybar cut = 30. The lower part shows the results of (the fraction for positive charged particles)/(the fraction for negative charged particles).

particles in this sample, the background template in $\mathrm{MM}_X(\gamma p, K^+)$ was constructed by assuming the kaon mass.

With this background template and Monte-Carlo simulated shapes of $\mathrm{MM}_X(\gamma p, K^+)$ for the Λ and Σ^0 productions in the same $\{|\vec{P}|,\ E_\gamma,\ \cos\theta^{K^+}_{c.m.}\}$ bin, the normalization of background template was obtained by fitting the experimental $\mathrm{MM}_X(\gamma p, K^+)$ data in the mass range of 1.0-1.26 GeV/c^2. The ranges of $|\vec{P}|$, E_γ, and $\cos\theta^{K^+}_{c.m.}$ kinematic variables are 0-3 GeV/c, 1.5-3.0 GeV and 0.6-1.0, respectively.

Fig. 4.33 shows the examples of side-band fitting in $0.9 < \cos\theta^{K^+}_{c.m.} < 1.0$, and $2.8 < E_\gamma < 2.9$ GeV for 10 momentum bins between 2.2 and 3.0 GeV/c.

After adjusting the normalization in each bin, we summed up the background templates over all the track momentum ($|\vec{P}|$) bins to obtain the combined background template in the $\{E_\gamma, \cos\theta^{K^+}_{c.m.}\}$ bin. The yields

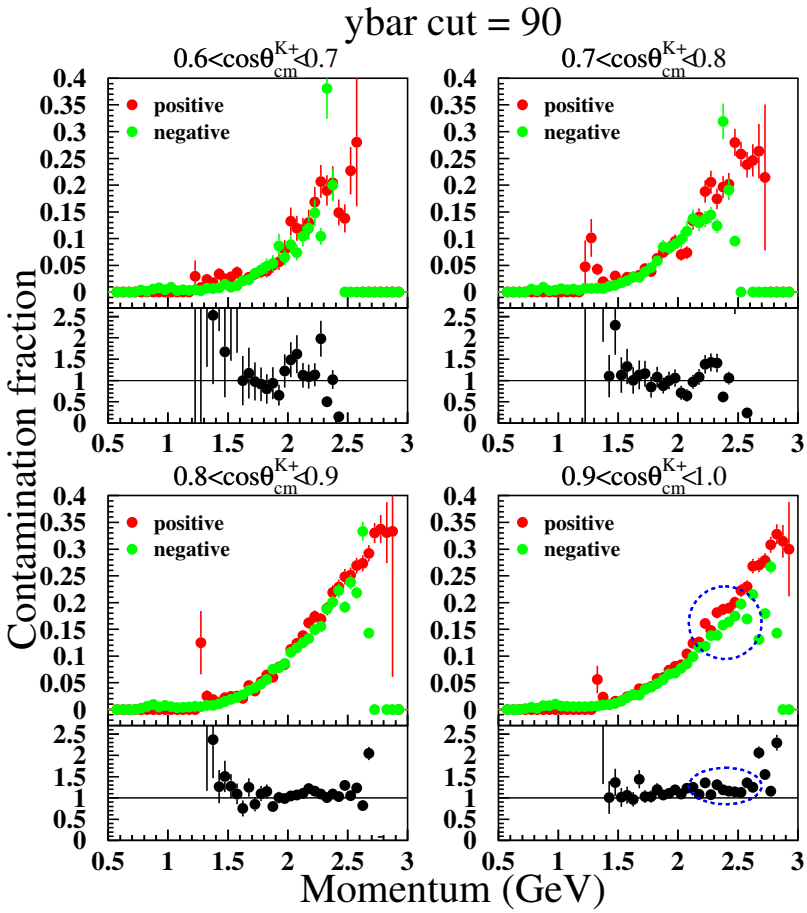

Figure 4.31: The upper parts in each sub-figure is the comparison of contamination fraction results of positive charged data with negative charged data with ybar cut = 90. The lower parts shows the results of (the fraction for positive charged particles)/(the fraction for negative charged particles).

of the $K^+\Lambda$ and $K^+\Sigma^0$ productions were extracted using another new fit of the missing mass spectrum with two Gaussian distributions with the constant centroids of their PDG values for the signals and the combined background template.

Fig. 4.34 shows the missing mass spectra from 1.0 to 1.6 GeV, where the missing mass through the signal region of the $K^+\Lambda$ and $K^+\Sigma^0$ events could be well fitted using two Gaussian distributions of signal (green dashed line for $K^+\Lambda$ and blue dashed-dotted line for $K^+\Sigma^0$) and the estimated background shape from the side-band method of the kaon PID regions (purple dotted line). The broad bump structure in the background under the Λ and Σ^0 peaks which is caused by the misidentification of π^+ in the $\gamma p \to \pi^+\Delta^0$ reaction could be observed clearly.

Fig. B.10 demonstrates the side-band fitting results at $\cos\theta^{K^+}_{c.m.}$=0.65,

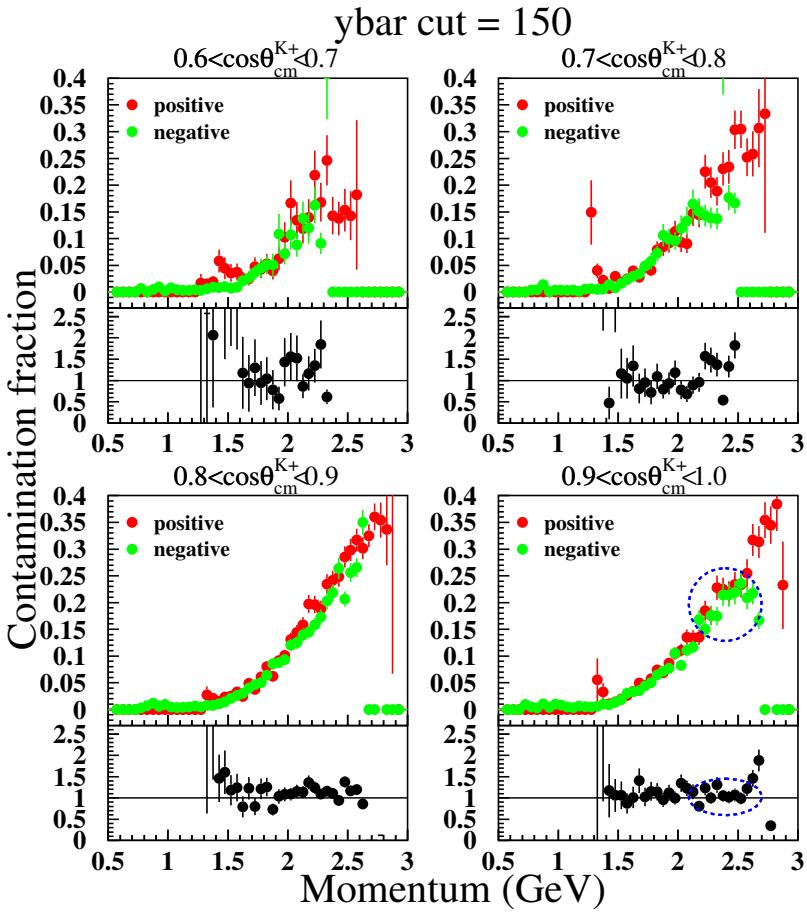

Figure 4.32: The upper parts in each sub-figure is the comparison of contamination fraction results of positive charged data with negative charged data with ybar cut = 150. The lower parts shows the results of (the fraction for positive charged particles)/(the fraction for negative charged particles).

E_γ=1.5-3.0 GeV. The red solid line, green, blue dotted line and the purple dotted line stand for the total fitting, Λ, Σ^0 peaks, and the background which also considered the $\gamma p \to \pi^+ n$ peak around missing mass equal to 0.9 GeV, respectively.

Since the missing-mass spectra across all bins are reasonably described, the contributions of signal and background could be reliably separated. The over all fittings are included in Appendix B.

4.4 Monte-Carlo

The Monte-Carlo simulation program is based on the GEANT3 software package [63]. The program called g3leps has been developed by LEPS collaboration [24]. The g3leps simulates the LEPS detectors with an event generator to generate the selecting reaction channel, the simulation of the response of each detector. For example, the energy loss

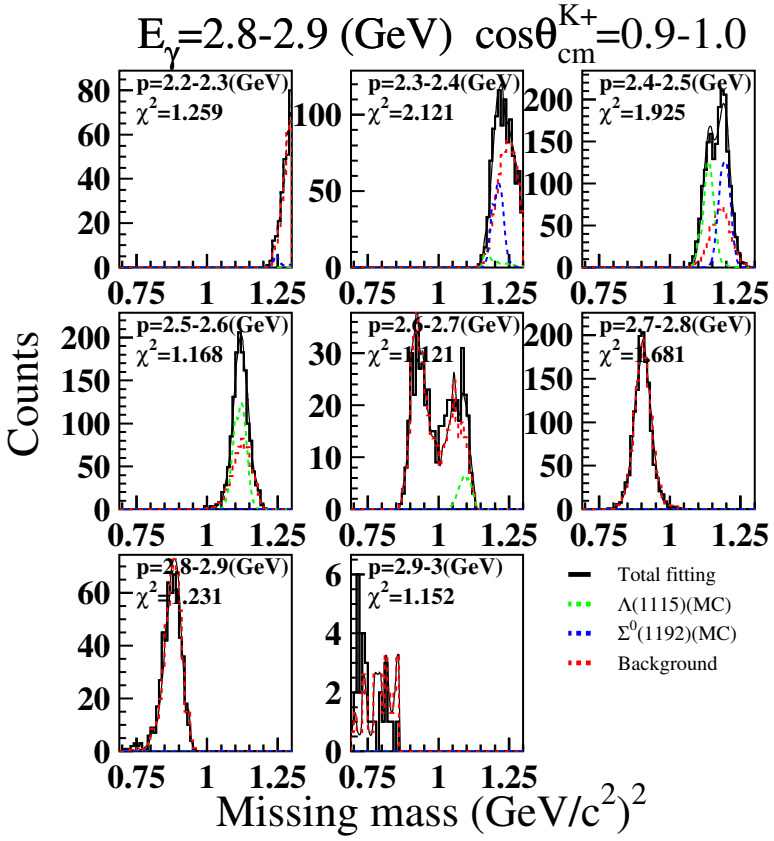

Figure 4.33: Side-band fitting in $0.9<\cos\theta^{K^+}_{c.m.}<1.0$, $2.8<E_\gamma<2.9$ GeV. The red dashed line shows the pion background, the green and blue dashed lines are the simulated Λ and Σ^0 shapes.

and multiple scattering for the produced particles are executed. After the simulation process finished, the output data with the same format of the experimental data are analysed in the same process with the experimental data. In order to simulate the real experimental apparatus, the resolutions of the SVTX, the DC's, the photon energy and the time-of-flight are considered with Gaussian distributions by assuming the realistic values. The Monte-Carlo simulation program was provided by Kohri-san, it is available on IPAS data storage at

`/sp8data3/shshiu/g3lepsk/asymk2`

It is noted that in this analysis, the parameter of time-of-flight resolution (numResoToF) of each TOF channel was set to 140 ps based on the discussion in sec. 4.2.1.

In this analysis, we heavily relied on Monte-Carlo simulation to get the $\mathrm{MM}_X(\gamma p, K^+)$ for the Λ and Σ^0 productions to estimate the

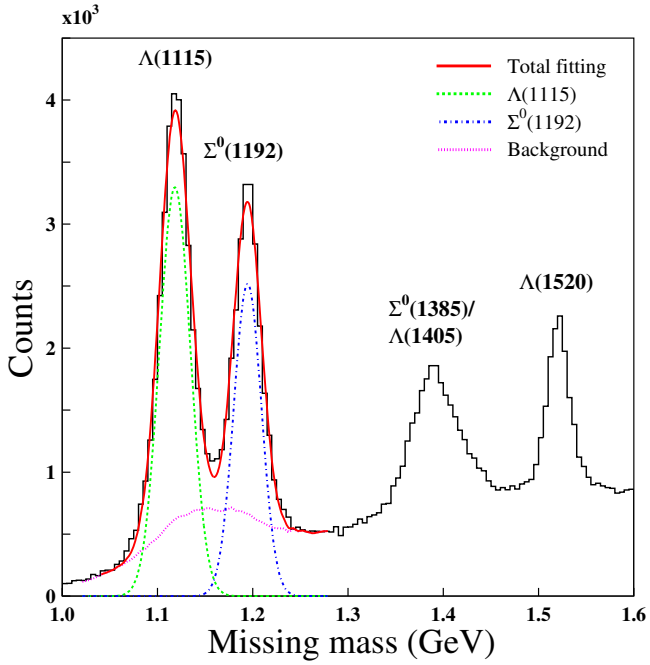

Figure 4.34: Missing mass spectrum of $\gamma p \to K^+ X$ reaction ($\mathrm{MM}_X(\gamma p, K^+)$) at E_γ=1.5-3.0 GeV.

background template. To make sure the fitting of $\mathrm{MM}_X(\gamma p, K^+)$ is valid, Monte-Carlo events of Λ and Σ^0 photoproduction were generated, and the consistency between MC events and real data in the missing mass spectra of K^+ were checked. The checked results for all $\cos\theta^{K^+}_{c.m.}$ and some of the E_γ bins are shown in Fig. 4.36a(E_γ=1.55 GeV), 4.36b(E_γ=1.95 GeV), 4.36c(E_γ=2.45 GeV), and 4.36d(E_γ=2.95 GeV). The green and blue solid line stand for the simulated Λ and Σ^0 shapes, respectively, overlaid with the solid black real data. The overall E_γ bins are shown in Appendix C.

For the calculation of cross sections, the K^+ detection efficiency and acceptance were estimated based on Monte-Carlo simulations by assuming a uniform production of $K^+\Lambda$ and $K^+\Sigma^0$ in E_γ and $\cos\theta^{K^+}_{c.m.}$.

Other possible background sources are the photoproduction of ϕ mesons and the non-resonant $\mathrm{K^+}$-$\mathrm{K^-}$-p events. The charged kaons produced from both the channels were also checked by Monte-Carlo simulation. From Fig. 4.37 , the missing mass distribution for ϕ production is above 1.5 GeV/c^2 and for non-resonant $\mathrm{K^+}$-$\mathrm{K^-}$-p is above 1.26 GeV/c^2. Therefore they do not constitute a background in the signal region of interest for the Λ and Σ^0 productions.

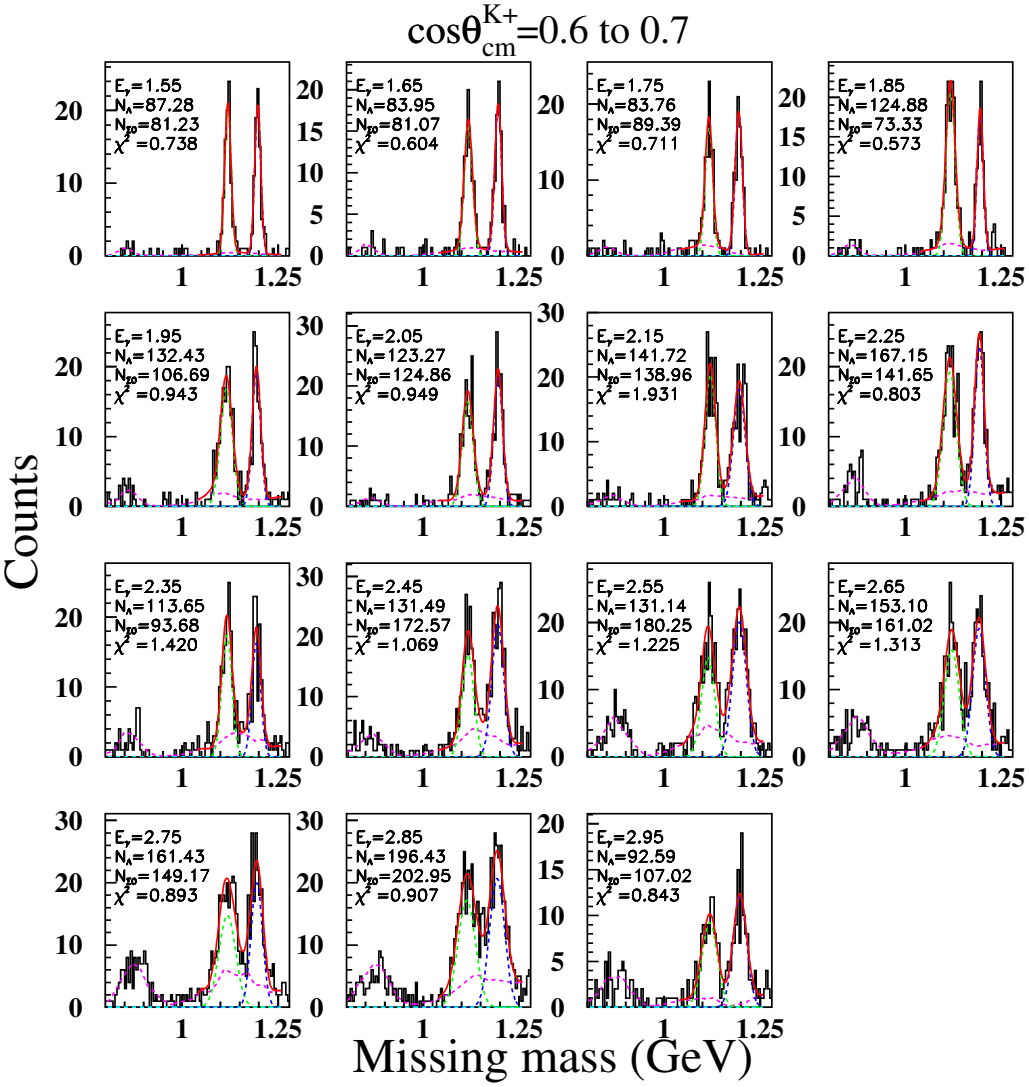

Figure 4.35: Side-band method fitting results at $\cos\theta^{K^+}_{c.m.}$=0.65, E_γ=1.5-3.0 GeV.

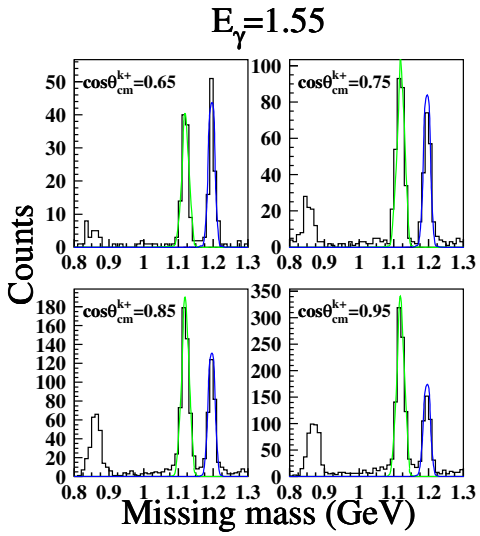

(a) The missing mass comparison of the generated MC events and real data at E_γ=1.55 GeV.

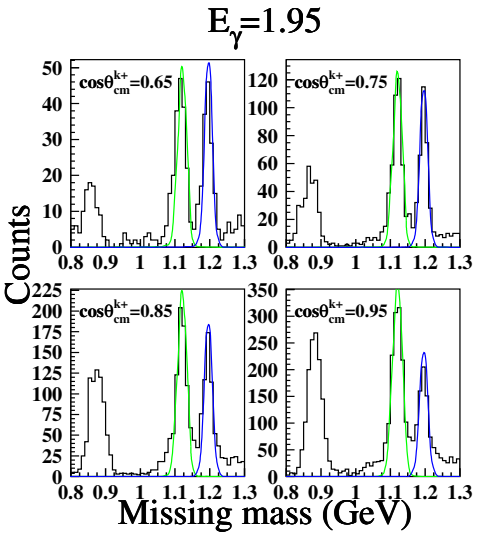

(b) The missing mass comparison of the generated MC events and real data at E_γ=1.95 GeV.

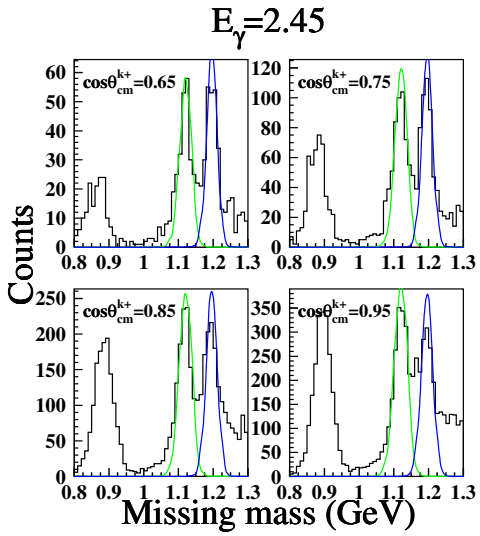

(c) The missing mass comparison of the generated MC events and real data at E_γ=2.45 GeV.

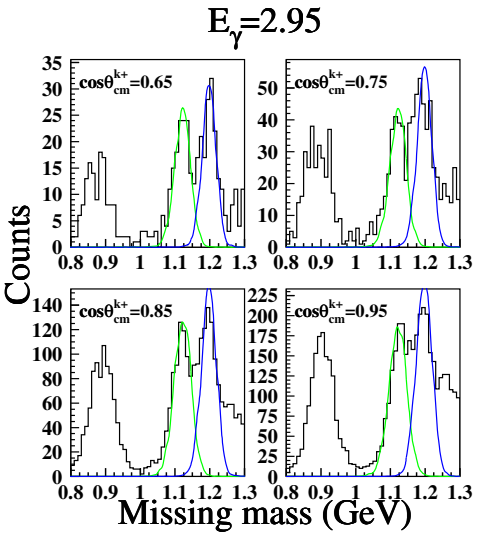

(d) The missing mass comparison of the generated MC events and real data at E_γ=2.95 GeV.

Figure 4.36: The missing mass comparison of the generated MC events and real data in various E_γ.

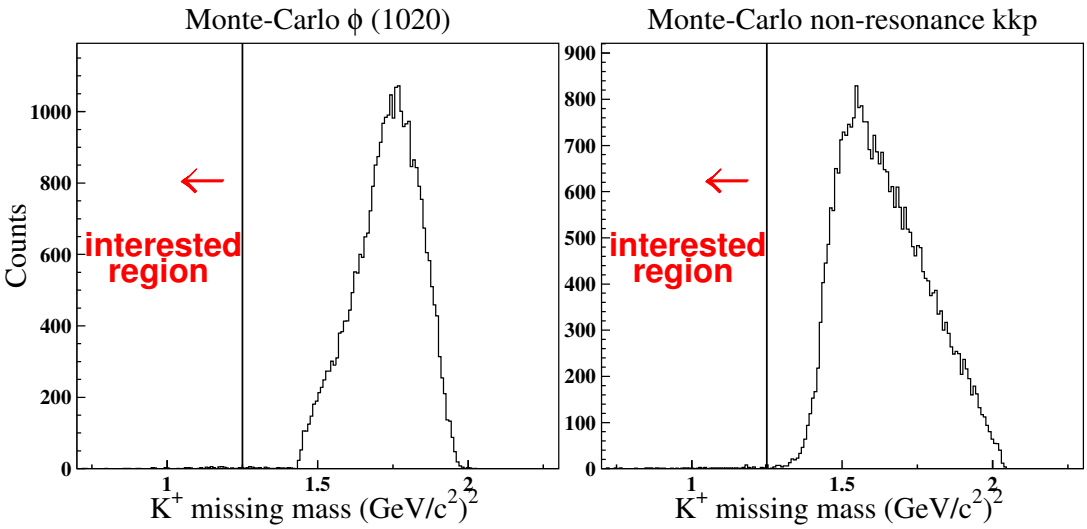

Figure 4.37: K^+ missing mass distribution of Monte-Carlo $\phi(1020)$ and non-resonant KKp events.

Chapter 5

Results and Discussions

This analysis aims at extracting the differential cross sections and photon-beam asymmetries for the photoproduction of $\gamma p \to K^+\Lambda$ and $K^+\Sigma^0$ via the K^+ detection mode.

The side-band methods to extract the yields of $K^+\Lambda$ and $K^+\Sigma^0$ are discussed in Sec 4.3.3. In this chapter the measurement and calculation of differential cross sections and the beam asymmetries will be explained in detail. The results compared to previous measurements and the theoretical calculations will also be shown. The estimation of systematic error associated with the determination of this analysis will be investigated. The physics discussion based on the measurement will also be described.

In this chapter, the calculation and results of differential cross sections and beam asymmetry will be described separately, at first. The discussion of the estimation of systematic error will be shown in the next. In the final section of this chapter, the physics discussion will be presented.

5.1 Differential cross sections

5.1.1 Calculation of differential cross sections

In each kinematic bin of E_γ (15-bins) and $\cos\theta^{K^+}_{c.m.}$(4-bins), the cross sections for the $K^+\Lambda$ and $K^+\Sigma^0$ photoproductions were obtained using the measured yields, the integrated photon flux from the tagger, liquid target density, the tagger correction factors for the K^+ detection, transmission probability, and the photon tagging correction factors. The K^+ detection efficiencies for $K^+\Lambda$ and $K^+\Sigma^0$ channels were estimated by Monte-Carlo simulations assuming a uniform production of $K^+\Lambda$ and

$K^+\Sigma^0$ in each E_γ and $\cos\theta^{K^+}_{c.m.}$.

The differential cross sections are calculated as,

$$\frac{d\sigma}{dcos\theta^{K+}_{c.m.}} = N_K/N_\gamma/N_t/dcos\theta^{K+}_{c.m.}. \tag{5.1}$$

Here the N_t is the number of protons in the liquid hydrogen target. The N_t has been calculated via the function below.

$$N_t = 0.0708\,[g/cm^3]\times 16\,[cm]\times 6.022\times 10^{23} = 6.822\times 10^{23}\,[protons/cm^2] \tag{5.2}$$

The density of target is $0.0708 g/cm^3$, and the target thickness is $16 cm$. The number of hydrogen nuclei in a unit area is $6.822\times 10^{23} protons/cm^2$

The N_γ denotes the number of photons which was described in [61]. The following function considered the probability of only one tagger hit ($fntag$), target transmission probability, and the tagger correction factor as,

$$N_\gamma = N'_\gamma \cdot P_{ntag=1} \cdot T \cdot C_{tagger}. \tag{5.3}$$

Where N'_γ is the number of measured photons by the tagger. $P_{ntag=1}$ which stands for the probability for having $fntag = 1$ is about 95%. The probability of $fntag = 1$ was obtained for events with all cuts except for $fntag = 1$. The T which is the transmission probability of photon beam from the straight section to the target is 0.526. The C_{tagger} is the tagger correction factor. The photon beam energy decided by the tagger counter is not smooth in the current E_γ bin size and make the E_γ distribution fluctuate. For getting smooth cross sections, the tagger correction factor was applied. The tagger correction factor was obtained by the analysis of tagger fibers, and the details were discussed in Ref. [65].

Simply steps to calculate the tagger correction factor are summarized below. First, the number of events for each tagger fiber for both forward and backward fibers is counted and normalized to 1. Second, the weighted normalized fiber number of each E_γ bin is counted. The weight factors are listed as follows,

$$weight_{front} = 0.0366 - 2 \times 1.91 \times 10^{-4} \times (ff) + 3 \times 7.06 \times 10^{-7} \times (ff)^2 \tag{5.4}$$

$$weight_{back} = 0.0367 - 2 \times 1.93 \times 10^{-4} \times (fb) + 3 \times 7.10 \times 10^{-7} \times (fb)^2 \tag{5.5}$$

The ff and fb denote the number of front tagger fibers and number of back tagger fibers in the tagging system. Third, the average of forward and backward weighted normalized fiber number of each E_γ bin is calculated. Finally, the normalized results of last step are the correction factor. The tagger correction factor results are shown in Fig. 5.1, the N_K is the yield of $K^+\Lambda$ or $K^+\Sigma^0$ divided by the spectrometer acceptance with the selection conditions and kaon graphic cut described in section 4.1.

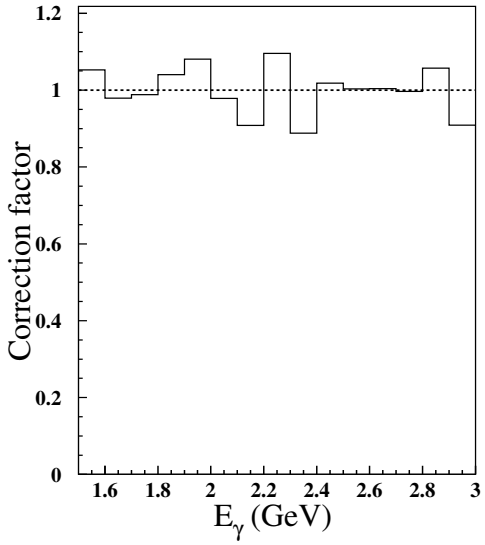

Figure 5.1: The tagger correction factor as a function of E_γ.

The acceptance was evaluated by the Monte-Carlo simulation. The detail about the checking of acceptance efficiency is described in Appendix D. The acceptance for $K^+\Lambda$ and $K^+\Sigma^0$ is shown in Fig. 5.2 and Fig. 5.3, respectively.

The yields of the $K^+\Lambda$ and $K^+\Sigma^0$ channels were extracted by a fitting of the missing mass spectrum with two Gaussian distribu-

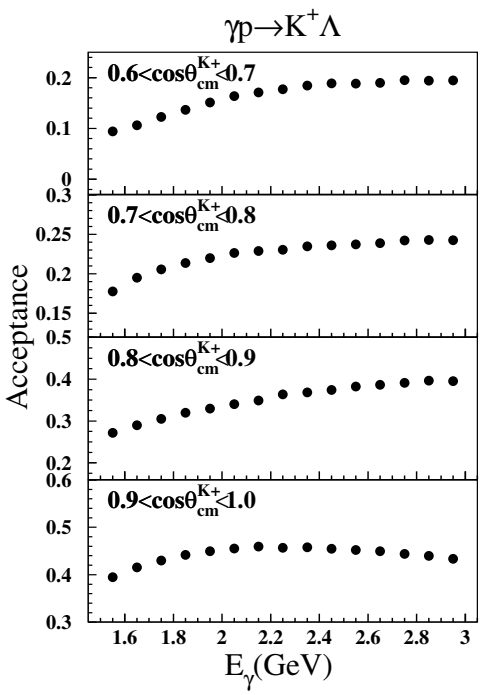

Figure 5.2: Acceptance of $K^+\Lambda$ as a function of E_γ in various $\cos\theta^{K^+}_{c.m.}$ bins.

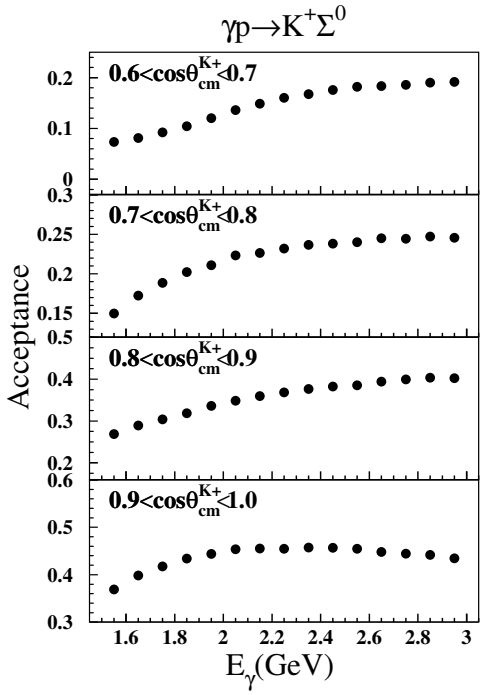

Figure 5.3: Acceptance of $K^+\Sigma^0$ as a function of E_γ in various $\cos\theta^{K^+}_{c.m.}$ bins.

tions for the interested signals and the combined background template. Fig. 5.4, 5.5 show the yields of $K^+\Lambda$ and $K^+\Sigma^0$ as a function of E_γ with various $\cos\theta^{K^+}_{c.m.}$. Due to the detector acceptance, the yields of $K^+\Lambda$ and $K^+\Sigma^0$ show a significant increasing trend when the $\cos\theta^{K^+}_{c.m.}$ becomes forward. Since the maximum energy of a BCS photon (Compton edge) in this experiment is 2.97 GeV, the yields between 2.9-3.0 GeV show a significant drop compare to other energy bins in each $\cos\theta^{K^+}_{c.m.}$ region.

The summary of the differential cross sections calculation is listed in Tab. 5.1.

5.1.2 Results of differential cross sections

The differential cross sections for the $K^+\Lambda$ channel are shown in Fig. 5.6 as a function of E_γ with various $\cos\theta^{K^+}_{c.m.}$ bins, in Fig. 5.8 as a function of $\cos\theta^{K^+}_{c.m.}$ with various E_γ bins. Corresponding results are shown for the $K^+\Sigma^0$ channel in Fig. 5.7 and Fig. 5.9.

Fig. 5.6 shows that the differential cross sections for the $K^+\Lambda$ channel decrease monotonically when the beam energy increases in all four bins of $\cos\theta^{K^+}_{c.m.}$ regions. In Fig. 5.7, the decreasing trend of the cross sections is relatively mild for the $K^+\Sigma^0$ channel compared with the $K^+\Lambda$

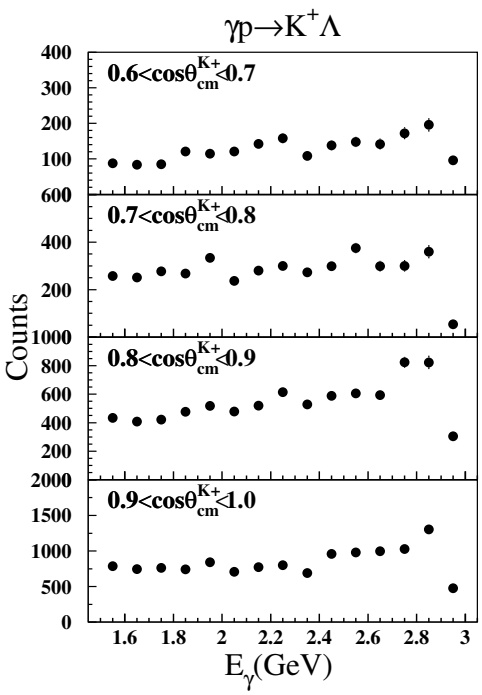

Figure 5.4: The yields of $K^+\Lambda$ as a function of E_γ in various $\cos\theta^{K^+}_{c.m.}$ bins.

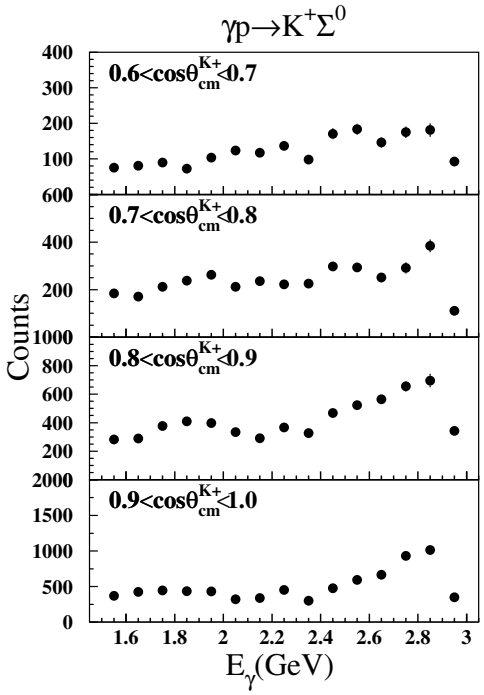

Figure 5.5: The yields of $K^+\Sigma^0$ as a function of E_γ in various $\cos\theta^{K^+}_{c.m.}$ bins.

Table 5.1: Summary of the calculations of differential cross sections

Number of Target (N_t) :
$N_t = 6.822 \times 10^{23}$ protons/cm^2
Probability of $fntag = 1$ ($P_{ntag=1}$) :
$P_{ntag=1}$=0.95
Transmission (T) :
T=0.526

E_γ (GeV)	C_{tagger}	N_γ ($\times 10^{10}$)
1.5-1.6	1.053	2.250
1.6-1.7	0.979	2.214
1.7-1.8	0.988	2.197
1.8-1.9	1.041	2.204
1.9-2.0	1.081	2.218
2.0-2.1	0.978	2.278
2.1-2.2	0.908	2.344
2.2-2.3	1.096	2.457
2.3-2.4	0.888	2.606
2.4-2.5	1.018	2.779
2.5-2.6	1.003	2.972
2.6-2.7	1.004	3.240
2.7-2.8	0.997	3.540
2.8-2.9	1.057	3.923
2.9-3.0	0.909	4.016

channel. No obvious narrow resonance structure can be observed for both the reactions. The decreasing trend of cross sections in $K^+\Sigma^0$ channel compare with $K^+\Lambda$ channel is relatively mild and not signifi-

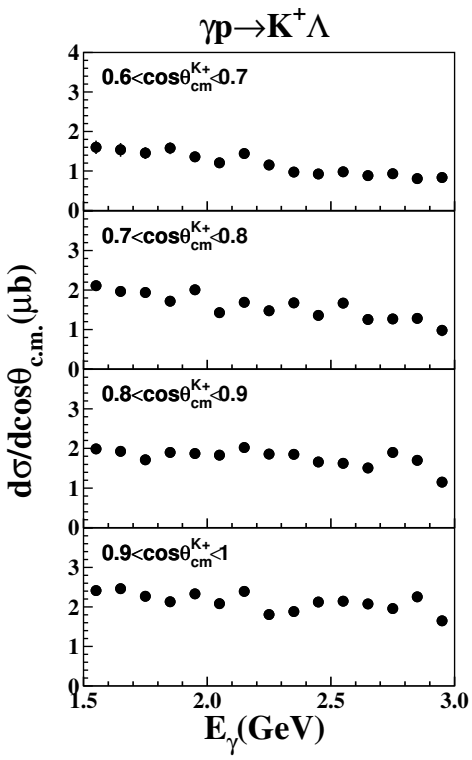

Figure 5.6: The cross sections of $K^+\Lambda$ as a function of E_γ.

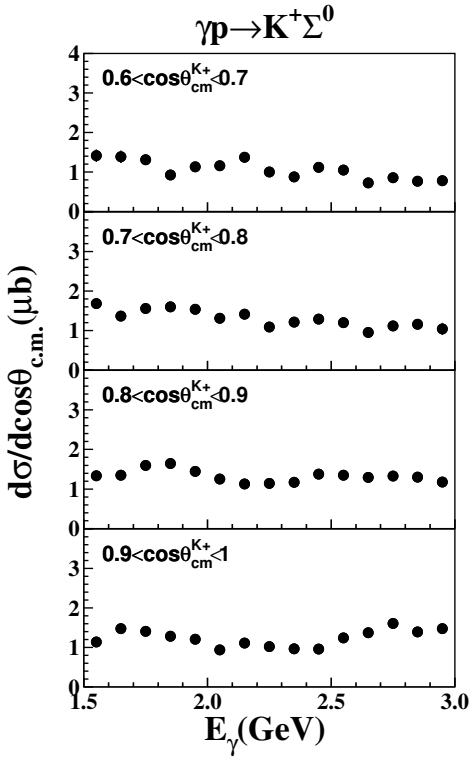

Figure 5.7: The cross sections of $K^+\Sigma^0$ as a function of E_γ.

cant.

Fig. 5.8 and Fig. 5.9 show the angular dependence of the differential cross sections for the $K^+\Lambda$ and $K^+\Sigma^0$ channels.

The differential cross sections for the $K^+\Lambda$ channel increase as the K^+ angle becomes forward. Forward peaking behaviour of the cross sections is observed, which indicates a strong t-channel contribution.

On the other hand, the angular dependence of the cross sections for the $K^+\Sigma^0$ reaction is relatively small and close to flat especially in the low energy regions. The t-channel contribution is inferred to be less dominant for the $K^+\Sigma^0$ channel. Although obvious peak or bump structures are not observed in the cross sections for the K+Sigma0 channel, there might be non-negligible s-channel contributions.

5.2 Beam asymmetry (Σ_γ)

5.2.1 Calculation of beam asymmetry (Σ_γ)

In this analysis, like the differential cross sections, the photon-beam asymmetries were determined as a function of E_γ in lab frame and $\cos\theta^{K^+}_{c.m.}$ in C.M. frame. The Fig. 5.10 shows the definition of angles

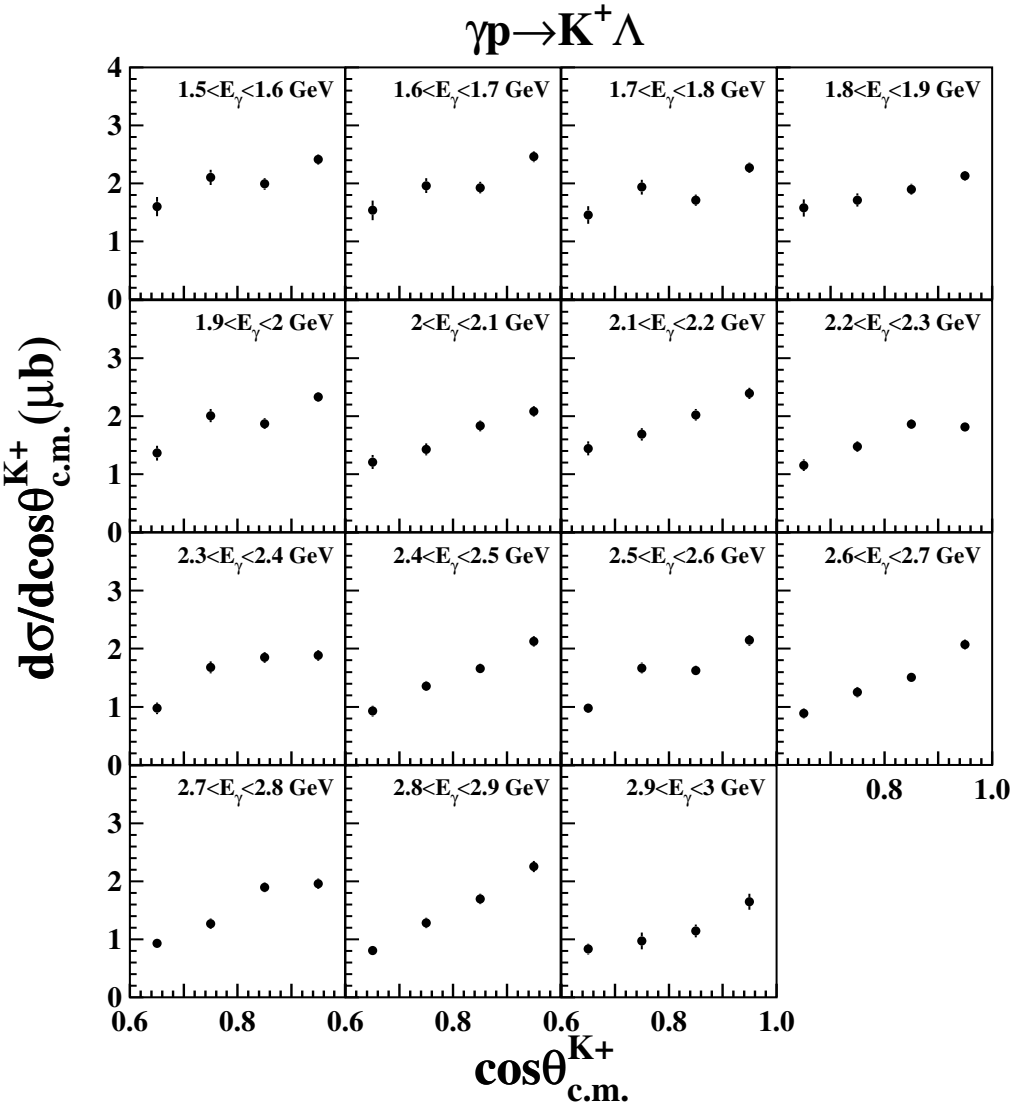

Figure 5.8: The cross sections of $K^+\Lambda$ as a function of $\cos\theta^{K^+}_{c.m.}$.

of ϕ and $\theta^{K^+}_{c.m.}$ that are used to determine the beam asymmetry.

To calculate the beam asymmetry, the discussion should be started from the differential cross sections of the kaon photoproduction for different types of linearly polarized photons.

The differential cross sections of the kaon photoproduction for linearly polarized photons in the vertical (v) and horizontal (h) directions are described as,

$$\frac{d\Omega}{d\Omega_v} = \frac{d\Omega}{d\Omega_{unpol}} \left[1 + P\Sigma_\gamma \cos\left(2\phi_{K^+}\right)\right], \tag{5.6}$$

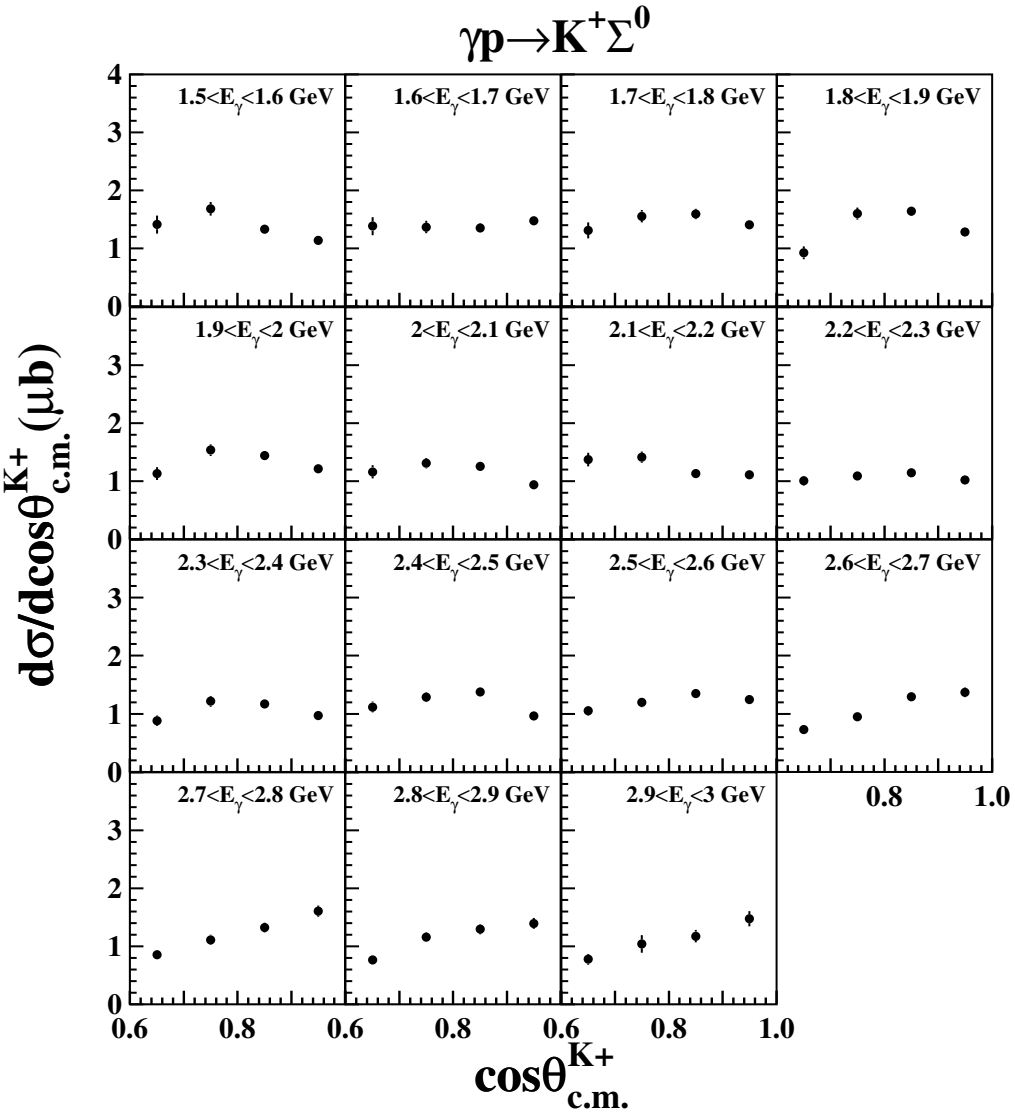

Figure 5.9: The cross sections of $K^+\Sigma^0$ as a function of $\cos\theta^{K^+}_{c.m.}$.

$$\frac{d\Omega}{d\Omega_h} = \frac{d\Omega}{d\Omega_{unpol}}\left[1 - P\Sigma_\gamma \cos\left(2\phi_{K^+}\right)\right]. \tag{5.7}$$

Here the P stands for the polarization of the BCS photons, and the Σ_γ is the photon-beam asymmetry. The ϕ_{K^+} is the K^+ azimuthal production angle. The polarization of the BCS photons is listed in Tab. 5.2.

The photon-beam asymmetry can be obtained by using vertically and horizontally polarized photons. The relation between the production yields and the photon-beam asymmetry is

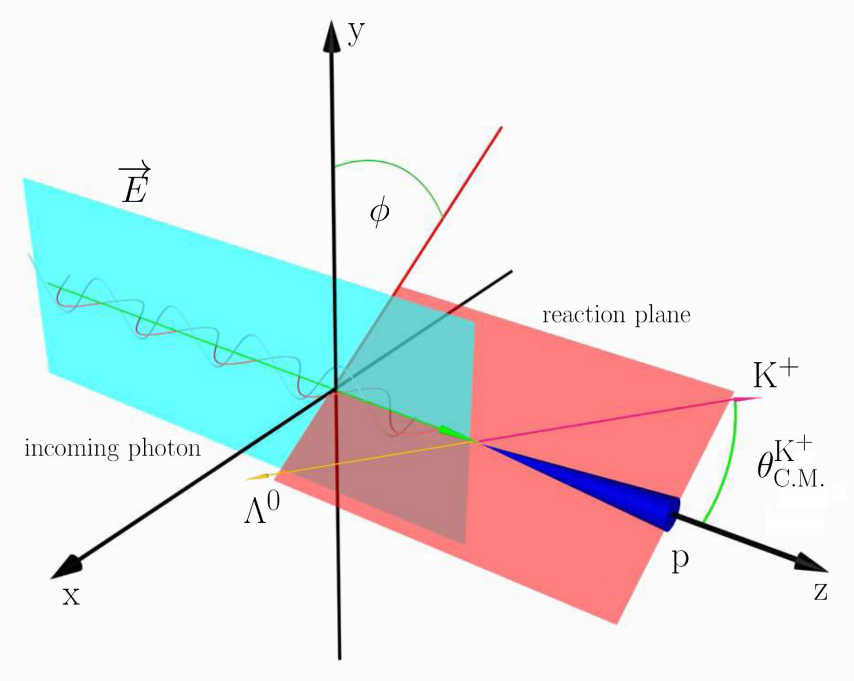

Figure 5.10: The definition of angles ϕ and $\theta^{K^+}_{c.m.}$ that are used to determine the beam asymmetry. The ϕ is the kaon azimuthal angle. The angle $\theta^{K^+}_{c.m.}$ is the kaon polar angle. This plot was taken from [87].

Table 5.2: List of polarization in different E_γ

E_γ	Polarization
1.8-2.0 GeV	0.516
2.0-2.2 GeV	0.639
2.2-2.4 GeV	0.746
2.4-2.6 GeV	0.826
2.6-2.8 GeV	0.876
2.8-3.0 GeV	0.898

$$\frac{n \cdot N_v - N_h}{n \cdot N_v + N_h} = P\Sigma_\gamma \cos(2\phi_{K^+}) \tag{5.8}$$

The N_v and N_h are the K^+ photoproduction yields with vertically and horizontally polarized photons, respectively. The n is the normalization factor defined by the number of photons ($n = n_h/n_v = 1.014$). Fig. 5.11 and Fig. 5.12 show the ratio of $(n \cdot N_v - N_h)/(n \cdot N_v + N_h)$ as a function of ϕ_{K^+} in E_γ=2.6-2.8 GeV for both the channels as examples. From Fig. 5.11 and Fig. 5.12, the ratio of $(n \cdot N_v - N_h)/(n \cdot N_v + N_h)$ shows a positive value around 0°, 180°, and 360°, and the ratio shows a negative value around 90° and 270°. Considering the function 5.8, the Σ_γ should be positive. The positive sign here indicates that the K^+ from

$K^+\Lambda$ and $K^+\Sigma^0$ channels tend to emit in the orthogonal direction to the photon polarization. The ratio data near 90° and 270° in the backward region are out of the acceptance region, and will not be considered in the fitting.

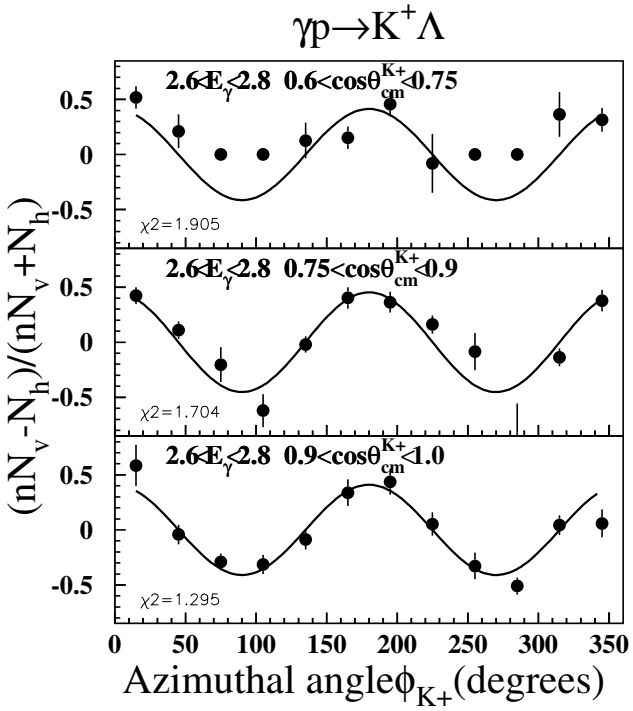

Figure 5.11: Azimuthal angle (ϕ_{K^+}) dependence of the ratio $(nN_{\rm V} - N_{\rm H})/(nN_{\rm V} + N_{\rm H})$ in Eq. 5.8 for the $K^+\Lambda$ channel at $E_\gamma = 2.6 - 2.8$ GeV and $\cos\theta^{K^+}_{c.m.} = 0.6 - 1.0$. The solid lines are the fit results using a function of $\cos 2\phi_{K^+}$.

5.2.2 Results of Photon-beam asymmetry (Σ_γ)

Fig. 5.13 and Fig. 5.14 show the photon beam asymmetry (Σ_γ) results for the $K^+\Lambda$ and $K^+\Sigma^0$ channels as a function of the center-of-mass kaon angle $\cos\theta^{K^+}_{c.m.}$. Fig. 5.15 shows the asymmetry results as a function of photon energy E_γ. The first obvious feature of the beam asymmetry results of $K^+\Lambda$ and $K^+\Sigma^0$ channel is positive values for the entire kinematic region. The beam asymmetry for $K^+\Sigma^0$ channel is potentially larger than that for $K^+\Lambda$ channel. In both reactions the beam asymmetries all decrease gradually with an increase of $\cos\theta^{K^+}_{c.m.}$while they increase gradually with photon energy.

5.3 Systematic error estimation

Systematic errors associated with the side-band analysis method were estimated based on two aspects. First, the systematic error origi-

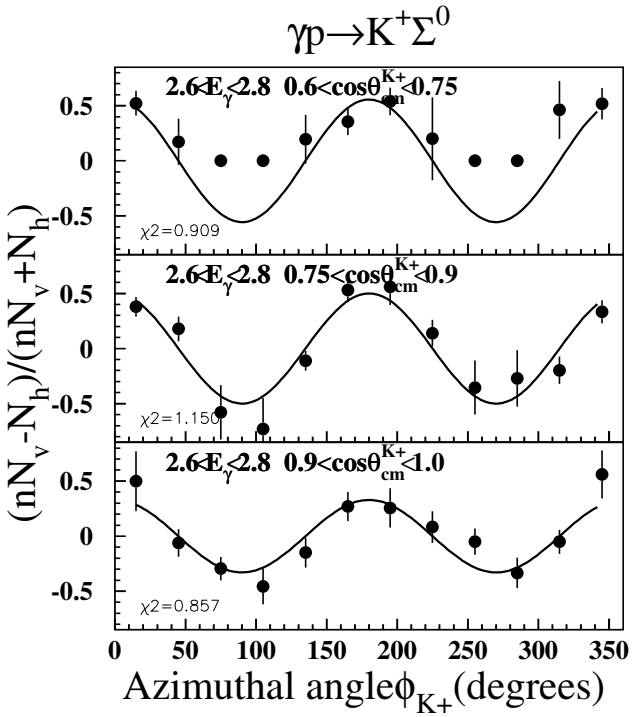

Figure 5.12: Azimuthal angle (ϕ_{K^+}) dependence of the ratio $(nN_{\rm V} - N_{\rm H})/(nN_{\rm V} + N_{\rm H})$ in Eq. 5.8 for the $K^+\Sigma^0$ channel at $E_\gamma = 2.6 - 2.8$ GeV and $\cos\theta^{K^+}_{c.m.} = 0.6 - 1.0$. The solid lines are the fit results using a function of $\cos 2\phi_{K^+}$.

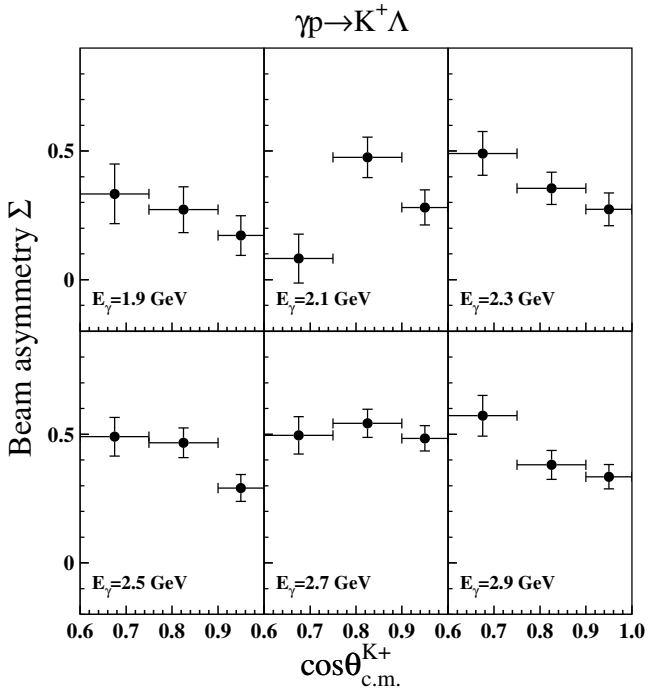

Figure 5.13: Photon-beam asymmetries (Σ_γ) for the $p(\gamma,K^+)\Lambda$ reaction as a function of $\cos\theta^{K^+}_{c.m.}$ for $1.8 < E_\gamma < 3.0$ GeV.

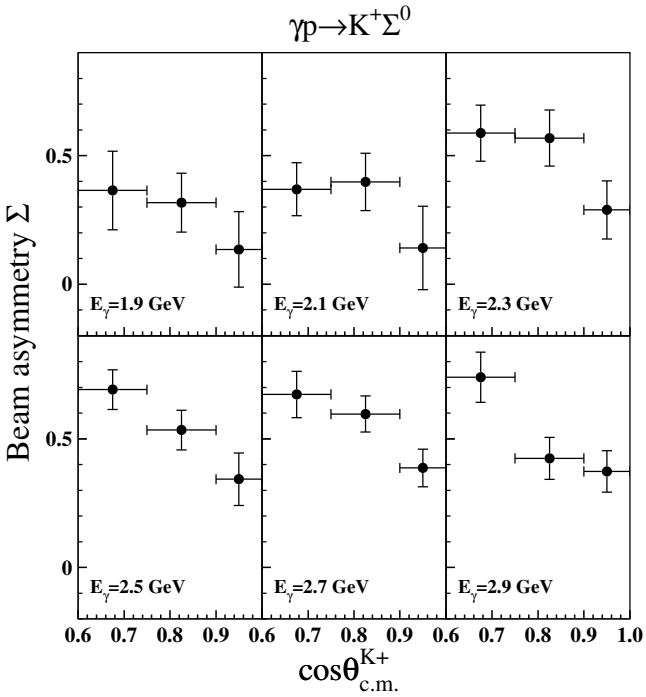

Figure 5.14: Photon-beam asymmetries (Σ_γ) for the $p(\gamma,K^+)\Sigma^0$ reaction as a function of $\cos\theta^{K^+}_{c.m.}$ for $1.8 < E_\gamma < 3.0$ GeV.

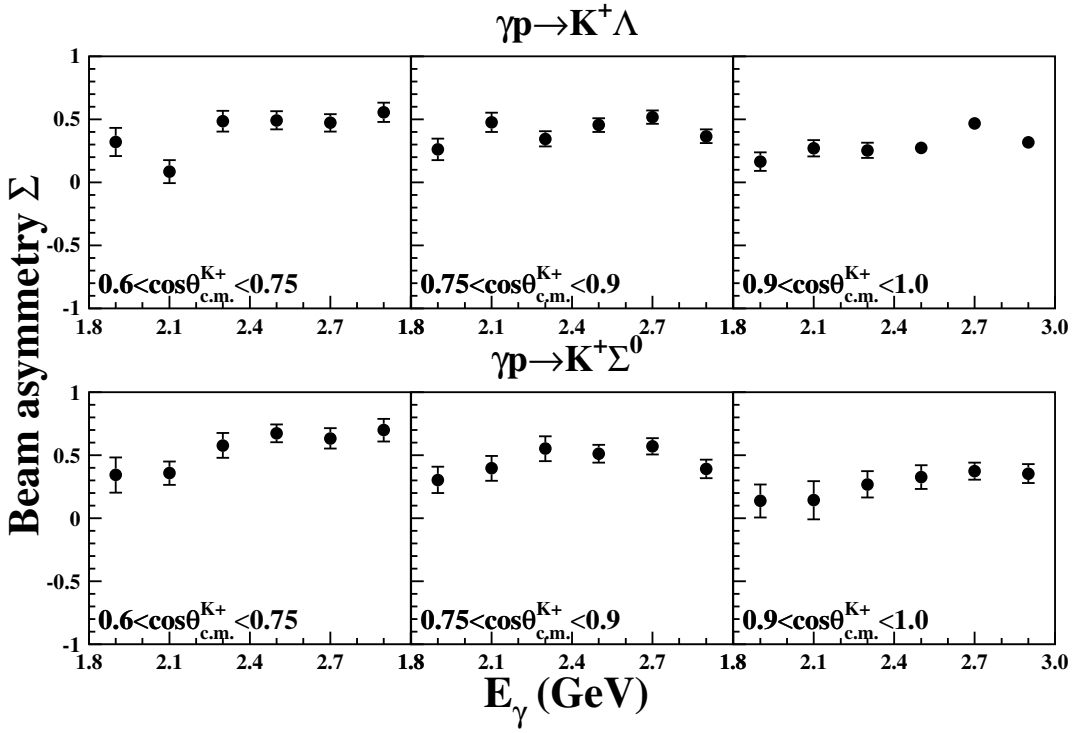

Figure 5.15: Photon-beam asymmetries (Σ_γ) for the $p(\gamma,K^+)\Lambda$ and $p(\gamma,K^+)\Sigma^0$ reactions as a function of photon energy $E_\gamma$for the kaon C.M. production polar angle $0.6 < \cos\theta^{K^+}_{c.m.} < 1.0$.

nated from the selection of pion region for background study. The second possible systematic error originated from the momentum slice size when we tried to get the contamination fraction by fitting the missing mass for the K^+ ($\mathrm{MM}_X(\gamma p, K^+)$).

The first systematic error originated from the selection of pion region for background study because of positron contamination. Since both the positron contamination fraction in our background pion data, and the K^+ contamination in pion data can not be addressed properly in MC, it is impossible to make a suitable cut to fix the background distribution. Various cut selections over all pion data graphic cut region were considered. The range of all the fitting results is considered to be the systematic uncertainty. Fig. 5.16 shows the schematic plot of the different cuts applied to pion graphic cut region for background study. The table Tab. 5.3 is the list of left and right boundaries of the mass square cut condition.

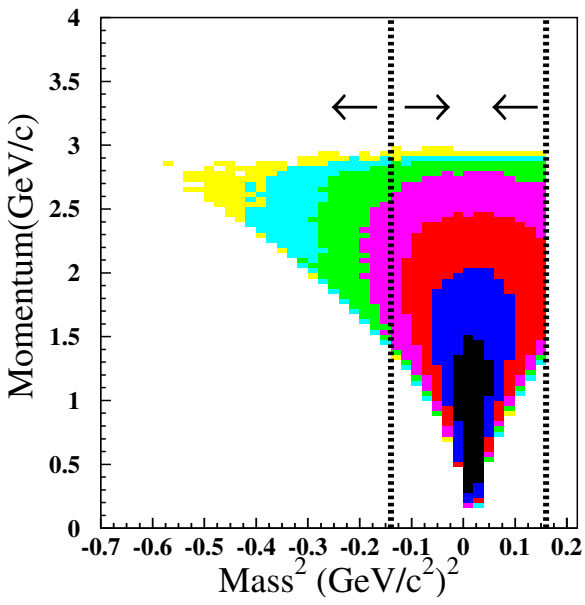

Figure 5.16: The schematic plot of the different cut over all pion data region. The left and right boundaries were changed.

The second systematic error originated from the bin size of momentum slice in obtaining the contamination fraction by the fit of the missing mass for the K^+ ($\mathrm{MM}_X(\gamma p, K^+)$). When the momentum slice

Table 5.3: List of left and right boundaries of the mass square cut conditions

mass square cut conditions	Left boundary (GeV^2)	Right boundary (GeV^2)
Condition 1	0.06	0.16
Condition 2	−0.04	0.16
Condition 3	−0.14	0.16
Condition 4	−0.7	0.16
Condition 5	−0.7	0.11
Condition 6	−0.7	0.06
Condition 7	−0.7	0.01
Condition 8	−0.7	−0.04

size become too large, the background distribution could not describe the real background well. In this analysis, the momentum slice size of 0.2, 0.15, 0.12, 0.1, 0.075, 0.05, 0.04, 0.0375, and 0.03 (the limit of momentum resolution) GeV were applied and systematic errors were estimated from the fluctuations.

5.4 Physics discussion

The differential cross sections for the $K^+\Lambda$ and $K^+\Sigma^0$ reactions as a function of photon beam energy E_γ in the range of $0.6 < \cos\theta^{K^+}_{c.m.} < 1.0$ are shown by black solid circles in Fig. 5.17. The error bars represent the statistical errors and the hatched area under each sub-figure represents the range of systematic uncertainty. The solid black line indicates the range of total errors. The theoretical predictions from the RPR model [66] with (RPR, solid red lines) and without resonances (RPR-Regge, dashed blue lines) as well as BG2014-02 solutions [67] of Bonn-Gatchina (BG) models (dot-dashed green lines) are overlaid for comparison. It is noted that the RPR-2011 solutions [72] for $K^+\Lambda$ and RPR-2007 solutions [71] for $K^+\Sigma^0$ are used.

The Regge-Plus-Resonance (RPR,RPR-Regge) model [70, 71, 72, 66] has been developed by the group at the University of Ghent. This model starts from considering the non-resonance contributions by two Reggeized t-channel exchanges in constant or rotation phase described by K and K^* Regge trajectory as background. After fixing the fitting results from the forward angle and high energy region cross sections and polarization data with only three fit parameters, the resonance contributions in s-channels are then added to the extrapolation background in the resonance regions. In the following discussions, the RPR stands

for the full fitting model with t- and s-channel considerations. The RPR-Regge stands for the model only consider the Reggeized t-channel exchanges for contrast.

The BG model by Bonn-Gatchina group [75], which is the result of coupled channels partial-wave analysis by considering $K^+\Lambda$, $K^+\Sigma^0$, $K^0\Sigma^+$, $\pi^- N$, and $p\eta$ photoproduction observables. The partial-wave analysis is based on the "operator expansion method" described in [74] which projects the t- and u-channel exchange amplitudes into s-channel partial waves.

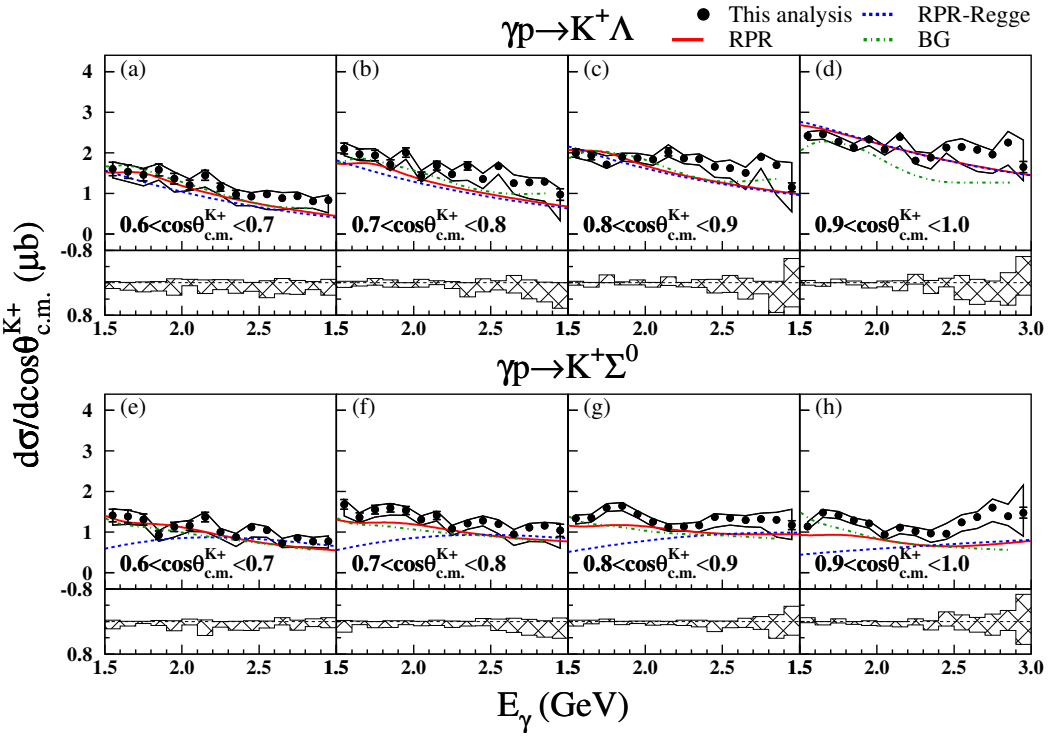

Figure 5.17: Differential cross sections for the $p(\gamma,K^+)\Lambda$ reaction (a)∼(d) and for $p(\gamma,K^+)\Sigma^0$ reaction (e)∼(h) as a function of photon energy E_γ for the kaon C.M. production polar angle $0.6 < \cos\theta^{K^+}_{c.m.} < 1.0$. The curves denote the predictions of Regge-model [66] calculation with (RPR, solid red lines) and without resonances (RPR-Regge, dashed blue lines), and Bonn-Gatchina model (BG, dot-dashed green lines). The hatched histograms indicate the systematic uncertainty. The solid black line indicates the range of total errors.

Within the consideration of systematic uncertainty, the differential cross sections for the $K^+\Lambda$ channel decrease steadily with increasing the beam energy in all four bins of $0.6 < \cos\theta^{K^+}_{c.m.} < 1.0$. No distinct narrow resonance structure is observed. The cross sections for the $K^+\Lambda$ channel are potentially larger than those for the $K^+\Sigma^0$ channel. The cross sections for the $K^+\Sigma^0$ channel also decrease with increasing the beam

energy whereas its energy dependence is relatively mild compared to the $K^+\Lambda$ channel. The mild energy dependence for the $K^+\Sigma^0$ channel is inferred to be due to non-negligible s-channel contributions. Although there is no distinct narrow structure in the $K^+\Sigma^0$ cross sections, some structures are seen at E_γ ~1.8 GeV and 2.8 GeV ($\sqrt{s}$ ~2.06 GeV and 2.47 GeV, respectively) at $\cos\theta^{K^+}_{c.m.}$=0.7-1.0. These structures have also been observed by CLAS at $\cos\theta^{K^+}_{c.m.}$=0.9 [28, 31]. Fig. 5.18 shows the results of cross sections by CLAS with the brown dashed circle to indicate the observed structures.

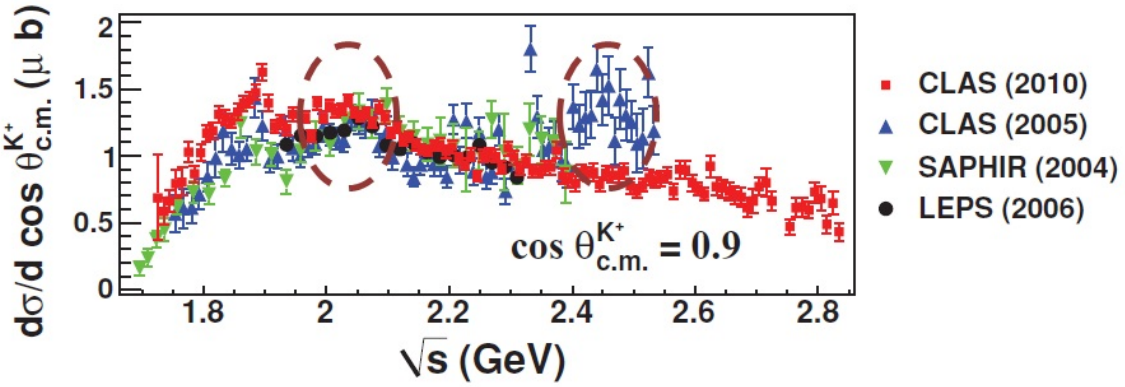

Figure 5.18: The cross sections results from CLAS 2010 [31] at $\cos\theta^{K^+}_{c.m.}$=0.9. The brown dashed circle indicates the observed structures close to $\sqrt{s}$ ~2.06 GeV and 2.47 GeV (E_γ ~1.8 GeV and 2.8 GeV).

Fig. 5.17 shows that the RPR and BG models can describe the cross sections data for the $K^+\Lambda$ and $K^+\Sigma^0$ reactions for 0.6 <$\cos\theta^{K^+}_{c.m.}$< 0.7. For 0.7 <$\cos\theta^{K^+}_{c.m.}$< 0.9, in the lower E_γ region, both models can give a good description of the $K^+\Lambda$ data but fail in the higher E_γ. The RPR calculation provides a better prediction of the cross sections data for 0.9 <$\cos\theta^{K^+}_{c.m.}$< 1.0 than the BG mmodel. Both the RPR and BG models underestimate the $K^+\Sigma^0$ data for 0.7 <$\cos\theta^{K^+}_{c.m.}$< 1.0. The difference between the predictions of RPR (red solid lines) and RPR-Regge (blue dashed lines) indicates the contributions of nucleon resonances in the s-channel in the $K^+\Sigma^0$ production at E_γ< 2.2 GeV.

Before starting to discuss the differential cross sections as a function of $|t-t_{min}|$ in $K^+\Lambda$ and $K^+\Sigma^0$ channels, it is worth discussing the Regge based calculation. It is expected that s-channel resonance is a significant component in the $K^+\Lambda$ and $K^+\Sigma^0$ reactions. It is interesting to see how

a model without such component works. The model of Guidal, Laget, and Vanderhaeghen [83, 84] is such a model; this model considers only the two linear Regge trajectories corresponding to the vector K^* and the pseudovector K. The model fit to higher energy photoproduction data where there is no contribution of the s-channel exchanges.

Fig. 5.19, 5.20 from [83] show the forward differential cross sections for four E_γ for the $p(\gamma,K^+)\Lambda$ and $p(\gamma,K^+)\Sigma^0$ reaction.

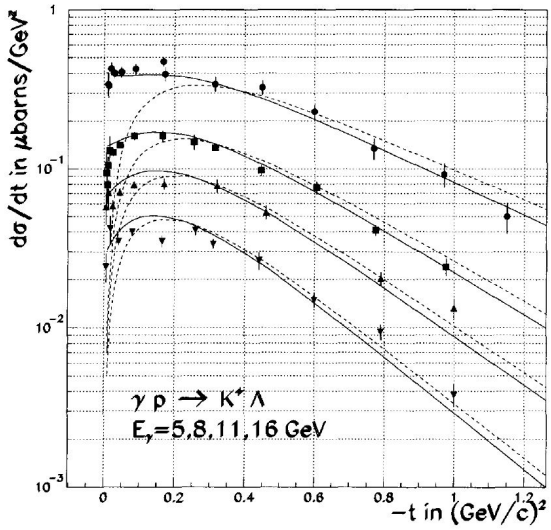

Figure 5.19: This figure is from [83]. Differential cross sections for the $p(\gamma,K^+)\Lambda$ reaction for four E_γ. Gauge invariant $K+K^*$ exchange model (full curves). K^*-exchange contribution (dashed curves).

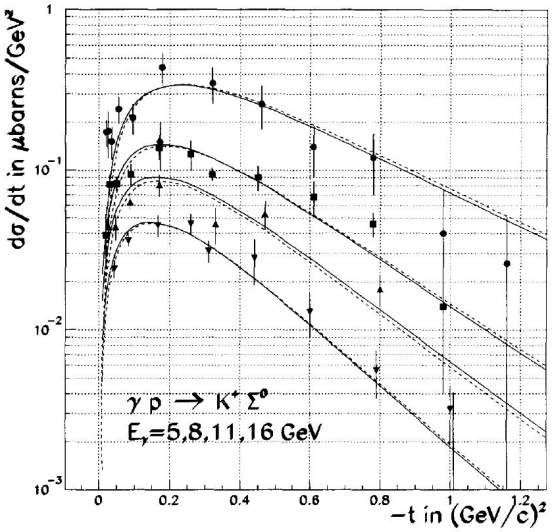

Figure 5.20: This figure is from [83]. Differential cross sections for the $p(\gamma,K^+)\Sigma^0$ reaction for four E_γ. Gauge invariant $K+K^*$ exchange model (full curves). K^*-exchange contribution (dashed curves).

In the larger $-t$ region, the main contributions to $K^+\Lambda$ production were described by the Reggeized K^* t-channel exchange and the differential cross sections were of an exponential shape in t-dependence but decreased quickly to zero at t=t_{min}. The plateau near t=t_{min} in the differential cross sections at E_γ=5 GeV was interpreted as due to the contributions of a Reggeized s-channel diagram which is necessitated to maintain the gauge invariance and only for the K exchange.

Except for the very forward region about $|t-t_{min}| \approx m_K^2$, i.e. 0.25 GeV^2, the K^*-exchange gives the main contribution to the cross sections. The lacking of similar plateau feature near t=t_{min} in $K^+\Sigma^0$ production is due to the relatively minor contribution of K-exchange arising from the weak coupling between K and Σ^0.

In figs. 5.21 and 5.22, the differential cross sections $(d\sigma/dt)$ are

shown as a function of the reduced four-momentum transfer $|t - t_{min}|$, for fifteen photon energy bins within E_γ=1.5-3.0 GeV. The cross sections with the form of $d\sigma/d\cos\theta^{K^+}_{c.m.}$ were transformed to those with the form $d\sigma/dt$. The t_{min} denotes the t at the production angle of zero degrees. To calculate the t for a two-body final state please refer to Fig. 1.10 where the two particles of momentum p_1 and p_2 and mass m_1 and m_2 scatter to particles of momentum p_3 and p_4 and mass m_3 and m_4.

For here, the Lorentz-invariant Mandelstam variable t is defined by

$$t = (p_1 - p_3)^2 = m_1^2 - 2E_1E_3 + 2p_1 \cdot p_3 + m_3^2. \tag{5.9}$$

In the center-of-mass frame

$$t = (E_{1cm} - E_{3cm})^2 - (p_{1cm} - p_{3cm})^2 - 4p_{1cm}p_{3cm}sin^2(\frac{\theta_{cm}}{2}). \tag{5.10}$$

The t_{min} could be calculated via

$$t_{min} = [\frac{m_1^2 - m_3^2 - m_2^2 + m_4^2}{2\sqrt{s}}]^2 - (p_{1cm} - p_{3cm})^2. \tag{5.11}$$

Other than the theoretical predictions of the RPR and BG models, the previous results of LEPS 2006 [24] (red open squares), SAPHIR 2004 [22] (yellow open cross), CLAS 2006 [28] (blue open triangles), and CLAS 2010 [30, 31] (purple open triangles) are compared with the present results. Within the total uncertainties, the current results show a good agreement with previous measurements in overlapping kinematic regions. The present $K^+\Lambda$ results agree better with the CLAS2010 data [30] than the CLAS2006 data [28], while the present $K^+\Sigma^0$ results show a better agreement with the CLAS2006 data [28] than the CLAS2010 data [31].

In figs. 5.21 and 5.22, at the very forward angle regions, the t-dependence of differential cross sections for $K^+\Lambda$ and $K^+\Sigma^0$ have very different features.

At low energies ($E_\gamma <$ 2.2 GeV), a clear increasing trend toward t=t_{min} is observed in the production of $K^+\Lambda$. Above $E_\gamma >$ 2.2 GeV, the presence of a plateau with a close-to-zero slope near t=t_{min} is observed for the $K^+\Lambda$ channel.

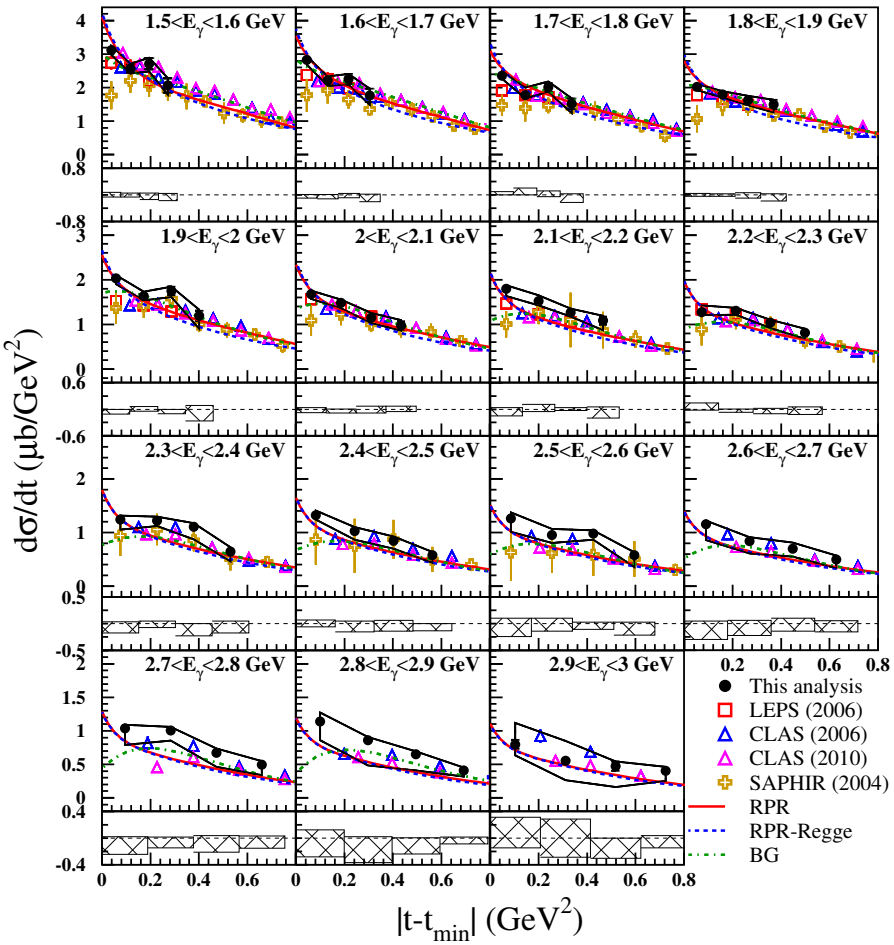

Figure 5.21: Differential cross sections for the $p(\gamma,K^+)\Lambda$ reaction as a function of $|t - t_{min}|$ for $1.5 < E_\gamma < 3.0$ GeV. The results of this measurement are shown by solid black circles. The results of LEPS 2006 [24] (red open squares), CLAS 2006 [28] (blue open triangles), CLAS 2010 [30] (purple open triangles), and SAPHIR 2004 [22] (yellow open cross) are also shown. The notations of curves are the same as those in Fig. 5.17. The shaded histograms show the systematic uncertainty.

As for the $K^+\Sigma^0$ production, the overall t-dependence is more or less flat for $E_\gamma < 1.7$ GeV. The plateau structure near t=t_{min} even with some finite negative slope beyond $|t - t_{min}|$ <0.3 GeV^2 is observed in E_γ=1.7-2.7 GeV. For the $E_\gamma > 2.7$ GeV, the t-dependence of differential cross sections changes to be close to a monotonic increase toward t=t_{min}.

For $K^+\Lambda$ channel, in Fig. 5.21, the observation of the plateau t dependence is consistent with the result of the model calculation by Guidal, Laget, and Vanderhaeghen [83]. The model of contributions of a Reggeized s-channel diagram for the K-exchange provided a reasonable qualitative description of what we observed in the hyperon production

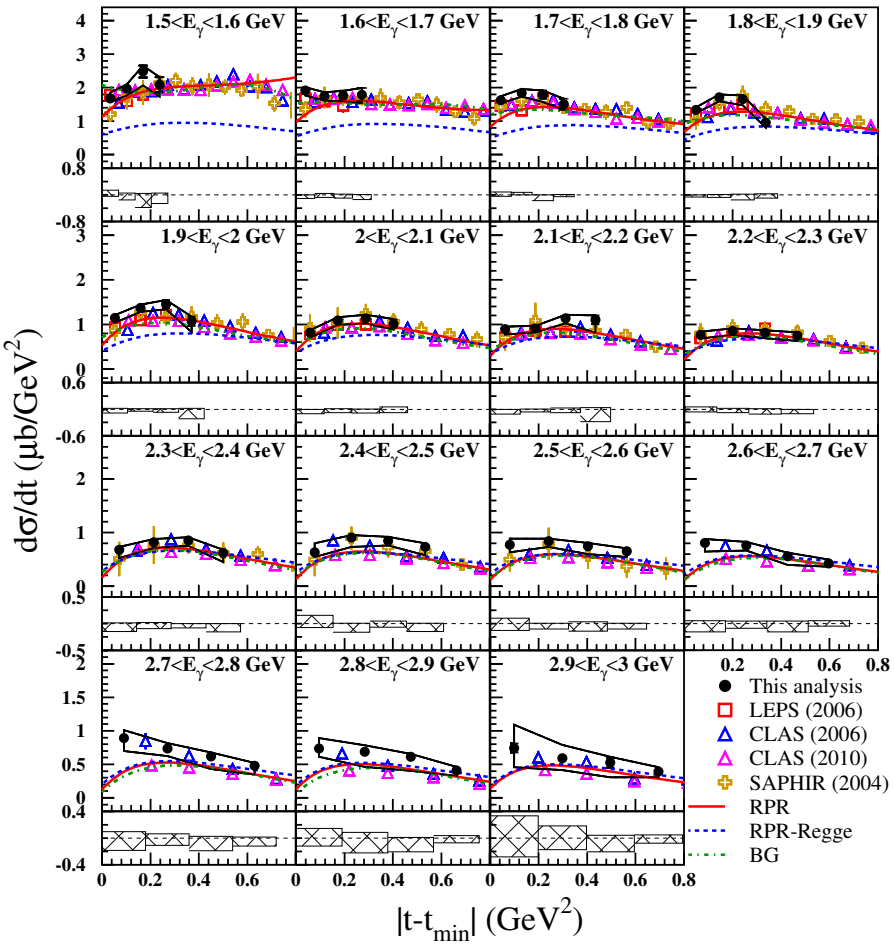

Figure 5.22: Differential cross sections for the $p(\gamma,K^+)\Sigma^0$ reaction as a function of $|t-t_{min}|$ for $1.5 < E_\gamma < 3.0$ GeV. The notations of points and curves are the same as those in Fig. 5.21. The shaded histograms show the systematic uncertainty.

at $E_\gamma = 1.5 - 3.0$ GeV. Here the same plateau structure in the cross sections results for $E_\gamma > 2.2$ GeV has been observed. As the energy decreases, the contribution of K-exchange, characterized by an increase of cross section toward t=t_{min}, becomes more important. This discussion of the K-exchange dominance could be refer to 2.1.3. In the framework of the Regge based model, the energy dependence of the differential cross sections at t=t_{min} scales as $s^{2\alpha_0-2}$ where α_0 is the intercept of the Regge trajectory at t=0 [83]. The smallness of α_0 of K Regge trajectory, compared with that of K^* trajectory, would lead to a increasingly strong contribution from the t-channel K-exchange toward low energies. This expectation indeed agrees with what is observed here.

For $K^+\Sigma^0$ production, in Fig. 5.22, since the contribution which

comes from the K-exchange is relatively small overall, the contributions of a Reggeized s-channel diagram for the K-exchange are also small. Due to the lack of the contribution from Reggeized s-channel diagram we do not observe a similar rising toward t=t_{min} at low energies. The relatively flat t-dependence reflects the importance of s-channel nucleon resonance contributions in this channel. This could be understood by the explanation that only the intermediate nucleon resonances with isospin $I = 1/2$ is allowed for $K^+\Lambda$ production while both $I = 1/2$ and $3/2$ resonances work for the case of $K^+\Sigma^0$.

In Fig. 5.21, for the $K^+\Lambda$ channel, the RPR model which is based on Regge theory surely describes the forward-peaking feature well. But when E_γ increases, the deviation of the calculation results from our data becomes larger. The BG model reproduces the present data better than the RPR model in the region of $|t - t_{min}| > 0.2$ GeV^2. But in the region of E_γ>1.9 GeV the BG model can not describe the forward peaking feature.

For $K^+\Sigma^0$ channel, in Fig. 5.22, the contribution of resonance is inferred to be significant for $E_\gamma < 2.25$ GeV judging from the difference between the predictions of RPR and RPR-Regge model. Large differences between the predictions of the RPR and RPR-Regge models are also seen in Fig. 5.17. In the region of E_γ<2.4 GeV both the predictions reasonably describe the more or less flat phenomenon of t-dependence, but there still exist some quantitative deviations from our data. It is noted that both models can not reproduce the appearance of forward-peaking in the region of $|t - t_{min}| < 0.3$ GeV^2 for $E_\gamma > 2.6$ GeV. This brings up the need of improving the description of Regge trajectories in t-channel contribution in this energy regime.

Figure 5.23 shows the photon-beam asymmetries for the $K^+\Lambda$ and $K^+\Sigma^0$ channels as a function of E_γ for $E_\gamma > 1.8$ GeV in three bins of production angle 0.6 <cos $\theta^{K^+}_{c.m.}$< 1.0.

The beam asymmetries at forward angles for the photon energy region of 2.4-3.0 GeV have been measured for the first time as shown in Fig. 5.23. Toward all the kinematic region the photon-beam asymmetries are positive and show a mild increase with beam energy. In both the

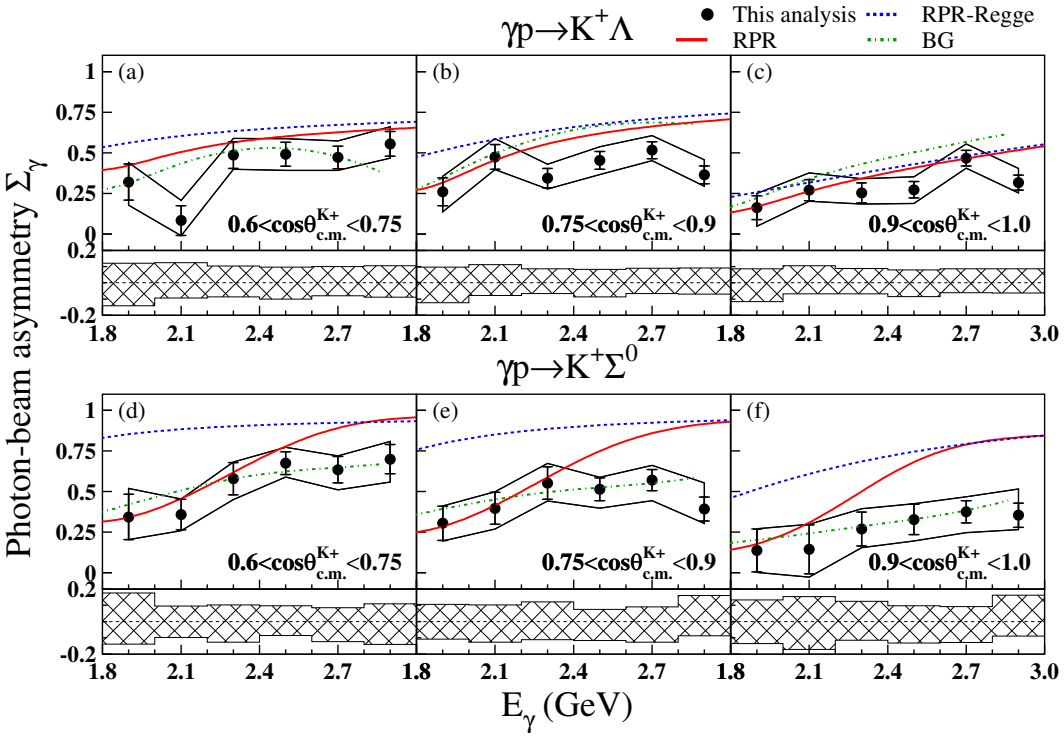

Figure 5.23: Photon-beam asymmetries (Σ_γ) for the $p(\gamma,K^+)\Lambda$ reaction (a)∼(c) and for $p(\gamma,K^+)\Sigma^0$ reaction (d)∼(f) with systematic uncertainty plotted in hatched histogram as a function of photon energy E_γ for the kaon C.M. production polar angle 0.6 $<\cos\theta^{K^+}_{c.m.}<$ 1.0. The notations of curves are the same as those in Fig. 5.17.

channels, a small drop of the photon-beam asymmetries at E_γ=2.9 GeV in the production angle 0.75 $<\cos\theta^{K^+}_{c.m.}<$ 1.0 is observed.

Assuming a t-channel dominance based on the observed forward-peaking feature in the differential cross sections, the positive values of photon-beam asymmetry suggest a dominating natural–parity exchange of K^* compared to the unnatural–parity exchange of K in the t-channel toward large E_γ. The positive sign here indicates that the K^+ from the $K^+\Lambda$ and $K^+\Sigma^0$ channels tends to be emitted in the orthogonal direction with respect to the photon polarization.

Furthermore, in Fig. 5.23 the photon-beam asymmetries for the $K^+\Sigma^0$ production are slightly larger than those for the $K^+\Lambda$ production for $E_\gamma > 2.4$ GeV. This indicates a relatively weaker strength of the unnatural–parity K-exchange in the $K^+\Sigma^0$ production. Here the positive (negative) trend of beam asymmetry which is expected by the dominance of natural–parity K^* (K) exchange. These interpretations are consistent with those in the discussions on the t-dependence of the

differential cross sections above.

The difference between data and the prediction from Regge trajectories only (RPR-Regge) model suggests the importance of the inclusion of contributions from the nucleon resonances in the s-channel for the photon-beam asymmetry of $K^+\Lambda$ production below $E_\gamma = 2.1$ GeV and $K^+\Sigma^0$ production below $E_\gamma = 2.4$ GeV. This feature was also obtained in the comparison of the production cross sections.

For $K^+\Lambda$ production above $E_\gamma = 2.1$ GeV, all predictions from the RPR, RPR-Regge and BG models converge at $\cos\theta^{K^+}_{c.m.} > 0.75$ and show certain deviations from the data. This suggests the need of including additional resonance contributions or a re-determination of Regge contributions with the current new data in the forward direction or both of them.

As for $K^+\Sigma^0$ production, the RPR model with no significant nucleon contributions overestimates the photon-beam asymmetries for $E_\gamma > 2.3$ GeV at all three angular bins. While the BG model gives a very good description of the photon-beam asymmetries over the whole regions. It is noted that nucleon resonances with spin J larger than $3/2$ are not included in the RPR model [71] but they are taken into account in the BG model [77, 78, 80]. This difference in including higher-spin resonances might account for the better prediction of the photon-beam asymmetries in the BG model. It is also noted that in the RPR 2007 model for $K^+\Sigma^0$ production, the Regge contributions were determined by the fit of the high energy data form 5 to 16 GeV [18, 19]. Dey and Meyer [81] conclude that there is a persistent normalization issue in the old high-energy differential cross-section data for a number of reactions, including $\gamma p \to K^+\Lambda$ and $\gamma p \to K^+\Sigma^0$ channels. The RPR 2012 results [72] also support this conclusion, so re-determination of Regge contributions with the current new data might be a good direction to improve theoretical understanding.

The photon-beam asymmetries in the whole region of $0.6 < \cos\theta^{K^+}_{c.m.} < 1.0$ together with previous LEPS 2006 results [24] at slightly lower energies is shown in Fig. 5.24. An increase of the photon-beam asymmetry with beam energy is more clearly illustrated.

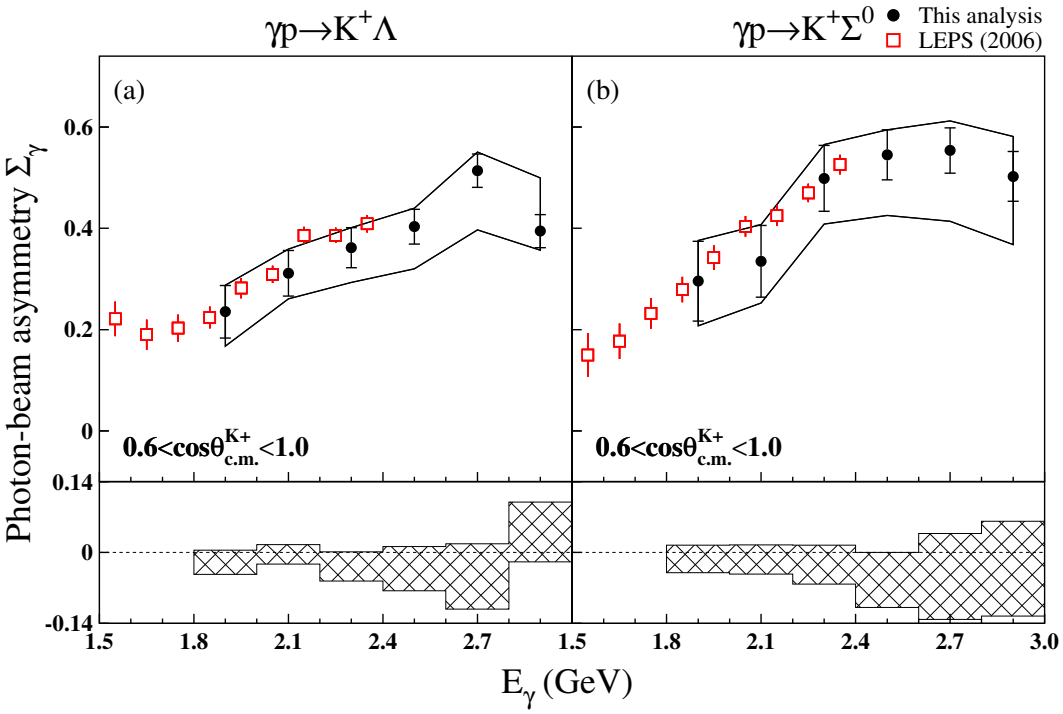

Figure 5.24: Photon-beam asymmetries (Σ_γ) for the $p(\gamma,K^+)\Lambda$ reaction (a) and $p(\gamma,K^+)\Sigma^0$ reaction (b) with systematic uncertainty plotted in hatched histogram as a function of E_γ for $0.6 < \cos\theta^{K^+}_{c.m.} < 1.0$. The results of this measurement and, LEPS 2006 are shown by solid black circles and red open squares. The solid black line indicates the range of total errors.

In Fig. 5.25 the photon-beam asymmetry results for the $K^+\Lambda$ and $K^+\Sigma^0$ channels as a function of $\cos\theta^{K^+}_{c.m.}$ are shown in six E_γ bins together with the previous results from LEPS [24] and the theoretical predictions. The agreement of the present data with the previous data is reasonably nice. Across all energy bins of E_γ from 1.8 to 3.0 GeV, the photon-beam asymmetries for the $K^+\Sigma^0$ channel at forward angles of $0.6 < \cos\theta^{K^+}_{c.m.} < 1.0$ show a decrease toward the zero degrees. Such decrease could possibly reflect an increasing importance of unnatural–parity K-exchange at smaller production angles, besides the trivial kinematic effect of vanishing photon-beam asymmetries at zero degrees. For $E_\gamma \leq 2.3$ GeV, both the RPR and BG models describe the data well and BG model clearly does a better job in describing the photon-beam asymmetries of $K^+\Sigma^0$ channel.

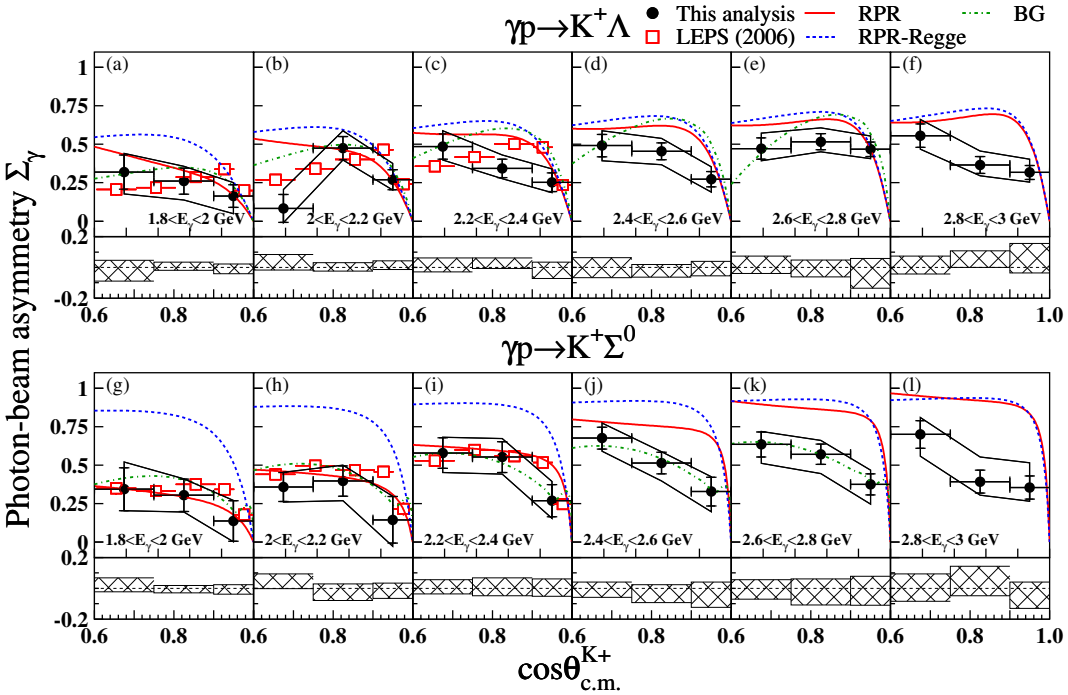

Figure 5.25: Photon-beam asymmetries (Σ_γ) for the $p(\gamma,K^+)\Lambda$ reaction (a)$\sim$(f) and $p(\gamma,K^+)\Sigma^0$ reaction (g)$\sim$(l) with systematic uncertainty plotted in hatched histogram as a function of $\cos\theta^{K^+}_{c.m.}$ for $1.8 < E_\gamma < 3.0$ GeV. The results of this measurement and, LEPS 2006 data are shown by solid black circles and red open squares, respectively. The notations of curves are the same as those in Fig. 5.17.

Chapter 6

Summary

In summary, we present the measurement of differential cross sections and photon-beam asymmetry of $K^+\Lambda$ and $K^+\Sigma^0$ photoproduction in the forward production angles 0.6 $<\cos\theta^{K^+}_{c.m.}<$ 1.0, at beam energy E_γ=1.5-3.0 GeV. The results are consistent with previous results [24]. The measurement provides more constraints for the phenomenological fits. We conclude that after the side-band background suppression, the differential cross sections and photon beam asymmetry of $K^+\Lambda$ and $K^+\Sigma^0$ photoproduction can be extracted from a strongly contaminated data with a reasonable systematic error. The t0 calibration improves the inconsistency between the Monte-Carlo and real data, which makes the acceptance calculation more reliable.

The production cross sections show a slowly decreasing trend with increasing the photon beam energy E_γ. There is no observation of distinct narrow structures on the energy dependence for both the reactions. But in the $K^+\Sigma^0$ cross sections, some structures, possibly due to nucleon resonances, are seen at E_γ $\sim$1.8 GeV and 2.8 GeV at $\cos\theta^{K^+}_{c.m.}$=0.7-1.0.

From the results in $K^+\Lambda$ channel the cross sections appear to rise with the decreasing of $|t-t_{min}|$, while in $K^+\Sigma^0$ channel the cross sections seems flat over in the lower beam energy region. This forward peaking behaviour in $K^+\Lambda$ channel is typically indicative of a strong t-channel contribution and the flat distribution in forward region in $K^+\Sigma^0$ channel would suggest that the t-channel meson exchange is less dominant here. This might reflect that the s-channel contributions from nucleon resonances are more effective in the production of $K^+\Sigma^0$. Based on the Reggeized t-channel framework, the results of cross sections near t=t_{min}

provide evidences of the existence of K-exchange in $K^+\Lambda$ production at low energies.

The photon-beam asymmetry is sensitive to the reaction mechanisms and the existence of nucleon resonances. The photon-beam asymmetries for both $K^+\Lambda$ and $K^+\Sigma^0$ channels are all positive for the entire kinematic region and show a mild increase with beam energy, from $\sim$0.1-0.2 at $E_\gamma = 1.9$ GeV to $\sim$0.5-0.6 at $E_\gamma = 2.9$ GeV. The photon-beam asymmetry, in the range of $E_\gamma > 2.4$ GeV were measured for the first time. The positive photon-beam asymmetry suggests a dominating natural–parity exchange of K^* in the t-channel. For $K^+\Lambda$ production above $E_\gamma = 2.1$ GeV, all predictions from RPR, RPR-Regge and BG converge at $\cos\theta^{K^+}_{c.m.} > 0.75$ and show certain deviations from the data. The BG model including higher-spin nucleon resonances describes nicely the photon-beam asymmetries for the $K^+\Sigma^0$ channel up to E_γ=2.8 GeV. All these observations strongly suggest the existence of nucleon resonance contributions at E_γ=2.4-3.0 GeV.

Comparison with theoretical predictions from RPR and BG models indicates that there is room for improvement of the theoretical modelling of Regge trajectories in t-channel as well as the contributions from the nucleon resonances. With the constraints of these new data of the hyperon Λ and Σ^0 photoproductions at very forward angle over the intermediate energy, we look forward to the progress from the theoretical modelling in near future.

In addition to some new data for both $K^+\Lambda$ and $K^+\Sigma^0$ channels are presented, some suggestions for improving the model calculations are also presented. But we know that this work presents by no means final answers and might inspire more interesting questions. Hope the future explorer can assume the responsibility of resolving the unanswered questions and continue the effort.

參 考 文 獻

[1] D. H. Perkins, *Introduction to High Energy Physics 4-th edition*, Cambridge University Press, (2000).

[2] D. Griffiths, *Introduction to Elementary Particles*, WILEY-VCH, (2004).

[3] M. E. Peskin and D. V. Schroeder, *An Introduction to Quantum Field Theory*, Westview Press, (1995).

[4] A. V. Anisovich, V. V. Anisovich, M. A. Matveev, V. A. Nikonov, J. Nyiri, and A. V. Sarantsev *MESON AND BARYONS Systematization and Methods of Analysis* , World Scientific Publishin Co. Pte. Ltd., (2008).

[5] A. De Rújula, Howard Georgi and S. L. Glashow, Phys. Rev. D **12**, 147 (1975).

[6] N. Isgur and G. Karl, Phys. Rev. D **18**, 4187 (1978).

[7] N. Isgur and G. Karl, Phys. Rev. D **19**, 2653 (1979).

[8] R. Koniuk and N. Isgur, Phys. Rev. D **21**, 1868 (1980).

[9] Particle Data Group, Phys. Rev. D **86** (2012).

[10] D. B. Lichtenberg *et al.* , Phys. Rev. Lett. **48**, 1653 (1982).

[11] R. A. Adelseck and B. Saghai, Phys. Rev. C **42**, 108 (1990).

[12] I. S. Barker, A. Donnachie, and J. K. Storrow, Nucl. Phys. B **95**, 347 (1975).

[13] S. Bethke, Prog. Part. Nucl. Phys. **58**, 351 (2007).

[14] D. B. Leinweber, Visualizations of the QCD vacuum, http://arxiv.org/ps/heplat/0004025 , (1999).

[15] http://www.particleadventure.org/ .

[16] D. J. Gross and F. Wilczek, Phys. Rev. Lett. **30**, 1343 (1973).

[17] D. Politzer, Phys. Rev. Lett. **30**, 1346 (1973).

[18] A. Boyarski *et al.*, Phys. Rev. Lett. **22**, 1131 (1969).

[19] D. J. Quinn, J. P. Rutherfoord, M. A. Shupe, D. J. Sherden, R. H. Siemann and C. K. Sinclair, Phys. Rev. D **20**, 1553 (1979).

[20] M. Bockhorst *et al.* (SAPHIR Collaboration), Z. Phys. C **63**, 37 (1994).

[21] M. Q. Tran *et al.* (SAPHIR Collaboration), Phys. Lett. B **445**, 20 (1998).

[22] K.-H. Glander *et al.* (SAPHIR Collaboration), Eur. Phys. Jour. A **19**, 251 (2004).

[23] R. G. T. Zegers *et al.* (LEPS Collaboration), Phys. Rev. Lett. **91**, 092001 (2003).

[24] M. Sumihama *et al.* (LEPS Collaboration), Phys. Rev. C **73**, 035214 (2006).

[25] K. Hicks *et al.* (LEPS Collaboration), Phys. Rev. C **76**, 042201(R) (2007).

[26] H. Kohri *et al.* (LEPS Collaboration), Phys. Rev. Lett. **97**, 082003 (2006).

[27] J. W. C. McNabb *et al.* (CLAS Collaboration), Phys. Rev. C **69**, 042201(R) (2004).

[28] R. Bradford *et al.* (CLAS Collaboration), Phys. Rev. C **73**, 035202 (2006).

[29] R. Bradford *et al.* (CLAS Collaboration), Phys. Rev. C **75**, 035205 (2007).

[30] M. E. McCracken *et al.* (CLAS Collaboration), Phys. Rev. C **81**, 025201 (2010).

[31] B. Dey *et al.* (CLAS Collaboration), Phys. Rev. C **82**, 025202 (2010).

[32] C. A. Paterson *et al.* (CLAS Collaboration), Phys. Rev. C **93**, 065201 (2016).

[33] A. Lleres *et al.* (GRAAL Collaboration), Eur. Phys. J. A **31**, 79 (2007).

[34] A. Lleres *et al.* (GRAAL Collaboration), Eur. Phys. J. A **39**, 149 (2009).

[35] O. Bartalini *et al.* (GRAAL Collaboration), Eur. Phys. J. A **26**, 399 (2005).

[36] T. C. Jude *et al.* (Crystal Ball Collaboration), Phys. Lett. B **735**, 112 (2014).

[37] A. Starostin *et al.* (Crystal Ball Collaboration), Phys. Rev. C **64**, 055205 (2001).

[38] Particle Data Group, Phys. Lett. B **667** (2008).

[39] T. Mart and C. Bennhold, Phys. Rev. C **61**, 012201(R) (1999).

[40] T. Mart and C. Bennhold, arXiv:nucl-th/0412097.

[41] S. Capstick and W. Roberts, Phys. Rev. D **49**, 4570 (1994).

[42] S. Capstick and W. Roberts, Phys. Rev. D **58**, 074011 (1998).

[43] T. Mart, C. Bennhold and C. E. Hyde-Wright, Phys. Rev. C **51**, R1074 (1995).

[44] T. Mart and C. Bennhold, Phys. Rev. C **61**, 012201(R) (1999).

[45] T. Mart and M. J. Kholili, Phys. Rev. C **86**, 022201(R) (2012).

[46] T. Mart, Phys. Rev. C **90**, 065202 (2014).

[47] T. Mart, S. Clymton and A. J. Arifi, Phys. Rev. D **92**, 094019 (2015).

[48] T. Mart and S. Sakinah, Phys. Rev. C **95**, 045205 (2017).

[49] F. X. Lee, T. Mart C. Bennhold, H. Haberzettl and L. E. Wright, Nucl. Phys. A **695**, 237 (2001).

[50] Aachen-Berlin-Bonn-Hamburg-Heidelberg-München Collaboration, Phys. Rev. **188**, 2060 (1969).

[51] M. Froissart, Phys. Rev. **123**, 1053 (1961).

[52] B.A. Mecking*et al.* Nucl. Instrum. Methods A **503**, 513 (2003).

[53] A. D'Angelo, O. Bartalini, V. Bellini, P. Levi Sandri, D. Moricciani, L. Nicoletti and A. Zucchiatti, Nucl. Phys. A **455**, 1 (2000).

[54] R.H. Milburn, Phys. Rev. Lett. **10**, 75 (1963).

[55] F.R. Arutyunyan, V.A. Tumanian, Phys. Lett. **4**, 176 (1963).

[56] K, Tsumaki, SPring-8 annual report **132**(1998).

[57] D.I. Sober*et al.* Nucl. Instrum. Methods A **440**, 263 (2000).

[58] https://edge.coherent.com/assets/pdf/Innova-Sabre-MotoFreD-Data-Sheet.pdf

[59] T. Matsumura, Master thesis, Osaka University, 2000.

[60] S. H. Hwang *et al.* (LEPS Collaboration), Phys. Rev. Lett. **108**, 092001 (2012).

[61] M. Sumihama LEPS Technical note No. 61

[62] S. H. Hwang LEPS Technical note No. 62

[63] CERN Application Software Group, GEANT3.2, CERN Program Library Writeup Report No. W5013 (1994)

[64] R. Frühwirth, Nucl. Instrum. Methods A **262**, 444 (1987).

[65] H. Kohri LEPS Technical note No. 74

[66] http://rprmodel.ugent.be/calc/

[67] http://pwa.hiskp.uni-bonn.de/BG2014_02_obs_int.htm

[68] https://maid.kph.uni-mainz.de/kaon/kaon-cross.html

[69] S. Janssen, J. Ryckebusch, D. Debruyne, and T. Van Cauteren, Phys. Rev. C **65**, 015201 (2001).

[70] T. Corthals, J. Ryckebusch, and T. Van Cauteren, Phys. Rev. C **73**, 045207 (2006).

[71] T. Corthals, T. Van Cauteren, J. Ryckebusch, and D. G. Ireland, Phys. Rev. C **75**, 045204 (2007).

[72] L. De Cruz, J. Ryckebusch, T. Vrancx, and P. Vancraeyveld, Phys. Rev. C **86**, 015212 (2012).

[73] T. Regge, Nuovo Cim. **14**, 951 (1959).

[74] A. V. Anisovich, E. Klempt, A. V. Sarantsev and U. Thoma, Eur. Phys. J. A **24**, 111 (2005).

[75] A. V. Sarantsev, V. A. Nikonov, A. V. Anisovich, E. Klempt and U. Thoma, Eur. Phys. J. A **25**, 441 (2005).

[76] A. V. Anisovich, V. Kleber, E. Klempt, V. A. Nikonov, A. V. Sarantsev and U. Thoma, Eur. Phys. J. A **34**, 243 (2007).

[77] A. V. Anisovich, E. Klempt, V. A. Nikonov, A. V. Sarantsev and U. Thoma, Eur. Phys. J. A **47**, 27 (2011).

[78] A. V. Anisovich, E. Klempt, V. A. Nikonov, A. V. Sarantsev and U. Thoma, Eur. Phys. J. A **47**, 153 (2011).

[79] A. V. Anisovich, R. Beck, E. Klempt, V. A. Nikonov, A. V. Sarantsev and U. Thoma, Eur. Phys. J. A **48**, 15 (2012).

[80] E. Gutz *et al.* (CBELSA/TAPS Collaboration), Eur. Phys. J. A **50**, 74 (2014).

[81] B. Dey and C. A. Meyer, arXiv:1106.0479.

[82] Y. Yanai, H. Kohri, S. H. Shiu *et al.* (LEPS Collaboration), *A new analysis method for subtracting backgrounds due to misidentified π^+ under hyperons produced by the $p(\gamma, K^+)X$ reaction in LEPS experiments*, preparing for publication.

[83] M. Guidal, J. M. Laget and M. Vanderhaeghen, Nucl. Phys. A **627**, 645 (1997).

[84] M. Guidal, J. M. Laget and M. Vanderhaeghen, Phys. Rev. C **68**, 058201 (2003).

[85] M. Sumihama, Ph.D. thesis, Osaka University, 2003.

[86] S. H. Hwang, Ph.D. thesis, Pusan National University, 2012.

[87] J. J. Melone, Ph.D. thesis, University of Glasgow, 2005.

Appendix A: The smallest χ^2 distribution for all Time of Flight slats

To decide the t0 shift for each time of flight slats, a fitting of the smallest χ^2 t0 shift associated with the ybar cut equal to 150, 160, 180, and 200 mm by a first-order polynomial function (P1) is done. The smallest χ^2 distribution for each slat is shown in Fig. A.1 to Fig. A.9

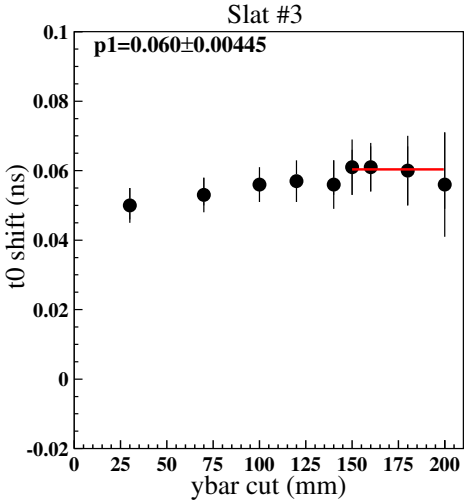

(a) The smallest χ^2 in slat # 3 with different ybar cut.

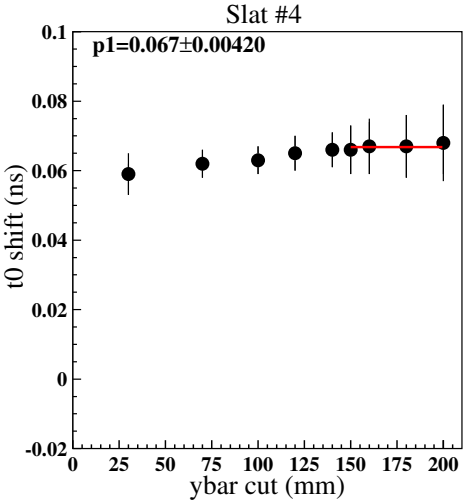

(b) The smallest χ^2 in slat # 4 with different ybar cut.

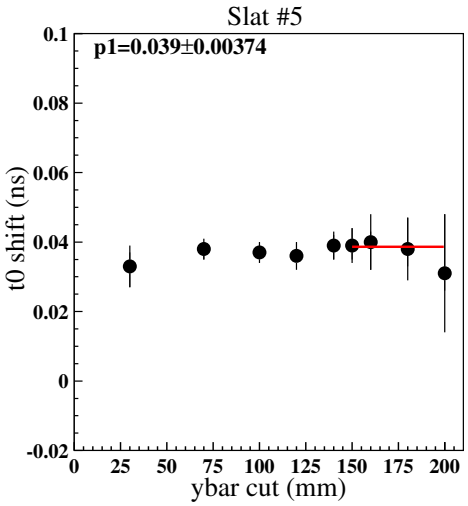

(c) The smallest χ^2 in slat # 5 with different ybar cut.

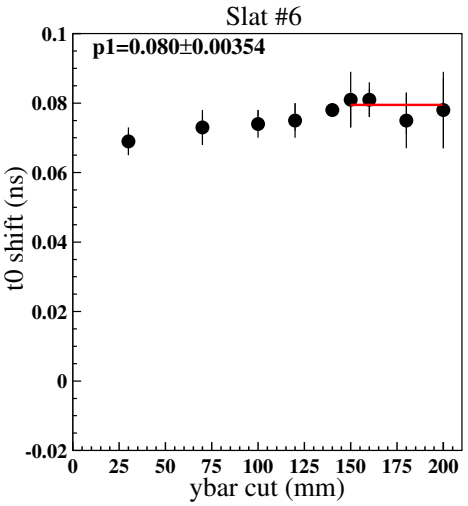

(d) The smallest χ^2 in slat # 6 with different ybar cut.

Figure A.1: The smallest χ^2 in various slat # with different ybar cut.

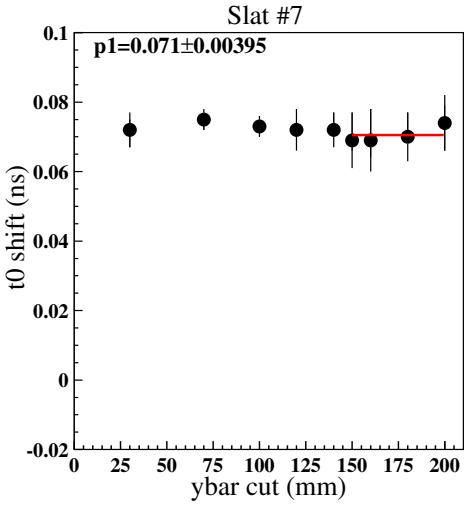

(a) The smallest χ^2 in slat # 7 with different ybar cut.

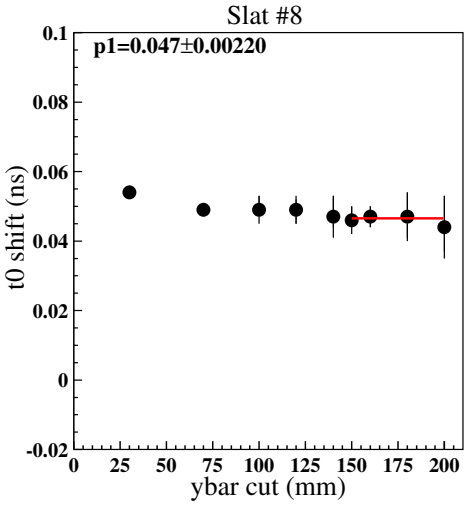

(b) The smallest χ^2 in slat # 8 with different ybar cut.

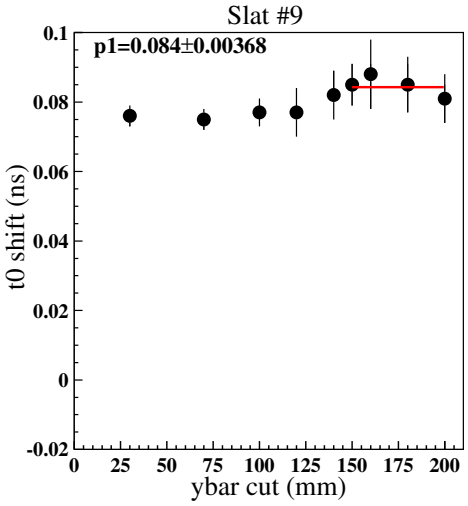

(c) The smallest χ^2 in slat # 9 with different ybar cut.

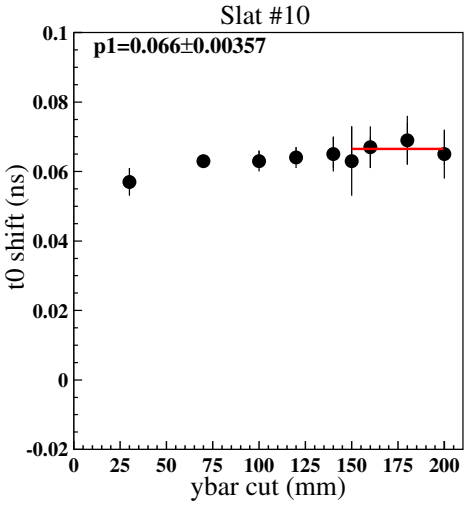

(d) The smallest χ^2 in slat # 10 with different ybar cut.

Figure A.2: The smallest χ^2 in various slat # with different ybar cut.

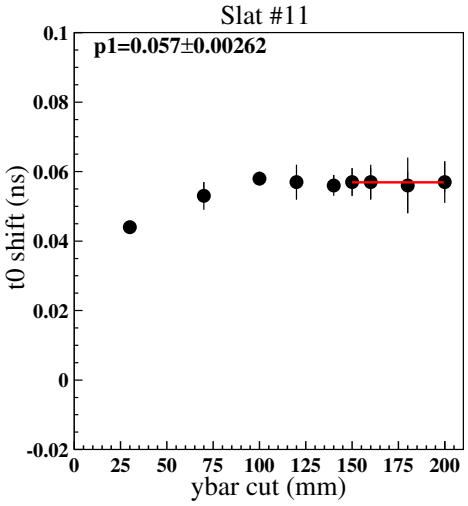

(a) The smallest χ^2 in slat # 11 with different ybar cut.

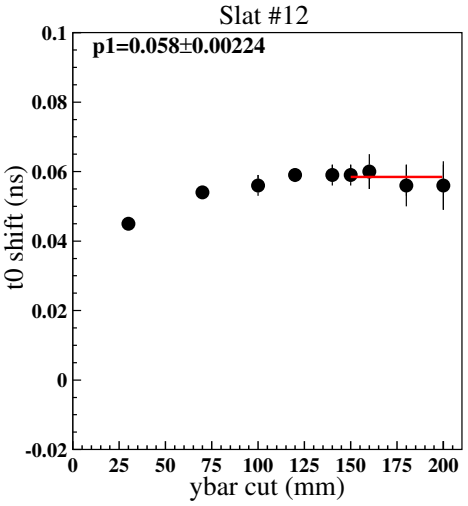

(b) The smallest χ^2 in slat # 12 with different ybar cut.

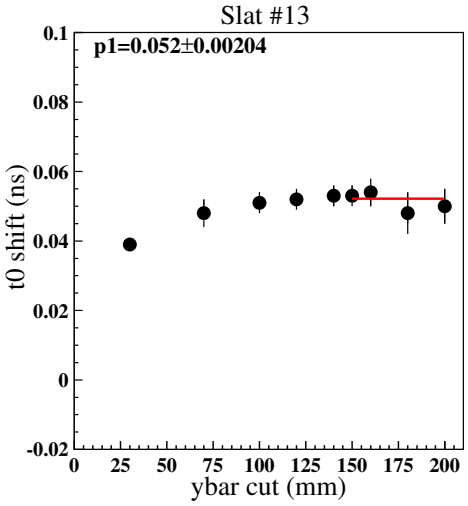

(c) The smallest χ^2 in slat # 13 with different ybar cut.

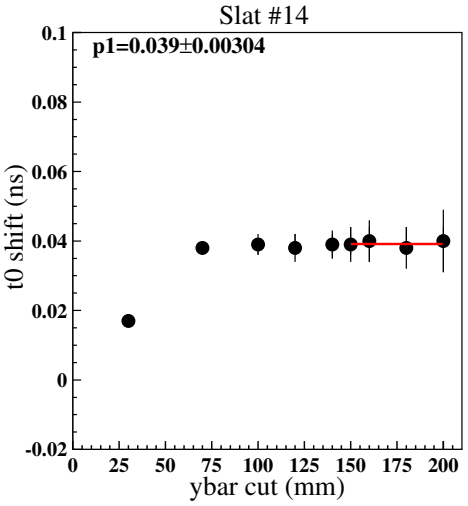

(d) The smallest χ^2 in slat # 14 with different ybar cut.

Figure A.3: The smallest χ^2 in various slat # with different ybar cut.

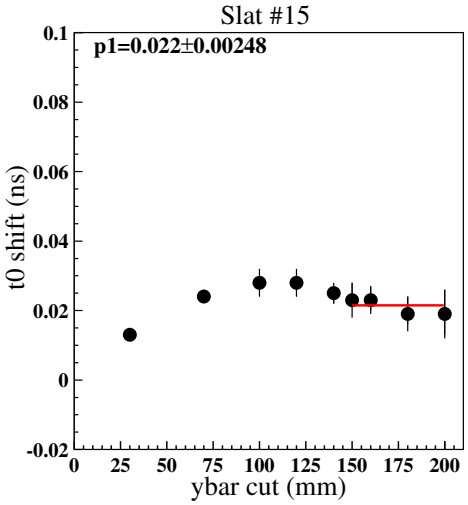

(a) The smallest χ^2 in slat # 15 with different ybar cut.

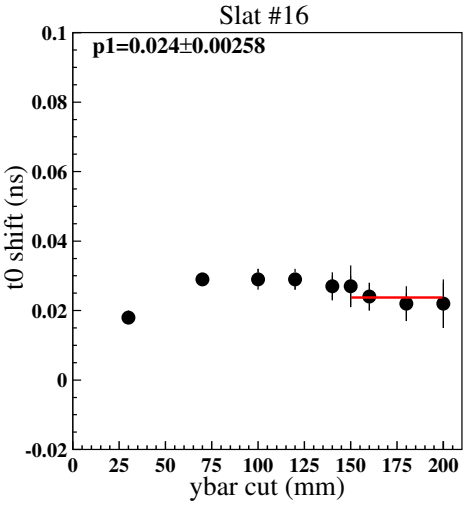

(b) The smallest χ^2 in slat # 16 with different ybar cut.

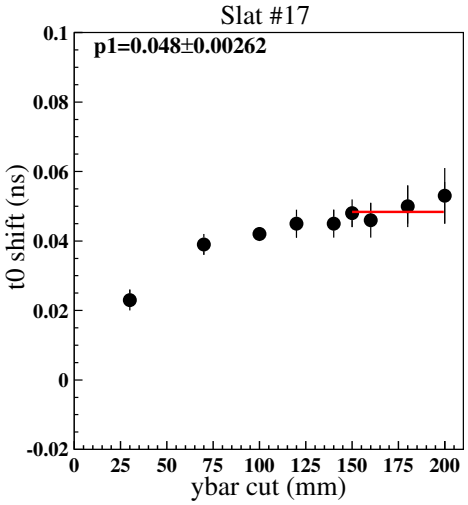

(c) The smallest χ^2 in slat # 17 with different ybar cut.

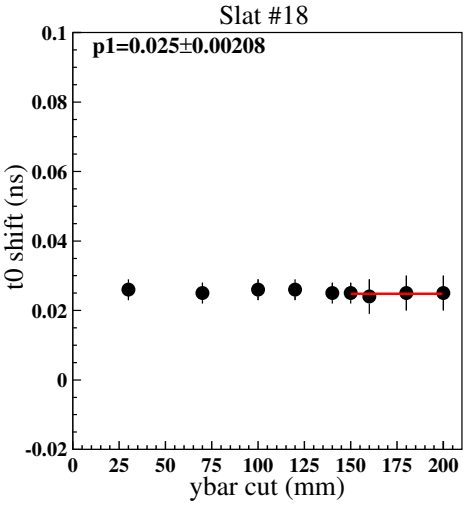

(d) The smallest χ^2 in slat # 18 with different ybar cut.

Figure A.4: The smallest χ^2 in various slat # with different ybar cut.

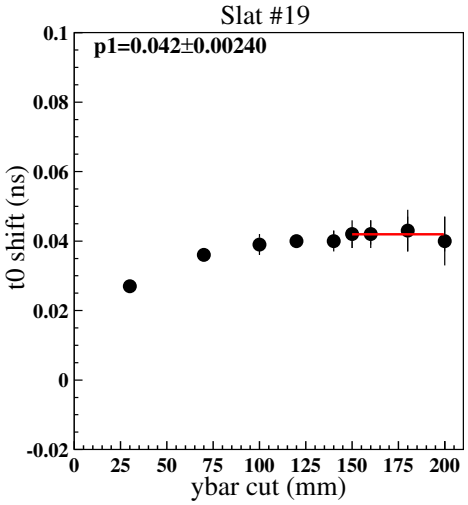

(a) The smallest χ^2 in slat # 19 with different ybar cut.

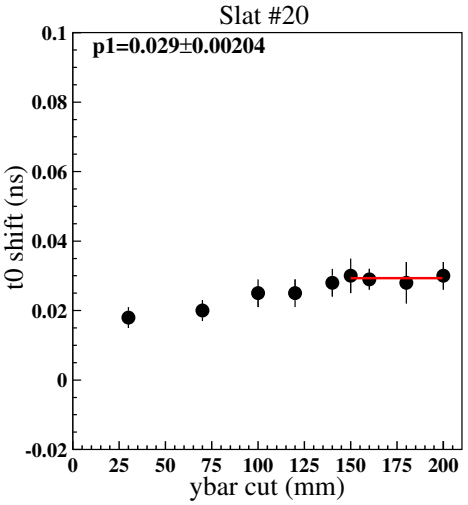

(b) The smallest χ^2 in slat # 20 with different ybar cut.

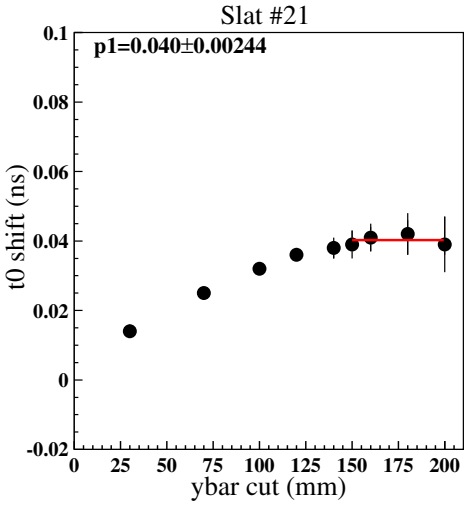

(c) The smallest χ^2 in slat # 21 with different ybar cut.

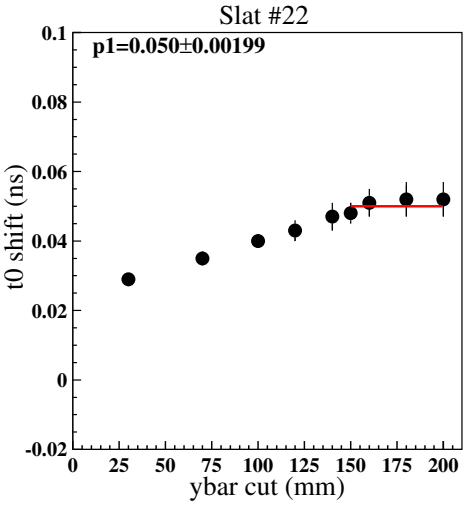

(d) The smallest χ^2 in slat # 22 with different ybar cut.

Figure A.5: The smallest χ^2 in various slat # with different ybar cut.

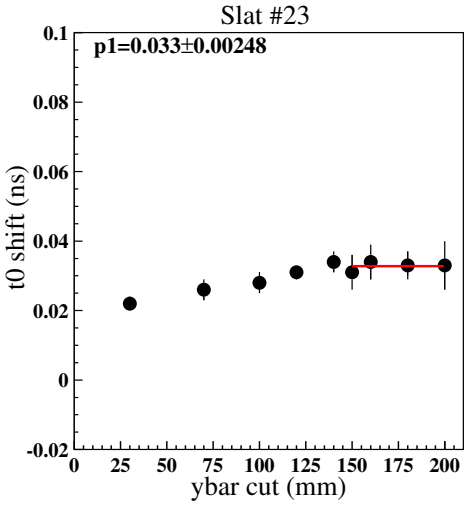

(a) The smallest χ^2 in slat # 23 with different ybar cut.

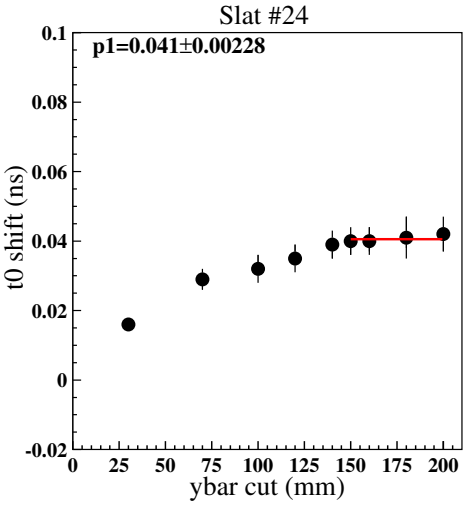

(b) The smallest χ^2 in slat # 24 with different ybar cut.

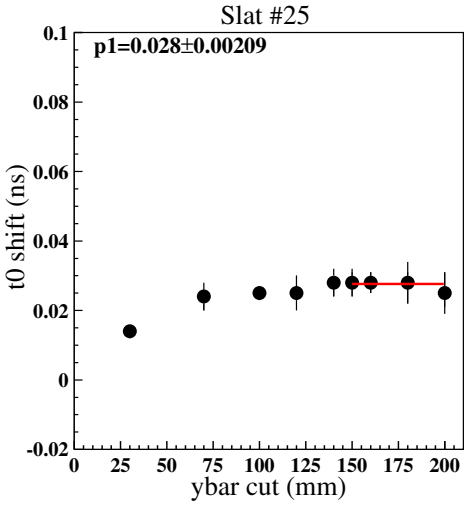

(c) The smallest χ^2 in slat # 25 with different ybar cut.

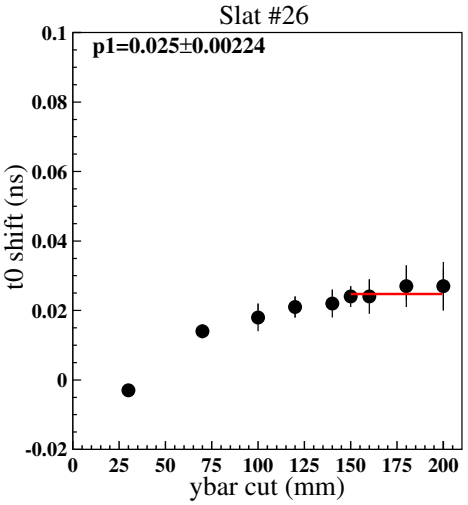

(d) The smallest χ^2 in slat # 26 with different ybar cut.

Figure A.6: The smallest χ^2 in various slat # with different ybar cut.

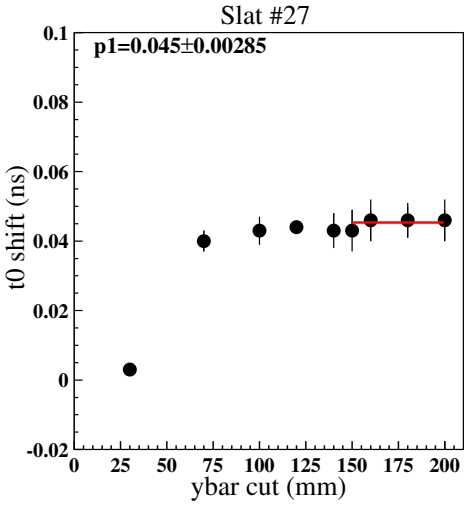

(a) The smallest χ^2 in slat # 27 with different ybar cut.

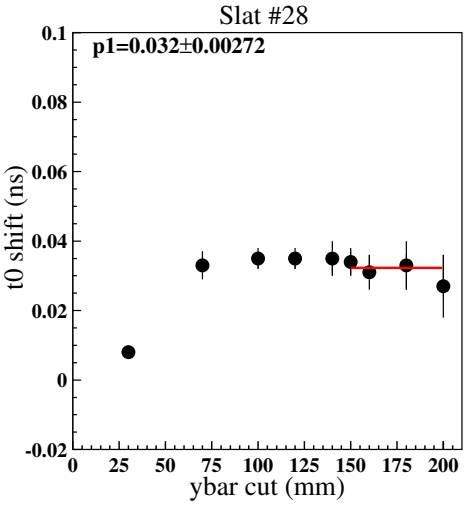

(b) The smallest χ^2 in slat # 28 with different ybar cut.

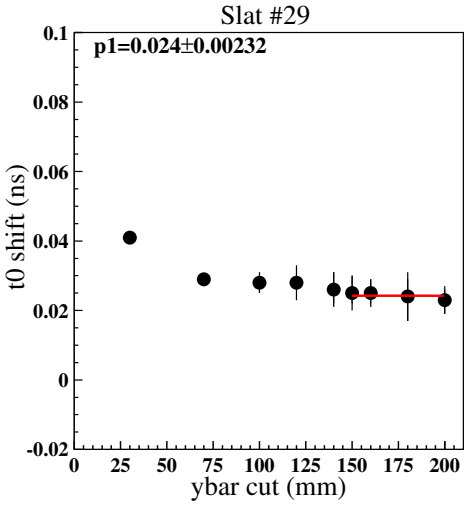

(c) The smallest χ^2 in slat # 29 with different ybar cut.

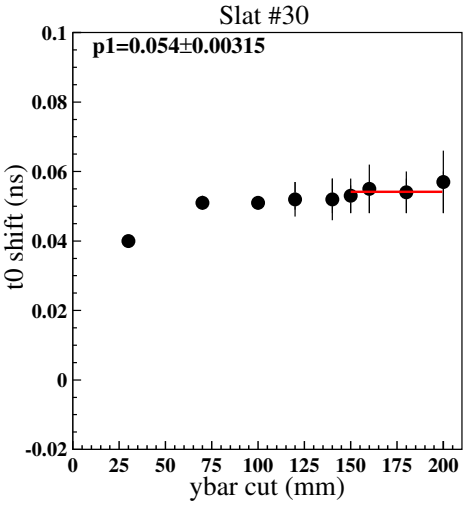

(d) The smallest χ^2 in slat # 30 with different ybar cut.

Figure A.7: The smallest χ^2 in various slat # with different ybar cut.

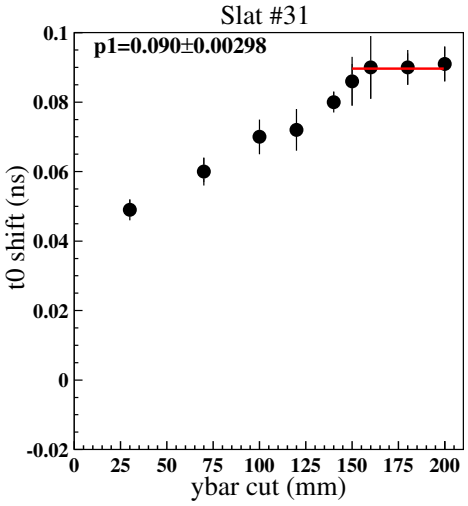

(a) The smallest χ^2 in slat # 31 with different ybar cut.

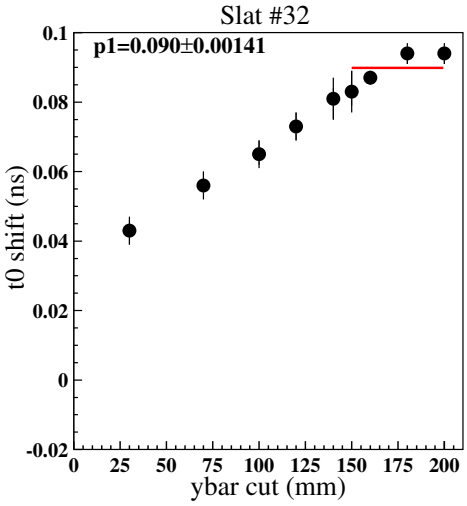

(b) The smallest χ^2 in slat # 32 with different ybar cut.

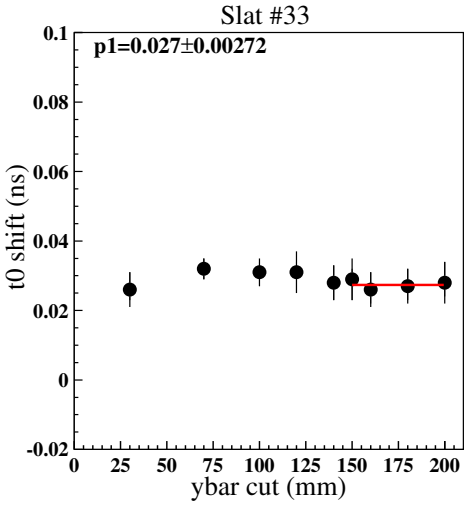

(c) The smallest χ^2 in slat # 33 with different ybar cut.

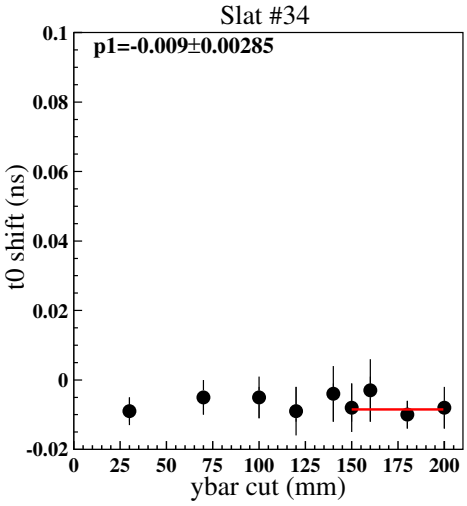

(d) The smallest χ^2 in slat # 34 with different ybar cut.

Figure A.8: The smallest χ^2 in various slat # with different ybar cut.

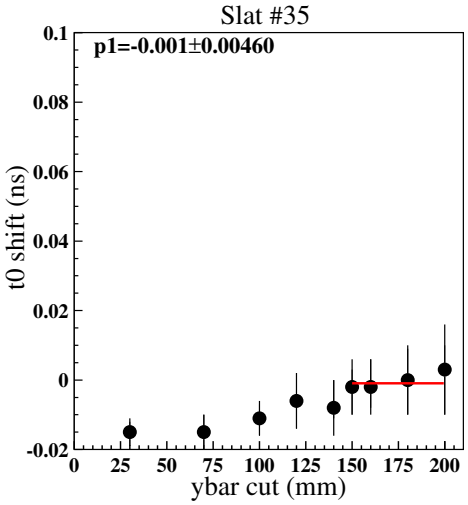

(a) The smallest χ^2 in slat # 35 with different ybar cut.

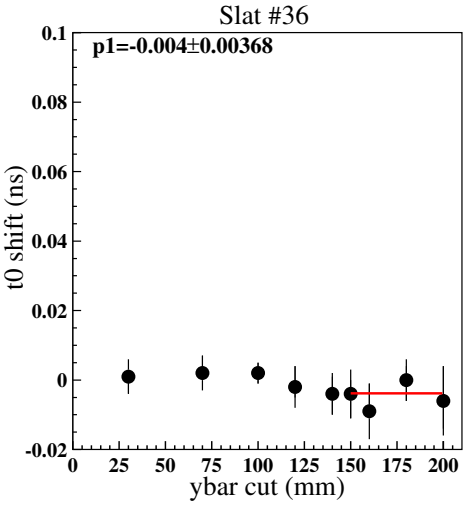

(b) The smallest χ^2 in slat # 36 with different ybar cut.

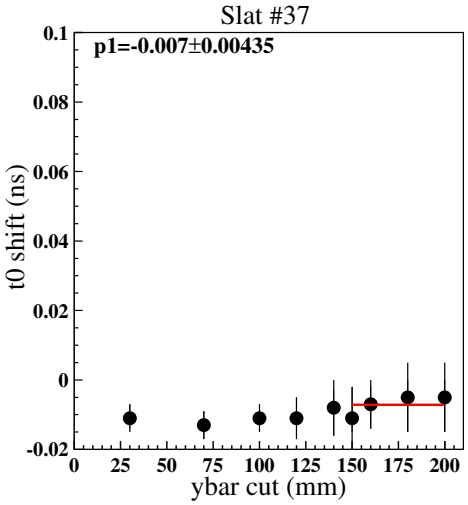

(c) The smallest χ^2 in slat # 37 with different ybar cut.

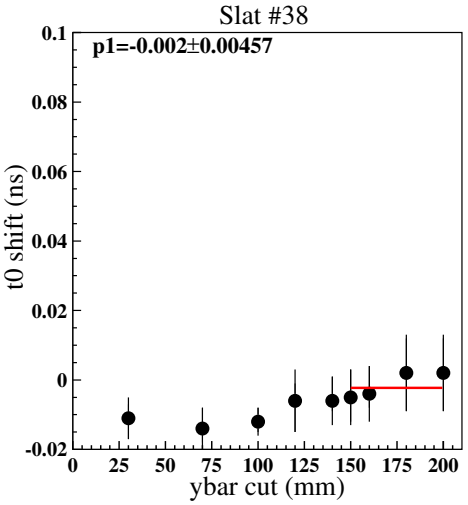

(d) The smallest χ^2 in slat # 38 with different ybar cut.

Figure A.9: The smallest χ^2 in various slat # with different ybar cut.

Appendix B: Fitting results

The side-band fitting results are shown in Fig. B.10 to Fig. B.13 The red solid line, green, blue dotted line and the purple dotted line stand for the total fitting, Λ, Σ^0 peaks, and the background which also considered the $\gamma p \to \pi^+ N$ peak around missing mass equal to 0.9 GeV, respectively.

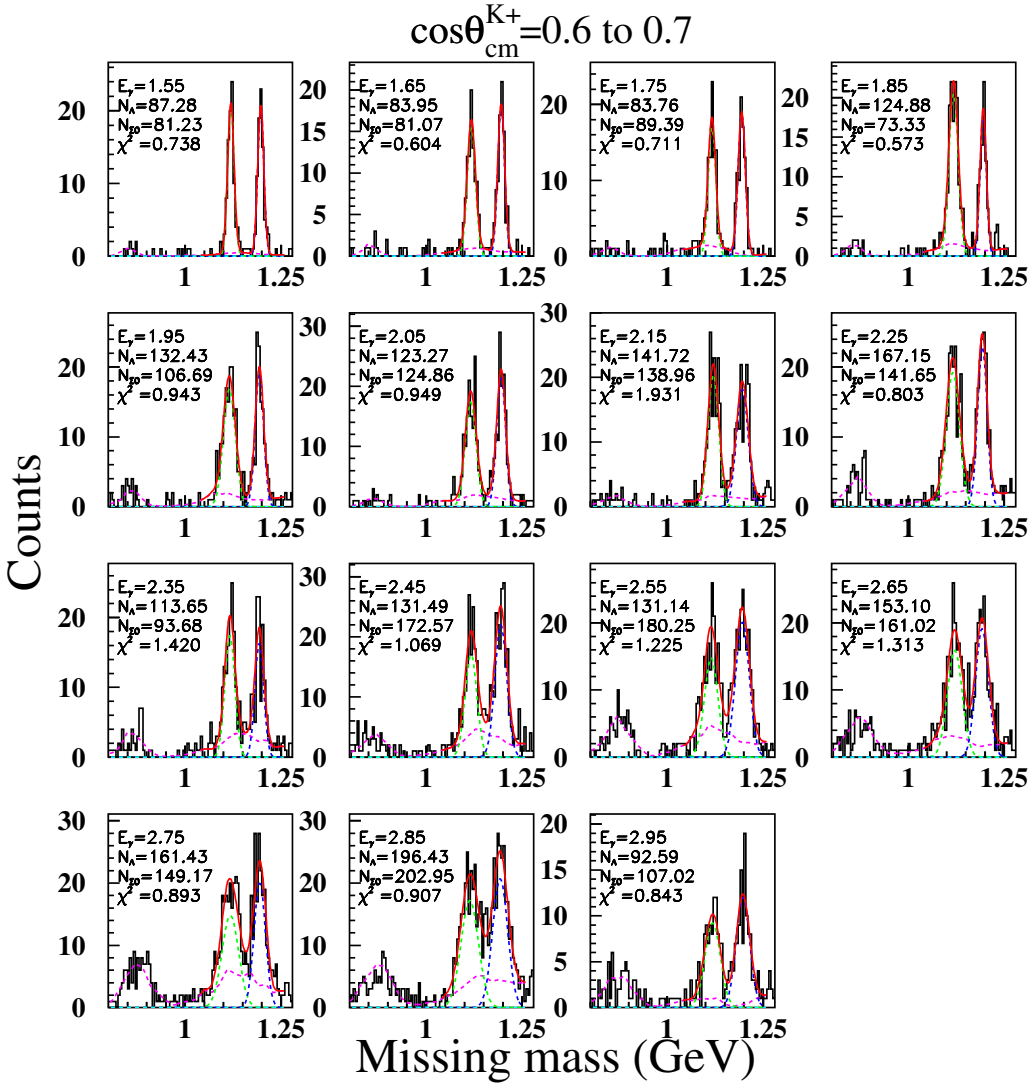

Figure B.10: Side-band method fitting results at $\cos\theta^{K^+}_{c.m.}$=0.6-0.7, E_γ=1.5-3.0 GeV.

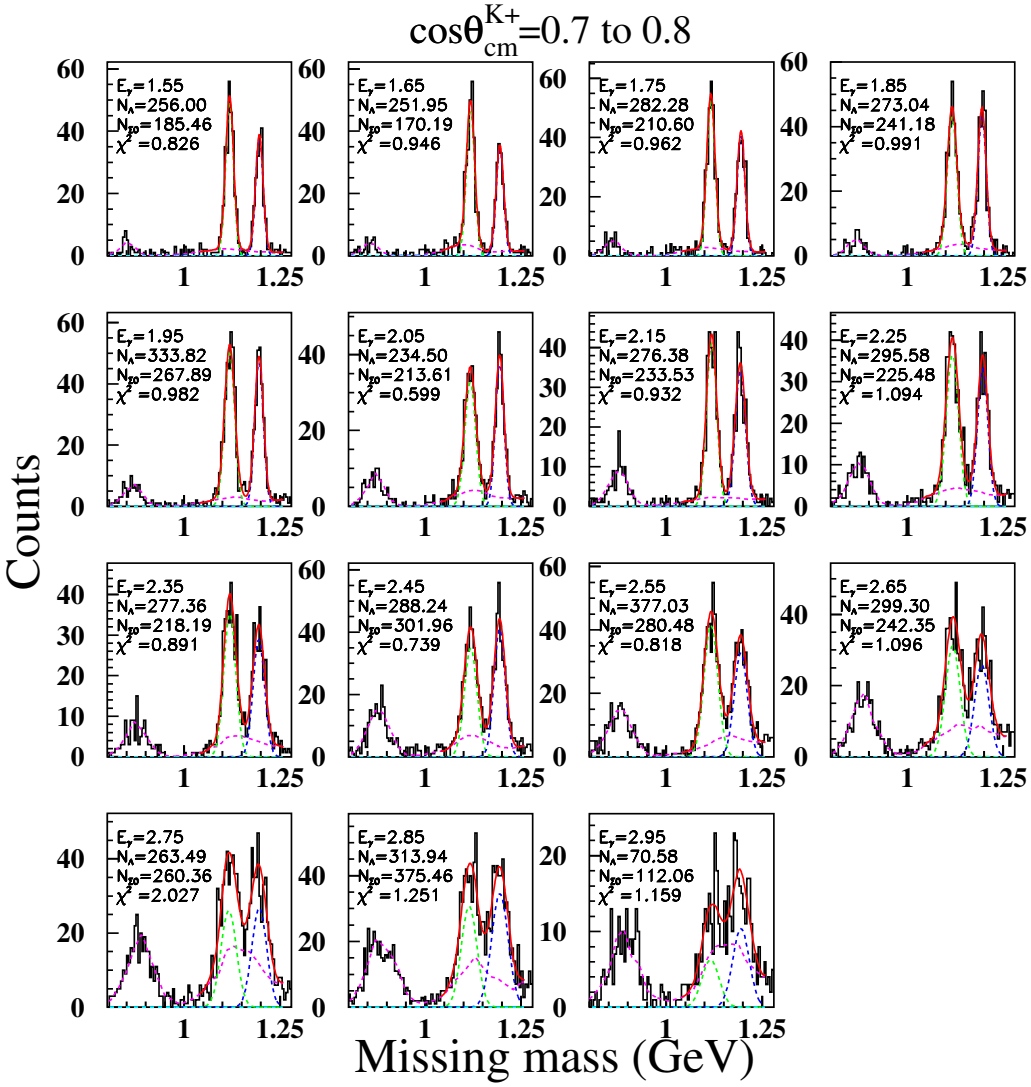

Figure B.11: Side-band method fitting results at $\cos\theta^{K^+}_{c.m.}$=0.7-0.8, E_γ=1.5-3.0 GeV.

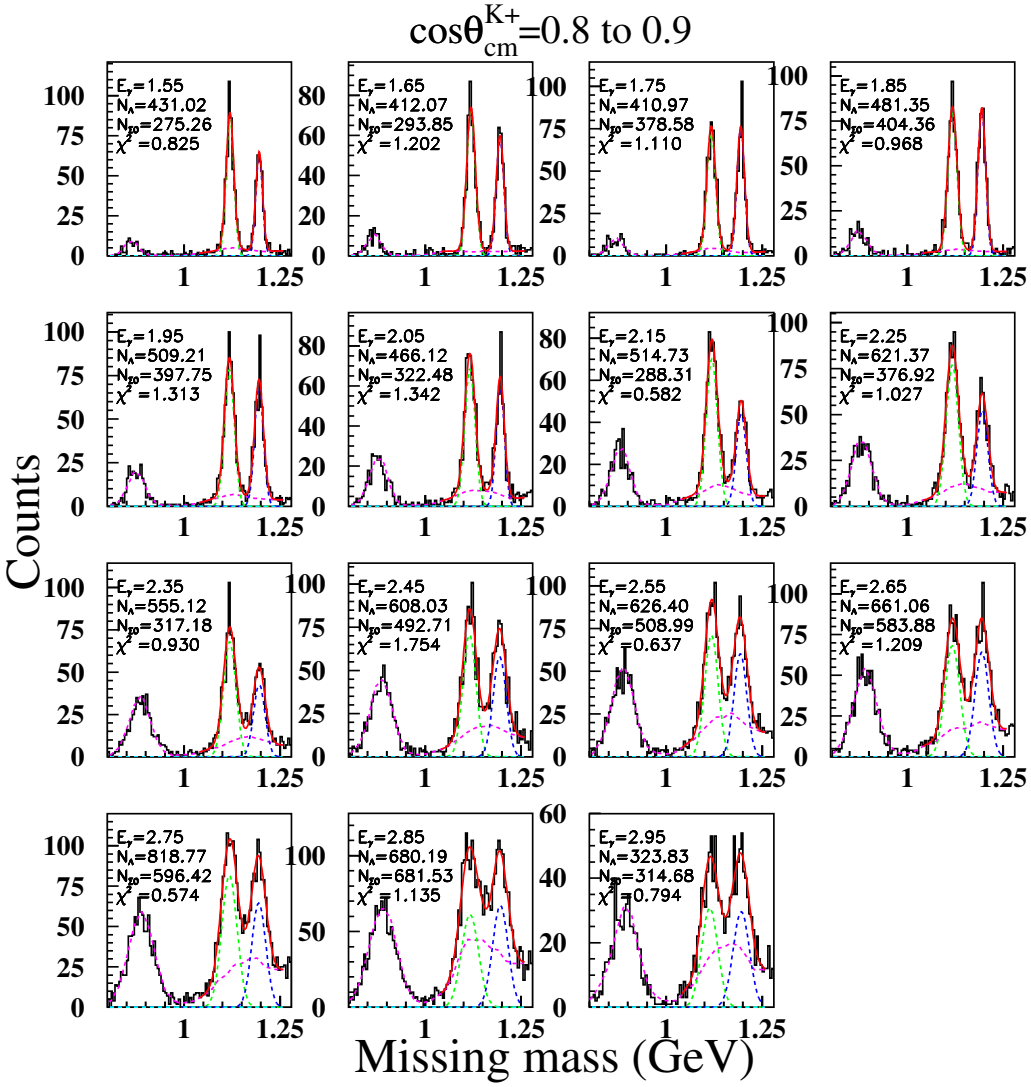

Figure B.12: Side-band method fitting results at $\cos\theta^{K^+}_{c.m.}$=0.8-0.9, E_γ=1.5-3.0 GeV.

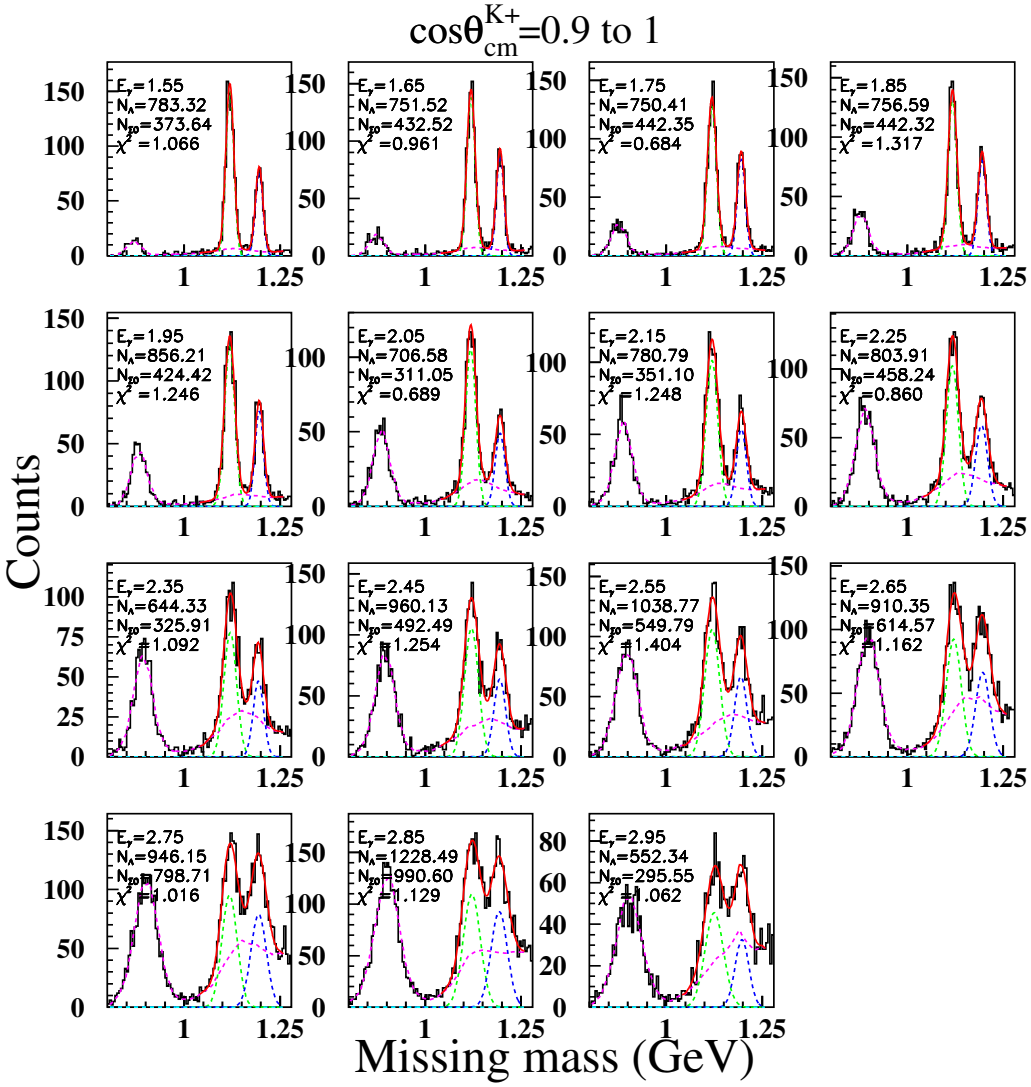

Figure B.13: Side-band method fitting results at $\cos\theta^{K^+}_{c.m.}$=0.9-1.0, E_γ=1.5-3.0 GeV.

Appendix C: The comparision of the real data and the simulated Λ and Σ^0 shape

The results for all production angles $\cos\theta^{K^+}_{c.m.}$ and beam energy E_γ bins are shown in Fig. C.14 to Fig. C.28. The green and blue solid lines stand for the simulated Λ and Σ^0 shapes overlaid with the solid black real data. The background events of $\gamma p \to \pi^+ n$ due to K^+/π^+ mis-identification, appearing as a peak at $\sim$0.85 Gev/c^2 become more significant in the regions of larger beam energy and forward production angle. In the lower E_γ and backward region, the Monte-Carlo simulated Λ and Σ^0 shapes can describe the real data missing mass shapes qualitatively well.

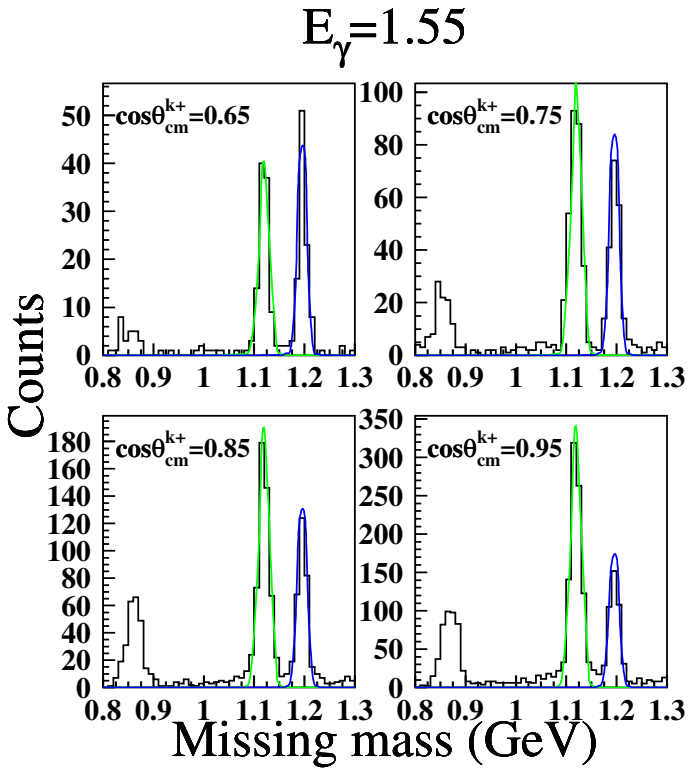

Figure C.14: The missing mass comparison of the generated Monte-Carlo simulation events and real data in E_γ=1.55 GeV.

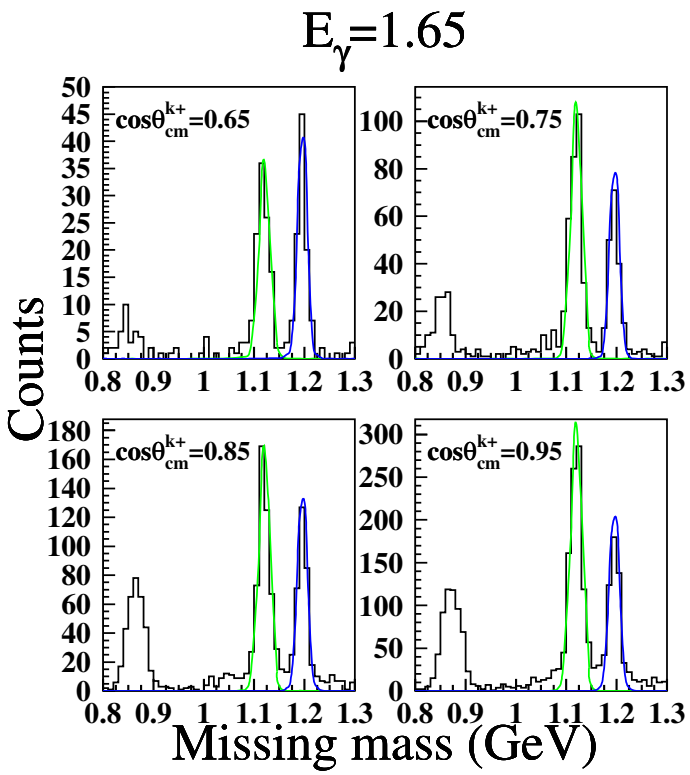

Figure C.15: The missing mass comparison of the generated Monte-Carlo simulation events and real data in E_γ=1.65 GeV.

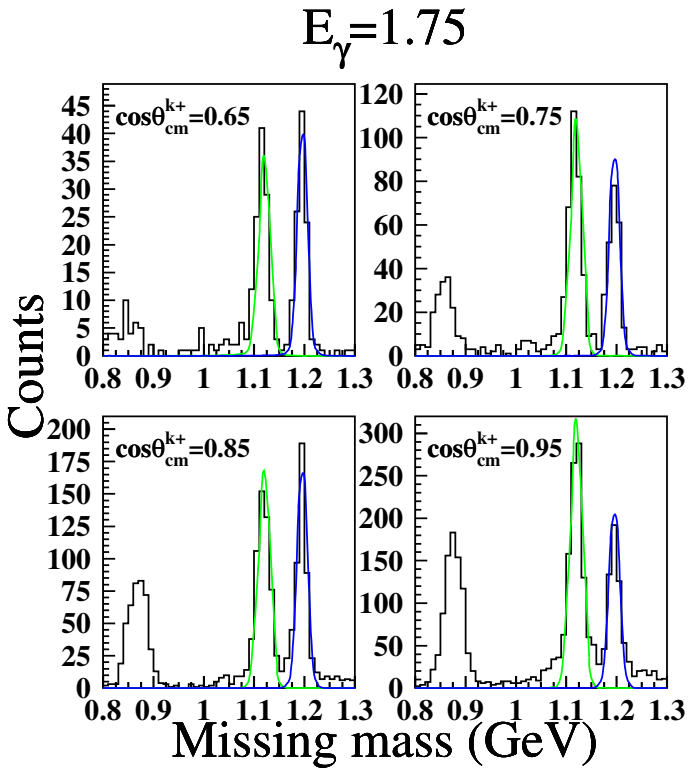

Figure C.16: The missing mass comparison of the generated Monte-Carlo simulation events and real data in E_γ=1.75 GeV.

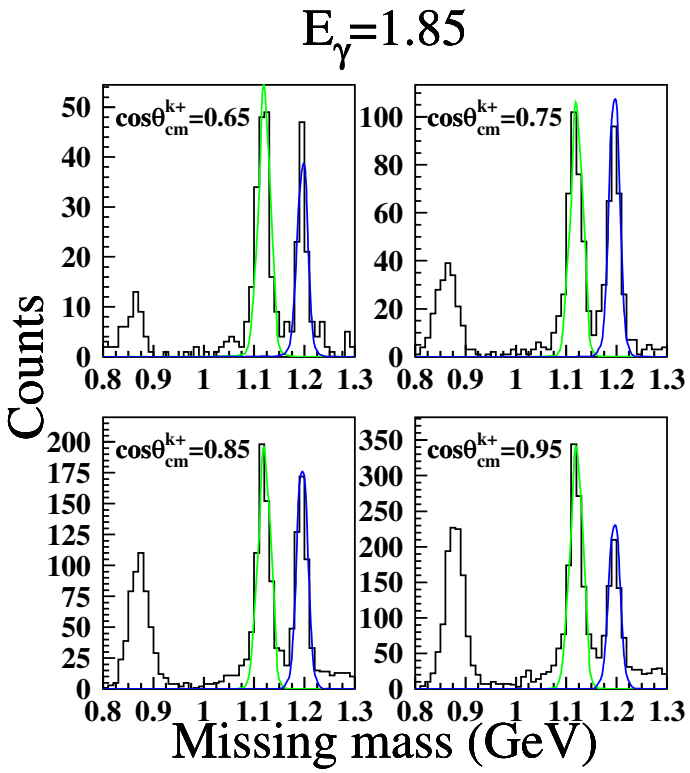

Figure C.17: The missing mass comparison of the generated Monte-Carlo simulation events and real data in E_γ=1.85 GeV.

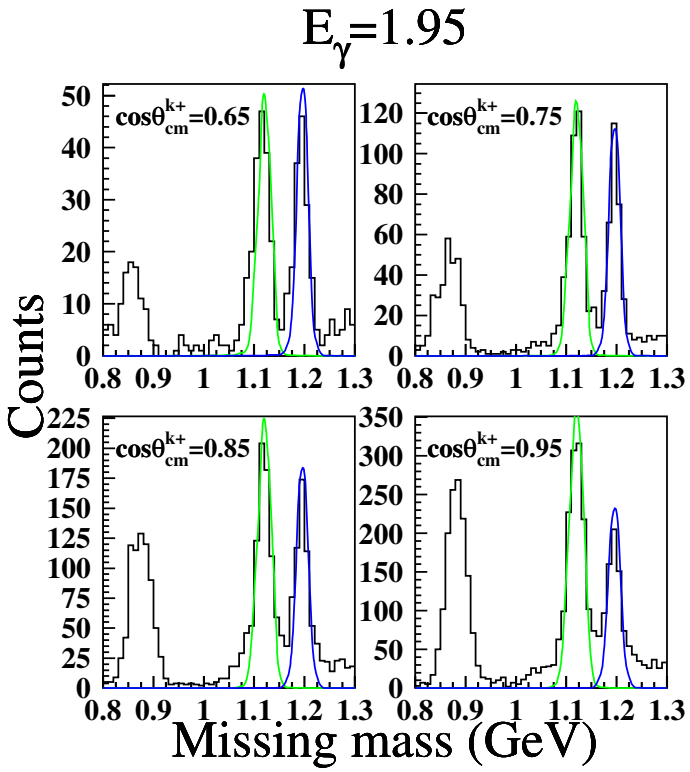

Figure C.18: The missing mass comparison of the generated Monte-Carlo simulation events and real data in E_γ=1.95 GeV.

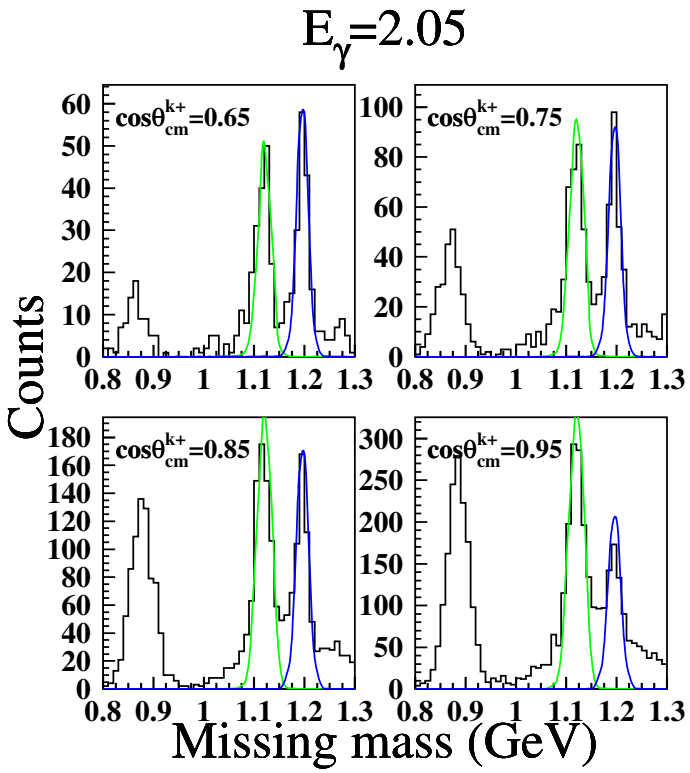

Figure C.19: The missing mass comparison of the generated Monte-Carlo simulation events and real data in E_γ=2.05 GeV.

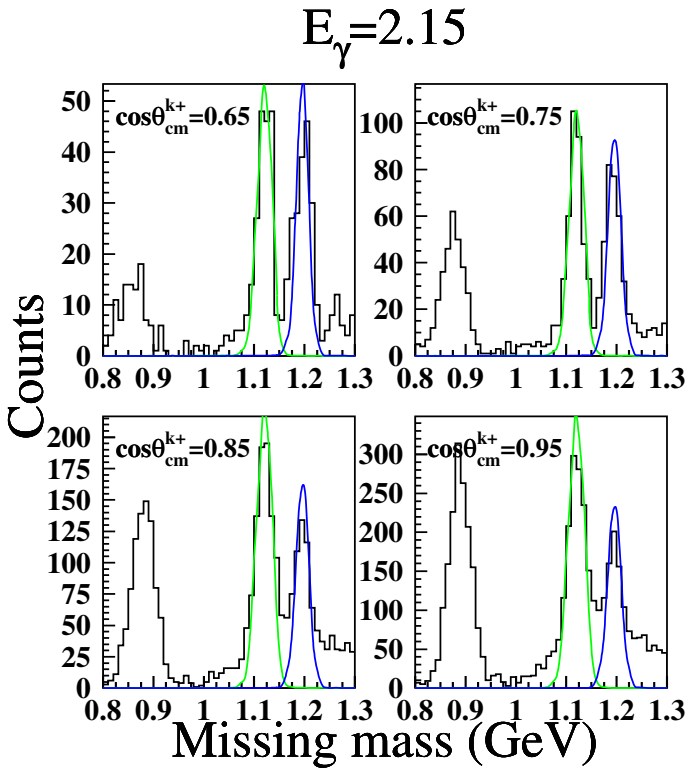

Figure C.20: The missing mass comparison of the generated Monte-Carlo simulation events and real data in E_γ=2.15 GeV.

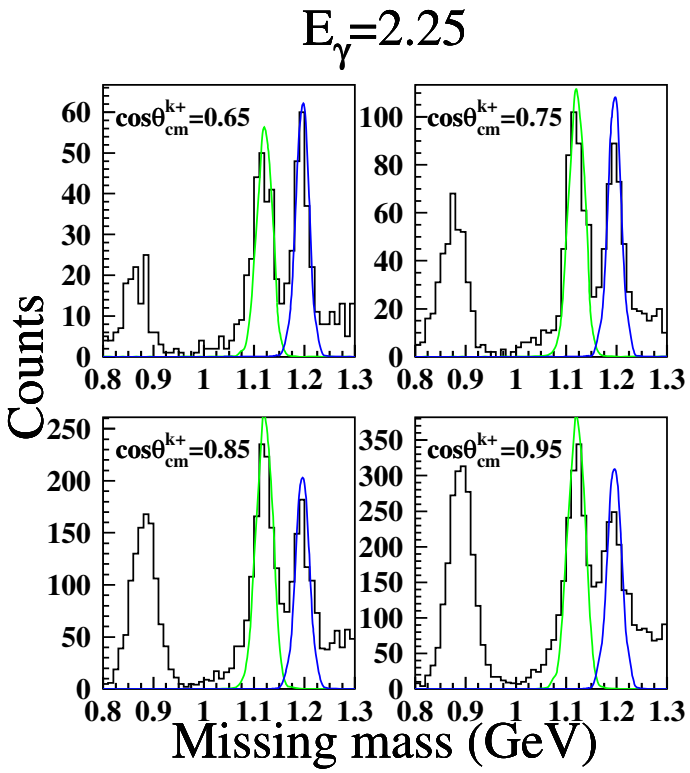

Figure C.21: The missing mass comparison of the generated Monte-Carlo simulation events and real data in E_γ=2.25 GeV.

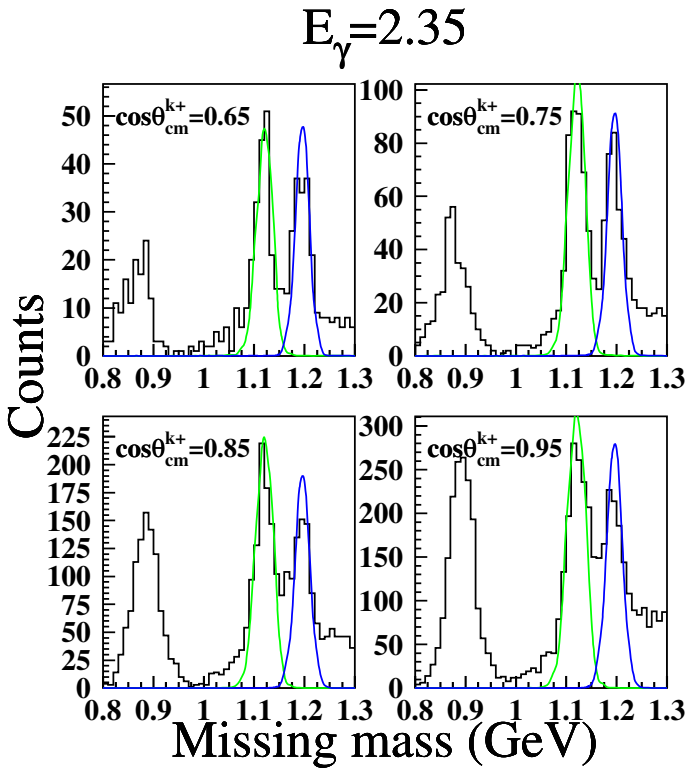

Figure C.22: The missing mass comparison of the generated Monte-Carlo simulation events and real data in E_γ=2.35 GeV.

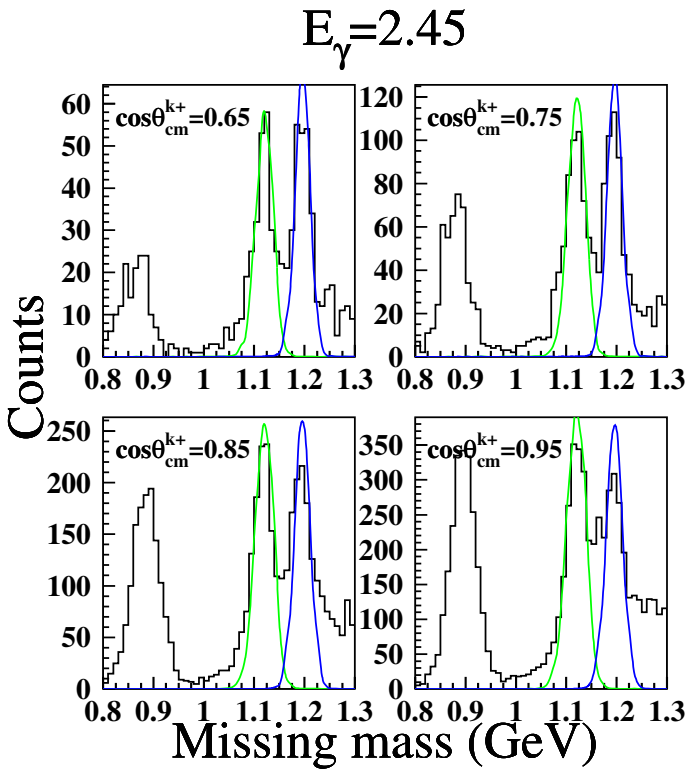

Figure C.23: The missing mass comparison of the generated Monte-Carlo simulation events and real data in E_γ=2.45 GeV.

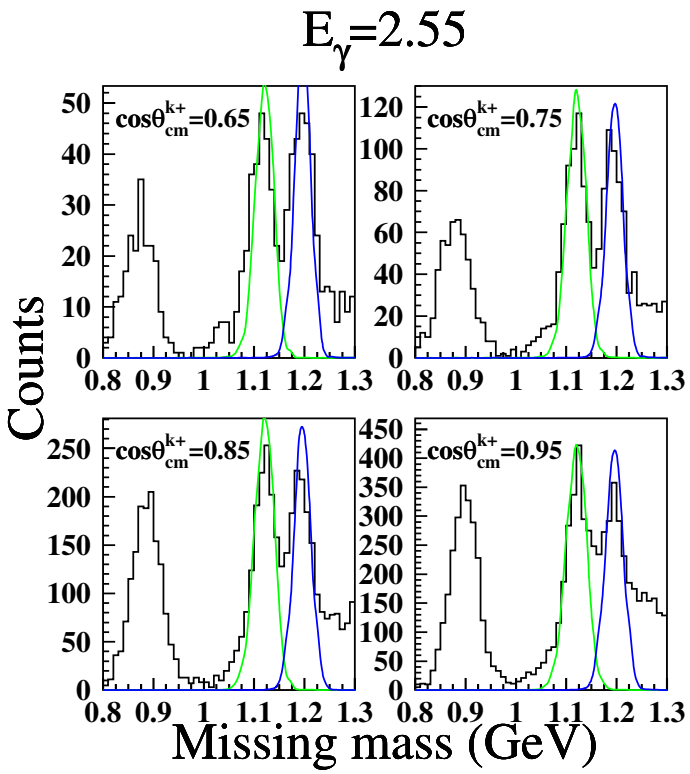

Figure C.24: The missing mass comparison of the generated Monte-Carlo simulation events and real data in E_γ=2.55 GeV.

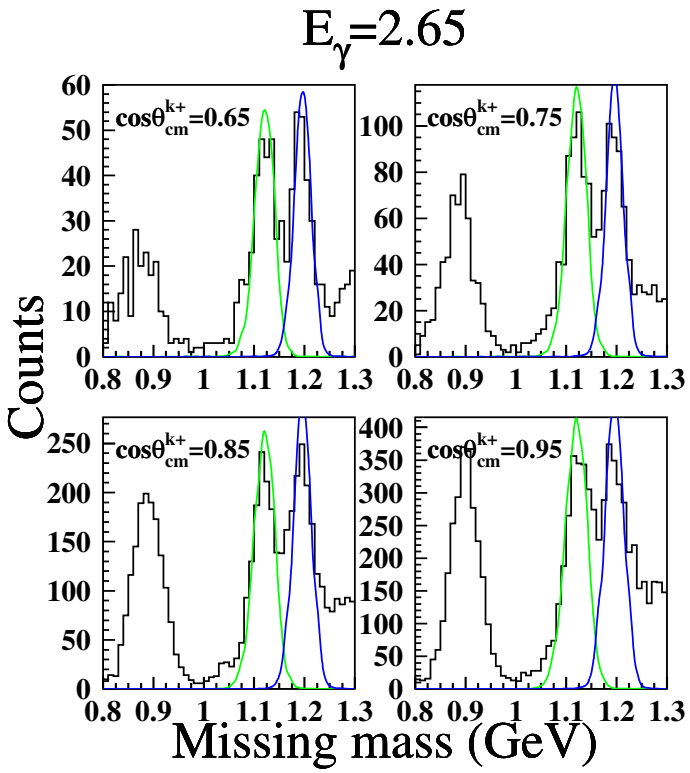

Figure C.25: The missing mass comparison of the generated Monte-Carlo simulation events and real data in E_γ=2.65 GeV.

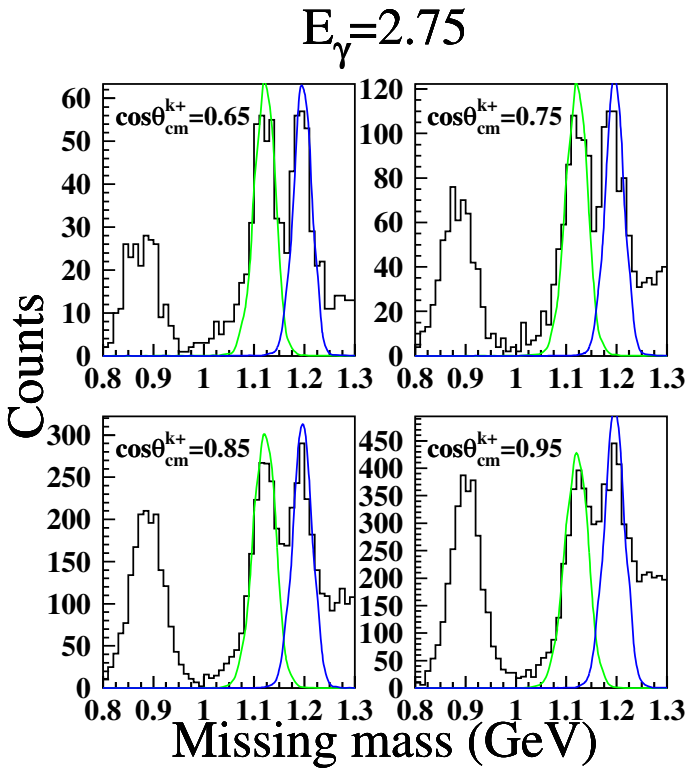

Figure C.26: The missing mass comparison of the generated Monte-Carlo simulation events and real data in E_γ=2.75 GeV.

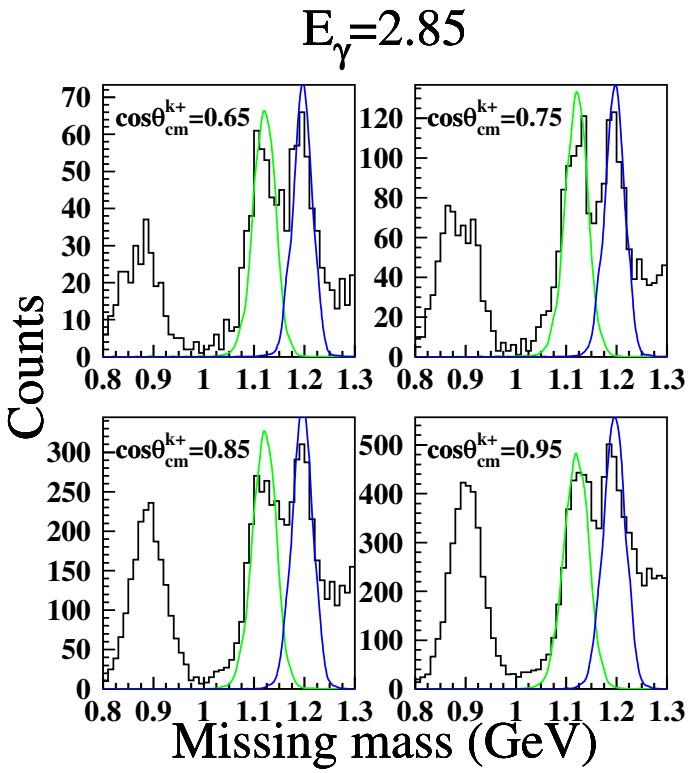

Figure C.27: The missing mass comparison of the generated Monte-Carlo simulation events and real data in E_γ=2.85 GeV.

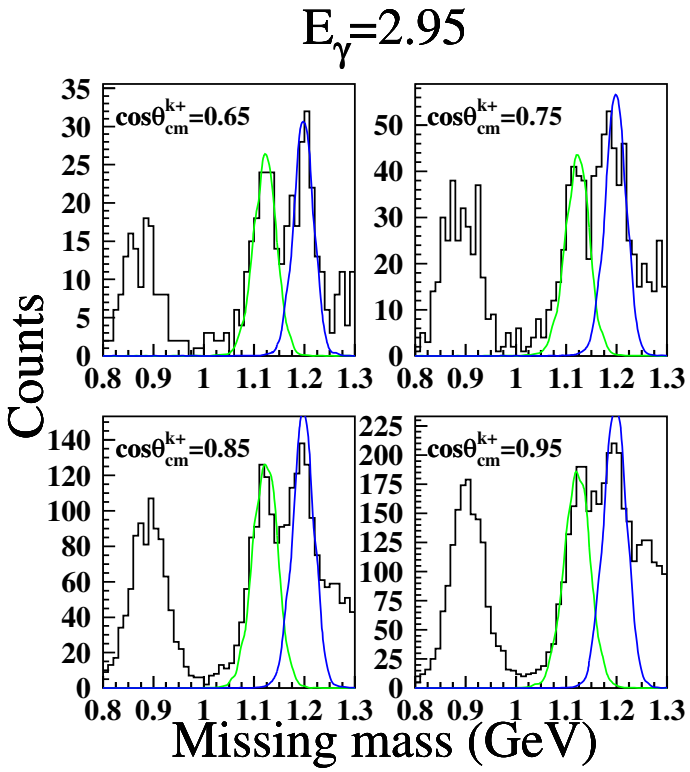

Figure C.28: The missing mass comparison of the generated Monte-Carlo simulation events and real data in E_γ=2.95 GeV.

Appendix D: Check the Monte-Carlo acceptance efficiency

The acceptance efficiency is checked by the following procedure. The checking procedure has been briefly described below. The checking starts from generating Monte-Carlo events with a flat angular distribution and the acceptance estimated by the flat distribution Monte-Carlo events were calculated. First-round cross sections calculated by the acceptance are obtained. Next, a new acceptance obtained by Monte-Carlo events weighted by the obtained angular slope is used for the evaluation of next-round differential cross sections. After a few iterations, the differential cross sections applied for the Monte-Carlo input and those obtained from the real data after the acceptance correction converge and remain unchanged. It also reflects that the Monte-Carlo-simulated acceptance becomes same as that of the real data. Fig. D.29 and Fig. D.30 show the weighted Monte-Carlo accepted data divided by real data counts which were obtained via the fitting with the estimated background and the K^+ missing mass of Λ and Σ^0 as a function of $\cos\theta^{K^+}_{c.m.}$ in various E_γ bins.

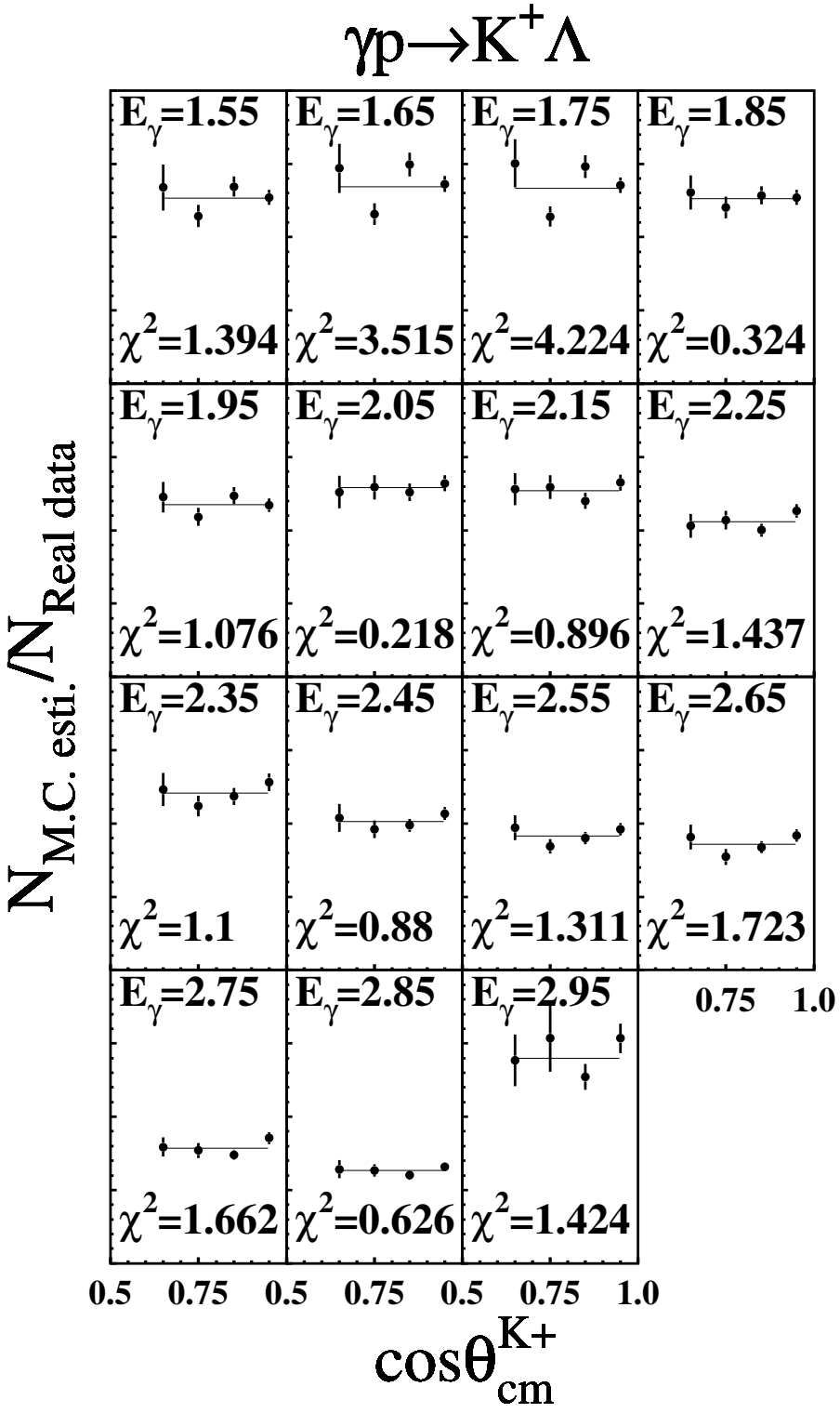

Figure D.29: Acceptance efficiency check for Λ as a function of $\cos\theta^{K^+}_{c.m.}$ in various E_γ bins.

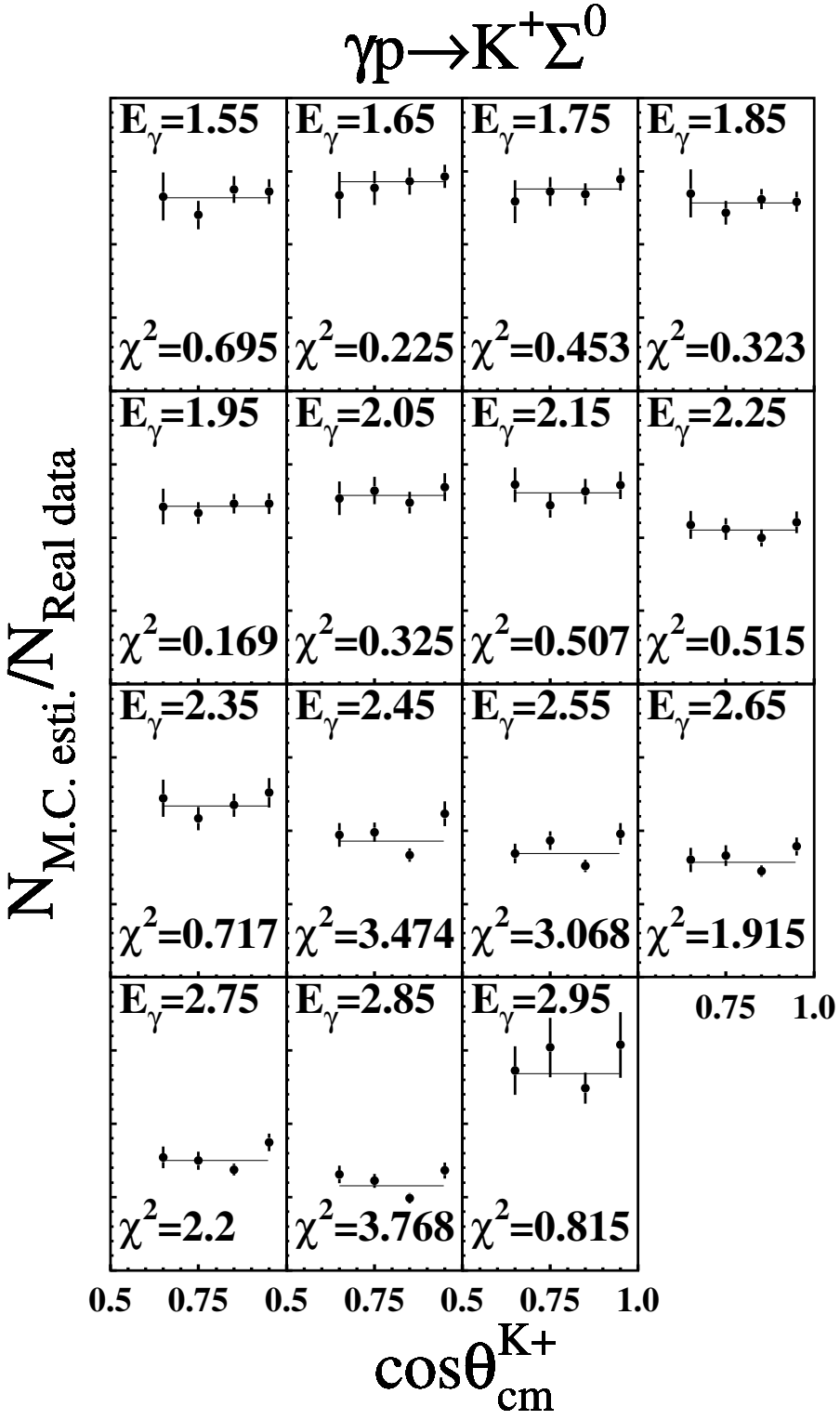

Figure D.30: Acceptance efficiency check for Σ^0 as a function of $\cos\theta^{K^+}_{c.m.}$ in various E_γ bins.